

University of Montana

ScholarWorks at University of Montana

Graduate Student Theses, Dissertations, &
Professional Papers

Graduate School

2004

Developing a satellite -based method of landscape drought assessment

James Plummer Riddering
The University of Montana

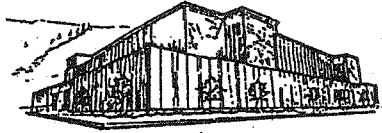
Follow this and additional works at: <https://scholarworks.umt.edu/etd>

Let us know how access to this document benefits you.

Recommended Citation

Riddering, James Plummer, "Developing a satellite -based method of landscape drought assessment" (2004). *Graduate Student Theses, Dissertations, & Professional Papers*. 9506.
<https://scholarworks.umt.edu/etd/9506>

This Dissertation is brought to you for free and open access by the Graduate School at ScholarWorks at University of Montana. It has been accepted for inclusion in Graduate Student Theses, Dissertations, & Professional Papers by an authorized administrator of ScholarWorks at University of Montana. For more information, please contact scholarworks@mso.umt.edu.



**Maureen and Mike
MANSFIELD LIBRARY**

The University of
Montana

Permission is granted by the author to reproduce this material in its entirety, provided that this material is used for scholarly purposes and is properly cited in published works and reports.

****Please check "Yes" or "No" and provide signature****

Yes, I grant permission

X

No, I do not grant permission

Author's Signature: James R. Riddley

Date: 26 May 2004

Any copying for commercial purposes or financial gain may be undertaken only with the author's explicit consent.

**DEVELOPING A SATELLITE-BASED METHOD OF
LANDSCAPE DROUGHT ASSESSMENT**

by

James Plummer Riddering

B.S. University of Montana, 1993


Presented in partial fulfillment of the requirements for the degree of

Doctor of Philosophy

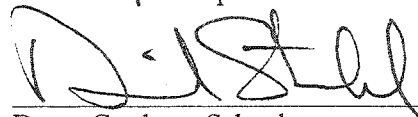
The University of Montana

May 2004

Approved by:



Committee Chairperson



Dean, Graduate School

5-26-04

Date

UMI Number: 3138418

INFORMATION TO USERS

The quality of this reproduction is dependent upon the quality of the copy submitted. Broken or indistinct print, colored or poor quality illustrations and photographs, print bleed-through, substandard margins, and improper alignment can adversely affect reproduction.

In the unlikely event that the author did not send a complete manuscript and there are missing pages, these will be noted. Also, if unauthorized copyright material had to be removed, a note will indicate the deletion.

UMI[®]

UMI Microform 3138418

Copyright 2004 by ProQuest Information and Learning Company.

All rights reserved. This microform edition is protected against unauthorized copying under Title 17, United States Code.

ProQuest Information and Learning Company
300 North Zeeb Road
P.O. Box 1346
Ann Arbor, MI 48106-1346

DEVELOPING A SATELLITE-BASED METHOD OF LANDSCAPE DROUGHT ASSESSMENT

Director: Dr. LLoyd P. Queen



This dissertation describes the major research components involved in the implementation, modification, and testing of a method for assessing surface moisture status with NOAA-AVHRR data, known as the Surface Moisture Index (SMI). Chapter two presents the initial landscape-scale development of the SMI model which is predicated on previous large-scale studies reviewed in chapter one. The initial landscape model relies on a moving neighborhood analysis that exploits the relationship between radiant surface temperature (T_s) and a spectral vegetation index, namely the Normalized Difference Vegetation Index (NDVI), to elucidate surface moisture status.

Chapter three describes the Water Deficit Index (WDI), another large-scale technique, the logic of which was adapted and used to modify the original SMI model. The WDI logic dictates the incorporation of near surface air temperature (T_a) as an input for the model. Since T_a is a critical component, a method for estimating this variable was necessary. Chapter four discusses the implementation and testing of the T_a technique used in subsequent model development. Three methods of estimating T_a were tested. These methods differed only in the manner that earth-sun-sensor geometry was used to impose constraints in the model calculations. The most rigorous method, which had the most sophisticated geometry constraints, resulted in the fewest actual predictions, but also showed the best results ($R = 0.742$, $MAE = 6.09$ °C).

The fifth chapter treats the final version of the SMI model. That model incorporates four significant revisions from the original model. Those are: (1) adaptation of the WDI logic for landscape-scale implementation, (2) inclusion of geometric constraints, (3) near-surface air temperature estimates, and (4) specification of a new landscape reporting unit. Validation exercises relied on a ten year comparison of SMI to the Palmer Z index, a popular index for tracking drought that relies on data from meteorological stations. The ability to predict Palmer Z from SMI values was assessed using the Autoregressive Integrated Moving Average (ARIMA) technique and resulted in excellent predictability with all coefficients being significant at the $\alpha = 0.05$ level.

Acknowledgements

I consider myself incredibly fortunate to have arrived at this stage and owe great debts of gratitude to many who have helped me along the way. My advisor, Dr. LLOYD Queen (...uggghhh...moose...), deserves special praise for all that he has done to facilitate my success. Dr. Queen has provided outstanding guidance, created opportunities for education that extended beyond the strict bounds of academia, and deserves special thanks for recruiting an outstanding cadre of employees and students throughout the years. I also wish to thank those who agreed to serve on my committee: Dr. Steve Running, Dr. Tom DeLuca, Dr. Ron Wakimoto, and Dr. Wei Min Hao, all of whom inspired me and provided top shelf advice and guidance. Additional salutes go to the past and present members of the Pixel Ranch, all of whom have had an impact on my academic career and my personal life. Special thanks to the following ranchers: Don Helmbrecht (an original bubba-fester) for his expertise and patience with my sometimes illiterate questions, Josh Rodriguez for his humor and his fearless approach to buckets of mixed hydrocarbons, and Eric Tangedahl for his technical expertise and for expanding the operational limitations of Toyota pickups. To the ranchers of old, Steve Brown, Eva Karau, and Kirsten Schmidt, who all helped make our corner of the science complex a great place to work, I offer my gratitude. To the new crop of pixel wranglers, I extend hearty thanks for continuing the tradition of irreverence and quality work. To Ken Brewer I say gracias and I hope you suffer no lasting effects from that fateful wall encounter. In considering all the people I've worked with, I must acknowledge my good friend Dr. Carl Seielstad. His insight, critical thought, and friendship have been instrumental to my success. Whether offering sagely advice or being a co-conspirator in any number of shenanigans, Carl was always there with good humor. How about a hearty sandwich and a round at the LT?

Throughout my tenure in this graduate program I have been very lucky to have worked with some outstanding people who have populated the island known as NTSG. These folks have and continue to inspire. Those deserving special recognition include Dr. Peter Thornton, Dr. Michael White, Dr. Rama Nemani, Joe Glassy, Saxon Holbrook, Petr Votava, and (the soon to be Dr.) Matt Jolly. Without these people, I often feel that I'd be in the weeds. Whether it be the incredible technical advice (not to mention the good humor in answering all my dumb questions) that Saxon, Peter, Joe, and Matt provided, or more importantly, the friendship and camaraderie that has developed over the years (the contributions to the Saxon poker fund notwithstanding). Perhaps the most gratifying part of being in this program is the fact that I get to work with the exceptional people that populate the west end of the science complex.

Others who deserve recognition include (soon to be Dr.) Colin (PD) Hardy, Alisa Keyser, Cate Crue, and Youngee Cho. Colin, who serves as a model of the person we can all aspire to be, has been a good friend and colleague and I thank him for everything. Alisa is a wonderfully valued friend who continues to make me laugh. Thank you for being you and approaching life with moxie. Cate and Youngee ride herd on this crazy stampede that is NTSG and the Fire Center. Without them the whole thing would likely fly apart.

Finally, I would like to thank three very special people to whom I owe everything. First, my mother Lynn Riddering, who taught me to be who I am, deserves special praise. Words can not do justice to what she has done for me, so a simple thank you will have to suffice. Second, my grandfather, Dr. Robert H. Plummer, who taught me the value of education and provided much of the means for my success, deserves acknowledgment. I do hope I have made him proud. Lastly, I would like to thank Dr. Hayley Hesselin, for everything over the years. Again my linguistic shortcomings prevent me from adequately saying what I wish to say. Therefore I will leave it with a simple thank you.

There are many others who have helped me along the way. The omission of their names in this section is not meant to belittle the role they have played. It has much more to do with my personal failings in doing justice to the acknowledgments these people so richly deserve. I hope I am forgiven by those I have failed to mention and will stand for vitamin R for all who dare at the corner of space and time. *Vita non est vivere sed valere vita est.*

Table of Contents

Abstract	ii
Acknowledgements	iii
Table of Contents	iv
List of Tables	vi
List of Figures	vii
PREFACE	1
CHAPTER 1: INTRODUCTION AND THEORY	2
BACKGROUND	2
LITERATURE REVIEW	4
SUMMARY	6
LITERATURE CITED	7
CHAPTER 2: DEVELOPMENT OF A LANDSCAPE SURFACE MOISTURE INDEX	9
ABSTRACT	9
INTRODUCTION	9
THE SURFACE MOISTURE INDEX MODEL	11
Algorithm Function	12
SURFACE MOISTURE INDEX PERFORMANCE	13
PERFORMANCE OF SMI AS A FIRE POTENTIAL INDEX	21
CONCLUSIONS	27
Compositing Method: Date and Geometry Effects	27
Stratification: Landcover and Terrain Effects	27
Operations: Computational Efficiency and Window Size	28
Suggestions for Further Research	29
LITERATURE CITED	30
CHAPTER 3: DERIVATION OF THE WATER DEFICIT INDEX	31
INTRODUCTION	31
THE WATER DEFICIT INDEX	32
Crop Water Stress Index	33
The Vegetation Index/Temperature Trapezoid	37
SUMMARY	42
LITERATURE CITED	43

CHAPTER 4: ESTIMATING NEAR-SURFACE AIR TEMPERATURE	44
INTRODUCTION	44
METHODS	45
Site Description.....	45
Satellite Data	47
Processing Stream.....	47
Surface Temperature (Part 1).....	49
Site Mask (Part 2)	50
Warm Edge Extraction - Ta technique (Part 3).....	51
DAYMET.....	54
Synchronization of DAYMET and T _a Estimate.....	55
Validation Strategy.....	56
RESULTS	57
v1- Goward	57
v2 – SATZ 30.....	59
v3 – SATZ30 & REL AZ.....	61
Summary	64
DISCUSSION AND CONCLUSIONS.....	64
Sources of Error	64
Efficiency.....	67
LITERATURE CITED	69
 CHAPTER 5: IMPLEMENTATION OF THE TRAPEZOID-BASED SURFACE MOISTURE INDEX ..	71
INTRODUCTION	71
MATERIALS AND METHODS	73
Trapezoid Development.....	73
Palmer Drought Indices.....	76
Data Structure	78
Time Series Analysis - Background.....	79
RESULTS	82
Time Series – Implementation	82
Autoregressive Integrated Moving Average	85
ARIMA Residual Analysis	88
DISCUSSION	88
CONCLUSIONS.....	95
APPENDIX A	97
LITERATURE CITED	160

List of Tables

CHAPTER 2	9
Table 1: Factor loadings for landcover, topography, and viewing geometry variables.....	14
Table 2: T_p /NDVI-Fire Size chi-square statistics for three landscapes	24
Table 3: Chi-square statistics for 'greenness' variables	24
CHAPTER 4	44
Table 1: Statistics for the three T_a implementations	59
Table 2: Regression coefficients for the three implementations of satellite T_a	59
CHAPTER 5	71
Table 1: Total cross-correlation for differenced Palmer Z and SMI for all years	82
Table 2: Cross-correlation (CC) and lag for differenced Palmer Z and SMI	84
Table 3: Lag adjusted cross-correlation for differenced Palmer Z and SMI	85
Table 4: ARIMA parameters for lag adjusted Palmer Z and SMI for all years.....	86
Table 5: ARIMA parameters for lag adjusted Palmer Z and SMI.....	87
Table A.1: Trapezoid parameters for each 4 th HUC.....	98

List of Figures

CHAPTER 1	2
Figure 1: Scatterplot showing water stress and non-stressed pixels.....	3
CHAPTER 2	9
Figure 1: Map of SMI values for the study area, composite	15
Figure 2: Ts/NDVI scatterplots stratified by date	17
Figure 3: Ts/NDVI scatterplots with water contamination	17
Figure 4: Map of SMI showing the edge effect around Fort Peck Reservoir in northeast Montana	19
Figure 5: Scatterplot with date bias.....	20
Figure 6: Scatterplot with edge effect illustrated	20
Figure 7: Land area within each stress category for composite Period 13	26
CHAPTER 3	31
Figure 1: WDI trapezoid	39
CHAPTER 4	44
Figure 1: Study site, Bitterroot Valley, western Montana, USA.....	46
Figure 2: Flowchart showing processing stream.....	48
Figure 3: Bitterroot Valley 4 th HUC and bottom 1000 feet.....	53
Figure 4: Scatterplot of Satellite air temperature estimates versus DAYMET air temperature	58
Figure 5: Satellite Zenith angle $\leq 30^\circ$	60
Figure 6: DAYMET T_a versus Satellite T_a (30° satellite zenith angle constraint).....	62
Figure 7: Scatterplot of satellite predicted T_a versus DAYMET T_a	63
CHAPTER 5	71
Figure 1: SMI processing stream flowchart	72
Figure 2: Montana 4 th Hydrologic Unit Codes.....	75
Figure 3: Montana climate divisions and counties.....	76
Figure A.1: Time sequence of SMI and Palmer Z for all climate divisions.....	100
Figure A.2: Cross-correlation by climate division	102
Figure A.3: Cross-correlogram for each year by climate division	106
Figure A.4: Palmer Z and predicted Palmer Z for all divisions	148
Figure A.5: P-P plots of ARIMA residuals by state climate division	152
Figure A.6: Palmer Z residuals versus SMI residuals, by climate division.....	156

PREFACE

The objective of this research is to develop a method of assessing surface moisture status/drought at landscape scales with satellite imagery. It is organized into five chapters, and begins with a brief review of the background and logic of the methods, which includes a review of the pertinent literature. Chapter two will discuss the original *landscape* implementation of the Surface Moisture Index (SMI) which was based on the work of Nemani et al. (1989) and Nemani and Running (1993). While engaged in the research presented in chapter two, a number of shortcomings were identified and discussed. To mitigate these problems, I chose to adopt some of the logic from the Water Deficit Index (WDI, Moran et al., 1994a) which will be explained in chapter three. One of the critical inputs for the WDI technique and the subsequently modified SMI method is that of near surface air temperature estimates (T_a). Chapter four will discuss the satellite-based techniques I developed to derive these air temperature estimates. Finally, chapter five will discuss the implementation and validation of the final satellite based landscape drought technique. A discussion is included therein that considers the performance of the final implementation and provides suggestions for future research.

CHAPTER 1

INTRODUCTION AND THEORY

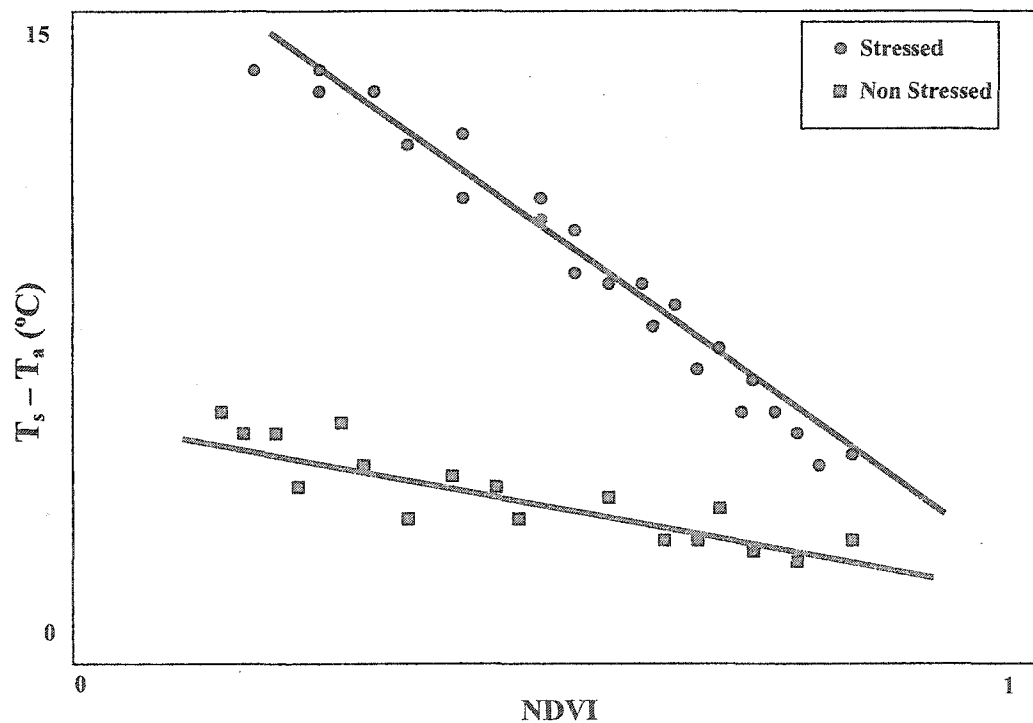
BACKGROUND

The relationship between radiant surface temperature (T_s) and spectral vegetation indices (e.g. Normalized Difference Vegetation Index) has often been used to investigate surface energy fluxes and as a surrogate for detecting vegetation water stress (Nemani and Running, 1989; Carlson et al., 1990; Smith and Choudhury, 1991; Nemani et al., 1993; Carlson et al., 1994; Kustas et al., 1994; Vidal et al., 1994; Vidal and Devaux-Ros, 1995; Moran et al., 1996; Laguette et al., 1998; Duchemin et al., 1999). The logic of coupling radiant surface temperature with vegetation indices to deduce surface moisture status relies on the covariance of these two parameters with changing surface moisture conditions. Two of the primary drivers of surface temperature (whether that surface is soil, vegetation or a mix) are net radiation (R_n) and the amount of water available for evaporation and/or transpiration (ET) (Jones, 1992; Moran et al., 1994b). For a given amount of radiant flux density incident at the surface and assuming consistent meteorological parameter (e.g. VPD, wind speed), the amount of available water dictates the partitioning of energy to sensible or latent heat flux. If the surface has water available, the primary partition will be to latent heat flux (Jones, 1992; Moran et al., 1994b; Nemani et al., 1993). The result is a comparatively "cool" radiant surface temperature. This relationship, however, varies with the fractional vegetation cover (Carlson et al., 1994; Moran et al., 1994b; Nemani et al., 1993; Smith and Choudhury, 1991).

Figure 1 displays a scatterplot of surface temperature minus air temperature ($T_s - T_a$) and Normalized Difference Vegetation Index (NDVI) for both moist and dry conditions. For an area with an adequate range of vegetation cover and plentiful water the slope of the line fit to the scatterplot will be nearly flat due to absorbed energy causing surface soil moisture evaporation in bare soil areas (Nemani et al., 1993). The result is a surface temperature near that of actively transpiring vegetation. The converse is also true where lack of surface moisture causes the slope of the line to become more negative. The bare areas will divert the energy to sensible heat flux resulting in surface temperatures above that of vegetation. This is

not to say that surface temperature of full vegetation does not change with water availability, rather, vegetation has access to sub-surface water and is better able to regulate water loss below that of bare soil (Jones, 1992). The resulting assumption is that in areas with diverse vegetation cover, the relationship between surface temperature and vegetation cover will change with water availability and this relationship can be exploited in the development of operational methods for monitoring surface moisture status and drought.

Figure 1: Theoretical scatterplot illustrating water stress and non-stressed pixels.



Most studies utilizing the T_s /spectral vegetation index (T_s/VI) logic have focused on large-scale (small geographic extent), low temporal resolution assessments of surface energy budgets (e.g. (Carlson et al., 1995; Nemani and Running, 1989; Saha, 1995; Smith and Choudhury, 1991; Vidal and Devaux-Ros, 1995)). Though many of these studies have been concerned specifically with solving surface energy parameters, the utility of this logic for monitoring drought and fire potential has been suggested (Moran et al., 1994a;

Nemani et al., 1993; Vidal and Devaux-Ros, 1995). Since both drought and vegetation fire potential can be modeled as a function of surface energy status (decreases of ET below potential ET is indicative of vegetation water stress), the use of these methods for drought and fire potential monitoring logically follows. In spite of this, there is, historically, a noticeable lack in the use of these techniques for surface moisture and drought monitoring applications. A notable exception being Vidal and Devaux-Ros (1995) who showed that large fire activity was correlated with a derivative of the T_s /spectral vegetation index (T_s /VI) logic.

LITERATURE REVIEW

One of the earliest studies combining surface temperature with a vegetation index to infer surface energy budget parameters was that of Nemani and Running (1989). They used the Advanced Very High Resolution Radiometer (AVHRR) to calculate the NDVI and surface temperature via a split window technique over the Lubrecht Experimental Forest in Montana. They tested how this relationship compared with modeled surface resistance for eight composite periods throughout the growing season. Forest-BGC and local meteorological data were used to simulate canopy resistance. A strong correlation between the slope of T_s /NDVI and simulated resistance was observed throughout the season. Interestingly, the T_s /NDVI slope was able to track a period of drought in June and July and drought recovery that came with August rains. The authors conclude by suggesting that since surface resistance is the primary control on latent heat flux, the T_s /NDVI relationship may be useful in regional studies of evapotranspiration by providing qualitative information on surface resistance.

Carlson and others (1990) attempted to derive fractional vegetation cover, surface energy fluxes, and root zone soil surface moisture in areas with partial vegetation cover. They combined a boundary layer model that contained vegetation and substrate parameters with two image products: T_s /NDVI and standard deviation of T_s versus T_s . Imagery was obtained from an airborne sensor with spatial resolution of approximately 4 m at nadir. It was assumed the T_s /NDVI relationship was controlled by fractional

vegetation cover. The information of T_s versus standard deviation of T_s was used to define the endpoints of full canopy coverage and complete bare soil. The boundary layer model was then used to calculate root zone and soil surface water content by forcing a solution for these parameters that resulted in a match between simulated and observed surface temperatures. The authors stated that the method required testing against various types of soil and vegetation and suggest that AVHRR might be useful in this endeavor. They also mention, however, that low spatial resolution sensors such as AVHRR may not be able to produce the complete range of NDVI and T_s values needed for this type of application.

Smith and Choudhury (1991) explored the relationship between surface temperature and spectral reflectance in Australia using a single Landsat Thematic Mapper (TM) image. They found overall negative relationships between a vegetation index and T_s in agricultural areas, but not in evergreen forests. Using a two-layer (soil and vegetation) energy balance model to explore the T_s /VI logic, they found fractional vegetation cover to be the major control on T_s . Residual variability in the relationship was attributed to differences in ambient air temperature, soil water availability, and stomatal resistance as controlled by phenological development. It was suggested that biome should be accounted for when modeling surface moisture parameters and that the SMI response is sensitive to soil and vegetation contributions. Overall, the authors were not confident about the ability of T_s /VI relationships to predict surface moisture status.

Building on their previous work, Nemani and others (1993) revisited the T_s /NDVI relationship and explored: 1) the effect of biome on T_s /NDVI, 2) automated methods of defining the T_s /NDVI relationship, 3) optimal window size, and 4) continental-scale comparisons of T_s /NDVI changes to moisture status. Several AVHRR images were obtained throughout the growing season for an area of 300x300 km for use in this study. The first conclusion drawn from this study was that the T_s /NDVI relationship is primarily controlled by vegetation fraction viewed by the sensor. Surface moisture status, however, was identified as being an important component of the T_s /NDVI response. It was found that date of imagery had no effect on optimum neighborhood size, while biome type did. A related conclusion was the idea that topographic effects must either be held constant or explicitly accounted for when implementing the T_s /NDVI logic in

complex terrain. The comparisons of $T_s/NDVI$ with landscape scale moisture status assessments proved encouraging. The crop moisture index (CMI), which measures short-term soil moisture variations in the top five feet, was used for comparison and $T_s/NDVI$ was found to track fluctuations in CMI. The authors conclude this paper with the statement that $T_s/NDVI$, upon further development, would be useful in monitoring fire danger.

SUMMARY

From the literature discussed above, four critical points can be identified when considering the implementation of a model for deducing surface moisture status based on the surface temperature and spectral vegetation index relationship. These are summarized as bullet points below.

- A diversity of vegetation cover, as measured by NDVI, is required to assess moisture status at the surface.
- The $T_s/NDVI$ relationship has been shown to change with water availability.
- The $T_s/NDVI$ relationship has been used or suggested for use in monitoring drought, evapotranspiration and surface resistance, surface moisture status, and fire danger. All of these are related insofar as water availability impacts vegetation.
- The basic logic of surface temperature and spectral vegetation indices can be applied over many biomes, however a control must be provided for biome.

Based on this foundation, the following chapters of this dissertation will describe the process followed in the development of a new method for assessing surface moisture status at landscape scales. Chapter 2 will discuss the original landscape implementation of the $T_s/NDVI$ technique and will include an assessment of the model performance. Chapter 3 will introduce the Water Deficit Index which serves as a foundation for subsequent developmental work. Chapter 4 describes a technique of estimating near surface air temperatures which is a critical component in elucidating surface moisture condition. Finally, chapter 5 will illustrate the final landscape technique for modeling surface moisture status.

LITERATURE CITED

- Carlson, T.N., Gillies, R.R. and Perry, E.M., 1994. A Method to Make Use of Thermal Infrared Temperature and NDVI Measurements to Infer Surface Soil Water Content and Fractional Vegetation Cover. *Remote Sensing Reviews*, 9: 161-173.
- Carlson, T.N., Gillies, R.R. and Schmugge, T.J., 1995. An Interpretation of Methodologies for Indirect Measurement of Soil Water Content. *Agricultural and Forest Meteorology*, 77: 191-205.
- Carlson, T.N., Perry, E.M. and Schmugge, T.J., 1990. Remote Estimation of Soil Moisture Availability and Fractional Vegetation Cover for Agricultural Fields. *Agricultural and Forest Meteorology*, 52: 45-69.
- Duchemin, R., Guyon, D. and Lagouarde, J.P., 1999. Potential and Limits of NOAA-AVHRR Temporal Composite Data for Phenology and Water Stress Monitoring of Temperate Forest Ecosystems. *International Journal of Remote Sensing*, 20(5): 895-917.
- Jones, H.G., 1992. *Plants and Microclimate: A Quantitative Approach to Environmental Plant Physiology*. Cambridge University Press, Cambridge, 428 pp.
- Kustas, W.P., Moran, M.S., Humes, K.S., Stannard, D.I., Pinter Jr., P.J., Hipps, L.E., Swiatek, E. and Goodrich, D.C., 1994. Surface Energy Balance Estimates at Local and Regional Scales Using Optical Remote Sensing from an Aircraft Platform and Atmospheric Data Collected Over Semiarid Rangelands. *Water Resources Research*, 30(5): 1241-1259.
- Laguet, S., Vidal, A. and Vossen, P., 1998. Using NOAA-AVHRR Data to Forecast Wheat Yields at a European Scale. In: D. Rijks, J.M. Terres and P. Vossen (Editors), *Agrometeorological Applications for Regional Crop Monitoring and Production Assessment*. Joint Research Centre, European Commission, pp. 131-146.
- Moran, M.S., Clarke, T.R., Inoue, Y. and Vidal, A., 1994a. Estimating Crop Water Deficit Using the Relation Between Surface-Air Temperature and Spectral Vegetation Index. *Remote Sensing of Environment*, 49: 246-263.
- Moran, M.S., Kustas, W.P., Vidal, A., Stannard, D.I., Blanford, J.H. and Nichols, W.D., 1994b. Use of Ground-based Remotely Sensed Data for Surface Energy Balance Evaluation of a Semiarid Rangeland. *Water Resources Research*, 30(5): 1339-1349.
- Moran, M.S., Rahman, A.F., Washburne, J.C., Goodrich, D.C., Weltz, M.A. and Kustas, W.P., 1996. Combining the Penman-Monteith Equation with Measurements of Surface Temperature and Reflectance to Estimate Evaporation Rates of Semiarid Grassland. *Agricultural and Forest Meteorology*, 80: 87-109.
- Nemani, R., Pierce, L., Running, S. and Goward, S., 1993. Developing Satellite-derived Estimates of Surface Moisture Status. *Journal of Applied Meteorology*, 32(3): 548-557.
- Nemani, R.R. and Running, S.W., 1989. Estimation of Regional Surface Resistance to Evapotranspiration from NDVI and Thermal-IR AVHRR Data. *Journal of Applied Meteorology*, 28(4): 276-284.
- Saha, S.K., 1995. Assessment of Regional Soil Moisture Conditions by Coupling Satellite Sensor Data with a Soil-Plant System Heat and Moisture Balance Model. *International Journal of Remote Sensing*, 16(5): 973-980.

- Smith, R.C.G. and Choudhury, B.J., 1991. Analysis of Normalized Difference and Surface Temperature Observations Over Southeastern Australia. *International Journal of Remote Sensing*, 12(10): 2021-2044.
- Vidal, A. and Devaux-Ros, C., 1995. Evaluating Forest Fire Hazard with a LANDSAT TM derived Water Stress Index. *Agricultural and Forest Meteorology*, 77: 207-224.
- Vidal, A., Pinglo, F., Durand, H., Devaux-Ros, C. and Maillet, A., 1994. Evaluation of a Temporal Fire Risk Index in Mediterranean Forests from NOAA Thermal IR. *Remote Sensing of Environment*, 49: 296-303.

CHAPTER 2

DEVELOPMENT OF A LANDSCAPE SURFACE MOISTURE INDEX

ABSTRACT

A new method for modeling surface moisture status at continental scales utilizing the Moderate Resolution Imaging Spectroradiometer (MODIS) surface resistance logic is under development for use in fire science. A preliminary implementation of the algorithm, using NOAA Advanced Very High Resolution Radiometer (AVHRR) data, has been completed. The surface moisture index (SMI) uses the Normalized Difference Vegetation Index (NDVI) and radiant surface temperature (T_s) to assess surface moisture status. The results of a validation effort designed to address algorithm performance issues, potential shortcomings in the current implementation, and areas where the logic and implementation perform in an adequate manner are presented. Fire potential validation efforts were made using an historic database of fire occurrence obtained from the U.S. Bureau of Land Management (BLM). The area of interest was constrained to Idaho and Montana for the summer of 1994 due to prevailing dry conditions across the landscape and high fire activity. Preliminary findings from this study are presented and potential users are introduced to the logic and applications of the MODIS surface moisture products.

INTRODUCTION

Heat flux at the earth's surface is driven primarily by incident solar radiation and water availability. Dry surfaces are dominated by sensible heat flux, which manifests itself by increasing radiant surface temperatures (T_s). Generally, as water availability increases, more energy is partitioned to latent heat flux resulting in a relative reduction in T_s (Monteith, 1981). The partitioning of energy between latent and sensible heat is also influenced by several other biophysical variables including vapor pressure deficit, boundary layer conductance, canopy surface resistance, wind speed, and surface roughness (Jones, 1992; Whitehead, 1998). Despite these potentially confounding effects, recent studies have shown that when thermal infrared measurements of T_s are coupled with spectral vegetation indices, surface wetness can be

inferred (Nemani and Running, 1989; Carlson et al., 1990; Nemani et al., 1993; Carlson et al., 1994).

Nemani et al. (1993) demonstrated that the slope of a T_s /Normalized Difference Vegetation Index (NDVI) line is strongly correlated with surface moisture status.

We believe this logic may be significant for regional-scale fire potential monitoring and have adopted it as the basis for development of an Earth Observing System (EOS) fire potential product. Using NOAA's Advanced Very High Resolution Radiometer (AVHRR), T_s /NDVI scores are calculated at continental scales to investigate its suitability for this application. By implementing the logic now, we are better prepared to adapt it to the upcoming EOS Moderate Resolution Imaging Spectroradiometer (MODIS) data stream. A surface moisture status product based on the work described here will become a post-launch product of MODIS in 2001.

Following, preliminary results from development of the fire potential index based on the Nemani et al.'s (1993) previously described logic are presented. The goal is to explore the performance of a computationally efficient version of the T_s /NDVI algorithm in Montana and Idaho during the 1994 fire season. Although the current implementation of T_s /NDVI logic is run for the conterminous United States, Idaho and Montana were selected as the initial test bed for assessing its performance as a fire potential index. The study area was selected for several reasons: it is diverse in terms of landcover and terrain, it is data rich, it has representation by multiple agencies, and has frequent fires. The area also is well known by the authors from previous fieldwork. The 1994 fire season was chosen because it was one of the busiest on record. In Idaho and Montana, 4,436 fires burned 899,818 acres on USFS and BLM land alone.

In this paper the following questions will be addressed: (1) what factors determine the performance of T_s /NDVI? (2) How can the algorithm be run efficiently while still accounting for subpixel cloud, water, and shaded slope contamination? (3) Can T_s /NDVI be effectively related to measures of actual fire potential?

THE SURFACE MOISTURE INDEX MODEL

The major control on surface temperature, excepting incident energy, is the amount of water available for diverting incident radiation from sensible heat flux to latent heat flux (Monteith, 1981; Shuttleworth, 1991). By attempting to assess moisture status without explicitly accounting for the role of vegetation in partitioning energy to latent heat, early studies of latent heat flux (e.g., Priestley and Taylor, 1972) missed the fundamental control limiting evaporative loss below the potential (where potential is defined by the physical environment only). This method of assessing moisture status relies on the previously discussed means of monitoring vegetation status and measuring surface temperature. By incorporating remote measures of vegetation condition coupled with temperature data, landscape moisture changes in the soil/vegetation surface can be more effectively monitored. The method relies on the strong negative relationship between radiometric surface temperature and fractional vegetation cover.

The logic behind the surface moisture index has been extensively described elsewhere (see Nemani and Running, 1989). Briefly, it relies on calculating the relationship between NDVI and T_s . Generally, for a given landscape, as NDVI increases, T_s will decrease. This is due to vegetation's ability to regulate T_s by partitioning absorbed radiation to latent heat flux (via evapotranspiration) rather than sensible heat flux. Absorbed radiation and water availability are the two primary controls on T_s for a given surface. As water becomes limited at that surface, whether vegetated or not, the absorbed energy will be partitioned to sensible heat flux and the radiant temperature of that surface will increase. The core of the SMI logic relies on these biophysical principals for monitoring surface moisture status. If a surface is wet, T_s will be low. However, as that surface dries, the T_s will increase accordingly. The relative increase in T_s is more significant in low NDVI areas, corresponding to bare soil or sparse vegetation. In high NDVI areas the relative change in T_s is not as noticeable due to the aforementioned ability of vegetation to regulate water relations. This is particularly true of forested areas that have access to sub-surface water. The result is a negative relationship between NDVI and T_s . As a given area dries, one would expect the relationship between NDVI and T_s , as measured by the slope of a line fit to the T_s /NDVI scatterplot, to become

increasingly negative due to an increased T_s for the low NDVI areas. It is this relationship that is the logical basis for the fire potential index.

Algorithm Function

Previous studies have explored local moisture status utilizing the relationship between T_s and NDVI in a fashion similar to this implementation (Nemani and Running, 1989; Nemani et al., 1993; Carlson et al., 1981; Carlson et al., 1990; Carlson et al., 1994). A primary point of departure, however, is that these studies were concerned with large-scale (small geographic extent) assessment whereas this logic has been implemented at continental scales. Regardless of the scale used, a neighborhood of NDVI values and their associated T_s is required to fit the line used to estimate stress. At large scales, this neighborhood would likely be defined simply to the boundaries of the watershed or forest of interest. At small scales, however, the neighborhood used must be explicitly defined and needs to account for landcover heterogeneity while still collecting a sample large enough for defining the T_s /NDVI relationship.

The current version of the SMI algorithm uses a 21 x 21 pixel neighborhood that moves across the images one pixel at a time. A neighborhood size of 21 was chosen based partly on the work of Nemani et al., (1993) and an assessment of sensitivity done with an early version of the SMI algorithm. It was discovered that this neighborhood size initially provided the best sensitivity while still conferring computational efficiency. In addition, the question of Type I and Type II errors was considered. It is preferable to overestimate "dryness" rather than underestimate it for fire applications. By sliding the window one pixel between calculations, it was hoped to address moisture status in a spatially explicit manner and to allow for landcover variations to influence the SMI gradually.

Similar to that of Nemani et al. (1993), channel 4 and channel 5 data are read by the algorithm and converted to T_s following the method of Price (1984). NDVI, from composite data, is then ingested and used to assign an NDVI value and T_s value to each pixel in the image. Next, neighborhoods are subset

beginning at pixel (1,1) and sorted such that the maximum T_s for each unique NDVI score greater than 0.2 in the neighborhood is retained for regression analysis. By sorting and retaining maximum T_s for each NDVI value, cloud contamination is minimized, near nadir pixels are preferentially selected, and shading is minimized (see Nemani et al., 1993 for full discussion). Constraining NDVI to values greater than 0.2 assures that only vegetated areas are used in the analysis and eliminates problems of sub-pixel water contamination. The value of 0.2 was empirically derived, but is similar to that of Carlson et al. (1994) who chose an NDVI score of 0.17 for uncontaminated bare ground pixels.

Upon completion of the sorting function, a least squares regression is fit to the retained pixels and the slope of the line is assigned to the *center* pixel of the neighborhood for use in the SMI. Other statistics such as R^2 and the Y intercept are also saved in separate files. The neighborhood window then shifts one pixel and begins again. It is worth noting that for each composite period, greater than 10 *billion* calculations are performed in the generation of SMI. Enough computational efficiency was met for continental runs such that total run time is approximately 2.5 hours with the current compute infrastructure (IBM 43P-240T UNIX workstation). These benchmarks are significant as the launch of MODIS-PM approaches and the desire for increased temporal resolution (daily) and tandem (MODIS and AVHRR) calculation of SMI products increases.

SURFACE MOISTURE INDEX PERFORMANCE

During each composite period of the 1994 fire season, the highest T_s /NDVI values consistently appear in valley bottoms and in the rolling high plains of eastern Montana (Figure 1). The mountain forests of central Idaho and the northern Rockies exhibit little stress throughout the growing season, despite the fact that this was one of the most active fire seasons on record. This observation suggests that estimates of T_s /NDVI are sensitive to landscape or biome type. Although Nemani et al. (1993) note that vegetation type and topography are important considerations in selection of window size for model execution, the effect of landscape heterogeneity remains untested at a regional scale.

A factor analysis was performed to explore the interdependence of landscape parameters that are relevant to $T_s/NDVI$ derived estimates of surface moisture (Table 1). The primary process-based drivers of variability are meteorology, topography, biome-type, and viewing geometry. The variables used in the factor analysis are slope, aspect, elevation, percent evergreen needleleaf forest (ENF), percent deciduous broadleaf forest (DBF), percent grass, percent agriculture (AG), date and satellite zenith angle (SATZ). The variables were chosen based upon their expected utility and upon availability; and do not include system-based effects such as data scaling, calibration, or signal/noise ratios. Meteorological variables are conspicuously absent from the analysis because spatially continuous data are not presently available.

Table 1: Factor loadings for landcover, topography, and viewing geometry variables. Factor 1 accounts for 22 percent of variance, factor 2, 19 percent, and factor 3, 8 percent.

Rotated Factor Matrix^a

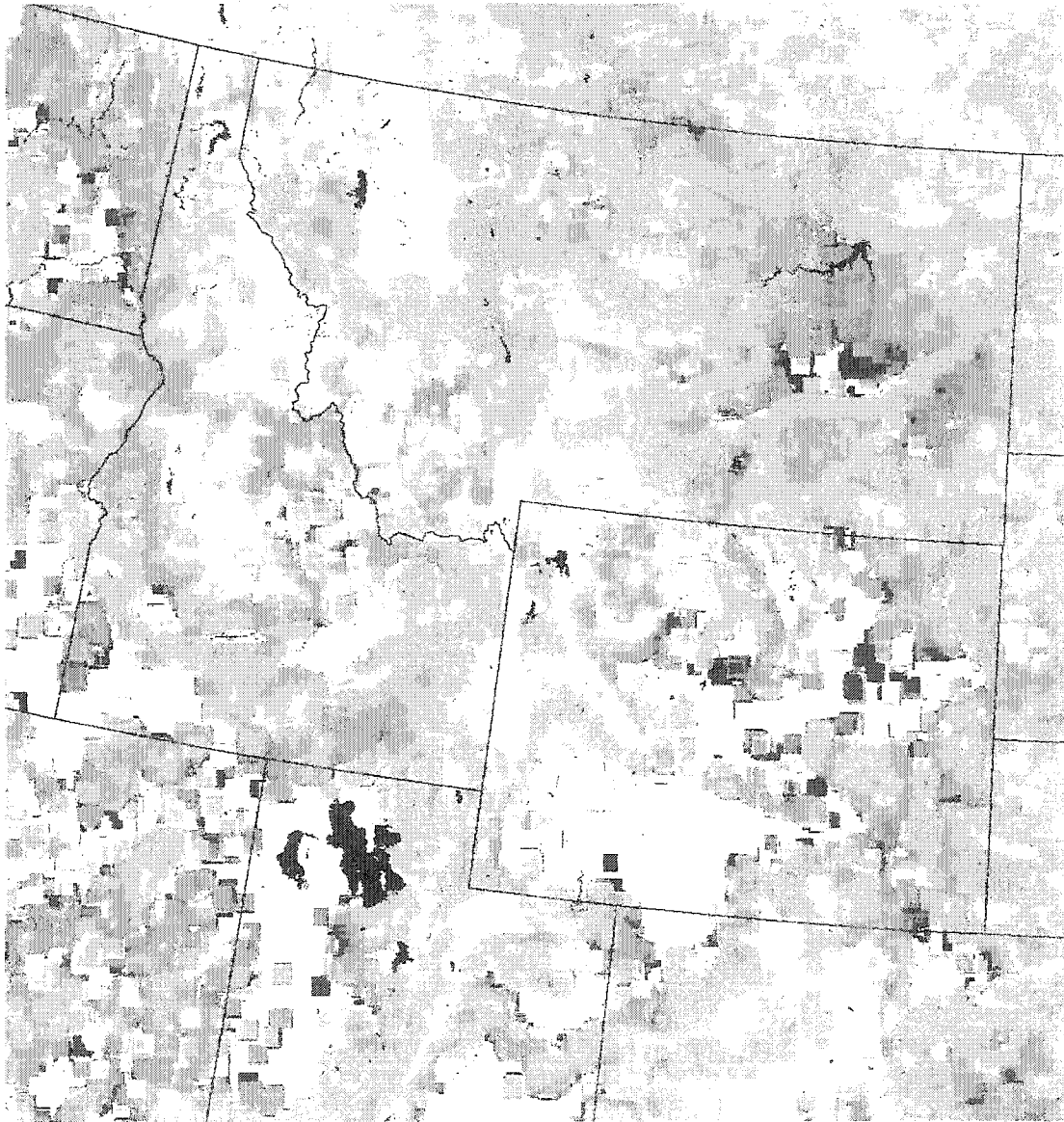
	Factor		
	1	2	3
SDI	-1.6E-02	-.301	1.90E-02
ENF	4.80E-02	.795	-.138
GRASS	-6.4E-02	-.360	-1.7E-02
SLOPE	6.59E-02	.707	-7.7E-03
ASPECT	1.51E-04	-2.3E-03	1.66E-02
ELEV	8.47E-02	.563	.204
SATZ	-.993	-.112	-2.1E-02
SOLZ	.972	.131	.195
DATE	.174	.126	.784

Extraction Method: Maximum Likelihood.
 Rotation Method: Varimax with Kaiser
 Normalization.

a. Rotation converged in 4 iterations.

A maximum likelihood extraction was utilized and an orthogonal varimax rotation employed. Three factors with eigenvalues greater than one emerged, accounting for forty-nine percent of variance cumulatively. While the percent of variation explained by the factor analysis is low; the factors showed a consistent, logical set of relationships between landscape variability and $T_s/NDVI$ performance. The first factor is clearly physiographic, representing rugged, mountainous terrain with coniferous forest. Percent evergreen needle leaf forest, slope, and elevation strongly load on this factor. SMI loads negatively, confirming the earlier observation that $T_s/NDVI$ does not currently discriminate spatial or temporal differences in surface wetness in mountainous conifer forests.

Figure 1: Map of SMI values for the study area, composite Period 13. Tan areas indicated no detectable stress. Stressed areas increase from yellow to dark red.



The second factor is a landcover factor represented by grass and agriculture. Although the vegetation dataset does not distinguish irrigated from dryland agriculture, the fact that grass and agriculture load oppositely on factor two suggests a biome sensitivity that is significantly different from variation observed in mountainous conifer forests.

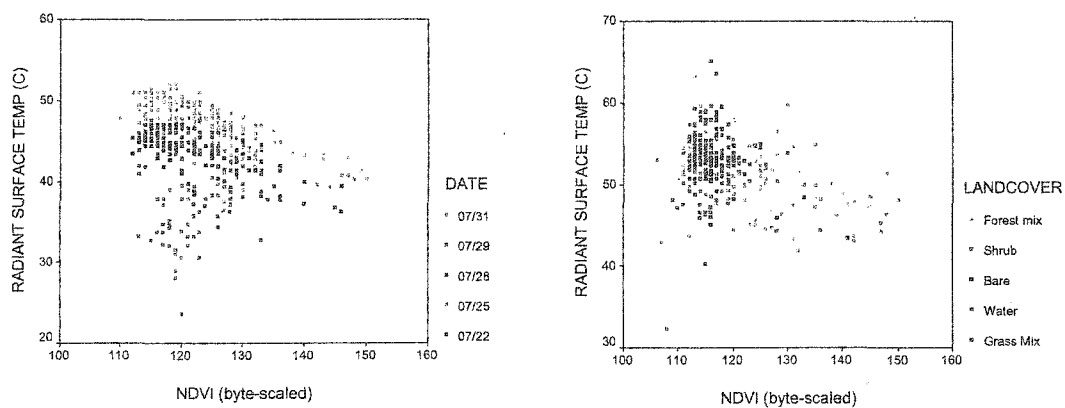
The third factor is a viewing geometry factor. Date, elevation, slope, and satellite look angle load on factor three. Because the current model implementation uses composited data (Eidenshink et al., 1992), image samples are derived from multiple target/sensor/sun geometries. Given the range in elevation, slope, and aspect values in mountainous terrain, this third factor is interpreted as being consistent with observed difficulties in validating SMI scores for pooled landcover/biome type settings. Based on the observed differences in SMI scores and the factor analysis, how the model actually derived SMI scores were re-examined. This involved decomposing the scatterplots of T_s versus NDVI for pooled samples (all landcover classes) as well as for specific biome types.

The purpose of analyzing selected scatterplots was to examine the effect of date/geometry, biome type, and contamination of retained pixels on the slope and intercept of the regression line. Furthermore, when scatterplots derived from image composites generated at times of high apparent fire danger are analyzed, the current model implementation fits a line that may have a low slope, in spite of the fact that portions of the scatterplot clearly indicate stress.

Figure 2 shows a T_s /NDVI scatterplot derived for a portion of the Bighorn Mountains (south of Hardin, MT) for the composite Period 13 (22 July – 4 August). The plot exhibits typical overall shape and dimensionality. Within the plot, however, the retained pixels were coded according to the date from within the period for which the pixel was retained. The legend clearly shows that samples from different dates occupy significantly different portions of the variable space. In a standard model run, all pixels occurring at the envelope or boundary of the plot (maximum T_s for each unique NDVI) would be used to fit the regression line. Yet that sample envelope is almost exclusively populated by pixels imaged on 31 July. If a regression line were fit to just a plot of 22 July or just to a plot of 28 July, one can see that each would have

approximately the same slope, but a different y-intercept. Pixels retained from other dates within the period (25 or 29 July) show a pattern quite different from other dates, with low ranges in NDVI but higher variability in T_s . This begs the question whether the effect is an artifact of scene geometry or possibly due to differences in illumination or setting/landcover. The fact remains that there are strong positional biases for pixel samples within the scatterplots. Pixels from any given date consistently occur in clusters within the area of interest.

Figures 2 and 3: T_s /NDVI scatterplots showing date (left) and water (right) contamination problems.



To examine the effect of biome type within the scatterplots, the landcover labels were identified for each pixel within each scatterplot. Figure 3 shows a plot for Period 13 (22 July- 4 August) for an area northwest of Boise, Idaho. Water pixels show low NDVI scores and cluster along the T_s axis, as expected. The landcover classification scheme (an AVHRR based global landcover classification developed by the University of Maryland, publication pending) does not allow for "water" to be mixed with other cover types. Yet when the mixed forest pixels are identified, a cloud of mixed forest (and other class) samples adjacent to the "water" pixels is observed. The hypothesis is that this portion of the plot shows contamination of the "forest" pixels by water, similar to what Nemani et al. (1993) noted for their study area. Figure 4 shows a portion of an image map resulting from a T_s /NDVI model run for Period 13 (22 July- 4 August). The area shown is Fort Peck Reservoir in northeastern Montana. The upper image shows an "alley" or edge effect around the reservoir, where the model derives a low slope (stress) score. This lack

of detectable stress occurs around virtually every water body in each composite period. The lower figure depicts the same area for the same composite period, with higher $T_s/NDVI$ scores assigned to the areas immediately adjacent to the reservoir. Apparently, when the window used to sample $T_s/NDVI$ scores includes samples that may be contaminated by water (mixed samples) this has the effect of flattening the slope of the regression line assigned to the window. The modification made to the model was to adopt a minimum NDVI threshold, below which the $T_s/NDVI$ pair would not be used to estimate the regression line. Based on a review of scatterplots over the entire season, a threshold at a scaled value of 120 was set. Beyond the effect of water on the retained pixel samples, clouds and snow may also affect the size, shape, and distribution of points within the scatterplot. By establishing an NDVI threshold, these contaminated pixels can be removed from the estimation of moisture stress.

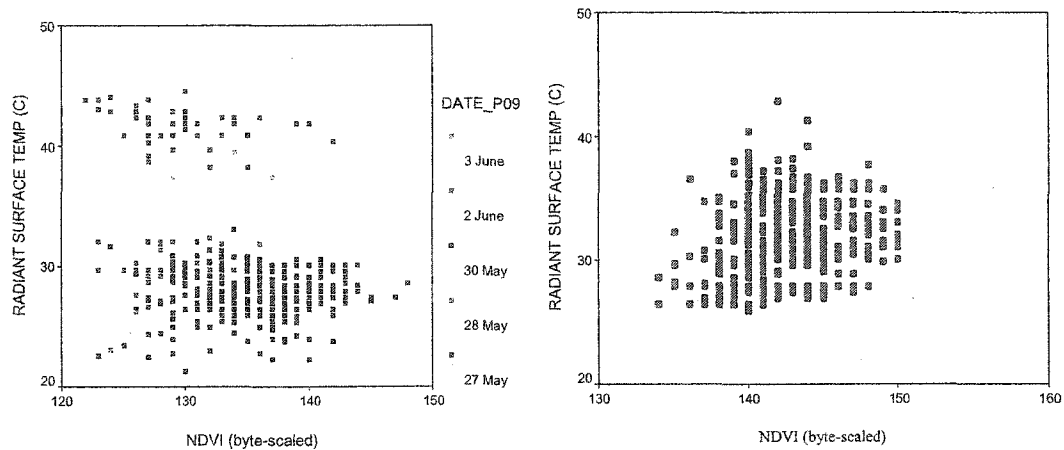
Figure 4: Map of Surface Moisture Index showing the edge effect around Fort Peck Reservoir in northeast Montana (top). Bottom map shows same area after NDVI thresholding at 0.2.



A closer look at the effect of biome type on T_s /NDVI performance can be gained by considering Figures 5 and 6. Shown for a grassland cover type sample south of Fort Peck Reservoir for Period 9 (27 May – 9

June), Figure 5 demonstrates the consistent variability in scatterplot samples according to imaging date. As noted above, there are strong temporal biases within any given sample. Regression line slopes fit to all samples (normal implementation), to 27 May or to the lower cluster would yield a similar slope value (stress level) but significantly different y-intercepts. Notable, this type of temporal bias has not appeared in any "forest" samples for the 1994 dataset; but it appears with some consistency in grassland settings.

Figures 5 and 6: Scatterplots illustrating date bias (left) and influence of lower left-edge pixels on SMI calculations (right).



The primary biome bias that this data shows occurs in ENF cover types. As the factor analysis suggested, this particular setting is quite complicated and more difficult to interpret (perhaps due at least in part to terrain). Figure 6 shows a scatterplot for ENF (Period 13, 22 July- 4 August). The scatterplot has a "trapezoidal" shape that is consistent with most ENF plots. The difficulty presented in fitting a regression line to this type of scattergram is the shape of the envelope of retained pixels. If a model were to retain all unique T_s /NDVI pairs (the upper boundary of the plot) the regression line would be very shallow to nearly flat. Yet closer examination of that boundary condition shows a series of T_s /NDVI samples at the upper right-hand edge of the cluster that are indicative of high-stress conditions. The effect of a model retaining all unique T_s /NDVI samples would then be to underestimate the potential stress indicated by the raw scatterplot. This may in part explain the low efficacy of the SMI model in ENF cover types in initial model runs. Unlike the grassland setting, however, establishing a minimum NDVI threshold of 118-120 will not

change model performance. ENF settings have expectedly higher NDVI scores; perhaps a higher NDVI or minimum T_s threshold could be set. Yet because it is not clear whether or not this lower-left edge effect is driven by contamination (clouds), illumination, poor surface/atmosphere coupling, geometry (ENF tends to occur in complex terrain), or the date bias shown in Figure 5, it is not clear at this time how the model needs to be adjusted.

Since ENF occurs across such large elevational gradients, a scatterplot of T_s /NDVI values may actually be composed of several individual clusters corresponding to elevation zones. Nemani et al. (1993) demonstrated the influence of elevation on the T_s /NDVI relationship suggesting that lower surface temperatures at high elevations are a function of adiabatic lapse rates and higher surface moisture associated with orographic precipitation. Given the results of Nemani et al. (1993), it may be possible to fit a unique T_s /NDVI regression line to each elevation zone that can be discriminated in a scatterplot. In exceptionally complex terrain, however, elevation zone clusters may not be distinct. In such cases, the single large clusters characteristic of ENF may actually represent a continuum of T_s /NDVI slopes each responding to an elevation zone. It is suggested that stratification by elevation zone or modification of window sizes in complex terrain may at least partially solve the lower-left edge problem described previously.

PERFORMANCE OF SMI AS A FIRE POTENTIAL INDEX

Fire danger across a landscape is a function of weather, topography, and fuels. Measurements of surface wetness provided by T_s /NDVI are only one part of the equation that defines fire danger. Complex interactions between temperature, relative humidity, wind, slope, aspect; fuel types, loadings, and arrangements largely determine how fires will actually behave. Consequently, it is important to note that the T_s /NDVI is not a fire danger rating index, but rather is an index of the potential for fire activity given the appropriate topographic, meteorological, and fuels variables.

Although several problems with the current implementation of $T_s/NDVI$ (outlined above) have been identified, the algorithm performs well enough, at least in some landscapes, to perform a preliminary comparison with actual fire potential. At the outset, it was noted that establishing a measure of actual fire potential is an imprecise endeavor. Certainly, actual fire potential should be linked in some way to occurrence and behavior of fires. However, because one is unable to isolate the surface moisture component from the weather-topography-fuels triangle and cannot identify a human intervention factor, the ability of variables like fire size to approximate fire potential must be relied upon. The assumption being that given a large enough sample (3,504 fires), fire potential can be generally represented by fire size.

The widely available fire occurrence data from U.S. Forest Service and Bureau of Land Management sources was used to estimate fire potential, recognizing the shortcomings of these datasets in terms of both accuracy and attribute diversity. Fires for both agencies are stored as points in similar format ArcInfo coverages. However, the attribute tables assembled by each agency are quite different in terms of the type, number, and arrangement of fields. In general, the BLM maintains more detailed records than does the USFS. The BLM dataset includes attribute fields for resource commitments, cost-codes, ownership, fuels, weather, and topography. Attribute fields common between agencies include fire location (latitude/longitude and UTM) detection and control dates, fire size, fire id number, and administrative unit.

Fire coverages were overlaid on projected raster layers of $T_s/NDVI$ and each fire point was assigned to its nearest neighbor pixel. If a fire point was within 500 meters of a pixel centroid, it was assigned to that raster and labeled as a fire. If the Euclidean distance between a pixel centroid and a fire exceeded 500 meters, the fire was flagged as possibly belonging to that pixel. Seventy-nine percent of the assignments were labeled fires and 21 percent were labeled possible fires, as expected based on raster geometry. $T_s/NDVI$ values were extracted for each fire pixel. For the purpose of this paper, possible fire pixels were excluded from further analysis (3,504 of 4,436 fires are included).

We chose fire size at time of control as an indicator of actual fire potential, recognizing the complex interactions of factors that govern the growth of a fire. Logic dictates that fire danger must be high if a fire becomes large, but may or may not be high if a fire remains small. Further, surface moisture status must be appropriately low for a fire to grow regardless of the other factors that govern fire behavior.

We divided fire pixels into two groups based on size class in order to facilitate chi-square analyses. All fires one acre in size or smaller formed the first group and those larger than one acre formed a second group. The one acre threshold was selected for two reasons. First, it was attempted to roughly balance the number of fires in each group. Second, anecdotal field experience suggests that fire potential is reasonably high if a fire grows beyond one acre. This latter point is recognized as fairly subjective and probably more true in forested landscapes than in grasslands. Readers should note that fire sizes reported by both the USFS and the BLM are usually estimated by field personnel either by eye or by pacing. Actual area burned is only measured on the very large fires, typically using airborne infrared line scanners. Our experience suggests that small fires are usually estimated at .10, .50, or 1.0 acres. As fires grow beyond one acre, field personnel are more likely to pace the perimeter and to calculate rough acreage using perimeter/shape/acreage tables. Finally, many of the very large fires burned for weeks or months. However, only those $T_s/NDVI$ values for pixels that a fire was detected in and for the composite period during which it was detected, were used. Presently, daily or weekly fire growth and perimeter data is lacking, so the ability to track the movement of fires through space and time was not possible.

A two-sample chi-square test was used to compare fire size with $T_s/NDVI$. Four categories of $T_s/NDVI$ were selected. Positive or zero-slope $T_s/NDVI$ values were classified as "no stress." A slope of -1 indicated "stress", a slope of -2 indicated higher stress, and so on. Again, the attempt was to roughly balance the number of observations in each $T_s/NDVI$ class.

A significant relationship between $T_s/NDVI$ and fire size was observed for grasslands, although the relationship was not strong (Table 2). Large fires occurred in areas of $T_s/NDVI$ -derived moisture stress

more frequently than one would expect due to chance alone. This result confirms earlier observations that $T_s/NDVI$ scores discriminate between surface moisture variations in non-forested areas during the peak of the 1994 fire season. As the fire season began to peak (AVHRR composite Period 13, 22 July – 4 August) 114 fires occurred in grassland/shrubland. Twenty of these fires occurred in areas of no detectable stress; of these, nine were less than five acres in size. Although 82.5 percent of fires occurred in areas exhibiting moisture stress, only 18 percent of the study area showed moderate to extreme stress (Figure 7.) As expected from earlier observations, no relationship was observed between $T_s/NDVI$ and fire size in forested areas or when all fire pixels were included in the analysis (Table 2).

Table 2: $T_s/NDVI$ -Fire size chi-square statistics for three landscapes (18 March – 15 September, 1994).

	<u>Chi-square</u>	<u>df</u>	<u>Significance</u>
Ts/NDVI (Grassland Fires)	4.374	3	.20
Ts/NDVI (Forest Fires)	1.885	3	-----
Ts/NDVI (All Fires)	2.446	3	-----

A second set of chi-square statistics was generated, this time comparing fire size class to NDVI and to Burgan et al.'s (1996) Relative Greenness and Departure from Average Greenness (Table 3). A hypothetical maximum range of positive NDVI scores (0.0 to 1.0) was divided into five equal classes and each class was populated with the NDVI scores of fire pixels. Both Relative Greenness and Departure from Average Greenness were split into six equal area classes.

Table 3: Chi-square statistics for 'greenness' variables (18 March – 15 September, 1994)

	<u>Chi-square</u>	<u>df</u>	<u>Significance</u>
NDVI (All Fires)	4.490	4	.25
Relative Greenness (All Fires)	8.846	5	.25
Departure (All Fires)	10.8445	5	.10

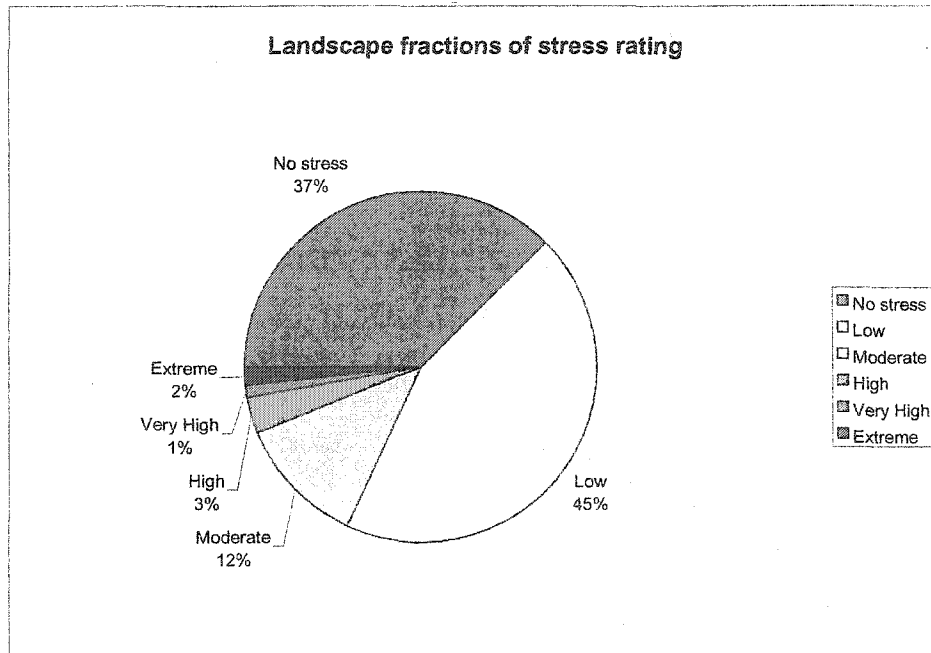
Significant relationships were observed between fire size class and each of the three 'greenness' variables. Again, large fires occurred more frequently than expected in areas of low NDVI/larger negative departures from normal. The strongest relationship was found in the Departure from Normal NDVI product.

We draw two significant conclusions from these results. First, NDVI and its surrogates appear to characterize fire potential better than the current implementation of $T_s/NDVI$. The NDVI component of the $T_s/NDVI$ index is probably also the primary driver of the observed relationship between $T_s/NDVI$ and fire size in grassland environments. Given the scatterplot results described previously, these findings are not surprising. Our second conclusion concerns the "Departure from Normal". Measures of departure may provide more meaningful characterizations of fire potential. Given the results from this exploratory analysis of the $T_s/NDVI$ scatterplots, the comparatively low performance of SMI is not surprising. The hypothesis, however, is that the $T_s/NDVI$ relationship can be more rigorously modeled using corrections or adjustments described above. Theoretically, one would expect that the $T_s/NDVI$ relationship would perform better than raw NDVI scores or derivatives. Results to-date are strongly suggestive of just such an increased sensitivity; although statistical significance at the present time is low.

Departure and cumulative indices are attractive alternatives to daily or weekly synoptic measurements because they provide an environmental context for each score. Given a relative level of inexperience with $T_s/NDVI$, it is difficult to interpret the response of fire potential to surface moisture measurements without such context. Departures and cumulative indices also expand the timeframes in which the environment is monitored. This is an especially important consideration in fire potential monitoring because a moisture index ideally must capture variations in moisture contents of different fuel size classes to be fully effective as an indicator of fire potential. To do so, an index must reflect surface wetness at several timescales. The Palmer Drought Index (PDI) is an example of a relatively long-term drought index that measures moisture status over periods of several months. The Palmer Index calculates a normalized water-balance by opposing precipitation and stored soil moisture with evapotranspiration, runoff, and soil recharge. As a long-term index, the Palmer is useful for regional assessments of moisture status and helps fire managers to

identify areas that may experience severe fire seasons. A shorter-term drought index, the Crop Moisture Index (CMI), is perhaps better suited for estimation of within-fire-season fire potential because it operates at a weekly timescale. The CMI utilizes mean weekly temperature and precipitation to credit or debit soil moisture in the crop/soil system from the previous week's values.

Figure 7: Land area within each stress category for composite Period 13. Of 114 fires on BLM lands, 82.5 percent occurred in stressed areas as mapped using SMI.



A significant shortcoming of both the PDI and the CMI is that they measure moisture status only at discrete locations. In fact, all drought indices that rely on meteorological variables as input are limited by the spatial discontinuity of reliable weather stations. Spatially continuous measurements of moisture status across the landscape would be far more useful to fire managers wishing to discriminate differences in fire potential between sub-regions or watersheds. As a result, satellite-based observations of such variables as vegetation condition are increasingly being looked to as surrogates for meteorological observations. The $T_s/NDVI$ presented here is a new biophysical model that incorporates satellite observations of surface temperature and vegetation status to calculate surface wetness.

CONCLUSIONS

The goal of this research was to identify sources of performance sensitivity, maximize responsiveness to surface condition/status, and to achieve computational consistency and efficiency. Although empirical validation of model performance is intractable at best, the results from assessing the performance of this model for the 1994 fire season in Montana and Idaho revealed several issues related to model performance and sensitivity. In this paper three primary effects that must be considered in further research and development of the method have been reported.

Compositing Method: Date and Geometry Effects

Recent studies have suggested that the maximum NDVI compositing method may not be the most rigorous for alternative uses of AVHRR data. While it generally results in relatively cloud free images, recent work shows that compositing may cause preferential selection of off-nadir pixels (Stoms et al., 1997). As look angles increase, thermal signals associated with that pixel will be attenuated simply because of the increased atmospheric path that signal must travel through. By using maximum NDVI composites, SMI algorithm performance may suffer from attenuated thermal signals, particularly over the two-week compositing period. These questions will be addressed by obtaining multiple daily data and investigating the range in model output variability due to compositing methods. Perhaps a better method of calculating SMI would be to implement a daily protocol (that also restricted samples to near-nadir locations) and composite SMI outputs via a maximum value rule at an appropriate time step.

Stratification: Landcover and Terrain Effects

The ability to consider the effect of biome type or landcover on SMI values is ultimately dependent on the availability and quality of a suitable cover type map. Our application of the MD Landcover map, derived from AVHRR data, allowed us to uncover a consistent and systematic performance difference in grassland

and ENF cover classes, as well as to document the effect of water contamination within a given sample window. Biome stratification and terrain corrections prior to SMI estimation are worthy of additional testing. The tension between capturing process at appropriate geographic (within biome or terrain strata) or temporal scales may ultimately depend more on the use and interpretation of the SMI and less on achieving a standard normal model form that is applicable in all conditions. That is, if the analyst or decision-maker is more concerned with conservative estimates of fine fuel condition and less interested in high elevation large fuels, a different model may need to be applied than for the reverse case.

Operations: Computational Efficiency and Window Size

Given model sensitivity, several adjustments to the initial model have been made (e.g., water adjacency effects) and additional changes are strongly suggested. There is, however, a need to maintain efficiency if practical application of the model is to be achieved. Window size, shape and iteration method could all be adjusted to fit unique conditions encountered during data processing. For example, to minimize the difficulties in estimates over ENF settings, higher elevation settings may simply be excluded from the analysis using an elevation threshold. Gradients along as well as across elevation zones may need to be considered.

Additionally, the desire to fit more than one regression line to an ENF scatterplot that does not show unique clusters within a scatterplot may place a real burden on the analyst. Based on a careful review of large numbers of scatterplots several unique and correctable sources of variation in SMI estimates were identified. These are driven by internal effects caused by the model implementation and data protocols and not by real-world variation in surface moisture condition. It is desirable to isolate, quantify, and wherever possible, mitigate these effects. A serious consideration in terms of model implementation is to allow analysts to explore each scatterplot to look for internal sources of variation that may not be related to actual ground condition.

Suggestions for Further Research

Perhaps the most pressing needs are for inclusion of surface meteorology and long-term climate data sets in any strategy designed to validate the SMI technique. The near-term availability of higher-quality, calibrated remote sensing data streams (e.g., MODIS) may reduce the occurrence of internal errors or inconsistencies. Yet this does not diminish the value of pathfinder SMI data. While researchers continue to adjust the model based on the effects noted above, one must recognize that a comprehensive validation strategy is difficult to achieve given that the parameter of interest cannot be practically (empirically) estimated at regional scales. Results to date suggest that analysts should adapt an NDVI threshold to eliminate contaminated pixels (compositing does not remove all cloud effects), should examine for temporal biases within composite data scatterplots, and may need to consider biome type and terrain stratification. Although not examined here, further decompositions of the T_s /NDVI scatterplot and analysis of y-intercept scores may prove useful as well.

Another area worthy of additional work is the need to develop departure/deviation indices. As the Chi Square results of Burgan's NDVI and Departure Index suggest, NDVI alone exhibits discriminating power; exactly what increase in efficacy is gained via adding T_s data is not a simple question to address. While theoretically robust, temporal and geographic variability make it hard to implement a run-time model and suggest that inter- and intra-annual traces of stress (T_s /NDVI slope) versus time will be critical for responding to fire manager and decision maker needs. As mentioned above, different fuels behave on significantly different time scales. In some cases (e.g., fine fuels) short interval snapshots are needed, while large fuel condition would be more likely to respond to a longer-time scale assessment of moisture stress (e.g., cumulative T_s /NDVI curves or departures from long-term "normals"). Baselines for estimating short and long-term departures are needed, and may become critical to adding context to new data streams that will derive from NASA's EOS program.

LITERATURE CITED

- Burgan, R.E., Hartford, R.A. and Eidenshink, J.C., 1996. Using NDVI to Assess Departure From Average Greenness and its Relation to Fire Business. INT-GTR-333, USDA Forest Service Intermountain Research Station. 8 pp.
- Carlson, T.N., Boland, F.E., Dodd, J.K. and Benjamin, S.G., 1981. Satellite Estimation of the Surface Energy Balance, Moisture Availability and Thermal Inertia. *Journal of Applied Meteorology*, 20: 67-87.
- Carlson, T.N., Gillies, R.R. and Perry, E.M., 1994. A Method to Make Use of Thermal Infrared Temperature and NDVI Measurements to Infer Surface Soil Water Content and Fractional Vegetation Cover. *Remote Sensing Reviews*, 9: 161-173.
- Carlson, T.N., Perry, E.M. and Schmugge, T.J., 1990. Remote Estimation of Soil Moisture Availability and Fractional Vegetation Cover for Agricultural Fields. *Agricultural and Forest Meteorology*, 52: 45-69.
- Eidenshink, J.C., 1992. The 1990 Conterminous U.S. AVHRR Data Set. *Photogrammetric Engineering and Remote Sensing*, 58: 809-813.
- Jones, H.G., 1992. *Plants and Microclimate: A Quantitative Approach to Environmental Plant Physiology*. Cambridge University Press, Cambridge, 428 pp.
- Monteith, J.L., 1981. Evaporation and surface temperature. *Quarterly Journal of the Royal Meteorological Society*, 107: 1-27.
- Nemani, R., Pierce, L., Running, S. and Goward, S., 1993. Developing Satellite-derived Estimates of Surface Moisture Status. *Journal of Applied Meteorology*, 32(3): 548-557.
- Nemani, R.R. and Running, S.W., 1989. Testing a Theoretical Climate-Soil-Leaf Area Hydrologic Equilibrium of Forests Using Satellite Data and Ecosystem Simulation. *Agricultural and Forest Meteorology*, 44: 245-260.
- Price, J.C., 1984. Land surface temperature measurements from the split window channels of NOAA-7/AVHRR. *Journal of Geophysical Research*, 89: 7231-7237.
- Priestly, C.H.B. and Taylor, R.J., 1972. On the assessment of surface heat flux and evaporation using large-scale parameters. *Mon. Wea. Rev.*, 100: 81-92.
- Shuttleworth, W.J., 1991. Insight from Large-scale Observational Studies of Land/Atmosphere Interactions. In: E. Wood (Editor), *Land Surface-Atmosphere Interactions for Climate Modeling: Observations, Models and Analysis*. Kluwer Academic Press, Norwell, Massachusetts, pp. 300-320.
- Stoms, D.M., Bueno, M.J. and Davis, F.W., 1997. Viewing Geometry of AVHRR Image Composites Derived Using Multiple Criteria. *Photogrammetric Engineering and Remote Sensing*, 6: 681-689.
- Whitehead, D., 1998. Regulation of Stomatal Conductance and Transpiration in Forest Canopies. *Tree Physiology*, 18: 633-644.

CHAPTER 3

DERIVATION OF THE WATER DEFICIT INDEX

INTRODUCTION

As mentioned in the previous chapter, there are a number of shortcomings associated with the SMI implementation illustrated in Chapter 2. Though that method shows some promise, particularly when considering the landscape scale at which it was implemented, the decision was made to incorporate alternative techniques in the attempt to improve model performance. One of the most promising uses of the generalized T_s /NDVI relationship was shown by Moran et al. (1994a). They developed the Water Deficit Index (W_sDI) which includes in its calculation an assessment of near surface air temperature. The incorporation of air temperature allows for increased discriminating power in surface moisture status due to the reconciliation of ambient air temperature impacts on radiant surface temperature. By being able to assess how much warmer the canopy surface temperature is in comparison to ambient air temperatures (i.e. surface temperature – air temperature), one can more robustly assess the sensible heat partitioning that is occurring. A canopy exhibiting a 10° C temperature above the ambient temperature is more likely to be suffering water stress than a canopy showing a 2° C increase, regardless of what the actual surface temperatures may be. The incorporation of surface meteorology in the WDI logic leads to an improved ability to assess surface moisture conditions.

Since the WDI logic shows great promise, the choice of modifying the original SMI implementation and incorporate much of the WDI technique into a new algorithm, was made. As the WDI logic is integral to the forthcoming SMI technique, a full treatment of its derivation is appropriate. This chapter will discuss the logic and derivation associated with the WDI. It will include a discussion of the Crop Water Stress Index (CWSI) which provides the predicate for the WDI.

THE WATER DEFICIT INDEX

Moran et al. (1994a) developed the water deficit index (WDI) for use in partially vegetated sites. The logic for this index comes from the Crop Water Stress Index (CWSI) (Jackson et al., 1981). The WDI is related, by definition, to the ratio of actual to potential evapotranspiration. The WDI can be computed based on remotely sensed information of red and near infrared reflectance and surface temperature, with a minimum of on-site meteorological data. The following begins with brief reviews of the surface energy budget, moves to the CWSI logic and conclude with the derivation of the WDI. The equations and concepts presented come directly from Moran et al. (1994a), but may be found in various other publications (Campbell and Norman, 1998; Jones, 1992).

The net radiation reaching the Earth's surface is conserved according to the following equation:

$$R_n = H + G + \lambda E_r + e \quad (1)$$

where R_n is net radiant heat flux density, H is the sensible heat flux density, G is the soil heat flux density, λE_r is the latent heat flux density (the product of evapotranspiration rate, E_r , and the latent heat of vaporization, λ), and e is an error term associated with minor components of the surface energy balance such as photosynthesis. All terms are in $W m^{-2}$ and are considered positive when directed away from the surface. The terms H and λE_r can be expressed, respectively as:

$$H = \frac{C_v(T_c - T_a)}{r_a} \quad (2)$$

$$\lambda E_r = \frac{C_v(VPD)}{[\gamma(r_a + r_c)]} \quad (3)$$

where C_v is the volumetric heat capacity of air, T_c is the crop foliage temperature, T_a is the air temperature, VPD is vapor pressure deficit, γ is the psychrometric constant, and r_a and r_c are aerodynamic and canopy resistances to vapor transport, respectively. The G term in Equation (1) is generally expressed as a linear function of fractional vegetation cover and net radiation. (Clothier et al., 1986) described G as $0.3 R_n$ for bare soil and $0.1 R_n$ for full vegetation cover. Assuming a full canopy cover and ignoring the usually minor impact of e (from Equation 1), equations (1), (2), and (3), can be rearranged such that:

$$(T_c - T_a) = \left[\frac{r_a R_n}{C_v} \right] \frac{[\gamma(1 + \frac{r_c}{r_a})]}{\{\Delta + \gamma(1 + \frac{r_c}{r_a})\}} - \left[\frac{VPD}{\{\Delta + \gamma(1 + \frac{r_c}{r_a})\}} \right] \quad (4)$$

where Δ equals the slope of the saturated vapor pressure-temperature relationship.

Crop Water Stress Index

The Crop Water Stress Index (CWSI) is commonly used for detecting plant moisture stress based on differences between air and vegetation temperature. It has been correlated with numerous surface water parameters such as soil moisture content, plant water potential, photosynthesis, and crop yield (Idso et al., 1986; Jackson et al., 1987; Moran et al., 1994a). The development of the CWSI by (Jackson et al., 1981) was made by combining equations 1-3 such that:

$$\lambda E_r = \frac{\left[\frac{\Delta R_n + C_v(VPD)}{r_a} \right]}{\left[\Delta + \gamma(1 + \frac{r_c}{r_a}) \right]} \quad (5)$$

Equation 5 is the Penman – Monteith equation for calculating evapotranspiration (Monteith, 1973b). By taking a ratio of actual to potential ET (actual ET for any r_c and $r_c = r_{cp}$ for potential ET) the following can be derived:

$$\frac{\lambda E_r}{\lambda E_{rp}} = \frac{\left[\Delta + \gamma \left(1 + \frac{r_{cp}}{r_a} \right) \right]}{\left[\Delta + \gamma \left(1 + \frac{r_c}{r_a} \right) \right]} \quad (6)$$

where r_{cp} is canopy resistance at potential ET (λE_{rp}). The range of the crop water stress index ranges from zero (ample water) to one (maximum stress), such that:

$$CWSI = \left(1 - \frac{\lambda E_r}{\lambda E_{rp}} \right) = \frac{\left[\gamma \left(1 + \frac{r_c}{r_a} \right) \right] - \left[\gamma \left(1 + \frac{r_{cp}}{r_a} \right) \right]}{\left[\Delta + \gamma \left(1 + \frac{r_c}{r_a} \right) \right]} \quad (7)$$

Equation 7 is solved for a value of r_c/r_a by rearranging equation 4:

$$\frac{r_c}{r_a} = \frac{\left\{ \left[\frac{r_a R_n}{C_v} \right] - [(T_c - T_a)(\Delta + \gamma)] - VPD \right\}}{\gamma \left[(T_c - T_a) - \frac{r_a R_n}{C_v} \right]} \quad (8)$$

Then, r_c / r_a is substituted in equation 7 to obtain the CWSI.

Alternatively, equation 7 can be solved by measuring $T_c - T_a$ and combining that with theoretical limits of $T_c - T_a$ (using equation 4) to calculate the CWSI as follows:

$$CWSI = 1 - \frac{\lambda E_r}{\lambda E_{rp}} = \frac{[(T_c - T_a)_m - (T_c - T_a)_r]}{[(T_c - T_a)_m - (T_c - T_a)_x]} \quad (9)$$

where the subscripts m, x, and r refer to minimum, maximum, and measured values, respectively. For well-watered full-canopy vegetation,

$$(T_c - T_a)_m = \left[\frac{r_a R_n}{C_v} \right] \left[\frac{\gamma \left(1 + \frac{r_{cm}}{r_a} \right)}{\left\{ \Delta + \gamma \left(1 + \frac{r_{cm}}{r_a} \right) \right\}} \right] - \left[\frac{VPD}{\Delta + \gamma \left(1 + \frac{r_{cm}}{r_a} \right)} \right] \quad (10)$$

where $r_{cm} = r_{cp}$. For full-canopy water-limited vegetation:

$$(T_c - T_a)_x = \left[\frac{r_a R_n}{C_v} \right] \left[\frac{\gamma \left(1 + \frac{r_{cx}}{r_a} \right)}{\left\{ \Delta + \gamma \left(1 + \frac{r_{cx}}{r_a} \right) \right\}} \right] - \left[\frac{VPD}{\Delta + \gamma \left(1 + \frac{r_{cx}}{r_a} \right)} \right] \quad (11)$$

where r_{cx} is the maximum canopy resistance resulting from complete stomatal closure ($r_{cx} \rightarrow \infty$). Values of r_{cx} and r_{cm} can be obtained from measurements of stomatal resistance (r_s) and leaf area index (LAI):

$$r_{cm} = r_{sm} / LAI \quad \text{and} \quad r_{cx} = r_{sx} / LAI \quad (12)$$

for LAI values greater than zero. Values of maximum and minimum stomatal resistance can be found in the literature for a variety of atmospheric conditions and vegetation types. In lieu of published values, estimates of $r_{sm} = 25-100 \text{ s m}^{-1}$ and $r_{sx} = 1000-1500 \text{ s m}^{-1}$ are reasonable and will not result in significant error (Moran et al., 1994a).

Though the CWSI, by definition, can not be applied to bare soil, the theory behind CWSI can. The result is a Water Deficit Index (WDI) introduced by Moran, et al. (1994a). Using equation 9 to determine the actual to potential soil evaporation (not ET) results in:

$$WDI = 1 - \frac{\lambda E_r}{\lambda E_{rp}} = \frac{[(T_o - T_a)_m - (T_o - T_a)_r]}{[(T_o - T_a)_m - (T_o - T_a)_x]} \quad (13)$$

where T_o equals the surface temperature of the soil and λE_r and λE_{rp} refer to actual and potential soil evaporation rates, respectively. Soil temperature may be determined in an equivalent manner as vegetation temperature using equation 4. In the application to bare soil, G is not negligible. In fact, G may reach $0.5R_n$ for dry soils (Idso et al., 1975; Moran et al., 1994b). Therefore, G must be incorporated into equation 4 and adjustments made to the r_c term such that it is appropriate for soil values. For well-watered bare soil ($r_c=0$):

$$(T_o - T_a)_m = \left[r_a (R_n - G) / C_v \right] \left[\frac{\gamma}{(\Delta + \gamma)} \right] - \left[\frac{VPD}{(\Delta + \gamma)} \right] \quad (14)$$

For dry bare soil, where $r_c = \infty$ (the soil analogue of complete stomatal closure):

$$(T_o - T_a)_m = \left[r_a (R_n - G) / C_v \right] \quad (15)$$

Equation 13 provides an index equivalent to the CWSI for bare soil depicting the ratio of actual to potential evaporation. The values, like those of CWSI, range from 0 – 1, where 0 describes a condition of abundant water availability ($\lambda E_r = \lambda E_{p0}$) and 1 depicts a large water deficit.

The Vegetation Index/Temperature Trapezoid

Moran et al. (1994a) hypothesized that a trapezoid shape would appear in a plot of fractional vegetation cover versus $(T_s - T_a)$. The vertices of this trapezoid would correspond to full vegetation cover and bare soil, both at moisture extremes (maximum water stress and maximum water availability). Figure 1 illustrates this concept (derived from Moran et al., 1994a). The value for the four vertices can be calculated as follows: for vertex 1 (well watered vegetation):

$$(T_s - T_a)_1 = \left[r_a (R_n - G) / C_v \right] \left[\frac{\gamma \left(1 + \frac{r_{cp}}{r_a} \right)}{\left\{ \Delta + \gamma \left(1 + \frac{r_{cp}}{r_a} \right) \right\}} \right] - \left[\frac{VPD}{\Delta + \gamma \left(1 + \frac{r_{cp}}{r_a} \right)} \right] \quad (16)$$

where the subscript 1 refers to vertex 1 in figure 1, and each additional numeric subscript in the $(T_s - T_a)_n$ will refer the respected vertex. For water stressed full cover vegetation (vertex 2):

$$(T_s - T_a)_2 = \left[\frac{r_a(R_n - G)}{C_v} \right] \left[\frac{\gamma \left(1 + \frac{r_{cx}}{r_a} \right)}{\left\{ \Delta + \gamma \left(1 + \frac{r_{cx}}{r_a} \right) \right\}} \right] - \left[\frac{VPD}{\Delta + \gamma \left(1 + \frac{r_{cx}}{r_a} \right)} \right] \quad (17)$$

where r_{cx} is the canopy resistance resulting from stomatal closure. Vertex 3 is calculated as:

$$(T_s - T_a)_3 = \left[\frac{r_a(R_n - G)}{C_v} \right] \left[\frac{\gamma}{(\Delta + \gamma)} \right] - \left[\frac{VPD}{\Delta + \gamma} \right] \quad (18)$$

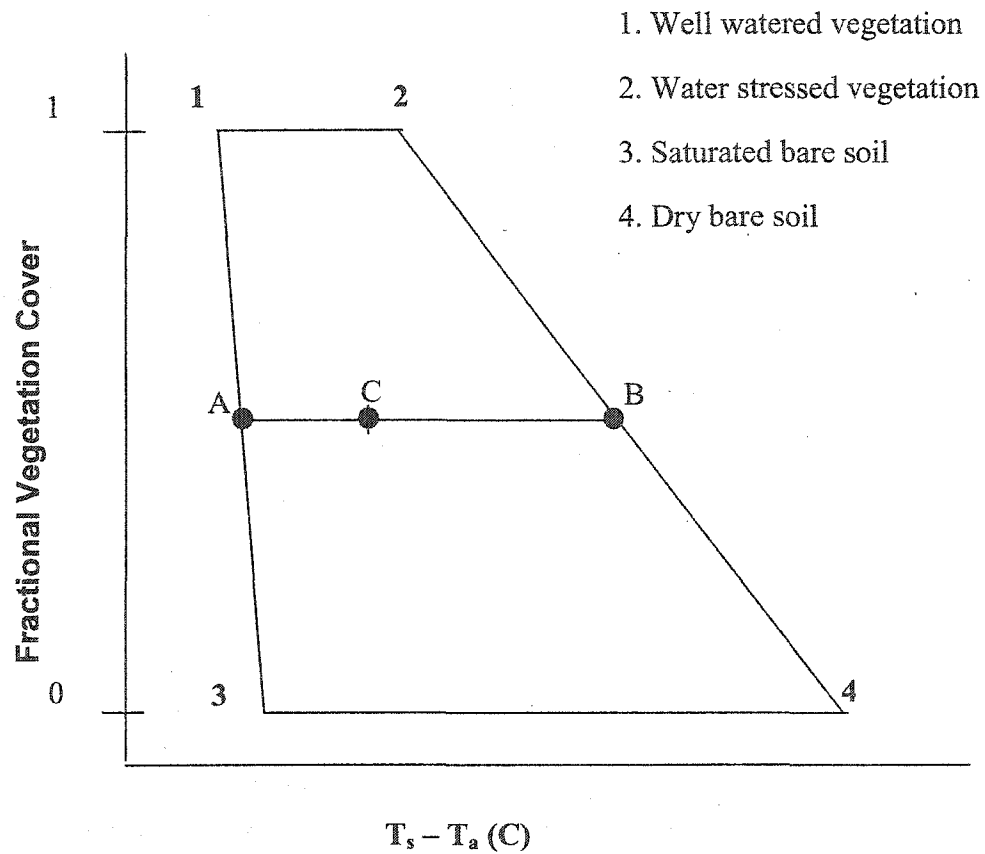
The dry bare soil vertex (vertex 4) is calculated as:

$$(T_s - T_a)_4 = \left[\frac{r_a(R_n - G)}{C_v} \right] \quad (19)$$

Based on this theory, it is possible to measure the fractional vegetation cover and temperature relationship for an area that should fit within the theoretical limits of the trapezoid. Then, the ratio of CB/AB would be equivalent to $\lambda E_r / \lambda E_{rp}$. Given knowledge of meteorological conditions, λE_{rp} could be computed and actual ET rates derived. Since CB/AB is equal to $\lambda E_r / \lambda E_{rp}$, the Water Deficit Index (WDI) is related to CB/AB as such (from equation 13):

$$WDI = 1 - \frac{\lambda E_r}{\lambda E_{rp}} = 1 - \frac{BC}{AB} \quad (20)$$

Figure 1: Water Deficit Index trapezoid.



As a proof of concept, Moran, et al., (1994a) conducted an experiment in an alfalfa field located in Arizona. Eighteen plots of alfalfa (2 replicates) were differentially irrigated to induce variable degrees of water stress at different times. Micrometeorological data were collected and evaporation rates measured consistently throughout the experiment. Additionally, a ground based multispectral radiometer (filtered to match TM band passes) collected red and near-infrared reflectance, and thermal emittance. From the radiometer data, the Soil Adjusted Vegetation Index (SAVI) (Huete, 1988) and surface temperature were calculated. SAVI was chosen based on the premise that the vegetation index needs to track variations of vegetation cover without being affected by soil background variability (particularly for areas with lower fractional

vegetation cover). Using the remotely sensed products and the meteorological data, the trapezoid for the experimental plots was realized and the WDI was tested against measurements of $\lambda E_r/\lambda E_{tp}$, and CWSI.

Overall, the WDI matched the calculated CWSI quite well, though WDI values were consistently higher. Based on lysimeter measurements and calculations of $\lambda E_r/\lambda E_{tp}$, WDI performed well in the first half of the growth cycle. Towards the end of the growing season, discrepancies began to appear. The authors, however, attribute these discrepancies to plant access to soil moisture below that which the lysimeters could measure. In concluding, it was suggested that the VIT concept and WDI were promising techniques for assessing ET rates and plant water stress.

Vidal and Devaux-Ros (1995) used the WDI method to develop spatially explicit maps of fire potential for an 888 km² area of Mediterranean forest in France. Their investigation was centered on two issues: first, the overall usefulness of the WDI in predicting fire starts, and second, testing the ability to create the trapezoid shape from remote sensor data with little ancillary information. To this end, Landsat Thematic Mapper data were acquired from three scenes from two different years (9 August, 1990, 29 July, 1992, and 14 August, 1992). These dates were chosen because they had little cloud cover and coincided with dry periods in the study area. Information on fire starts was obtained from a French database of location, areal extent, and miscellaneous ancillary data for use in comparative analysis with the WDI.

The vertices of the trapezoid were estimated two ways. The first method used was theoretical calculations of the trapezoid limits using satellite derived surface temperature, NDVI, and meteorological data. The second method relied on the satellite data and air temperature to define the vertices. The satellite-derived trapezoid was defined according to the following rules for a scatterplot of T_s and NDVI:

1. Vertices 1 and 3 correspond to the minimum value of $T_s - T_a$ from the image and meteorological data.
2. Vertices 1 and 2 are the maximum values of NDVI observed within the image.
3. Line 2-4 follows the right limit of the scatterplot.
4. Line 3-4 is defined by an NDVI value of 0.09, identified as the bare soil maximum NDVI score.

For the August scenes of 1990 and 1992, overall correspondence between the theoretical method and the scatterplot method was high. For July 1992, however, image derived trapezoid limits were not highly correlated. The authors suggest this was caused by above average rainfall for the month resulting in a decreased estimation of the “warm edge” (the area of maximum $T_s - T_a$ for each NDVI, line 2-4). The result illustrates an assumption that the image will contain all possible degrees of water stress for given fractional vegetation cover. This assumption was clearly not met in July 1992, while in August of 1990 and 1992 it may very well have been met. The CWSI was also calculated for these periods and used in comparison with WDI values. It was found that for low NDVI values, both CWSI and WDI are very similar while high NDVI values cause CWSI to underestimate the stress level. This underestimation, according to the authors, grows stronger as stress increases.

Regardless of the poor showing in July 1992, the authors were interested in developing an index rather than absolute estimates of latent heat flux. Therefore, they tested the value of WDI in estimating fire potential. For 9 August, 1990 CWSI and WDI were calculated from meteorological and TM data, respectively. Fire starts occurring after the TM overpass and greater than 1 ha were also extracted from the government fire database for comparisons.

The authors report that both CWSI and WDI performed well at predicting fire events in the study area. For the WDI, areas with values greater than 0.6 were coincident with all fires greater than 1 ha. This performance was met while only classifying 19-20 percent of the landscape as greater than 0.6 WDI. The CWSI showed very similar results. The benefit of using an image-derived WDI in fire danger predictions comes from the fact that comprehensive meteorological data is not required. Rather, estimates of air temperature extrapolated across the landscape are the only non-remote sensor data input. This method still relies on the assumption that complete categories of water stress are contained within the image.

SUMMARY

As shown in the preceding pages, WDI is logically related to the ratio of actual to potential ET. Since actual ET is limited below that of potential ET in water limited conditions, the WDI is a rational method for assessing surface moisture status. One of the primary benefits of WDI is the rational theoretical basis from which it was derived. Additionally, as discussed above, Vidal and Devaux-Ros (1995) showed the WDI technique functioned well as a fire danger indicator in Mediterranean forest types. All of these combined form the basis for my inclusion of the WDI logic in the re-formulation of the SMI algorithm (chapter 5).

The WDI logic requires the inclusion of near surface air temperatures in its calculation. Since landscape assessment of moisture status was the primary concern, it was not possible to use meteorological station data in the WDI formulation. By attempting to include actual station measurements of air temperature, the complexity of the SMI model would have increased to such a degree that the one of the stated goals of maintaining computational efficiency would likely have been lost. The result was the requirement that a robust and logical technique for estimating near surface air temperatures be developed that provided adequate results while maintaining computational efficiency. Chapter 3 is concerned with this issue and will discuss the methods used for the critical air temperature estimates.

LITERATURE CITED

- Campbell, G.S. and Norman, J.M., 1998. *An Introduction to Environmental Biophysics*. Springer-Verlag, New York, 286 pp.
- Clothier, B.E., Clawson, K.L., Pinter, P.J.J., Moran, M.S., Reginato, R.J. and Jackson, R.D., 1986. Estimation of Soil Heat Flux from Net Radiation During the Growth of Alfalfa. *Agricultural and Forest Meteorology*, 37: 319-329.
- Huete, A.R., 1988. A soil-adjusted vegetation index (SAVI). *Remote Sensing of Environment*, 27: 47-57.
- Idso, S.B., Clawson, K.L. and Anderson, M.G., 1986. Foliage Temperature: Effects of Environmental Factors With Implications for Plant Water Stress Assessment and the CO₂/Climate Connection. *Water Resources Research*, 22: 1702-1716.
- Idso, S.B., Schmugge, T.J., Jackson, R.D. and Reginato, R.J., 1975. The Utility of Surface Temperature Measurements for the Remote Sensing of Surface Soil Water Status. *Journal of Geophysical Research*, 80(21): 3044-3049.
- Jackson, R.D., Idso, D.B., Reginato, R.J. and Pinter, P.J.J., 1981. Canopy Temperature as a Crop Water Stress Indicator. *Water Resources Research*, 17: 1133-1138.
- Jackson, R.D., Moran, M.S., Gay, L.W. and Raymond, L.H., 1987. Evaluating Evaporation from Field Crops Using Airborne Radiometry and Ground-based Meteorological Data. *Irrigation Science*, 8: 81-90.
- Jones, H.G., 1992. *Plants and Microclimate: A Quantitative Approach to Environmental Plant Physiology*. Cambridge University Press, Cambridge, 428 pp.
- Monteith, J.L., 1973. *Principles of Environmental Physics*. Edward Arnold, London, 241 pp.
- Moran, M.S., Clarke, T.R., Inoue, Y. and Vidal, A., 1994a. Estimating Crop Water Deficit Using the Relation Between Surface-Air Temperature and Spectral Vegetation Index. *Remote Sensing of Environment*, 49: 246-263.
- Moran, M.S., Kustas, W.P., Vidal, A., Stannard, D.I., Blanford, J.H. and Nichols, W.D., 1994b. Use of Ground-based Remotely Sensed Data for Surface Energy Balance Evaluation of a Semiarid Rangeland. *Water Resources Research*, 30(5): 1339-1349.
- Vidal, A. and Devaux-Ros, C., 1995. Evaluating Forest Fire Hazard with a LANDSAT TM derived Water Stress Index. *Agricultural and Forest Meteorology*, 77: 207-224.

CHAPTER 4

ESTIMATING NEAR-SURFACE AIR TEMPERATURE

INTRODUCTION

Gridded near surface air temperature (T_a) has been a much sought after variable in the realm of earth system science because of the importance T_a plays in regulating many terrestrial processes. Approaches to deriving these surfaces have resulted in varying techniques, ranging from spatial interpolations of meteorological station data to satellite and aircraft remote sensing methods of predicting T_a . The various station-based interpolation techniques suffer from an arbitrary location of weather stations that often lack near real time data access ability. This has driven many researchers to look for satellite-based methods of filling the gaps.

The relationship between vegetation indices and surface temperature (T_s) has been well established and exploited for a variety of means. Examples include surface resistance and vegetation water balance (Carlson et al., 1994; Nemani et al., 1993; Nemani and Running, 1989), atmospheric water vapor (Prince et al., 1998), and predictive fire danger (Vidal and Devaux-Ros, 1995). However, one of the more interesting applications of the T_s and vegetation index (T_s/VI) relationship has been the derivation of T_a (Czajkowski et al., 2000; Goward et al., 1994; Prihodko and Goward, 1997).

The more common satellite based techniques for estimating T_a rely on the negative relationship between a vegetation index (VI), often the Normalized Difference Vegetation Index (NDVI), and a calculated T_s from thermal channel data. A relationship is defined through regression analysis and extrapolations occur to some theoretical VI value that represents a full canopy as viewed by the sensor. The theoretical full canopy is important due to the low thermal mass of the canopy and the notion that this canopy T_s will likely be near the local T_a . Indeed, microclimate studies have shown this to be the case (Aston and van Bavel, 1972; Gates, 1980; Geiger, 1965). Most examples of satellite based T_a estimation follow this concept and rely on a neighborhood analysis for defining the T_s/VI relationship. Goward et al. (1994), Prihodko and Goward

(1997), Prince et al. (1998), and Lakshmi et al. (2001) all use a neighborhood of Advanced Very High Resolution Radiometer (AVHRR) pixels to define the relationship and extrapolate accordingly. Comparisons are typically made with weather station data (Goward et al., 1994; Prihoko and Goward, 1997; Prince et al., 1998) or with other remote sensing derived air temperature estimates (Lakshmi et al., 2001).

This chapter will test a method of estimating near surface air temperature using NOAA AVHRR *composite* data in an area of complex terrain. Composite data was chosen because it is readily available and efficient with which to work. Since composite data are being used, a non-neighborhood technique will be presented. The goals are to achieve provide robust estimates of air temperature from satellite data while maintaining computational efficiency. This study was conducted over one complete growing season and utilizes independent gridded air temperature surfaces for direct time of satellite overpass comparisons.

METHODS

Site Description:

This study was conducted in the Bitterroot Valley of Western Montana, USA (Figure 1). It was chosen because it is representative of both the complex terrain and vegetation cover found in the Northwestern United States. The geographic extent was defined by the 1:100,000 scale 11 digit 4th Hydrologic Unit Code (HUC) developed by the USDA Natural Resources Conservation Service, Montana State office. The 4th HUC defines major drainage basins and in this case delineates the Bitterroot River and major tributaries. The Bitterroot Valley is characterized by a major mountain range on its' western border and a lesser range on the eastern border. Vegetation is typically agriculture and grasslands with riparian vegetation along river corridors at low elevations and mixed conifers at mid to high elevations. The mixed conifers transition from *Pinus Ponderosa/Pseudotsuga menziesii* through *Pinus contorta* and into *Picea/Abies* mixes at higher elevations. The highest peaks are characterized by alpine vegetation on the Western edge of the

study area. Elevations range from approximately 976 meters where the Bitterroot River joins the Clark Fork of the Columbia River to 3098 meters at Trapper peak. The Bitterroot HUC stretches approximately 157 km north-south, approximately 58 km east-west, and contains approximately 743,000 Hectares.

Figure 1: Study site, Bitterroot Valley, western Montana, USA.



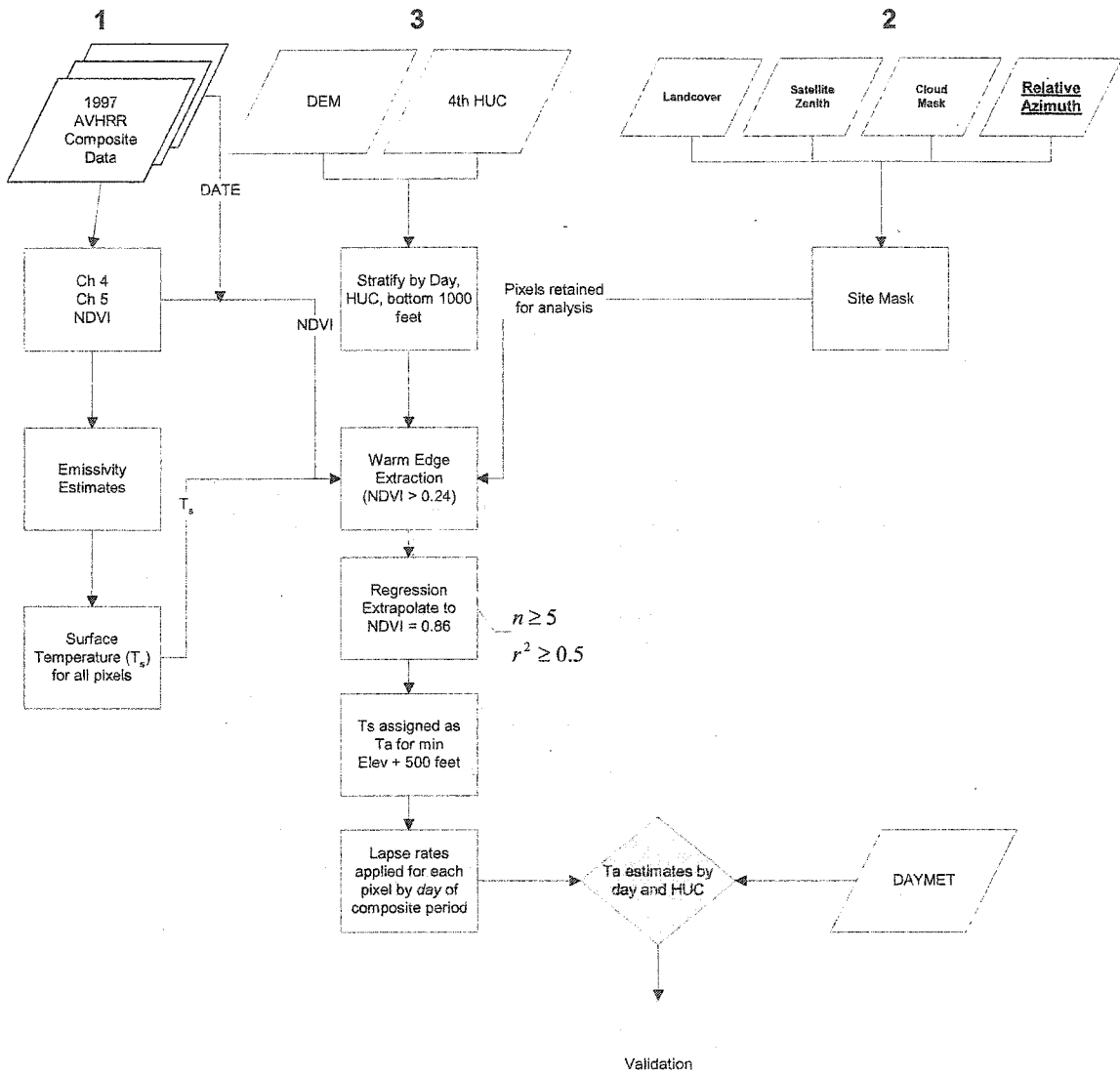
Satellite Data

Since 1987, the U.S. Geological Survey's EROS Data Center (EDC) has been receiving, processing, and archiving AVHRR data. For this study biweekly maximum NDVI composites derived from afternoon overpasses of NOAA-14 were obtained. The maximum NDVI compositing technique relies upon 14 daily calculations of NDVI. The maximum NDVI observed per pixel in that period is retained and all individual channel data (channels 1-5) from the day of maximum NDVI observation are also retained in the data set. Additionally, there are three geometry files included: satellite zenith, solar zenith, and relative zenith angles as well as a date file referencing the day of data retention within the composite period. The channel data are converted to percent reflectance (channels 1 and 2) and brightness temperature (channels 3-5). The maximum NDVI composite technique is used to minimize cloud contamination (Holben, 1986), however, recent studies indicate a preferential selection of off-nadir pixels (Stoms et al., 1997). In addition to calibration and compositing, all data are registered and projected at EDC into Lambert's Azimuthal Equal Area projection to facilitate expeditious use in geographic studies. 1997 composite periods P10 through P19 (9 May – 25 September) were used in this study. No radiometric or geometric post processing of the EDC data was done.

Processing Stream

Figure 2 describes a conceptual layout of the processing stream used to estimate air temperature. This flowchart will be referenced in the explanation of the methods. Part one refers to the calculation of surface temperature and emissivity estimates. Part two discusses the site mask imposed on the analysis, and part three explains the central processing loop. The core process relies on inputs from parts one and two and produces *day* specific output from the composite data for all pixels not removed by the masking criteria.

Figure 2: Flowchart showing processing stream.



Surface Temperature (Part 1)

The split window technique of Ulivieri et al. (1994) was used in this study to calculate surface temperature. The primary reason for using this technique is its simple formulation, accurate results (Vazquez et al., 1997; Ouaidrari et al., 2002), applicability across multiple AVHRR sensors (Ouaidrari et al., 2002; Ulivieri et al., 1994) and its relative resistance to emissivity errors (Vazquez et al., 1997). The surface temperature (T_s) formulation is as follows:

$$T_s = T_4 + 1.8(T_4 - T_5) + 48(1 - \epsilon) - 75(\epsilon_4 - \epsilon_5) \quad (\text{eq. 1})$$

where T_4 and T_5 are brightness temperatures of AVHRR channels 4 and 5, respectively, ϵ_4 and ϵ_5 are emissivity estimates for channels 4 and 5, and ϵ is mean emissivity of channels 4 and 5.

The choice was made to estimate emissivity in an attempt to reduce the associated error in T_s calculation, which can be quite large. The methods of van de Griend and Owe (1994) for estimating ϵ_4 (equation 2) and the Thornton method (Thornton, 1998), which was developed over a region that includes this study area, were used to estimate the difference in channel 4 and 5 emissivities ($\Delta\epsilon$). Average emissivity (ϵ) and ϵ_5 were then calculated from the estimated parameters. Equations two and three are empirical relationships while four and five are simply algebraic expressions. Formulations are as follows:

$$\varepsilon_4 = 0.99 - 0.09 \frac{(0.7 - NDVI)}{0.6} \quad (\text{eq. 2})$$

$$\Delta\varepsilon = -0.02938 + 0.04957 * NDVI \quad (\text{eq. 3})$$

$$\varepsilon_5 = \varepsilon_4 - \Delta\varepsilon \quad (\text{eq. 4})$$

$$\varepsilon = \frac{\varepsilon_4 + \varepsilon_5}{2} \quad (\text{eq. 5})$$

Site Mask (Part 2)

There were a series of constraints imposed upon the estimation of T_a to remove pixels that contained cloud contamination, undesirable landcover classes, extreme satellite zenith angles, or relative azimuth angles that would likely lead to poor predictions of air temperature. Any pixel in the data that failed to meet the listed criteria was removed from further analysis. Cloud contamination, undesirable landcover classes, and satellite zenith angles will be discussed below. The addition of the relative azimuth constraint will be discussed in the results section.

The methods of defining cloud-contaminated pixels were based on the methods of Flasse and Ceccato (1996), Thornton (1998), and Seielstad et al. (2002).

Pixels were considered cloud contaminated if they met any of the following criteria:

1. Channel 1 reflectance > 0.2 (eq. 6)

2. $Q < 1.20$ ($Q = \text{NIR/red}$) (eq. 7)

3. $\Delta T_{45} > 4.5$ (K) OR $dT_{45} < -1.5$ (K) (eq. 8)

4. $\Delta T_{34} > 15$ (K) (eq. 9)

If the pixel was shown to be cloud-contaminated in a given composite period, that pixel was flagged and removed from subsequent analysis.

The land cover constraint was based on the U.S. Geological Survey's North America Land Cover Characteristics Data Base (2000). This is a generalized landcover map showing such classes as shrubland, irrigated cropland, evergreen needleleaf forest, etc. The primary goal was to remove pixels that contained potentially confounding landcover practices such as agriculture, water, or urban/developed or those that were potentially mislabeled (evergreen broadleaf forest in Montana, for example). The resulting mask retained only those pixels from the following landcover classes:

- Grassland
- Shrubland
- Deciduous Broadleaf Forest
- Evergreen Needleleaf Forest
- Mixed Forest

A simple satellite zenith angle truncation was included to remove extreme look angles from the dataset. As suggested by Prihodko and Goward (1997), a zenith angle greater than 40 degrees was removed in the initial implementation to minimize the thermal attenuation caused by long atmospheric path lengths. Subsequent examination of the estimates, however, resulted in the satellite zenith angle constraint being changed to 30 degrees. The impacts of zenith angles are discussed in greater detail below.

Warm Edge Extraction - T_a technique (Part 3)

Many implementations of the T_s/VI technique for estimating T_a rely on a contextual approach where a neighborhood of pixels is used for the regression analysis. The "window" is then shifted (usually one row or column) and the calculation is repeated. This technique relies on spatial autocorrelation of adjacent pixels for the solution of T_a . Unfortunately, it results in an effective reduction in the spatial resolution of the solution itself (Prince et al., 1998). Other studies have exploited the T_s/VI relationship in a different manner. While not used explicitly for T_a estimation, some authors chose combinations of contextual

analysis with a data reduction technique. For example, Nemani and Running (1993) and Carlson et al. (1995) limited their analysis to only those NDVI/ T_s pairs that showed maximum T_s for each unique NDVI, the so-called warm edge extraction. The logic behind this selection suggests that those pixels are most likely well illuminated, near nadir, and in thermal equilibrium at time of satellite overpass.

Since one of the primary interests is in a relatively simple and computationally efficient technique of estimating air temperature at landscape scales, a method was chosen that combines both contextual and non-contextual elements. A stepwise explanation of the process follows.

First, a digital elevation model (DEM) was used to build a mask of the lowest 1000 feet of the Bitterroot HUC (figure 3). The assumption here is that an estimate of mean valley temperature could be used with a simple adiabatic lapse rate to calculate temperatures at higher elevations. The bottom 1000 feet was chosen because it gave an adequate number of T_s and NDVI values for use in the air temperature estimates and provided enough of the required diversity in landcover (hence NDVI scores, see Riddering et al., 1999) to define the NDVI/ T_s relationship. For this bottom 1000 feet, the data were then stratified into individual year-day bins so that only data from the same day was used in the individual initial air temperature estimate for the valley floor.

Figure 3: Bitterroot Valley 4th Hydrologic Unit Code and bottom 1000 feet shown in green (in green) used in initial daily air temperature estimates.



Once sorted by day, NDVI scores of 0.24 and below (and the associated T_s) were removed from the analysis. This minimum value was based on empirical observation of NDVI/ T_s pairs and reported minimum NDVI values for vegetated surfaces (Carlson et al., 1994), effectively removing confounding pixels while reducing the size of the dataset. Next, the “warm edge” was extracted, resulting in more data reduction. Then a least squares line was fit to the data. Regression constraints were imposed on the data such that any line composed of less than 5 pixels ($n=5$) or exhibiting a coefficient of determination (r^2) less than 0.5 were removed from further consideration. This has the effect of maintaining a minimal quality control standard in the data. Finally, the equation describing this line was extrapolated to NDVI = 0.86 to

estimate the associated full canopy T_s , which was used as a surrogate for the mean valley temperature. A value of 0.86 as the full canopy NDVI was chosen, following the reports of Prihodko (1997) and based on long-term maximum NDVI scores (Burgan and Chase, 1998) for known full canopy vegetation typical of Western Montana Forests. The extrapolated value of T_s (which is the initial T_a value) was assumed to be the mean value of the bottom 1000 feet and was therefore assigned to the mean elevation of the bottom 1000 feet (minimum + 500 feet, therefore, 3700 feet for the Bitterroot Valley). Finally, a simple environmental lapse rate of 1.98 K/1000 feet (Barry and Chorley, 1998) was used to adjust temperatures according to DEM derived elevations. The result is pixel-based T_a estimates that are unique for each day of data within the composite period.

DAYMET

Most studies have used point weather station data for comparisons to satellite estimates of T_a with varying degrees of success. Our goal, however, was to test the T_a logic across a gridded topographically complex landscape. Therefore, it was desirable to test the T_a estimates against an independent gridded surface of air temperature. As a result, the DAYMET model was chosen to derive the independent air temperature grids for model comparison.

Daymet has been described in detail elsewhere (Thornton et al., 1997). Briefly, Daymet is a computer program that produces daily gridded meteorological variables (maximum and minimum temperature, precipitation, radiation, and humidity) over complex terrain from weather station observations. It utilizes a weighted Gaussian filter and iterative processes to first predict known station values (sequentially removed from the analysis) and subsequent extrapolated values. A DEM is required to account for the vertical variation in the landscape and to calculate the horizontal relationships of temperature in complex terrain in a spatially explicit manner. Daymet has been shown to be a robust method of generating meteorological surfaces in complex terrain with reported Mean Absolute Errors (MAE) in yearly temperature prediction between 0.7 C and 1.2 C for maximum temperature (T_{max}) and minimum temperature (T_{min}), respectively.

Daily errors in temperature are reported at 1.8 C and 2.0 C, respectively for Tmax and Tmin. The spatial resolution of DAYMET grids used in this study was 1 km, matching composite AVHRR resolution.

Synchronization of DAYMET and T_aEstimate

For this study, T_{max} and T_{min} for each pixel in the study area from the DAYMET record was extracted.

Temperature at time of satellite overpass, discussed below, was calculated and this served as “ground truth” for comparison to satellite estimates of near surface air temperature.

Time of satellite overpass was estimated following the methods of Thornton (1998), which uses solar zenith angle and the equation defining earth-sun geometry used in the DAYMET model for incoming radiation calculations. Hour angle (*h*, where 0 degrees = local solar noon) is then converted to local solar time with the following equations:

$$h = \arccos \left[\frac{(\cos(z) - \sin(l) \sin(\text{decl}))}{(\cos(l) \cos(\text{decl}))} \right] \quad (\text{eq. 10})$$

$$\text{decl} = -23.45 \cos[(\text{yearday} + 11.25)0.9863] \quad (\text{eq. 11})$$

$$T_{so} = 12.0 + \left(\frac{1}{15}\right)h \quad (\text{eq. 12})$$

where *z* is solar zenith angle, *l* equals latitude of each pixel, *T_{so}* is time of satellite overpass, and *decl* is the Earth’s rotational axis declination relative to the principal plane.

With time of satellite overpass known, T_{max} and T_{min} from Daymet and the equations of Campbell and Norman (1998) were used to calculate a Daymet derived temperature coincident with satellite overpass.

Daymet temperature was calculated in the following manner:

$$\Gamma_{(t)} = 0.44 - 0.46 \sin(\omega t + 0.9) + 0.11 \sin(2\omega t + 0.9) \quad (\text{eq. 13})$$

where $\omega = \pi/12$ and t is time of day (hours, 12 at solar noon). Then, this function can be used to calculate temperature at any time of day (t):

$$\begin{aligned} T_{(t)} &= T_{x,i-1} \Gamma(t) + T_{n,i} [1 - \Gamma(t)] & 0 < t \leq 5 \\ T_{(t)} &= T_{x,i} \Gamma(t) + T_{n,i} [1 - \Gamma(t)] & 5 < t \leq 14 \\ T_{(t)} &= T_{x,i-1} \Gamma(t) + T_{n,i+1} [1 - \Gamma(t)] & 14 < t \leq 24 \end{aligned} \quad (\text{eq. 14})$$

where T_x and T_n are daily maximum and minimum temperature, respectively, i is present day, $i-1$ is previous day, and $i+1$ is the next day. Temperatures were then compared with a series of hourly Remote Automated Weather Station (RAWS) observations over multiple days in 1997 to check correspondence (data not shown).

Validation Strategy

The validation strategy relies on comparisons of co-located grids of DAYMET temperature at time of satellite overpass and the AVHRR based T_a estimate. As mentioned above, the AVHRR based T_a estimate is day specific. The DAYMET surface was developed to match that day at the time of satellite overpass and is treated as the ground truth. For example, the composite period date raster was used as a mask in the DAYMET surfaces so that the individual DAYMET pixels match the day of satellite acquisition. The result is day-specific comparisons between pixels in the two rasters. Results are reported primarily as pooled results (entire record) except when specific interests warrant otherwise. Reported statistics include

Mean Absolute Error (MAE) defined as the average of the absolute difference between DAYMET T_a and satellite T_a estimates, Pearson's correlation coefficient, and regression coefficients.

RESULTS

The results will be presented in three parts. The first reports the original implementation with no relative azimuth constraint and a satellite zenith maximum of 40 degrees (called v1-Goward below). The second set of results was a consequence of increased scrutiny of the satellite zenith angles where a 30 degree limit was imposed (v2-SATZ30). Finally the third set of results show the impact of relative azimuth constraints added to the estimation of T_a (v3-SATZ30 & REL AZ). The addition of relative azimuth constraints was due to the observed impact that westerly look directions had on the error structure of T_a estimates.

v1- Goward

With the initial implementation, an attempt was made to use all composite periods (p10 – p19) coupled with cloud screening and satellite zenith angle constraints (40 degrees as per Prihodko and Goward, 1997). Due to these constraints and the regression requirements listed above, the algorithm was unable to calculate any air temperatures for composite periods 10 – 13 (9 May – 3 July). The resulting period of assessment is 4 July – 25 September, composed of composite periods 14 – 19.

Plots of estimated T_a versus Daymet T_a are shown in Figure 4 and statistical summaries of regression analysis and correlation assessment are shown in Table 1. Additionally, mean absolute error (average absolute difference between T_{est} and Daymet T_a) was derived. Air temperature estimates and Daymet actual air temperatures showed a Pearson's Correlation coefficient of 0.576 (Table 2) and an MAE of 6.96° C for all days and a total of 28 unique day-based predictions ($n = 28$).

Figure 4: Scatterplot of Satellite air temperature estimates versus DAYMET air temperature estimates for the original implementation (satellite zenith angle constraint $\leq 40^\circ$). MAE = 6.96, R = 0.576.

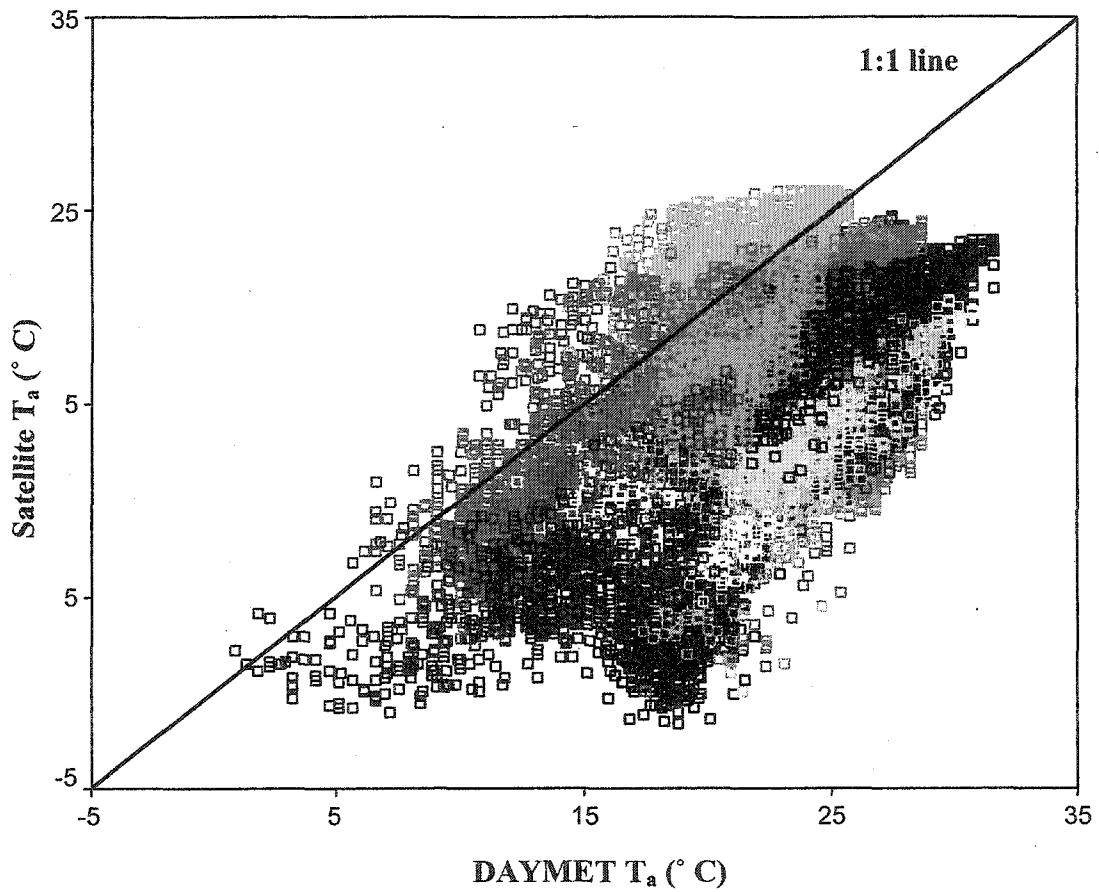


Table 1: Regression coefficients for the three implementations of satellite T_a . Dependant variable (Y) is satellite T_a and independent variable (X) is DAYMET derived T_a , with equations taking the form of $Y = mX + B$.

Regression Parameters

	n	m	B	Correlation Coefficient (R)	Std. Error of the Estimate
Original Implementation	33065	0.634	1.403	0.576	3.69
Satellite Zenith 30	28498	.449	6.109	.410	3.38
Satellite Zenith 30 and Relative Azimuth	7460	.818	-2.149	.742	2.73

Table 2: Mean Absolute Error (MAE), Correlation Coefficients, number of days, and membership in each MAE difference class ($0 \leq \text{Class 1} \leq 2.0^\circ\text{C}$; $2.0^\circ\text{C} < \text{Class 2} \leq 5.0^\circ\text{C}$; $5.0^\circ\text{C} < \text{Class 3} \leq 8.0^\circ\text{C}$).

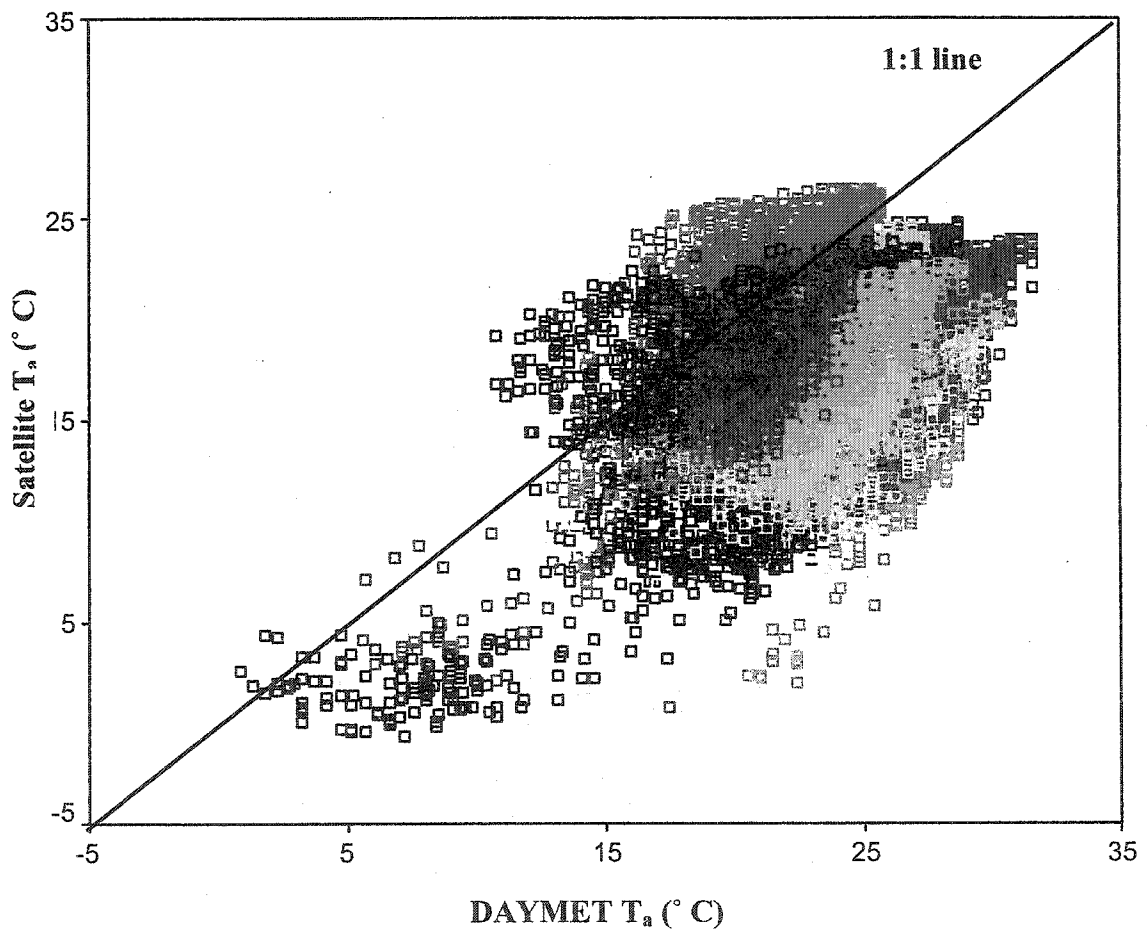
	MAE	Correlation (R)	Number of days	Class 1 (n)	% Class 1	Class 2 (n)	% Class 2	Class 3 (n)	% Class 3	Total pixels
Original Implementation	6.96	0.576	28	3336	0.10	7261	0.22	9423	0.28	33065
Satellite Zenith 30	6.47	0.410	20	3430	0.12	6671	0.23	8270	0.29	28498
Satellite Zenith 30 and Relative Azimuth	6.09	0.742	12	463	0.06	2226	0.30	3024	0.41	7460

v2 – SATZ 30

When comparing satellite zenith angles to predicted temperature poor predictive ability was observed when zenith angles were greater than 30 degrees (data not shown). The code was modified to change the satellite

zenith angle constraint from 40 degrees to 30 degrees and the model was re-run for all composite periods. The enhanced zenith angle constraint had the effect of removing even more days from the total analysis ($n = 20$). The MAE improved to 6.47 degrees C, but the correlation coefficient dropped to 0.410 (see Table 1 and Figure 5).

Figure 5: Satellite Zenith angle $\leq 30^\circ$. MAE = 6.47, R = 0.413.



With the satellite zenith angle information, look directions were calculate and the analysis was split accordingly. Satellite zenith angle of 90 degrees denote nadir views while anything greater than 90 degrees are westerly looks and less than 90 degrees are easterly looks. As shown in Figure 6, when the satellite is recording information with a westerly look, the predictive ability appears to suffer. Westerly looks give an MAE of 6.75° C and an R of 0.163 while easterly looks have an MAE of 5.74° C and an R of 0.766, a remarkable difference.

It is worth noting that the above look direction assessments where made on the final air temperature prediction product. There was no masking based on look direction in the original estimation of valley air temperature or subsequent temperatures based on lapse rates. Rather, they were used to stratify pixels from the analysis after the lapse rates were applied. While it appears an incorporation of look angle will dramatically improve the correlation in the final product, there was no attempt to constrain pixels used in the above analysis by look direction. The result is a likely decrease in the predictability of the overall air temperature estimate due to the undesirable look directions. Based on this finding, the relative azimuth information was included as an initial masking constraint in the third version discussed below.

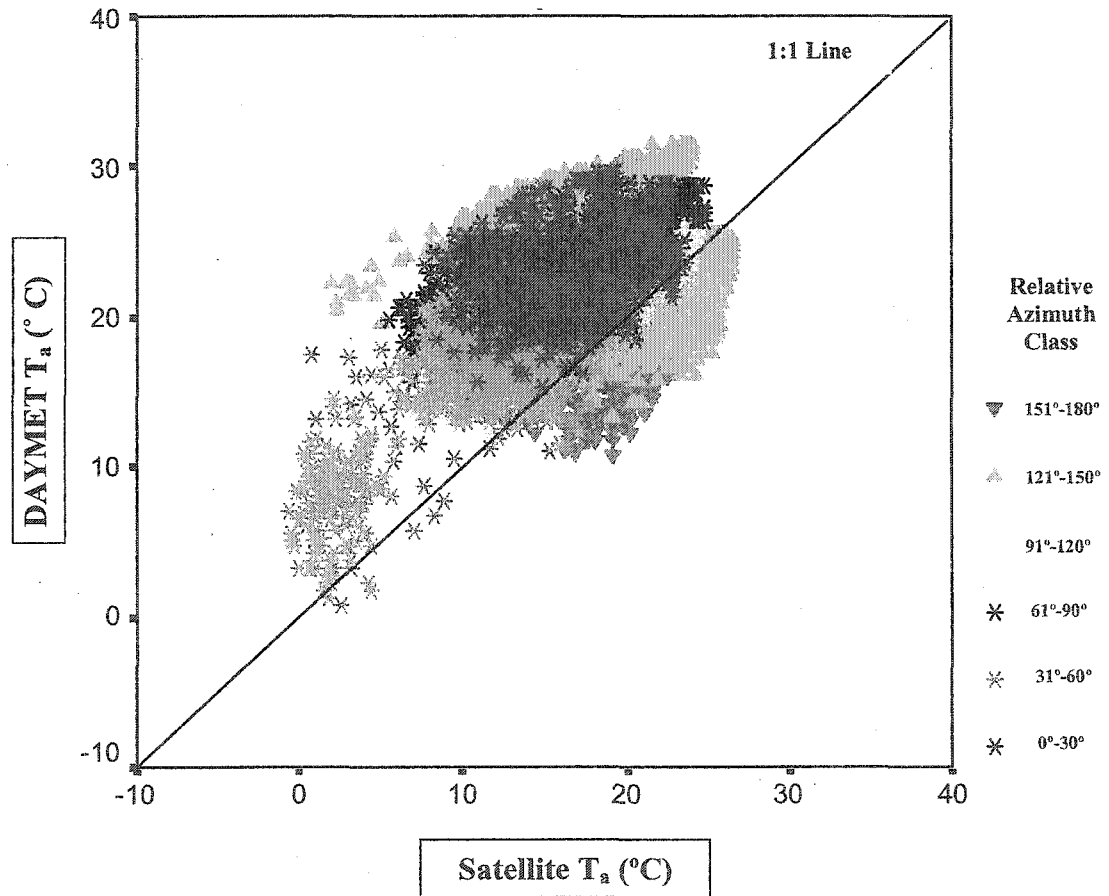
v3 – SATZ30 & REL AZ

Relative azimuth is typically provided in the AVHRR dataset for atmospheric correction algorithms. It is defined as the absolute difference between the solar azimuth and the satellite azimuth angles and it ranges from zero to 180 degrees. Satellite and solar azimuth are the actual true azimuths *from* a given pixel to both the satellite and the sun, respectively. Therefore, relative azimuths of 180 degrees define a sun-surface-sensor geometry where the satellite is looking directly into the solar plane.

Due to the directional impacts discussed above, the relative azimuth data was categorized in order to provide an initial assessment of the impact that look direction has on air temperature estimates. Classes were defined at 30 degree increments of relative azimuth such that class one contained zero to 30 degrees,

class two contained 31 to 60 degrees, and so on up to 180 degrees. The result is 6 categories of relative azimuth. Figure 6 shows the previous predicted versus observed air temperatures using the 30 degree satellite zenith constraint and are marked by relative azimuth class.

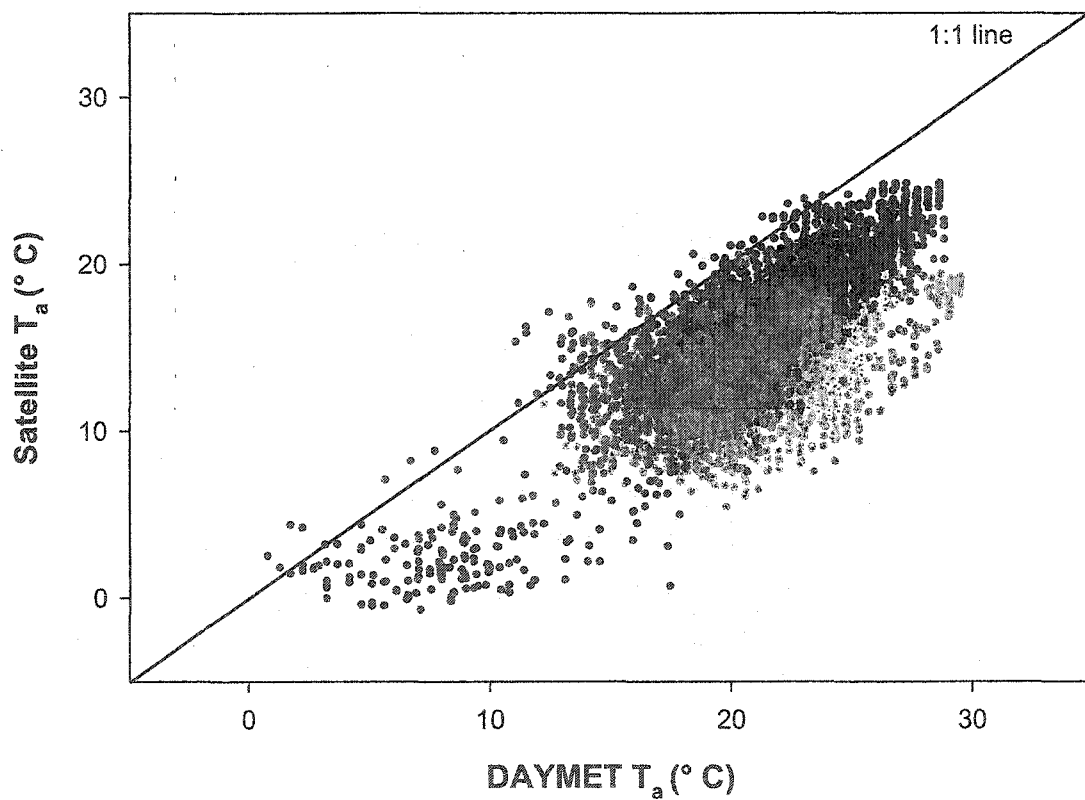
Figure 6: DAYMET T_a versus Satellite T_a (30° satellite zenith angle constraint). Markers denote relative azimuth classes. Classes are 0°-30° for class one, 31°-60° for class two, etc. up to 180°.



Based on figure 6, relative azimuth classes five and six were included in the mask and the algorithm was re-run. By incorporating this relative azimuth constraint, the extreme westerly looks in the initial valley bottom air temperature prediction were removed. Subsequent lapse rate calculations were made as before. Adding the relative azimuth mask resulted in further reduction of the data set. For the composite periods

14 – 19, there were 12 individual days of data. Interestingly, the MAE dropped to 6.09 degrees C and the correlation coefficient rose to 0.742 (Table 1) when using the satellite zenith constraint of 30 degrees and the relative azimuth mask. Figure 7 shows estimate air temperature versus DAYMET derived temperature stratified by day.

Figure 7: Scatterplot of satellite predicted T_a versus DAYMET T_a . Satellite Zenith angle ≤ 30 degrees and Relative Azimuth ≤ 120 degrees. MAE = 6.09, R = 0.742.



Summary

Table 1 lists the three methods of predicting air temperature and the landscape membership of difference classes. Class one was defined as the absolute difference in T_{est} and Daymet T_a of 0 – 2 C, class two of 2.1 – 5 C, and class three of 5.1 – 8.0 C. As discussed earlier, the addition of relative azimuth and 30 degree satellite zenith constraints reduced the total number of available pixels while improving the overall performance of the technique. The greatest improvement came in difference class two while a reduction in class one was observed. Overall, approximately 60 % of all T_{est} pixels fell within 8 C of Daymet surfaces. However, the more stringent analysis provided increased correlation and decreased MAE for the entire record. Regression analysis for all implementations is shown in table 2.

DISCUSSION AND CONCLUSIONS

Sources of Error

There are numerous sources of potential error in this study, both in air temperature estimation, and the Daymet derived reference source. Surface temperature errors, including water vapor impacts and emissivity errors, residual cloud contamination, and choice of static environmental lapse rates all impact the estimated air temperature. Conversely, there is a known error structure associated with Daymet derived surfaces that were used as “ground truth” and some error in interpolated air temperature at time of satellite overpass.

Perhaps the largest potential error in this study comes from surface temperature calculations. The Ulivieri (1994) method was chosen because of its applicability to various NOAA AVHRR sensors and its reported resistance to errors in land surface emissivity calculations (Ulivieri et al., 1994; Vazquez et al., 1997). However, there is still a large potential error in the T_s calculation when atmospheric water vapor is not considered in the model. Ouaidrari, et al. (2002) report possible errors in T_s due to water vapor ranging from a minimum of –7.73 K to a maximum of 3.08 K when using a low water vapor formulation of the T_s

equation in the presence of high actual atmospheric water vapor content. These authors state that analysis of data from NASA's Data Assimilation Office (DAO) show that the base assumption of low atmospheric water content while formulating many split window techniques may not be valid. The presence of higher water vapor content than originally assumed is fairly common. While the confounding effect of atmospheric water vapor was not specifically studied, it is reasonable to assume that there is a potential influence in the study site, particularly in 1997, which was an atypically rainy year in Western Montana.

Emissivity is a critical component in calculating T_s . While the Ulivieri (1994) method has shown great resistance to errors in emissivity, the potential for miscalculation of T_s does exist. Our choice in estimating emissivity following the techniques of van de Griend and Owe (1994) and Thornton (1998) was based on the desire to develop a robust yet efficient means of estimating T_a at landscape scales. Ouaidrari et al. (2002) calculated potential errors in T_s from faulty emissivity calculations and showed that great variation may occur when emissivity is not adequately estimated. The reported potential RMS errors with the Ulivieri (1994) T_s method range from 1.10 K to 3.91 K depending on the magnitude of emissivity error.

Another possible source of error is the choice of a static environmental lapse rate used throughout the season in this study. Again, due to the desire to keep the technique simple a single lapse rate was chosen for adjusting temperatures as a function of DEM elevation. While it is acknowledged that this is probably not the most robust means of adjusting temperatures throughout the season, and is likely a source of error, there is no way of calculating a lapse rate for each composite period and subsequent day. Information does exist for seasonal trends in lapse rates for the adjacent Bitterroot-Selway Wilderness area (Finklin, 1983) and future work will investigate the utility of incorporating these seasonal adjustments.

Finally, the gridded Daymet derived T_{max} and T_{min} surfaces to interpolate temperatures at time of satellite overpass were used. Daymet, however, has its own set of possible errors associated with it. Thornton et al. (1997) report a daily MAE for T_{max} and T_{min} of 1.8 C and 2.0 C, respectively. Since an absolute value of the differences between predicted and observed is what the MAE assessment give, one does not know the

direction of this reported error. However, adding and subtracting 1.9 C to the Daymet temperatures and recalculating the MAE's and correlations show interesting results. Correlations stay constant, but subtracting results in a new MAE in predicted air temperature and Daymet air temperature of 4.3 C for the final implementation of the model (data not shown).

The numerous constraints imposed on the estimation of T_a warrant some discussion, primarily the NDVI limits and the minimum regression parameters used in the initial valley bottom estimation of air temperature. There is ample opportunity to adjust many of the constraints made in this project and future work will examine the impact these choices have in the performance of the air temperature estimation.

The minimum NDVI value of 0.24 was empirically derived and is similar to values reported by other authors of uncontaminated bare ground pixels (Carlson et al., 1994; Riddering et al., 1999). The inclusion of low NDVI values (less than 0.24) results in a decreased ability to derive a good T_s /NDVI relationship. Similarly, the choice of 0.86 as the extrapolation value was based on other published values and the fact that this number corresponds with known full canopy vegetation in western Montana, as shown in the long term NDVI records (Burgan and Chase, 1998). Though other studies have used different values of NDVI, the absolute difference in air temperature estimates as a function of NDVI score is minor. Prihodko et al. (1997) report changes in NDVI from 0.86 to 0.873 resulted in air temperature changes of only 0.15° C.

Since this technique uses composite data, neighborhood functions could not be used to derive an estimate of air temperature. Therefore, constraints were placed on the regression component of the central air temperature estimation loop. Since the site mask removes a great number of valley bottom pixels, regression parameters were kept fairly non-restrictive ($n \geq 5$ and $r^2 \geq 0.5$) to allow for a larger number of air temperatures to be calculated. Additionally, there were many occasions in the data where a significant number of pixels occurred on a given date, but only a few pixels from that date occurred in the valley bottom. The low number of required pixels allowed us to perform estimates of T_a in this situation. Interestingly, while there were few dates that had a low number of valley bottom pixels (5-10), when this

occurred the correlations between satellite estimate and DAYMET temperature were similar to dates with a larger n (data not shown).

Efficiency

Developing a simple, efficient, and robust method of estimating air temperature was the primary goal of this study. Through the use of composite satellite data, a robust surface temperature algorithm, and basic assumptions on temperature variations with elevation, this goal was achieved. These results are similar to those reported in previous studies. With continued investigation, these techniques can be improved even further. To improve future performance of the algorithm, some suggestions can be made. First, through the use of weekly composites, it is likely the total number of T_a estimates throughout the growing season can be improved, thereby giving a more complete assessment of air temperature. Though biweekly composites encompass 14 days of data, it is more typical to see only four to five days of retained data within an area defined by a 4th HUC. The increased temporal resolution of weekly composites would likely provide a more distributed and complete coverage of air temperature estimates throughout the growing season.

Second, seasonal variations in lapse rate need to be studied further. These data exist in the Selway-Bitterroot Wilderness of Western Montana and North Idaho (Finklin, 1983). Further studies should investigate the utility of this record for application to the Bitterroot valley and the applicability to typical complex terrain in this region. It is highly unlikely that a single environmental lapse rate is sufficient to describe the complex atmospheric relationships between elevation and temperature throughout the year. Such simple components as increased atmospheric water vapor or inversions can seriously impact the assessment of air temperature as a function of elevation.

Finally, a more complete assessment of sun-surface-sensor geometry needs to be made as evidenced by the results in the relative azimuth mask. The precise reasons why large relative azimuths tend to result in poor

agreement in estimated versus observed air temperatures are not known as that was beyond the scope of this study. However, it is hypothesized that by looking into the solar plane, the sensor is suffering from solar contamination, either through increased path radiance or other means. A look direction constraint based on the differentiation of fore and/or backscatter would likely benefit future research in satellite based air temperature estimates.

Overall, the algorithm described in this paper performed remarkably well considering the list of potential confounding issues discussed above. It is expected that improved capability may be achieved with more site-specific corrections to the algorithm, such as improved lapse rates, and better understanding of the geometric issues presented. Additionally, the logic presented here can be applied to more advanced sensors and data currently available such as the Moderate Resolution Imaging Spectroradiometer (MODIS). With the improved calibration and radiometry of MODIS and the efficiency of this T_a technique, relatively simple estimates of T_a may be computed with high degrees of confidence.

With the ability to predict near surface air temperatures as described above, one of the most critical components of the WDI logic has been met. As described, a robust model was formulated that produced air temperature estimates of sufficient accuracy to include in the continued adaptation of the SMI model for the assessment surface moisture status. Chapter 5 will describe the development and implementation of the final SMI algorithm. While the algorithm described in the following chapter borrows from the WDI logic discussed in Chapter 3, it also includes descriptions of the adaptations necessary to convert from a large-scale (small area) model to the desired small-scale (large area) algorithm for landscape assessment.

LITERATURE CITED

2000. North American Land Cover Characteristics Data Base. U.S. Geological Survey.
- Aston, A.R. and van Bavel, C.H.M., 1972. Soil Surface Water Depletion and Leaf Temperature. *Agronomy Journal*, 64: 368-373.
- Barry, R.G. and Chorley, R.J., 1998. *Atmosphere, Weather, and Climate*. Routledge, New York, 409 pp.
- Burgan, R.E. and Chase, C.H., 1998. NDVI and Derived Image Data. RMRS-GTR-9-CD. Rocky Mountain Research Station, Missoula Fire Sciences Laboratory, Missoula, MT, pp. Compact Disc.
- Campbell, G.S. and Norman, J.M., 1998. *An Introduction to Environmental Biophysics*. Springer-Verlag, New York, 286 pp.
- Carlson, T.N., Gillies, R., R. and Schmugge, T.J., 1995. An Interpretation of Methodologies for Indirect Measurement of Soil Water Content. *Agricultural and Forest Meteorology*, 77: 191-205.
- Carlson, T.N., Gillies, R.R. and Perry, E.M., 1994. A Method to Make Use of Thermal Infrared Temperature and NDVI Measurements to Infer Surface Soil Water Content and Fractional Vegetation Cover. *Remote Sensing Reviews*, 9: 161-173.
- Czajkowski, K.P., Goward, S.N., Stadler, S.J. and Walz, A., 2000. Thermal Remote Sensing of Near Surface Environmental Variables: Application Over the Oklahoma Mesonet. *Professional Geographer*, 52(2): 345-357.
- Finklin, A.I., 1983. *Weather and Climate of the Selway-Bitterroot Wilderness*, 144. University Press of Idaho, Moscow, ID, 144 pp.
- Flasse, S.P. and Ceccato, P., 1996. A Contextual Algorithm for AVHRR Fire Detection. *International Journal of Remote Sensing*, 17(2): 419-424.
- Gates, D.M., 1980. *Biophysical Ecology*. Springer-Verlag, New York, 611 pp.
- Geiger, R., 1965. *Climate Near the Ground*. Harvard University Press, Cambridge, 611 pp.
- Goward, S.N., Waring, R.H., Dye, D.G. and Yang, J., 1994. Ecological Remote Sensing at OTTER: Satellite Macroscale Observations. *Ecological Applications*, 4(2): 322-343.
- Holben, B.N., 1986. Characteristics of Maximum-Value Composite Images from Temporal AVHRR Data. *International Journal of Remote Sensing*, 7(11): 1417.
- Lakshmi, V., Czajkowski, K., Dubayah, R. and Susskind, J., 2001. Land Surface Air Temperature Mapping Using TOVS and AVHRR. *International Journal of Remote Sensing*, 22(4): 643-662.
- Nemani, R., Pierce, L., Running, S. and Goward, S., 1993. Developing Satellite-derived Estimates of Surface Moisture Status. *Journal of Applied Meteorology*, 32(3): 548-557.
- Nemani, R.R. and Running, S.W., 1989. Estimation of Regional Surface Resistance to Evapotranspiration from NDVI and Thermal-IR AVHRR Data. *Journal of Applied Meteorology*, 28(4): 276-284.

- Ouaidrari, H., Goward, S.N., Czajkowski, K.P., Sobrino, J.A. and Vermote, E., 2002. Land Surface Temperature Estimation from AVHRR Thermal Infrared Measurements: An Assessment for the AVHRR Land Pathfinder II Data Set. *Remote Sensing of Environment*, 81: 114-128.
- Prihodko, L. and Goward, S.N., 1997. Estimation of Air Temperature from Remotely Sensed Surface Observations. *Remote Sensing of Environment*, 60: 335-346.
- Prince, S.D., Goetz, S.J., Dubayah, R.O., Czajkowski, K.P. and Thawley, M., 1998. Inference of Surface and Air Temperature, Atmospheric Precipitable Water and Vapor Pressure Deficit Using Advanced Very High-Resolution Radiometer Satellite Observations: Comparison with Field Observations. *Journal of Hydrology*, 212(213): 230-249.
- Riddering, J.P., Seielstad, C.A. and Queen, L.P., 1999. Developing a Computationally Efficient Fire Potential Index from Satellite Derived Estimates of Surface Moisture Status, American Society of Photogrammetry and Remote Sensing Annual Conference, Portland, OR. 296-307.
- Seielstad, C.A., Riddering, J.P., Brown, S.R., Queen, L.P. and Hao, W.M., 2002. Testing the Sensitivity of a MODIS-Like Daytime Active Fire Detection Model in Alaska Using NOAA/AVHRR Infrared Data. *Photogrammetric Engineering and Remote Sensing*, 68(8): 831-838.
- Stoms, D.M., Bueno, M.J. and Davis, F.W., 1997. Viewing Geometry of AVHRR Image Composites Derived Using Multiple Criteria. *Photogrammetric Engineering and Remote Sensing*, 63(6): 681-689.
- Thornton, P.E., 1998. Regional Ecosystem Simulation: Combining Surface- and Satellite-Based Observations to Study Linkages between Terrestrial Energy and Mass Budgets. Ph.D. Dissertation Thesis, University of Montana, Missoula, 280 pp.
- Thornton, P.E., Running, S.W. and White, M.A., 1997. Generating Surfaces of Daily Meteorological Variables Over Large Regions of Complex Terrain. *Journal of Hydrology*, 190: 214-251.
- Ulivieri, C., Castronuovo, M.M., Francioni, R. and Cardillo, A., 1994. A Split Window Algorithm for Estimating Land Surface Temperature from Satellites. *Advances in Space Research*, 14(3): 59-65.
- van de Griend, A.A. and Owe, M., 1994. Bare Soil Surface Resistance to Evaporation by Vapor Diffusion Under Semiarid Conditions. *Water Resources Research*, 30(2): 181-188.
- Vazquez, D.P., Reyes, F.J.O. and Arboledas, L.A., 1997. A Comparative Study of Algorithms for Estimating Land Surface Temperature from AVHRR Data. *Remote Sensing of Environment*, 62: 215-222.
- Vidal, A. and Devaux-Ros, C., 1995. Evaluating Forest Fire Hazard with a LANDSAT TM derived Water Stress Index. *Agricultural and Forest Meteorology*, 77: 207-224.

CHAPTER 5

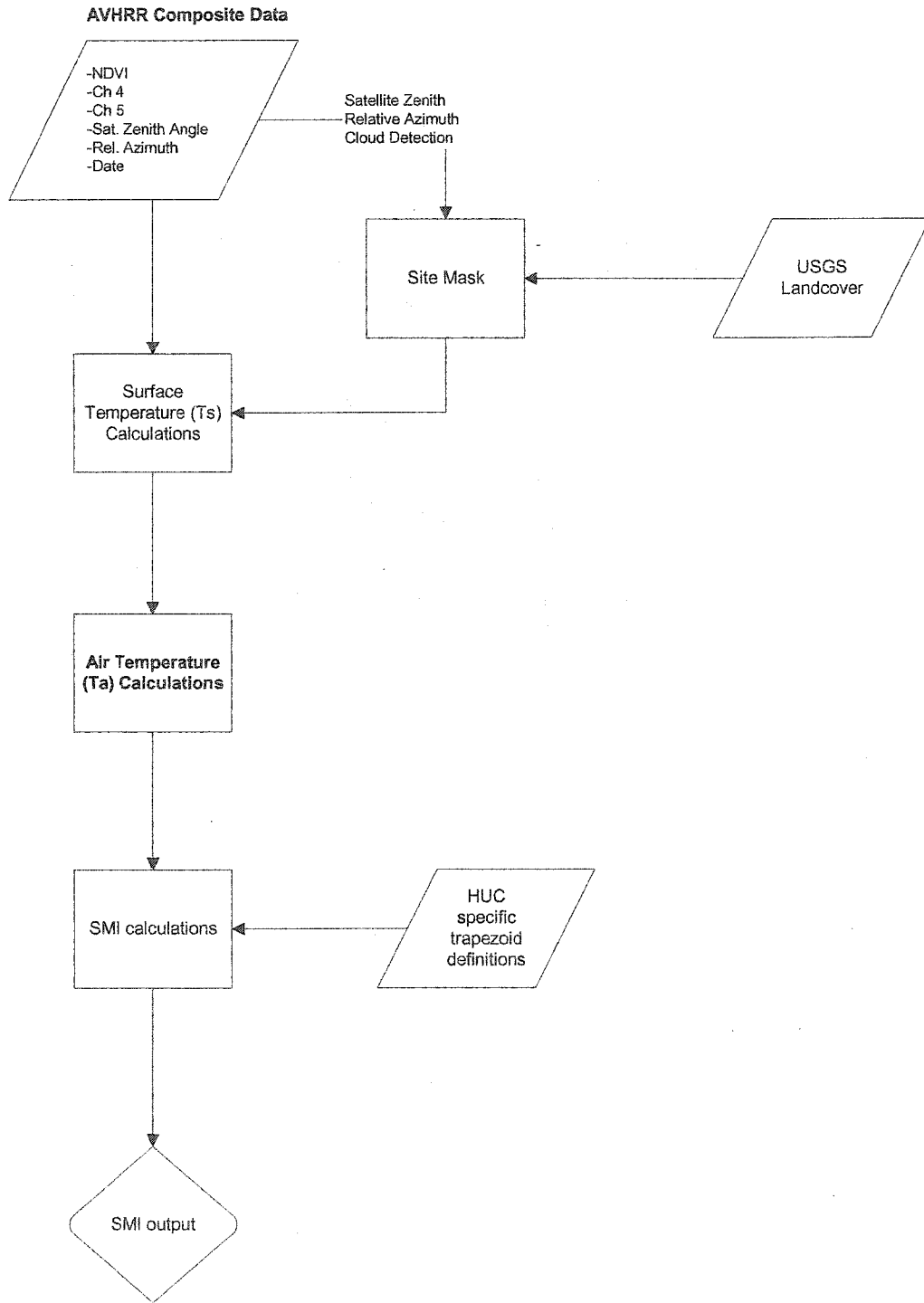
IMPLEMENTATION OF THE TRAPEZOID-BASED SURFACE MOISTURE INDEX

INTRODUCTION

The Crop Water Stress Index (CWSI) and the derived Water Deficit Index (WDI, see Chapter 3) was originally designed for and implemented at large-scales (small areas). The primary goal of this dissertation is the development of landscape-scale techniques for monitoring drought/surface moisture status. To that end, this section will be primarily concerned with the adaptation of the WDI logic for landscape implementation and assessment of its performance. In order to differentiate between the original CWSI/WDI logic and the landscape techniques presented here, the new index will be referred to as the Surface Moisture Index (SMI). The use of SMI in this chapter will refer to the methods discussed in this chapter and will supersede the SMI techniques discussed in Chapter 2. Of paramount concern during the development of SMI was the desire to keep the model responsive to both temporal and spatial resolution while providing for robust estimation of surface moisture status. Therefore, this chapter will present the landscape units of SMI implementation and assessment, temporal issues involved with the calculations, and the methods used in validating the index.

Chapter 4 showed that adequate estimation of near-surface air temperature is possible; and these techniques were incorporated directly into the development of trapezoids and the subsequent calculation of SMI. The estimation of air temperature occurs early in the algorithm (Figure 1). The result is that any constraint imposed within the air temperature module (e.g. geometry) is carried throughout the entire algorithm, both during trapezoid development and actual SMI calculations. These constraints resulted in a significant data truncation, thus forcing development of an alternative approach to landscape aggregation.

Figure 1: SMI processing stream flowchart. See Chapter 4 for detailed discussion of air temperature estimation.



Perhaps the most important component of the development of SMI was a robust method of comparing SMI to current methods of mapping drought for validation purposes. The Palmer drought severity indices were chosen as the preferred standard of comparison. The methods of analysis come from the field of Econometrics, specifically Time Series Analysis. Palmer was chosen because of its long history and common implementation across the landscape both in this country and others. While there may be some criticisms of the Palmer methods, there is no single technique for mapping drought that presents itself as significantly more favorable (e.g. Standardized Precipitation Index, Surface Water Supply Index). The exploitation of time series analysis provides enhanced ability to assess the parallel performance of two independently derived drought-monitoring techniques.

Finally, some of the issues encountered during the development of SMI will be discussed and suggestions for future exploration will be made. The intent of this part of Chapter 5 is to describe the development and initial testing of the SMI logic. It is not intended for these equations to be implemented as predictions. Rather, the intent is to propose a method utilizing satellite remote sensing alone to assess surface moisture status. The equations and analysis are presented to affirm the relationships and validity of the logic and guide future studies of SMI as a means of mapping drought. That said, SMI shows great promise in spite of the data-dependent issues discussed, and deserves a critical consideration for satellite-based assessment of surface moisture status.

MATERIALS AND METHODS

Trapezoid Development

The initial stage of implementation of SMI was the development of historic trapezoids required by the SMI logic. Appropriate spatial and temporal extents had to be identified in order to maintain adequate spatial diversity and a temporal period that would not cause a loss of responsiveness. For the trapezoid

elucidation, afternoon AVHRR data from the years 1991-2000 were used. The period 1991-1998 is composed of biweekly composites, 1999 contained duplicates of weekly and biweekly data, while 2000 had only weekly data. The spatial grain at which SMI was implemented was at the 4th Hydrologic Unit Code (HUC), which is simply major river drainage basins (see Figure 2) obtained from the USDA Natural Resource Conservation Service via the Montana Natural Resource Information System (<http://nris.state.mt.us/>) GIS data service. The 4th HUC's allow an adequate level of spatial discrimination while still providing enough data to meet the requirements of the logic itself. The air temperature estimation removes a significant fraction of available pixels and by constraining the implementation to major drainage basins, the algorithm was able to maintain enough pixels to estimate the trapezoid parameters for SMI implementation.

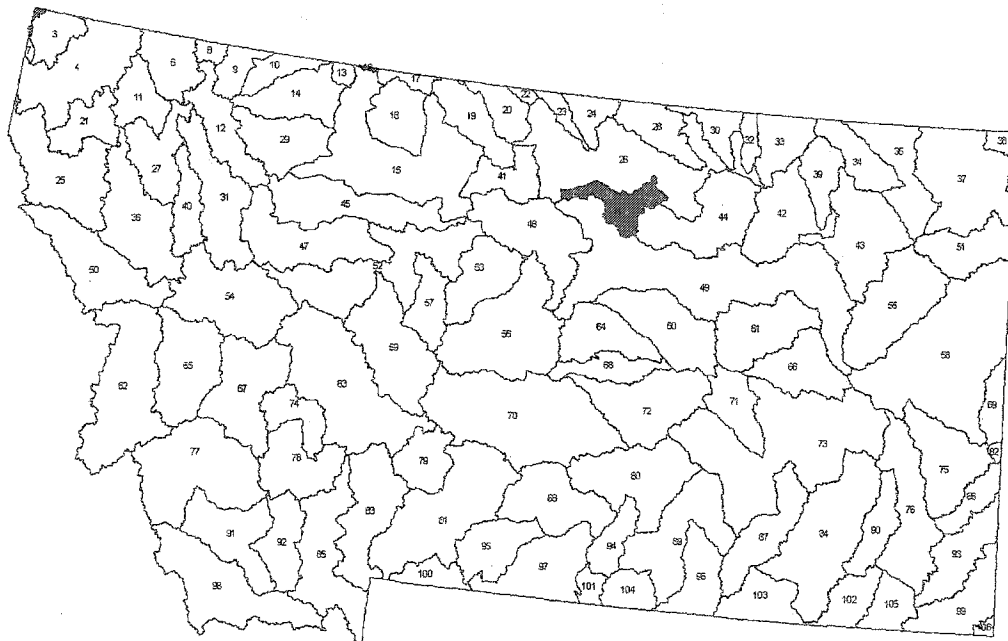
The first step in the trapezoid derivation was to run the eleven-year record of AVHRR data through the new SMI algorithm in a manner similar to the original SMI implementation (Chapter 2) and output least squares regression lines for NDVI versus surface temperature minus air temperature ($T_s - T_a$). The primary difference between the original SMI method (Chapter 2) and the trapezoid development (excluding the air temperature estimation, which used the 30° satellite zenith angle *and* relative azimuth mask) was the incorporation of constraints based on regression parameters. If a warm edge line was calculated from fewer than five points or the coefficient of determination (r^2) was less than 0.5, those lines were removed from further analysis. Additionally, a phenology component (White et al., 1997) was added to define growing season and ensure that lines maintained were within the growing season. As imposed, this constraint confined the candidate composite periods to a year-specific growing season (as defined by the half-on, half-off endpoints) extended by two composite periods (one month). Any line derived outside this temporal period was removed from further consideration.

The result of these calculations is the extraction of warm edge lines (similar to Chapter 2) for each 4th HUC, for each composite period in the record. It is important to note that the trapezoid parameters are calculated from the warm edge only. Lines from each 4th HUC were then manually sorted for the

maximum and minimum trapezoid boundaries. Finally, the equations describing these lines were incorporated into the algorithm as HUC specific trapezoids to be used in the SMI calculations.

Montana has 106 4th HUC's (Figure 2), of which only four failed to result in usable trapezoids. Of those four, one was purposefully removed because it straddled the Montana/Idaho border and had such small area as to be inappropriate for calculation (HUC 2). Final trapezoid parameters denoting slope and intercept of the maximum and minimum line are shown in the appendix (table A.1).

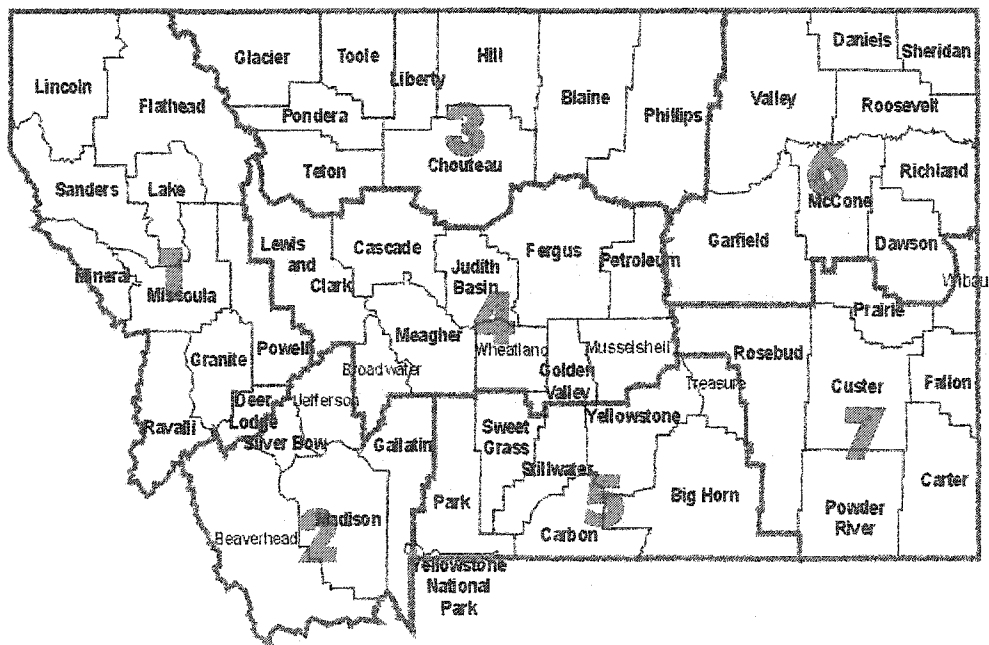
Figure 2: Montana 4th Hydrologic Unit Codes. Polygons in red denote no trapezoid data.



Once the trapezoids were developed and line equations added to the algorithm, the SMI model was run for all years, initially stratified by day *and* HUC (for the air temperature module), then on a pixel-by-pixel basis to calculate the SMI as a function of the HUC trapezoid. The result was SMI values from retained pixels within each HUC. There were a number of instances where individual HUC's failed to produce any

SMI output. This was most likely due to the significant constraints imposed in the air temperature estimation, though the cloud detection and landcover mask likely influenced the output as well. As a result of this data gap, SMI was re-aggregated to the state climate zone level through a simple mean calculation for each zone (which is discussed below). Montana is composed of seven state climate zones as shown in figure 3. The resultant re-aggregation actually simplified the comparisons to common drought indices as the National Climate Data Center (NCDC), the source of historic indices, commonly reports drought data at the state climate zone level.

Figure 3: Montana climate divisions and counties (from Montana Natural Resource Information System).



Palmer Drought Indices

In 1965, Palmer published a drought monitoring technique that incorporates precipitation, moisture supply, and moisture demand (as evapotranspirational losses based on Thornthwaite's techniques) (Palmer, 1965;

Thornthwaite, 1931) into a system that effectively serves as a water balance model. This method requires daily precipitation and temperature and is converted to a drought index that is reported monthly. The so-called “Palmer Index” actually refers to three related components known as the Palmer Z Index (Palmer Z or PZ), the Palmer Hydrologic Drought Index (PHDI), and the Palmer Drought Severity Index (PDSI). Simply stated, the PDSI is a long-term meteorological drought index where drought is dictated by the prevailing weather conditions. The PHDI refers to the long-term hydrologic condition of an area where the changes in meteorological conditions may take a certain time to manifest as either a hydrologic drought or a non-drought event. That is to say that a period of extreme precipitation bringing an end to drought may not be manifest as an increase in water availability for some time after the precipitation occurs. The Palmer Z index is simply a measure of short-term moisture anomaly for a given month and may or may not significantly impact the drought conditions as measured by the PDSI or PHSI (Heim, 2002 drought review).

There have been numerous publications exploring the shortcomings of Palmer’s techniques (e.g. Alley, 1984; Hu and Willson, 2000; Karl, 1986) and many subsequent developments in drought monitoring (e.g. (Doesken et al., 1991; Keetch and Byram, 1968; McKee et al., 1993; Shear and Steila, 1974). However, Palmer is arguably the most popular method of drought monitoring and no single method of drought monitoring/mapping has proven superior enough to cause abandonment of Palmer’s model (Heim, 2002). To this end, the Palmer Z Index was chosen as the index of choice for comparison with SMI.

The Palmer Z score measures the deviation from “normal” moisture for a given month as defined by a 30-year calibration time series. Quite simply, Palmer Z measures the moisture anomaly (either wet or dry) and is used as the primary input for the other long-term compounding Palmer indices (e.g. PDSI, PHSI). The benefit of Palmer Z is that it does not rely on values from the previous months in its derivation (Quiring and Papakryiakou, 2003). This means that the Z index simply measures the short-term moisture anomaly, if any, present in the area being assessed and will likely track SMI since both indices provide “snapshots” of current moisture status without previous or future month’s values impacting the current values.

All Palmer index values can be either negative or positive. Negative values indicate a drought while positive scores indicate moisture surplus. As the deviation from zero increases, the drought or surplus becomes more extreme. Palmer Z values of -2.75 and below are typically categorized as extreme drought, while values of 3.5 and above indicate extreme moisture surplus (Heim, 2002) though these are simply guidelines. All Palmer drought products were obtained from the National Climate Data Center and are delivered as month-averaged values for each Montana Climate Division.

The SMI logic dictates moisture status is measured at the time of satellite overpass with no compounding function that turns these measures into long-term drought products. Rather, it is a technique that illustrates current moisture status of the area being observed. Because vegetation moisture status is an integrator of moisture condition in the observed area, any moisture stress shown by vegetation should be somewhat temporally coincident with the Palmer Z anomalies. However, it is not likely that a direct temporal coincidence between Palmer Z and SMI simply because Palmer Z can be viewed as an immediate calculation whereas vegetation moisture stress, as measured by SMI, will take a certain amount of time to manifest itself. However, the use of Palmer Z scores is the most appropriate choice for comparative analysis with SMI because they both effectively measure the same process. Additionally, the ability to predict Palmer Z from SMI provides the opportunity for future exploration of the conversion to long-term drought products (e.g. PDSI).

Data Structure

The Palmer Drought Indices were obtained from the National Climate Data Center and are reported as mean monthly values aggregated to Montana Climate Zones. There is no sub-monthly information provided. As a result it is impossible to assess what the daily or weekly variations in precipitation are on monthly Palmer Values. Related is the fact that the monthly delineations are “hard-wired” in that a three-day storm that occurs at the transition between months is treated as an individual discreet event. That is to

say two days of rain at the end of June with one day of rain on the first day of July are essentially treated as discrete events and are assigned to the appropriate monthly category, in spite of the true continuous nature of the event.

Since SMI was based on either biweekly or weekly composites and these composites rarely coincide with the categorical variable of month, an assignment technique was necessary to map SMI to monthly categories for use in comparison with Palmer. Values are initially averaged by HUC and assigned to each of the fourteen days in the composite period. With the discovery of a lack of spatial and temporal coverage in each year, a manual re-aggregation was made to state climate zones where every non-zero pixel contained by the climate zone was used in a calculation of the arithmetic mean. To aggregate SMI to monthly values that match the temporal range of the Palmer indices, a simple yearday-to-month assignment was made where the number of days in a composite contained by that month received the SMI value for each of those days. For example, one fourteen day SMI composite may contribute five days of SMI to June and nine days to July. Finally, SMI was averaged by month. Despite the fact the AVHRR composite data contain information on daily membership of individual pixels (and resultant SMI values), this information was not used in the assignment of SMI to monthly categories. To do so would introduce a temporal specificity in the comparisons that the Palmer data is unable to match since these data contain no information on what individual days contributed the most to total monthly Palmer Z values. Therefore, the resultant SMI dataset contains monthly values that have an inherent temporal lag structure associated with it.

Time Series Analysis - Background

Time series analysis is the field of study, borne out of econometrics, where time is an essential component of the data to be analyzed. These data are typically temporally ordered and time is viewed as an independent variable. While the temporal ordering is critical, time may not always be explicitly treated as a predictor in modeling exercises. In paired variable time series regression analysis, the ordering of the

variables has as much importance as the pairs themselves, even if time is not used as an independent variable in the analysis.

Early in its development, time series analysis referred to a method developed by Box and Jenkins (1970) known as *autoregressive integrated moving averages* (ARIMA). This technique relied primarily on a given variables past behavior as a means of predicting the variables future behavior, hence autoregression.

The ARIMA method has fairly modest theoretical requirements. Primary of which is the data exhibit *stationarity*. A variable is stationary if the mean and variance do not change over the time of analysis. Box and Jenkins (1970) recommended a casual means of testing stationarity and proposed a simple transformation to correct for non-stationary data. Simple plots of the time ordered variable and its correlogram are used for stationarity assessment. If the correlogram, which is a lag ordered plot of autocorrelation, shows a dramatic decrease in autocorrelation coefficients after lags of one or two and simple sequence plots of the variable show random fluctuations around the mean (with constant variance), the data are assumed to be stationary. If the data exhibit non-stationarity, the recommended transformation is a simple differencing. That is to say that the first variable is subtracted from the second, the second is subtracted from the third, and so on. Occasionally, second differencing, which is a difference of the differences, is used to modify data that exhibit extreme non-stationary behavior. It is not typical to do more than a second differencing (Kennedy, 2003).

The ARIMA model description typically takes the form: ARIMA (p, d, q) as suggested by Box and Jenkins (1970). The autoregressive parameter is denoted as p , the order of the differencing is d , and the magnitude of the moving average is q . The autoregressive parameter, as mentioned above, refers to the number of previous values used in the prediction of the current value. The difference parameter, d , is simply the order of differencing (typically no more than two). The moving average is the number of previous values and weighting used in the moving average calculation. Moving averages are incorporated in the ARIMA technique to ensure that nonsystematic variations in the data are removed. It relies on the notion that

systematic components display autocorrelation and by removing the nonsystematic components through moving average calculation, one can more effectively model the variable. The ARIMA models take the form of:

$$Y'_t = \phi_1 * Y'_{t-1} + \phi_2 * Y'_{t-2} + \dots + \phi_p * Y'_{t-p} + \varepsilon_t + \theta_1 \varepsilon_{t-1} + \theta_2 \varepsilon_{t-2} + \dots + \theta_q \varepsilon_{t-q}$$

(Equation 5-1)

Where Y' is the differenced variable of interest, ϕ and θ are coefficients to be determined, and ε is the error term (Kennedy, 2003). The subscripts p and q are the same as mentioned above and t is the time ordering subscript.

Originally, the ARIMA method was developed as an autoregressive technique where one variable was used to predict itself as a function of the past behavior. However, it is possible to use the ARIMA technique in a two-variable modeling exercise. If two variables exhibit stationarity and significant cross-correlation, as measured by the cross-correlation coefficient (equivalent to Pearson's R), cross regression modeling may be used to predict a dependent variable from an independent variable (McCuen, 2003). It is this latter approach that will be discussed in the analysis. The functional form in this situation is:

$$Y'_t = \phi_1 * X'_{t-1} + \phi_2 * X'_{t-2} + \dots + \phi_p * X'_{t-p} + \varepsilon_t + \theta_1 \varepsilon_{t-1} + \theta_2 \varepsilon_{t-2} + \dots + \theta_q \varepsilon_{t-q}$$

(Equation 5-2)

Where Y' is the dependant variable (Palmer Z in this example) and X' is the independent variable (SMI).

The other variables are the same as above.

RESULTS

Time Series – Implementation

Sequence plots for Palmer Z and SMI are shown in figure A.1 in the appendix. The first plot (a.) in each figure shows the raw data as a time sequence. 1999 and 1999_wk are replicates of the year 1999 as discussed above. The second sequence in each figure shows the same plot after a first differencing. Both figures show an increase in the stationarity, as indicated by a stable mean and consistent variance, thus satisfying the first assumption of ARIMA analysis.

The second component of ARIMA analysis for two variables is to show a meaningful cross-correlation as a function of the lag. Cross-correlation for all years combined, stratified by climate division, are shown in figure A.2 in the appendix and summarized in table 1. Cross-correlations stratified by climate division *and* year, are shown in figure A.3 in the appendix. Because drought conditions manifest themselves as negative Palmer Z values and high (greater than 0.6) (Vidal and Devaux-Ros, 1995) SMI values, a negative cross-correlation would be expected. That is to say that as an area suffers from drought, Palmer Z scores will be driven down while SMI scores will continue to increase.

Table 1: Total cross-correlation for differenced Palmer Z and SMI for all years. Data are stratified by climate division.

	Cross-correlation	Lag
Division 1	-0.009	0
Division 2	No negative correlation	
Division 3	-0.108	1
Division 4	-0.086	0
Division 5	-0.168	0
Division 6	-0.041	-1
Division 7	-0.141	0

As discussed above, the Palmer Z data simply show monthly averages. The temporal resolution does not allow for the investigation of when the daily changes occurred within that month. For example, consider a month that is very dry up until the last week. Then, perhaps, significant precipitation occurs that drives the monthly Z score toward zero. The only conclusion to be made, based on the resultant monthly Palmer Z information is that the month experienced “typical” moisture, when the reality is that the month was, for the most part, very dry. Also, consider that there is an expected time lag between actual precipitation and vegetation response driven simply by the physics of water transfer through the soil-vegetation-atmospheric continuum. Combine these issues with the biweekly SMI data structure and it becomes apparent how temporal correlations between SMI and Palmer Z can be confounded with no clear indication of lag *direction*. Finally, treat the entire 11-year time series together and the expectation of high cross-correlation coefficients between Palmer Z and SMI is problematic (Table 1).

Due to the apparent low cross-correlation between monthly Palmer and biweekly SMI composites (Table 1), adjustments were made to the data so that a more meaningful analysis could be performed. However, these adjustments were constrained to lag of either zero, one, or negative one as suggested by year stratified cross-correlations (appendix Figures A.3) and summarized in Table 2 which shows the highest observed cross-correlation and its associated lag. The lack of temporal precision in weather condition, in the case of Palmer Z, and the biweekly composite issue for SMI, dictates that a legitimate lag adjustment of the data, in either direction, may occur.

Table 2: Cross-correlation (CC) and lag for differenced Palmer Z and SMI. Data stratified by climate division and year. No correlations were observed for Div 3 or 6 in 1992 and 1993, respectively.

YEAR	Division 1		Division 2		Division 3		Division 4		Division 5		Division 6		Division 7	
	CC	lag	CC	lag	CC	lag	CC	lag	CC	lag	CC	lag	CC	lag
1991	-0.525	1	-0.102	-1	-0.917	1	-0.654	1	-0.594	0	-0.890	1	-0.201	1
1992	-0.626	0	-0.350	0	---	---	-0.290	-1	-0.750	2	-0.594	1	-0.874	0
1993	-0.576	2	-0.129	-1	-0.254	-1	-0.769	2	-0.375	2	---	---	-0.127	0
1994	-0.695	-1	-0.709	1	-0.620	-1	-0.707	1	-0.283	1	-0.323	0	-0.521	0
1995	-0.367	-1	-0.238	-1	-0.898	1	-0.914	0	-0.627	-2	-0.575	0	-0.527	0
1996	-0.221	-1	-0.154	-1	-0.522	0	-0.764	0	-0.673	0	-0.717	1	-0.677	0
1997	-0.683	0	0.083	0	-0.566	-1	-0.582	0	-0.298	0	-0.012	-1	-0.386	-1
1998	-0.219	0	-0.533	1	-0.414	-1	-0.565	0	-0.931	0	-0.416	-1	-0.173	-1
1999	-0.817	0	-0.113	0	-0.410	0	-0.722	2	-0.875	2	-0.296	0	-0.324	1
1999_wk	-0.622	-1	-0.153	0	-0.521	0	-0.184	0	0.609	2	-0.769	2	-0.277	1
2000	-0.485	0	-0.418	0	-0.963	0	-0.806	0	-0.810	0	-0.572	0	-0.347	-1

All data were manually adjusted such that the new series was set to a lag of zero for each year, with a few exceptions. As table 2 describes, some years show very high correlation when a lag of 2 is considered. As previously mentioned a lag of one, in either direction (or zero), is logical by virtue of the temporal categorization of SMI and Palmer Z. In the reconstruction, all lags of greater than one or less than negative one were left intact. The result is a synchronized dataset for each division that contains high cross-correlations for lag zero and some extraneous data with an optimum lag outside of the lag constraints imposed. It is acknowledge that these long lag constituents will likely confound the comparisons, however, it is illogical to adjust the time series to account for a lag of two months or more and those years exhibiting longer lags were left intact. The cross-correlations for the adjusted data are shown in Table 3.

Table 3: Lag adjusted cross-correlation for differenced Palmer Z and SMI. Data stratified by climate division and grouped for all years.

	Cross-correlation	lag
Division 1	-0.296	0
Division 2	-0.183	0
Division 3	-0.384	0
Division 4	-0.350	0
Division 5	-0.214	0
Division 6	-0.274	0
Division 7	-0.278	0

To summarize, table 3 shows cross-correlations for the manually adjusted data by climate division. If a given year had an optimum (as defined by the highest cross-correlation) lag of -1 or 1 (see Table 2), the data were synchronized so that the year in question now had an optimum cross-correlation at lag zero. To do this, each years data was displayed in columns. If the optimum lag was 1, the appropriate column was shifted down one row so that the resultant optimum cross-correlation would show a lag of zero. The converse is true if the optimum lag was -1. For those individual years where optimum lags were anything else (e.g. zero, two, etc.) no adjustment was made. Cross-correlations for all years pooled were recalculated and the results are shown in Table 3. As expected, optimum lags for all climate divisions are zero due to the manual adjustments, though if stratified by individual year, any year showing a lag of greater than 1 or less than -1 in Table 2 will still show that same optimum lag. All others would now display optimum lags at zero. The primary reason for this manual adjustment is so *one* model for each individual climate zone can be built to predict Palmer Z from SMI.

Autoregressive Integrated Moving Average

Given the notion that a yearly lag of zero or one (in either direction) is acceptable and expected, the data were manually adjusted so that a synchronized dataset for each climate zone with an optimum lag of zero was created (Table 3). With the cross-correlations showing adequate values, it was possible to proceed with the time-series analysis and build an ARIMA model to relate SMI to Palmer Z.

When implementing a two-variable ARIMA, it is possible to incorporate an autoregressive term (p) on the dependant variable. The function of the autoregressive term is to use the dependant variables' *previous* values in combination with the independent variable to predict the current dependent variable. That is to say that Y is a function of X and previous Y . Because the goal of this study was to assess the potential relationship of Palmer Z to SMI, the autoregressive term was set to zero thereby assuring that only SMI was used in the analysis to derive Palmer Z . The moving average term (q) was also set to zero so no averaging occurred and the order of the differencing (d) was set to one, which is a single differencing of the values to assure stationarity in the data. The ARIMA technique also allows for constants to be included in the model formulation. Constants were excluded from the equation in order to simplify the analysis. Results from the lag adjusted ARIMA for each climate division, where all years are used in the calculation, are shown in table 4. SPSS was used to derive the model parameters. Outputs from SPSS include the ARIMA coefficient (B), T-ratio (basically a t score), and approximate probability (approximate because the ARIMA relies on a user-defined iterative-convergent technique).

Table 4: Auto-Regressive Integrated Moving Average (ARIMA) parameters for lag adjusted Palmer Z and SMI for all years.

	B	t-ratio	Probability
Division 1	-3.3243	-2.9401	0.0044
Division 2	-3.4362	-1.8812	0.0644
Division 3	-7.2298	-3.3078	0.0015
Division 4	-5.2731	-3.2589	0.0017
Division 5	-2.753	-1.8691	0.0656
Division 6	-5.3434	-2.504	0.0151
Division 7	-5.8158	-2.5746	0.0124

When adjusting the data to account for the lag, any years that fell outside of the logical lag (-1 to 1) were not adjusted. In order to better test the ability of SMI to predict Palmer Z , years from each climate division that showed lags outside of the one-month constraint were deleted. Additionally, 1993 was removed from analysis for all years because of its low correlation and/or high lag values for all climate divisions (see Table 2). The ARIMA models were recalculated in the same fashion as the first exercise, with the

questionable years removed. ARIMA parameters are summarized in table 5. Figure A.4 in the appendix shows the time sequence plots of Palmer Z versus the Palmer Z predicted from SMI, by climate division.

Table 5: Auto-Regressive Integrated Moving Average (ARIMA) parameters for lag adjusted Palmer Z and SMI. Listed years were not included in the analysis due to low correlations or extreme lags (summarized in Table 2).

	B	t-ratio	Probability	years removed
Division 1	-3.3417	-3.2943	0.0016	93
Division 2	-3.447	-2.1394	0.0364	93
Division 3	-6.0367	-3.6613	0.0006	92, 93
Division 4	-5.2098	-3.7454	0.0004	93, 99
Division 5	-7.3818	-3.918	0.0003	92, 93, 95, 99, 99_WK
Division 6	-6.2997	-4.0324	0.0002	93, 99_WK
Division 7	-5.4504	-2.6254	0.0111	93

Utilizing the above parameters, the final form of the equation would be:

$$Pz_t = [(SMI_t - SMI_{t-1}) * B] + Pz_{t-1}$$

(Equation 5-3)

Where Pz is Palmer Z index, B is the regression coefficient, the subscript t denotes current time (current Pz for example), t-1 is previous time period, and SMI is self explanatory. Note, the differencing of SMI and the final addition term of Palmer Z to account for the first differencing of the original data.

To summarize, Table 5 shows ARIMA parameters for the manually adjusted data discussed above where optimum cross-correlations occur at lag zero. Additionally, any year showing optimum lags of greater than 1 or less than -1 were deleted. The years removed column in table 5 corresponds to these unacceptable lags shown in Table 2. It is also worth noting the probability values in Table 4 and Table 5. In all cases, the probability improved when the questionable years were removed, particularly in climate division 5.

ARIMA Residual Analysis

As with any modeling exercise, one must investigate the residuals to test for normal distribution and heteroskedastic behavior. Residual analysis was done on the lag adjusted ARIMA models (summarized in Table 5). Probability plot (P-P in SPSS) were created to test for normal distribution. The P-P function allows you choose a test distribution (normal in this case) to compare the residuals against. If the points appear along the diagonal line, it is assumed the distribution matches the test distribution. To test heteroskedasticity, residuals were plotted against the independent variable in a scatter plot. In this example, a random distribution around zero with no discernable pattern indicates the lack of heteroskedasticity. The P-P and scatter plots by climate division are shown in figures A.5 and A.6 in the appendix.

DISCUSSION

As evidenced by the data shown in Table 5 and the time sequence plots in the appendix (Figure A.4), SMI tracks the Palmer Z index. When problematic years are removed (summarized in Table 5), all coefficients are significant at the $\alpha=0.05$ level and most show significance at much higher standards. Of special consideration is the fact that SMI was able to track Palmer Z in climate zones 1 and 2, which contain the most complex terrain in the state, and arguably are the regions which one might expect to derive the lowest correlations. This expectation is borne primarily of the difficulty in estimating air temperatures in complex terrain, though also includes the problems associated with more continuous snow cover and higher cloud cover during early and late growing season. In fact, the opposite is true particularly when one considers that only 1993 was removed from the second ARIMA analysis for these climate zones.

As alluded to in the introduction, air temperature estimation plays a critical role in SMI calculations. In order to achieve robust air temperature estimates, severe constraints were imposed in the algorithm, which resulted in significant data reduction. Once a pixel is removed from the analysis in the air temperature

package, it remains absent from any subsequent consideration for that composite period. The result is a dataset composed of dramatically fewer pixels than the original AVHRR scenes. The distribution of these pixels is not consistent for each composite period for each 4th HUC. That is to say that there is no way to predict which pixels will be retained from each 4th HUC, though one must remember that there are pixels consistently excluded as a function of the landcover mask. While the relative location of each pixel used in the analysis may change, it still mimics, conceptually at least, the meteorologically based Palmer calculations. Palmer relies on averaged monthly values from distributed weather stations (at fixed locations) aggregated by climate division. The SMI protocol may in fact provide a more robust sampling technique by virtue of a larger sample size that is more evenly distributed over each state climate zone.

One of the primary issues with SMI in its current form is the fact that the AVHRR composites tend to inhibit a more robust assessment. First is the issue of composite period straddling months. The assessment could be improved by collecting coincident weekly or biweekly Palmer Z data for comparisons, though these datasets do not exist in the current NCDC archive. The second major confounding factor with AVHRR composite data is the preferential selection of off-nadir pixels by the compositing algorithm (Stoms et al., 1997). This off-nadir selection leads to data removal in the air temperature calculation caused by the satellite zenith angle constraints (see Chapter 4). If a real-time monitoring of drought were to be implemented using the SMI logic, implementation of the code earlier in the AVHRR processing stream would be advised to remove the impact of the maximum NDVI compositing protocol. A possible solution would be to calculate SMI on a daily time step and allow the cloud detection and angle constraints to remove questionable pixels as currently implemented. A composite of maximum SMI value at the most desirable time step (weekly, biweekly, monthly) could then be produced. The result would likely be a more temporally precise assessment of surface moisture status and a method certainly worth exploring in greater detail.

The year 1993 was removed from the second ARIMA analysis for all climate divisions. Table 2 shows that 1993 produced either low cross-correlations or unacceptable lags for each state climate division (as

discussed above). While these cross-correlations and lags may not be out of line with other years when considering climate zones individually, the fact that 1993 was a consistent poor performer for all divisions is worthy of further investigation. While spatially explicit meteorological analysis is beyond the scope of this paper, anecdotal evidence suggests interesting reasons for statewide poor performance of SMI in 1993. According to NCDC climate records (data not shown), 1993 was an exceptionally wet year in Montana. Considering the period of record (1895-2004, 109 years) and the state as a whole, June, July, and August 1993 rank as the 25th, 1st, and 11th wettest of those specific months on record, respectively. With this increased precipitation comes an increase in cloud cover. This alone may explain poor correspondence between SMI and Palmer Z in 1993 by one of two mechanisms. Either the number of available observations was decreased due to cloud obscuration or the sub-pixel cloud detection technique in the air temperature module excluded a large enough number of pixels to prohibit sufficient sampling of the surface thereby causing a loss of relationship between SMI and Palmer Z.

An alternate explanation for the poor SMI performance in 1993 may lie within the logic of SMI itself. Inherent in the technique is the notion that moisture stress must be present in order for the secondary response (elevated surface temperature) to be detected by the satellite. It is feasible in 1993 that there was such a surplus of available moisture for the vegetation that the signal was simply below the detection limits of the algorithm, or that it did not exist at all. Either explanation is certainly reasonable considering the excess precipitation experienced in Montana that year.

The aggregation strategy employed in this exercise also deserves further attention. There was a desire to maintain a moderate spatial resolution within the model, yet provide adequate spatial extent for robust trapezoid estimation. Additionally, there was a desire to keep the landscape delineation logical in that it corresponded to ecological or hydrological process boundaries rather than rely on arbitrary borders (e.g. political boundaries). The 4th HUC's were chosen because they provide moderate spatial resolution and define actual hydrologic units associated with water processes. The result is the logical ability to

differentiate, with the current implementation, between the surface moisture/drought status of meaningful, that is to say, hydrologically based landscape units.

Although the trapezoids are defined at the 4th HUC level, the final output of SMI failed to give consistent results for each 4th HUC across the landscape. This was primarily caused by the stringent masking in the air temperature estimation module. This lack of coverage resulted in the re-aggregation to state climate zones, as discussed above. By leaving the original assessment at the HUC level rather than recalculating climate zone specific trapezoids, the spatial resolution provided by the 4th HUC delineation and the physical basis for the landscape units are maintained in the best way possible. It is logically more appropriate to maintain a delineation based on physical principles (insomuch as the major drainages integrate watershed processes) in the initial assessment of SMI and incorporate a subsequent re-aggregation to the pseudo-physical climate zones (since climate zones incorporate political boundaries) than it is to accept the rather arbitrary demarcation of climate zones which have little relationship to ecological or hydrological process boundaries. Though it is acknowledged that the state boundary does truncate those HUC's that extend beyond its confines. By maintaining the HUC boundaries in the algorithm, SMI performance can be better assessed in future large scale (small area) studies. Such studies might include the use of gauging stations and localized meteorological data for comparison with SMI to more fully understand exactly what SMI is responding to.

As previously mentioned, the date of satellite acquisition information was not used in temporal assignment of SMI values to month categories. The reasoning for this decision is two-fold and rather simple. First, Palmer Z is a calculated index that does not incorporate any physical process, *per se*, in the derivation of the numbers, whereas SMI is an observed process that will likely show a response that is some function of time after a rain event. For example, precipitation that falls on a given day is immediately used in the running calculation of Palmer Z. Conversely, SMI may not respond immediately to a precipitation event, especially if one considers the fact that SMI relies on secondary responses to water transfer through the soil-vegetation-atmospheric (SVAT) continuum. One can envision a certain time lag requirement for water

movement through all the SVAT components before a satellite is able to detect the subsequent surface temperature responses.

The second reason for not utilizing the date information contained in the AVHRR record is the idea that is better to degrade one dataset than it is to imply a false resolution in another dataset. By accepting the inherent time lag between SMI and Palmer Z, it was possible to assess the ability of SMI to track Palmer Z. If the date information were to be used in the assignment of SMI values to month, the implication would be that an ability to resolve the behavior of SMI and Palmer Z at daily time steps was possible. Because of the way the Palmer indices are calculated and archived, this daily time step simply does not exist. Rather than imply a false temporal resolution, an inherent time lag structure was accepted, which in the final estimation, did not hinder the analysis.

In spite of the issues discussed above, it is worth exploring the overall relationship observed between SMI and the Palmer Z index in greater detail. Appendix Figure A.4 (sequence plots) shows the time sequence of observed Palmer Z scores with the predicted Palmer Z (from SMI) for the years calculated in the final assessment (the parameters of which are summarized in Table 5). Again, these are the observed versus predicted for the final assessment where some years (summarized in Table 5) were removed from analysis. Observed Palmer Z scores are plotted for all years while the predicted Palmer Z scores are only for those years maintained in the final ARIMA analysis. It is also worth reiterating that the predictions were not for whole years. Rather, the algorithm was only run on the phenologically appropriate period (growing season \pm month) within each year.

The sequence plots (appendix Figure A.4) show some interesting results. For all climate divisions, except division five (due to the removal of 1995 in this division), there exists an initial gross underestimation of Palmer Z in 1995. This is most apparent in climate division three and six, though the others also show this tendency. In spite of the initial underestimation of Palmer Z, all divisions show a rapid re-synchronization with actual Palmer Z scores. In fact, if climate divisions one is considered as an example, the predicted

values rapidly parallel the observed and continue along the same trajectory throughout the year. The reasons for this dramatic failure of prediction at the beginning of the year are not known. However, it is possible to speculate that this is a function of early season vegetation growth coupled with a lingering drought from the previous year that is transitioning to a year which experienced more normal precipitation. For all divisions, 1994 was a dry year while 1995 showed a moderate recovery. One hypothesis would be that as the vegetation begins to come out of dormancy early in the growing season and use the available moisture, that vegetation will show a certain amount of water stress due to the moisture deficit left from the previous year. This is confirmed by the early season PDSI scores for 1995 (not shown). However, as 1995 progressed, all climate divisions showed recovery from the drought. Considering the expected SMI response (and therefore the predicted Palmer Z scores) It is suggested that the initial under-prediction of Palmer Z was simply an early season measurement of the lingering drought followed by a recovery. The sequence plots actually confirm this when one considers the observed Palmer Z from 1994. The subsequent predicted Palmer Z scores for early 1995 are not out of line with the observed values at the end of the growing season in 1994. Overall, it is suggested that this initial prediction discrepancy in 1995 is simply the SMI technique (therefore predicted Palmer Z) capturing an early season moisture stress. The predicted Palmer Z scores then quickly re-synchronize and continue to track the observed Palmer Z.

As previously discussed, both weekly and bi-weekly composite data for 1999 were used in this analysis. For those climate divisions where both years were maintained in the final assessment (divisions 1, 2, 3, and 7) there is evidence that the weekly composites show a higher temporal resolution, particularly in climate division one. If the biweekly composites are compared to the weekly composites in division one, there is a much higher fidelity in the predicted values tracking the observed values. Bearing in mind that the observed Palmer Z plots do not change, one can see the predicted values better capturing the fluctuations of the observed values in the weekly composite data. While perhaps not surprising, it is certainly encouraging to see the finer temporal resolution data providing a better and more complete assessment of the actual changes in the observed data. The implications of this observation are two-fold. First, the data suggests that it should be possible to capture drought variations at finer time steps. The benefits of the finer time

scale are apparent if one hopes to track slight variations in moisture status as a function of time. Additionally, there will always be some composites that fail to produce SMI values for a given HUC (or climate division) due to the masking functions employed in the algorithm. With weekly composites, it is less likely long periods of time will pass without deriving SMI values for that HUC due to the increased sampling ability the weekly data provide (52 composites per year versus 26 for the biweekly).

The second implication of the finer temporal resolution has to do with suggested implementation of the SMI technique in the future. In order to obtain a more robust assessment of surface moisture status, a daily time step for the calculations of SMI would be suggested. Granted, the masking of clouds and undesirable earth-sun-sensor geometries will undoubtedly remove a great number of pixels at a daily time-step. However, if this logic were to be implemented for drought monitoring, the increased sampling ability the daily time-step provides may outweigh the loss of data caused by the masking. In a given one week composite, there are approximately seven chances for a given pixel to be viewed (perhaps more depending on orbital mechanics). Of those seven observations, only one is maintained in the final weekly composite. Some of the literature suggests (ASPRS paper) that off-nadir pixels are preferentially selected by the maximum NDVI compositing technique. If these pixels are far enough off nadir, they will be removed by the geometry mask imposed in the air temperature module of the algorithm. The result is one actual observation lost and at least six other potential observations of this pixel that are also lost. Of those six, it is likely a certain fraction will contain clouds or undesirable geometries as well. However, if daily data are used, the opportunity may exist for the sensor to observe this given pixel more than one time in a given one week composite period. Given that the data suggests finer temporal resolution results in an increased ability of SMI to track Palmer Z, it appears reasonable to assume that one may increase the temporal resolution and increase our overall ability to assess surface moisture status. Future studies should investigate this assertion more fully.

Finally, climate division five did not result in very much output through the years of this study. Five of the eleven possible years were removed. This removal is undoubtedly a function of the air temperature module

in the algorithm. In spite of the failure to derive SMI scores for so many years, when data were produced, the results were quite good. Table 2 shows that four of the five removed years had high cross correlations at a lag of two. Of those years, some of the correlations are quite high. Regardless of why the extreme lags show such quality cross-correlations, if the probabilities in table 5 are considered, after the removal of the questionable years, the results are exceptional. The probability of the coefficients are much less than 0.001. Consider this value and the time sequence plots (figure A.4 appendix) and a remarkable ability of the predicted to track the observed results is evident, especially in 1996 which showed very complex fluctuations throughout the year. In spite of the loss of nearly half of the available years, the ability of SMI derived Palmer Z to track the observed Palmer Z is still remarkable. Again, this may be improved through the use of higher temporal resolution data.

CONCLUSIONS

The results of this study indicate that the SMI technique shows great potential in its ability to map drought at landscape scales. SMI and Palmer Z show coincident trajectories throughout all years of this experiment. While it is desirous to provide actual equations for the derivation of Palmer indices from SMI, the true nature of this study is a proof of concept. Therefore, it can be legitimately argued that the significance of the coefficients is *not* the issue. Instead, it is the correlation between SMI and Palmer Z that is paramount in this study. The fact that the derived time series coefficients are significant at acceptable levels adds credence to the entire exercise, thus showing the promise for landscape assessment of drought status that SMI holds and indicating the utility of further exploration.

Regardless of the shortcomings of the current implementation, the SMI technique provides a clear method of predicting a familiar drought index. Since Palmer Z is well modeled, and Palmer Z is a precursor to the long-term Palmer indices, it would be relatively simple to convert to an SMI based calculation of the other Palmer indices (e.g. PDSI). With an increased understanding of the behavior of SMI, and an increased data richness by virtue of higher temporal calculations, it is likely SMI could be used to calculate drought and

surface moisture status in areas where weather station do not exist, or their placement may be cost prohibitive. While it is unlikely this logic will replace the current method of calculating Palmer indices in North America, it may be an appropriate technology for locations such as Africa or the Boreal regions of Asia. SMI would prove a cost effective method for providing spatially explicit information on surface moisture status. Additionally, the techniques can be applied to other platforms, such as AQUA MODIS, where the superior design of the sensor and its derived terrestrial products (surface temperature, vegetation, etc.) will likely result in higher fidelity drought products.

EPILOGUE

The research presented in this document illustrates the progression I followed in developing a method for assessing drought at landscape scales using NOAA-AVHRR data. I began by utilizing promising large-scale techniques (T_s /NDVI models) and modifying those techniques for application at smaller (landscape) scales. Upon testing the original SMI model performance (chapter 2), certain shortcomings were discovered. These issues were addressed by the incorporation of the WDI logic into a second generation SMI model. In order to fully exploit the logic presented in the WDI derivation, it was necessary to develop a technique to estimate the critical near surface air temperatures at the equivalent landscape scale. Although constraints imposed in the air temperature module removed a large number of pixels from the analysis, it proved a robust estimator and was incorporated in the development of the final SMI model. Finally, the trapezoid-based WDI logic was implemented and tested at the landscape scale (chapter 5). As was shown, the final SMI model closely matched, in space and time, a popular meteorological station based drought index (Palmer Z). Furthermore, the SMI model requires only AVHRR satellite data as inputs.

APPENDIX A

Table A.1: Trapezoid parameters for each 4th HUC. Note, there is no HUC 1, HUC 2 was removed, and algorithm failed to derive values for HUC's 5, 16, and 46.

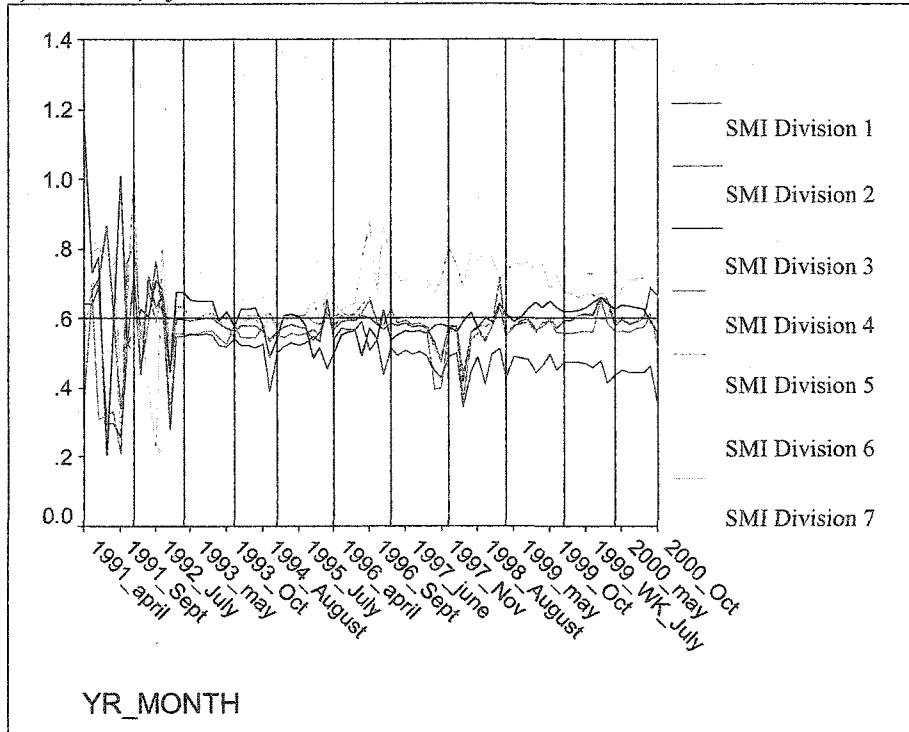
HUC	Max Slope	Max intercept	Min slope	Min intercept	HUC	Max Slope	Max intercept	Min slope	Min intercept
3	-70.8089	63.17464	-23.734	12.63884	38	-65.5648	57.1752	-26.6496	21.01836
4	-68.9293	63.01224	-20.8428	10.38902	39	-89.7355	81.1443	-31.9218	19.76161
5					40	-75.5647	68.8905	-15.8424	9.652939
6	-109.334	96.34461	-24.2087	15.01582	41	-113.937	106.659	-23.3469	12.38569
7	-57.3067	55.31637	-15.9701	11.53213	42	-117.228	104.9839	-16.3666	10.03849
8	-31.6643	26.18764	-30.125	22.98639	43	-94.676	84.08698	-17.6916	8.434703
9	-112.278	108.0502	-19.9738	12.241	44	-147.758	136.9017	-18.6106	10.57146
10	-75.5289	78.53613	-23.6431	15.66226	45	-81.6142	76.46227	-25.9848	14.80378
11	-110.805	100.1336	-16.6343	12.1223	46	---	---	---	---
12	-80.6202	71.8128	-27.8882	20.55269	47	-98.6618	88.62082	-20.4686	11.66403
13	-27.9222	24.06089	-23.9185	18.986	48	-137.016	125.8258	-23.4312	11.423
14	-82.1029	77.52799	-19.1212	8.534692	49	-133.774	127.799	-38.0053	17.3766
15	-123.866	110.6927	-24.6883	14.79226	50	-100.251	89.33881	-21.8378	16.31468
16	---	---	---	---	51	-138.938	121.3947	-22.1371	13.78183
17	-120.07	112.1213	-24.286	14.32551	52	-75.8667	72.36227	-28.6152	14.89059
18	-105.677	98.46101	-21.9924	16.75848	53	-105.329	99.74573	-21.4049	12.08971
19	-95.9914	88.85017	-20.7761	13.96107	54	-87.6215	77.7939	-23.5126	16.97307
20	-110.571	96.25177	-13.1761	7.576127	55	-114.209	102.5654	-25.6098	12.58638
21	-125.845	113.8652	-31.9357	24.32874	56	-64.0228	68.71739	-30.5944	15.53726
22	-87.1887	76.35423	-19.1037	13.63949	57	-102.24	97.6588	-22.3737	15.67505
23	-68.0305	58.61748	-13.6886	9.276328	58	-114.421	98.39673	-22.2077	8.043068
24	-119.386	104.4509	-27.7956	16.52829	59	-99.9207	92.26113	-33.6823	24.047
25	-82.1411	73.55742	-22.2223	17.34402	60	-87.3888	85.59878	-29.7786	17.94122
26	-101.755	88.54659	-23.4002	13.53459	61	-86.1079	79.85793	-17.3154	10.79869
27	-101.539	93.21545	-20.7844	15.36065	62	-91.7669	82.38452	-19.1375	13.98486
28	-84.6283	76.79299	-25.9328	23.06884	63	-127.033	116.0022	-22.0848	15.15276
29	-93.0632	86.76849	-24.3584	15.48007	64	-67.1474	63.81761	-26.21	10.61784
30	-78.4823	68.96512	-30.52	24.57468	65	-141.282	123.3685	-21.2997	14.70431
31	-42.388	42.13838	-15.5998	11.50151	66	-102.743	94.07105	-25.6204	15.52244
32	-66.2237	60.12592	-33.9358	20.0904	67	-144.675	125.5357	-16.3552	11.84752
33	-89.8917	84.97411	-14.3644	8.259284	68	-86.5304	64.97958	-23.2717	17.12092
34	-49.4083	47.816	-13.989	11.48881	69	-84.9551	79.12882	-18.5831	13.96585
35	-74.7089	77.94342	-26.0179	14.56844	70	-126.776	116.1008	-21.9168	13.95415
36	-124.388	110.331	-26.2151	19.94451	71	-117.274	109.0863	-24.6569	16.66908
37	-83.6296	75.30048	-18.2115	11.33283	72	-147.788	132.6343	-22.8093	14.00995

Table A.1: Trapezoid parameters for each 4th HUC. Note, there is no HUC 1, HUC 2 was removed, and algorithm failed to derive values for HUC's 5, 16, and 46 (CONTINUED).

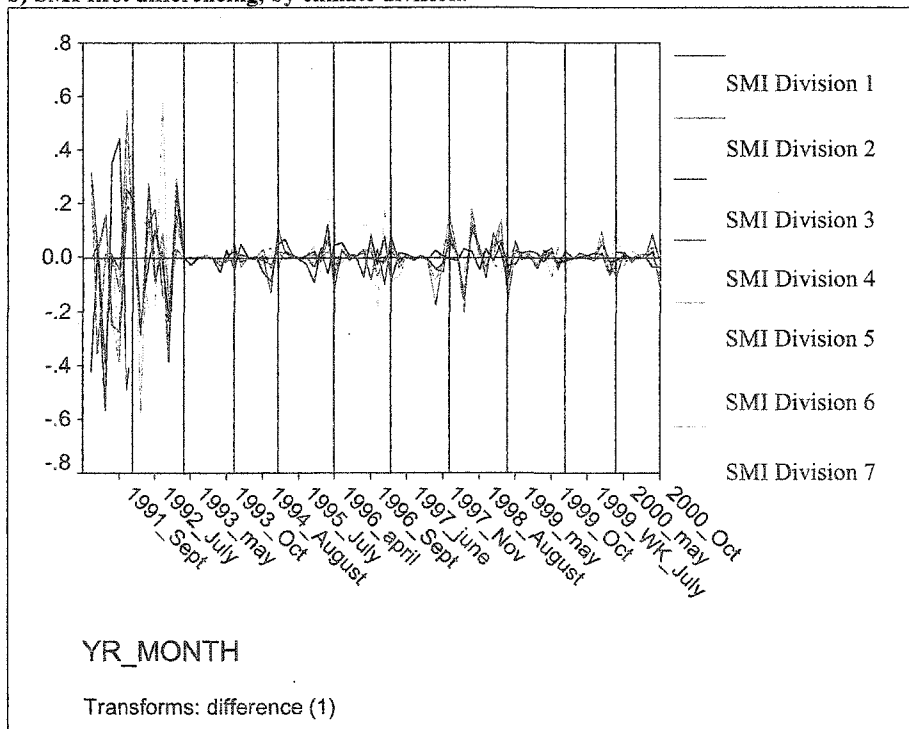
HUC	Max Slope	Max intercept	Min slope	Min intercept
73	-128.802	116.0596	-17.7936	11.70019
74	-97.6126	90.19289	-22.555	15.02623
75	-107.186	94.85503	-28.2956	16.83603
76	-101.687	92.3931	-25.4946	14.69887
77	-117.042	106.3887	-22.8682	10.09385
78	-98.3506	89.35116	-25.745	16.14591
79	-80.5626	84.9748	-20.6968	12.69503
80	-91.1379	80.34972	-23.0672	13.56649
81	-111.032	99.22098	-21.4224	14.41016
82	-84.6942	73.70065	-20.1506	13.60071
83	-78.0668	74.48007	-22.868	11.66611
84	-90.6994	84.6056	-26.3714	15.42855
85	-60.9486	50.38476	-15.941	10.80814
86	-52.0768	49.50488	-22.3193	15.36054
87	-30.5659	27.85468	-26.6554	13.58566
88	-41.6866	35.22319	-29.4142	17.40933
89	-79.0744	71.6012	-24.1015	13.88018
90	-51.834	53.71454	-26.7835	15.18693
91	-29.4083	27.26549	-16.7108	13.08145
92	-31.3861	28.32819	-14.5912	9.103303
93	-48.744	51.89315	-16.1959	9.753709
94	-83.0551	75.5079	-22.214	12.13247
95	-50.4635	45.028	-24.1436	17.0158
96	-19.7538	21.38082	-20.7654	13.71834
97	-40.9716	38.93089	-14.8265	9.892314
98	-28.3496	24.51251	-20.1594	14.46347
99	-40.1602	31.63116	-23.2317	16.4275
100	-43.3228	39.48298	-38.5218	31.4767
101	-19.141	16.85452	-17.0688	14.51533
102	-47.6482	44.31785	-27.5448	16.7301
103	-16.8765	16.87073	-8.25228	7.34927
104	-32.0545	29.27614	-25.2744	20.87415
105	-45.4674	46.12521	-26.4903	15.26349
106	-18.3443	16.37878	-16.9566	13.47344

Figure A.1: Time sequence of SMI and Palmer Z for all climate divisions. a) is SMI raw data, b) shows SMI first differencing, c) is Palmer Z raw data, d) shows Palmer Z first differencing. Colors denote climate divisions.

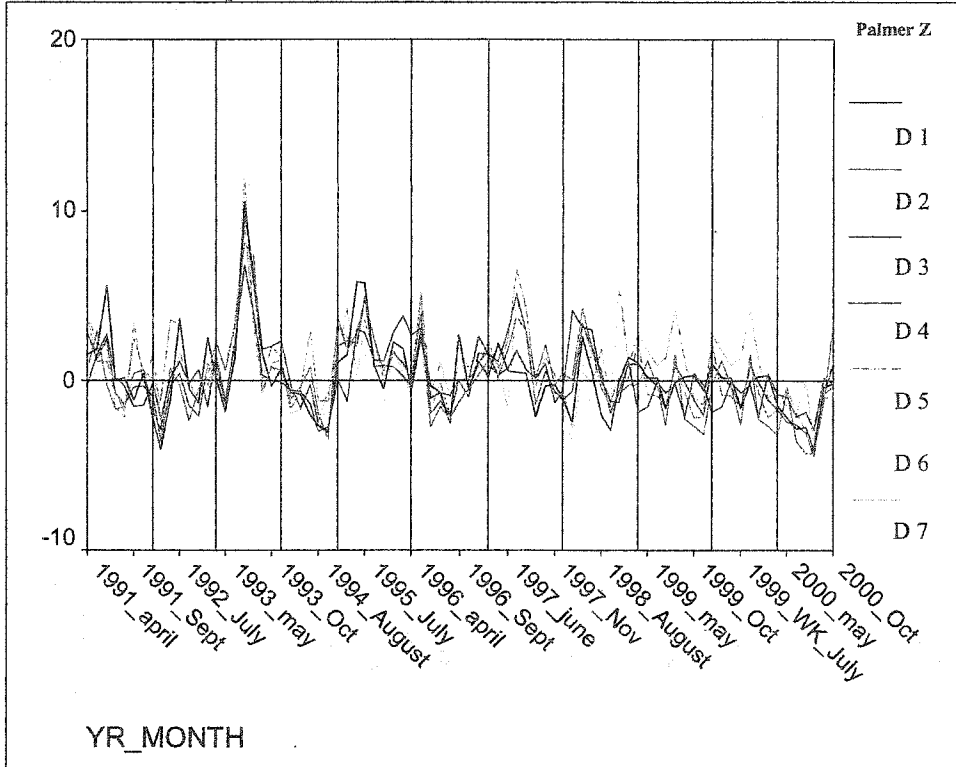
a) SMI raw, by climate division.



b) SMI first differencing, by climate division.



c) Palmer Z raw sequence by climate division.



d) Palmer Z first differencing, by climate division.

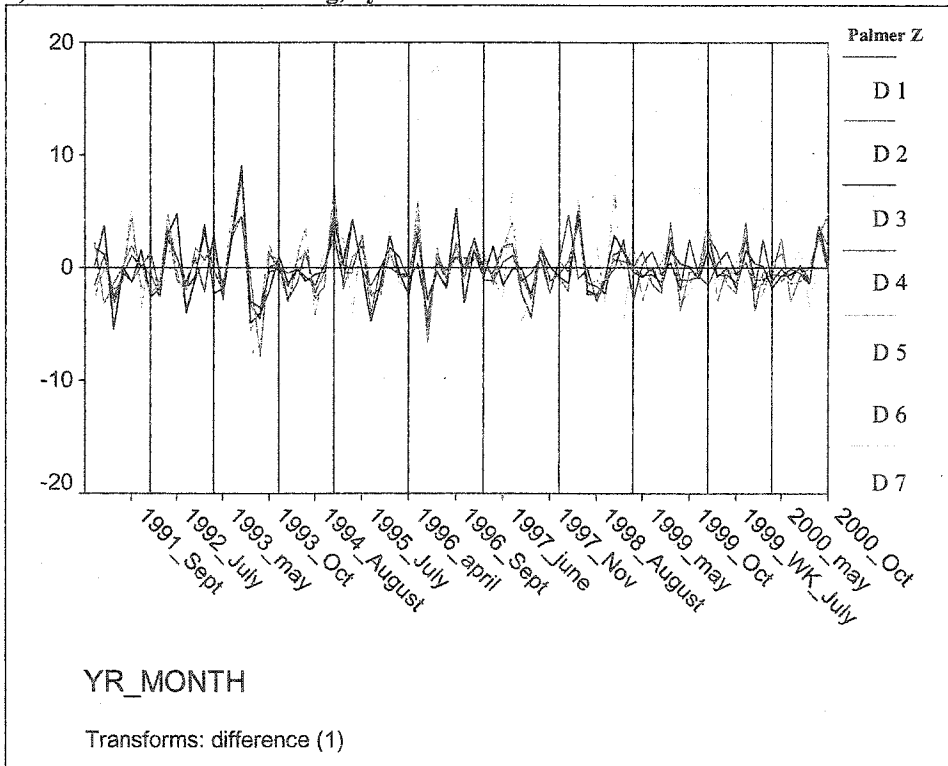


Figure A.2: Cross-correlation by climate division. Figures are for all years combined. All data have been transformed (first difference).

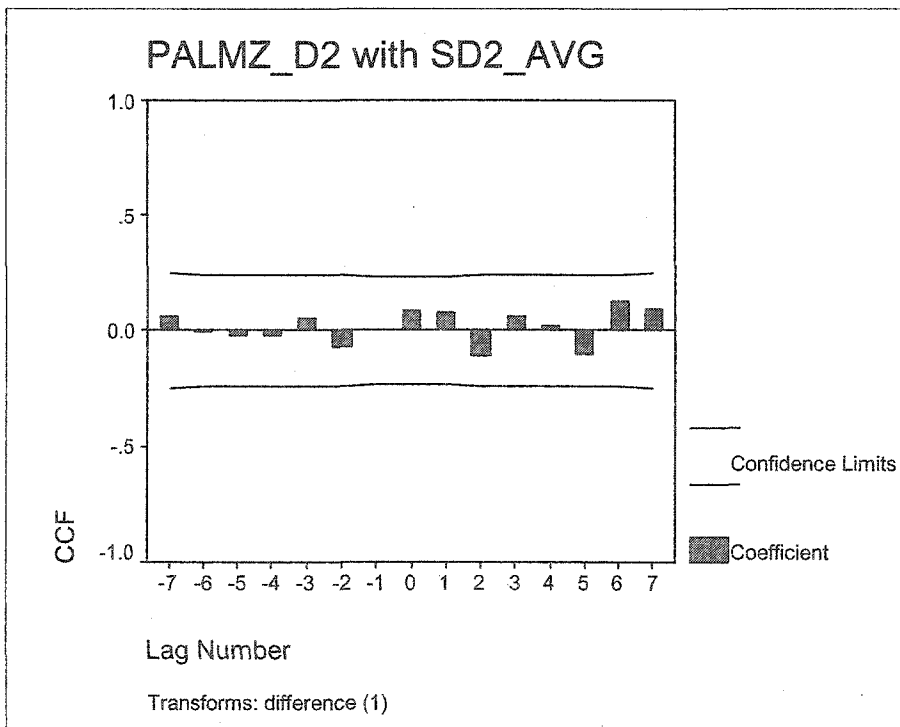
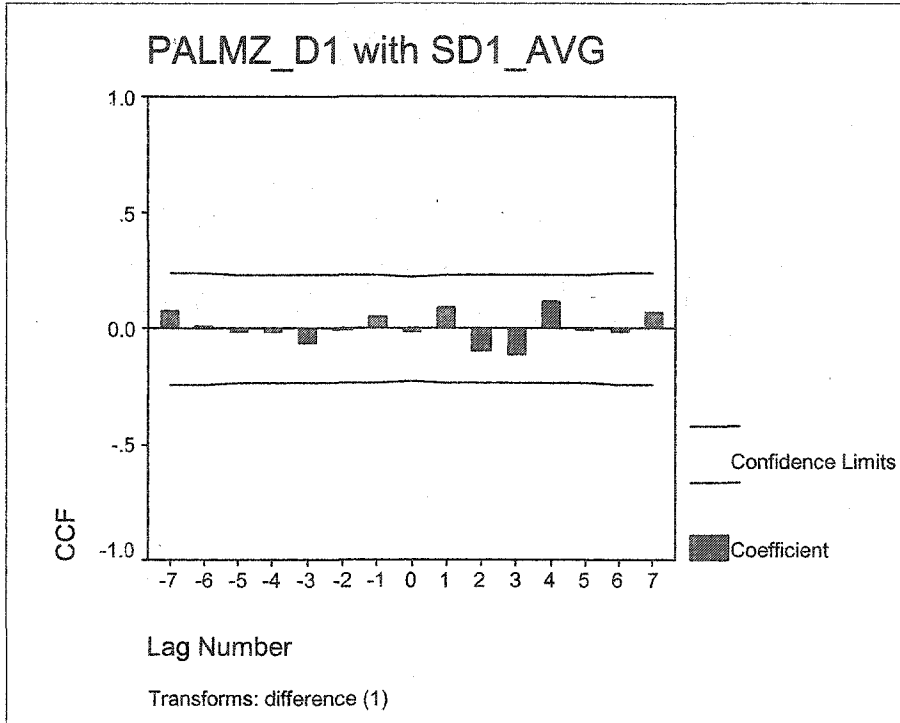


Figure A.2: Cross-correlation by climate division (CONTINUED).

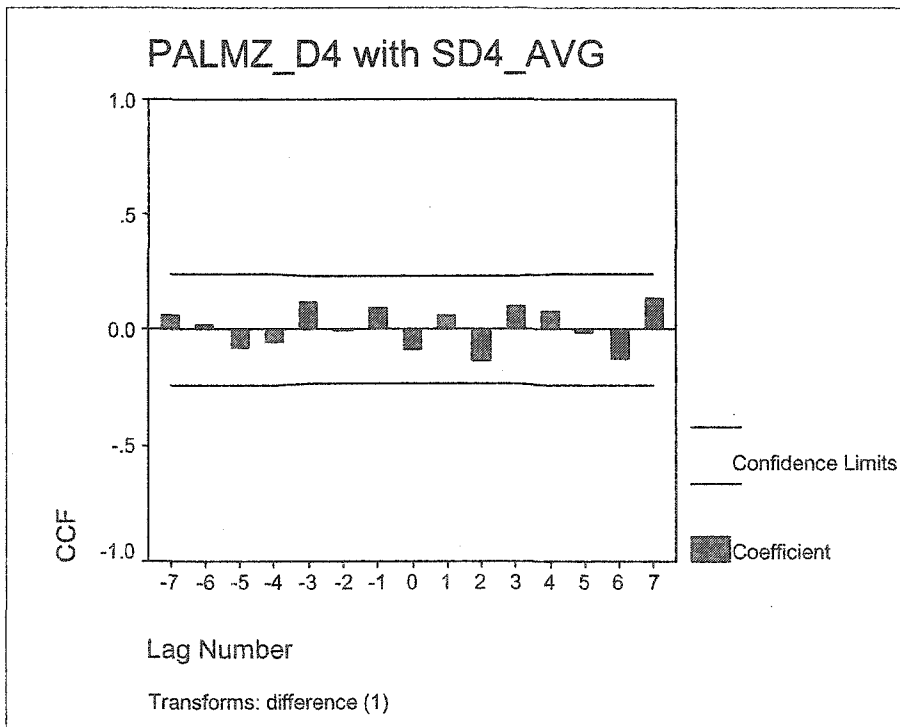
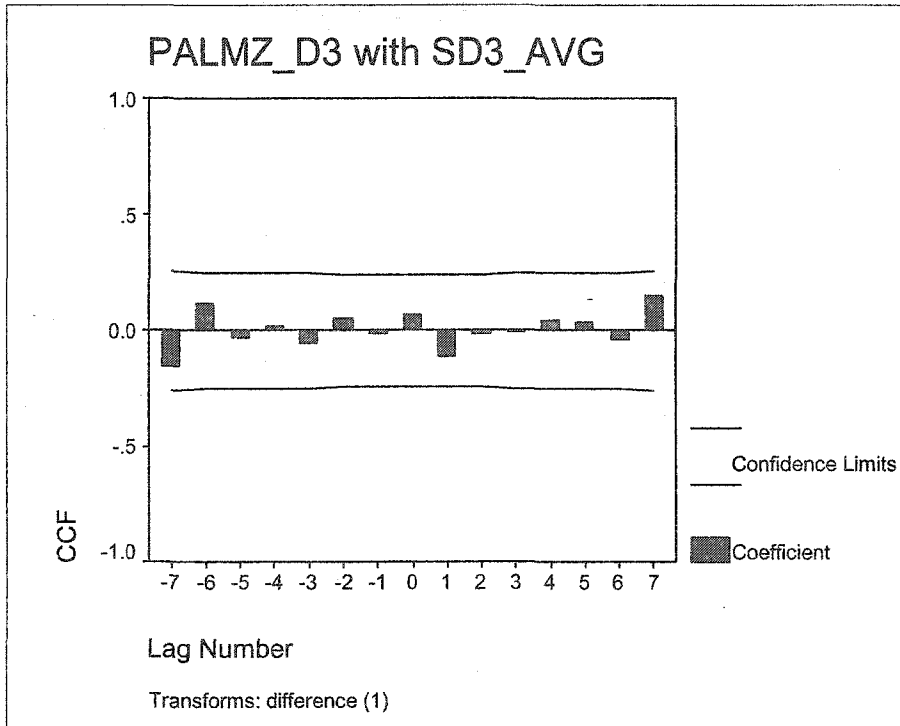


Figure A.2: Cross-correlation by climate division (CONTINUED).

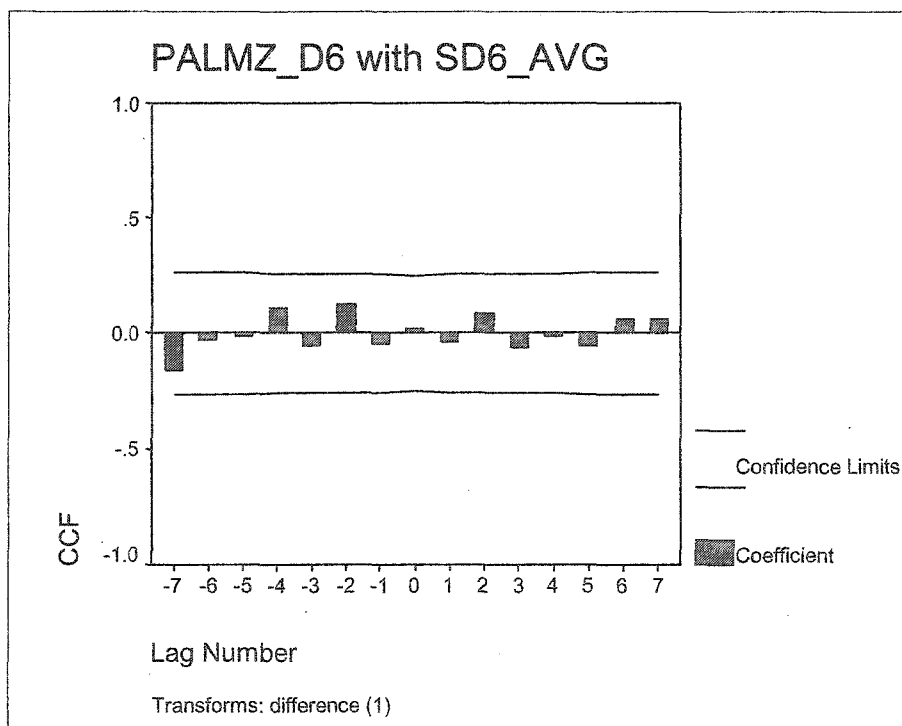
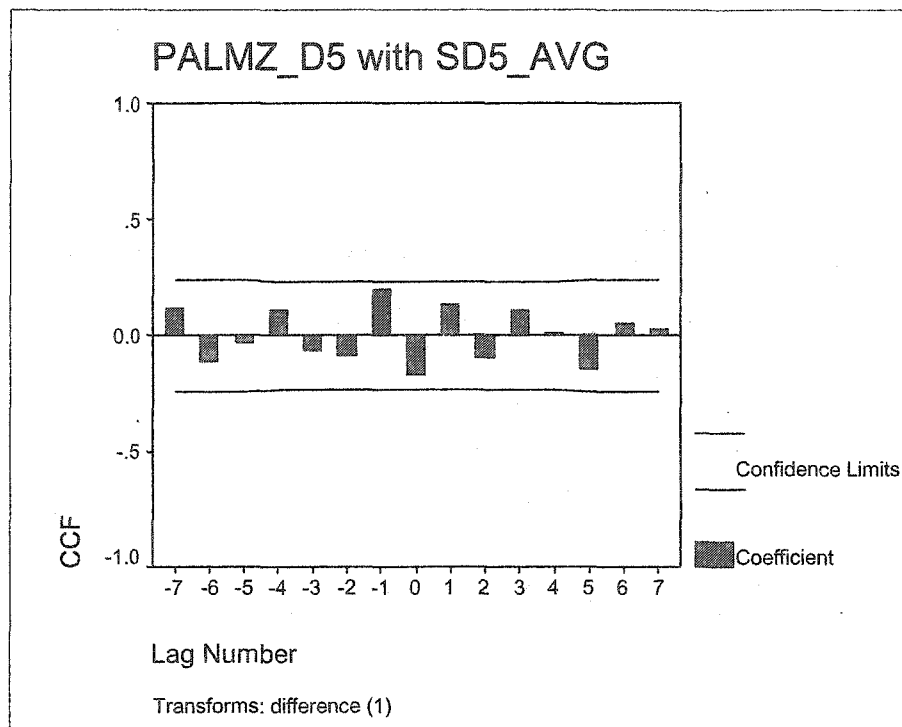


Figure A.2: Cross-correlation by climate division (CONTINUED).

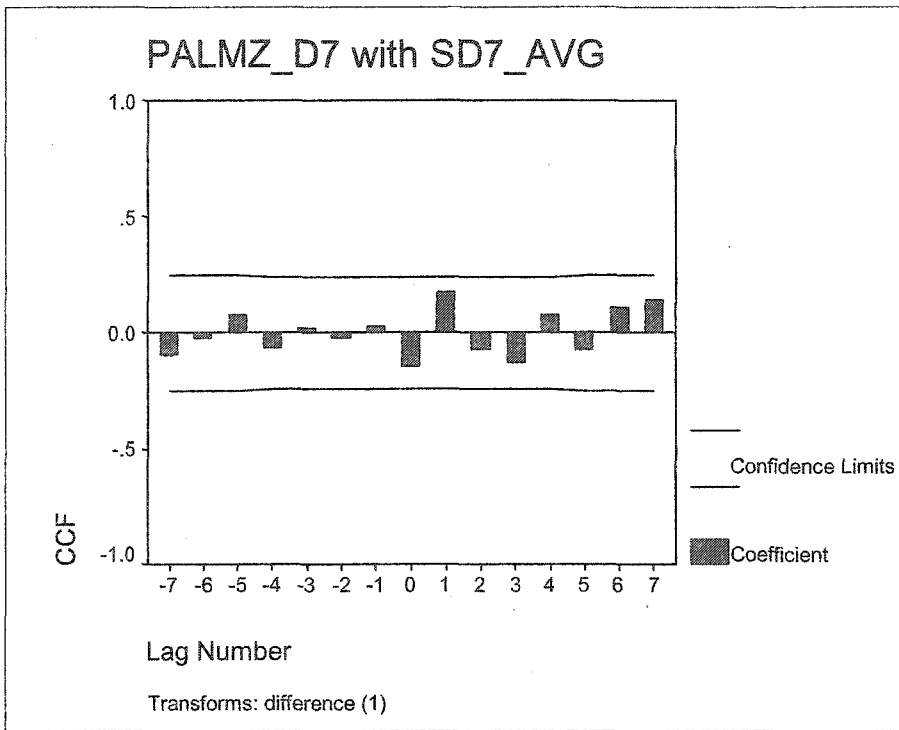


Figure A.3.a: Climate Division 1 cross-correlogram of Palmer Z and SMI, by year.

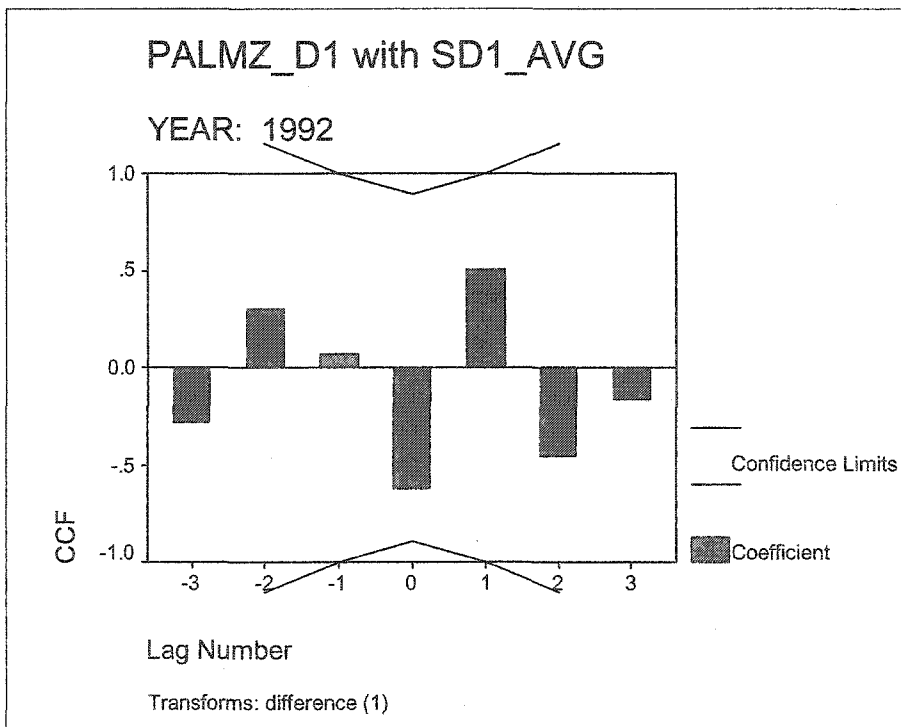
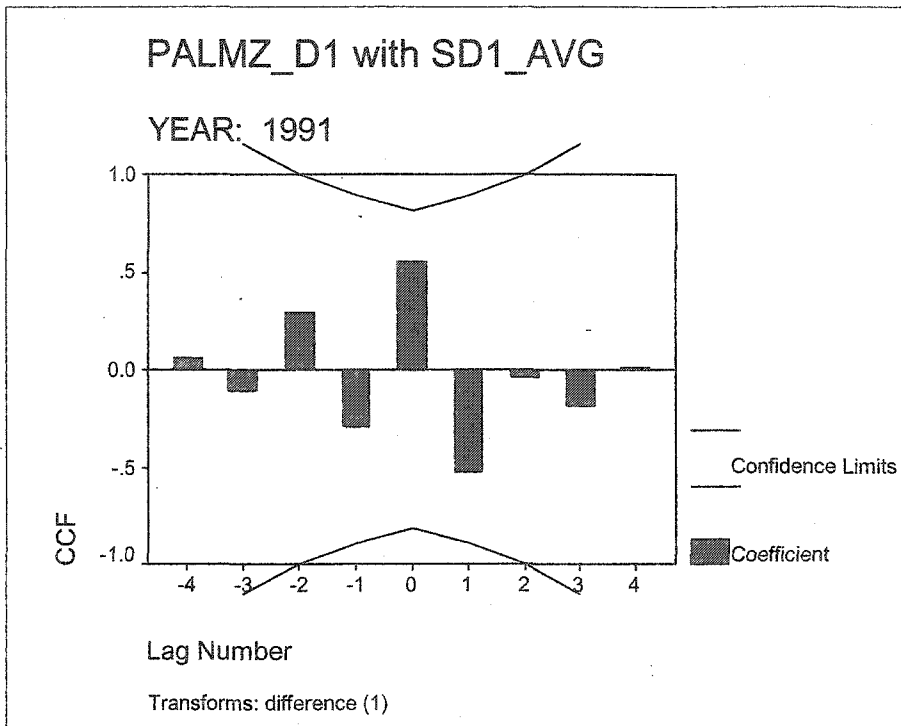


Figure A.3.a: Climate Division 1 cross-correlogram of Palmer Z and SMI, by year.
(CONTINUED)

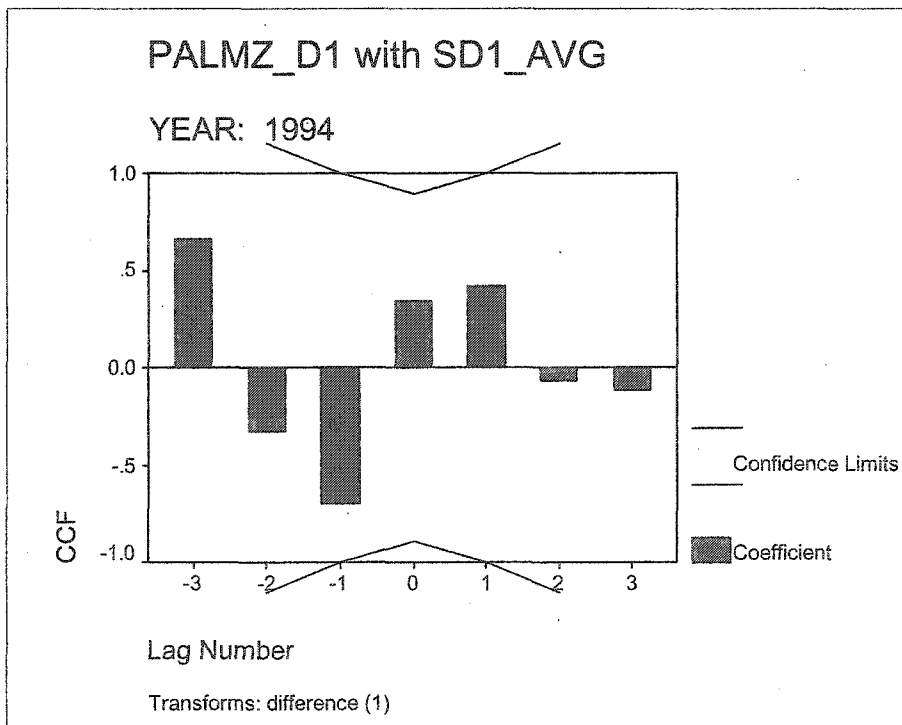
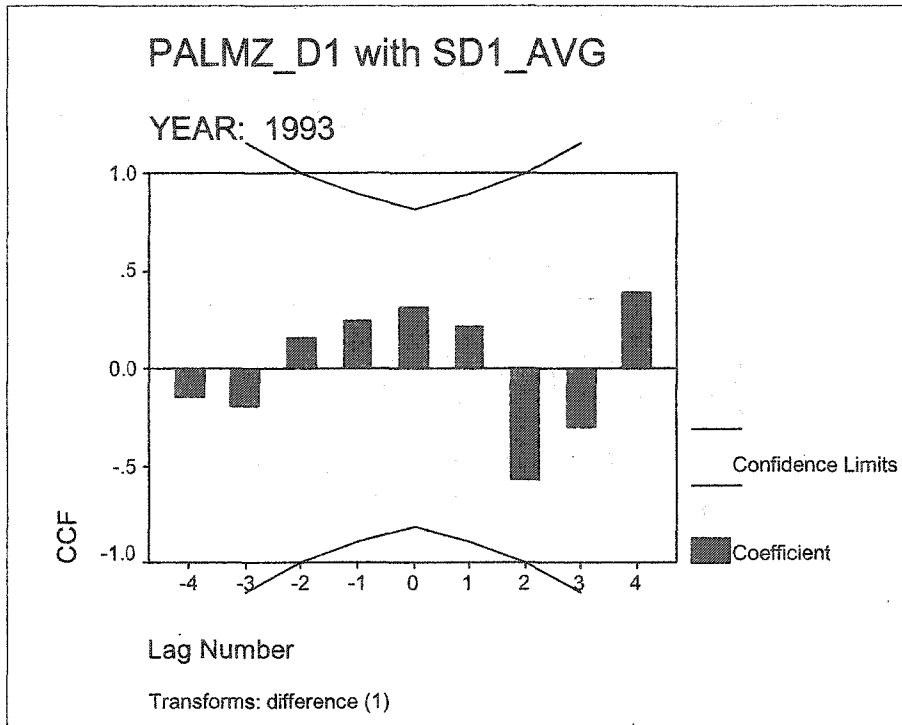


Figure A.3.a: Climate Division 1 cross-correlogram of Palmer Z and SMI, by year.
(CONTINUED)

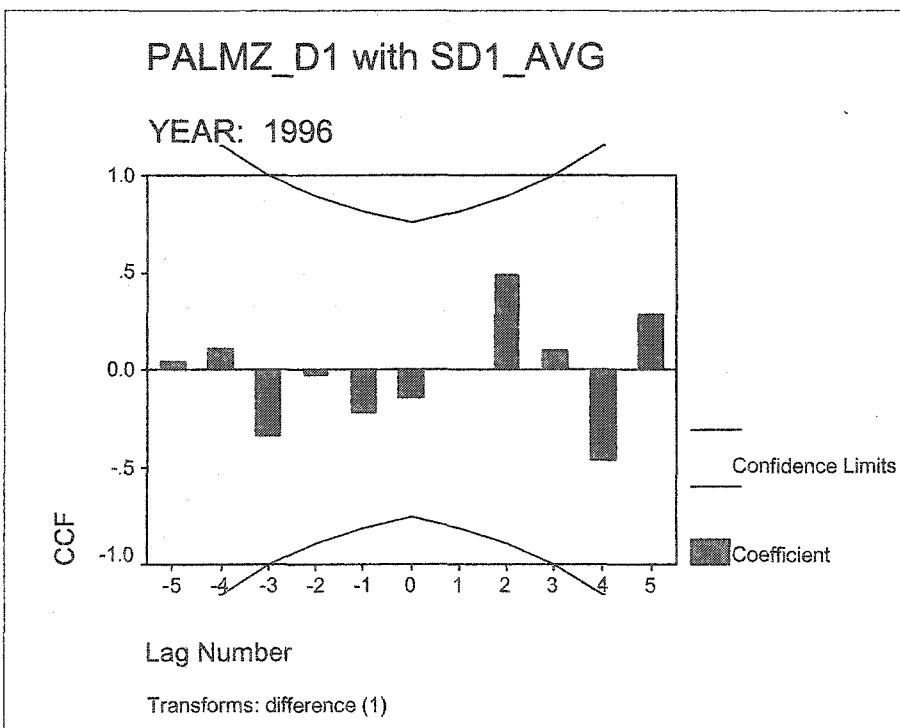
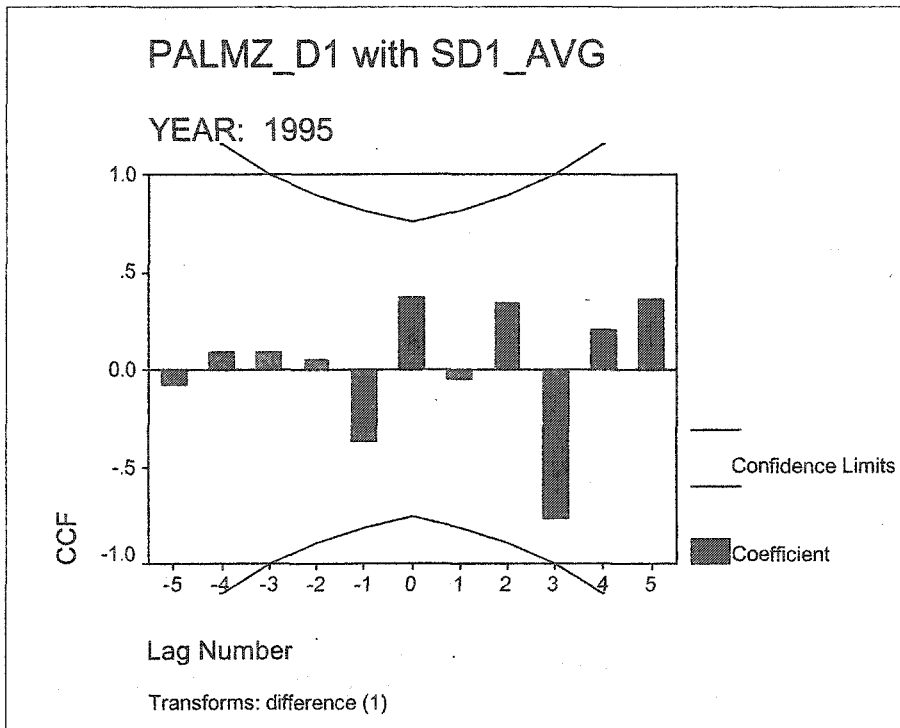


Figure A.3.a: Climate Division 1 cross-correlogram of Palmer Z and SMI, by year.
(CONTINUED)

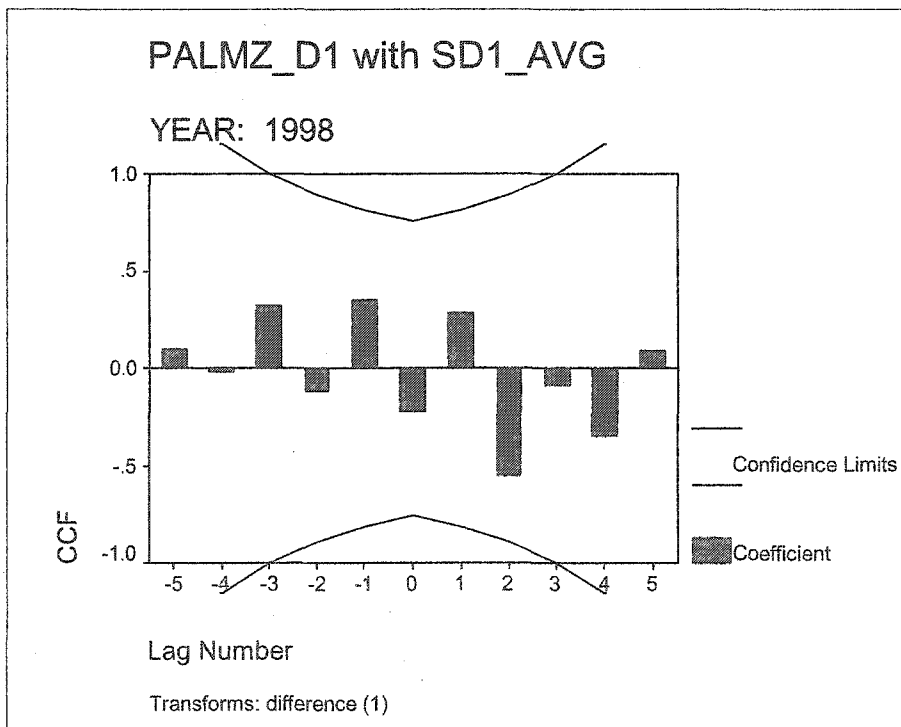
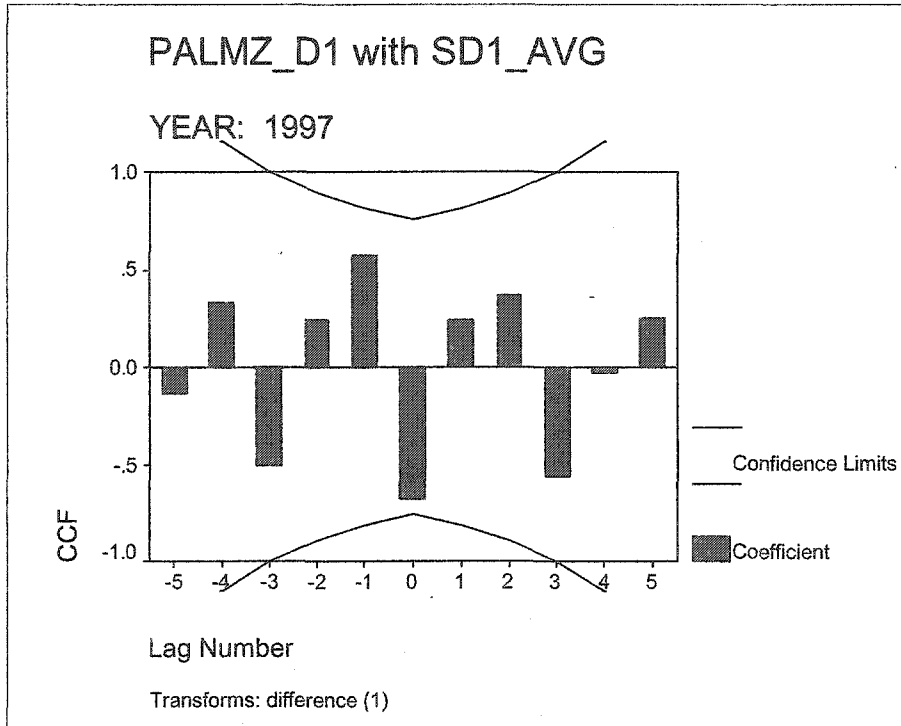


Figure A.3.a: Climate Division 1 cross-correlogram of Palmer Z and SMI, by year.
(CONTINUED)

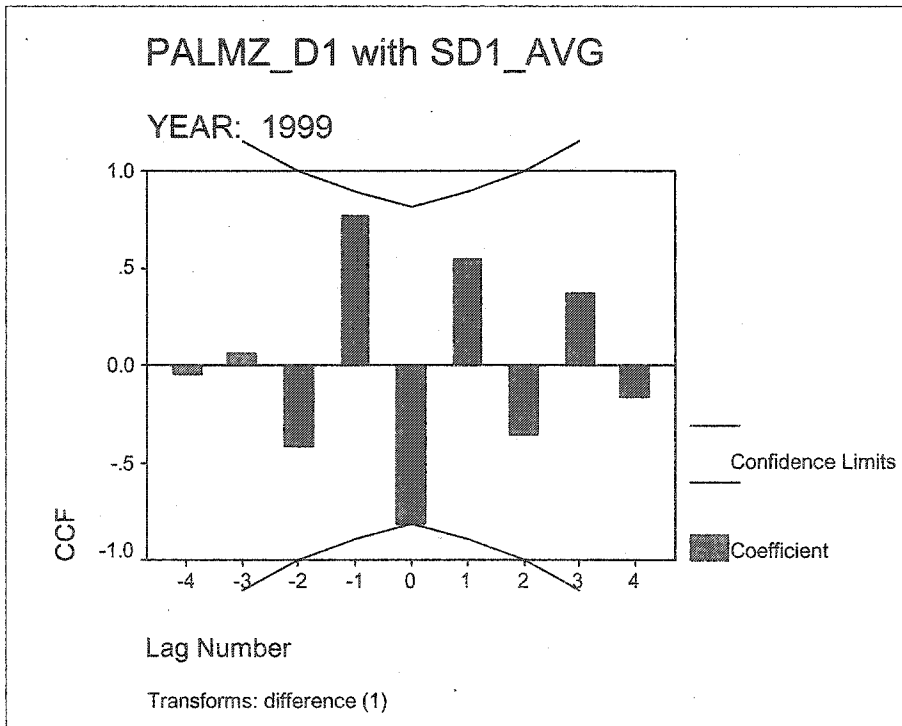
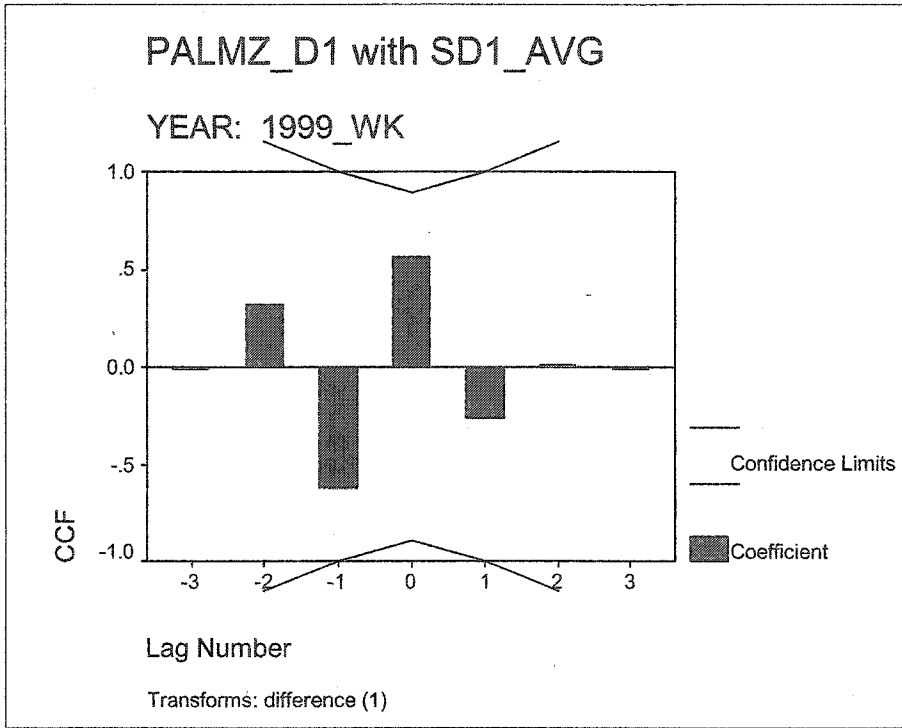


Figure A.3.a: Climate Division 1 cross-correlogram of Palmer Z and SMI, by year.
(CONTINUED)

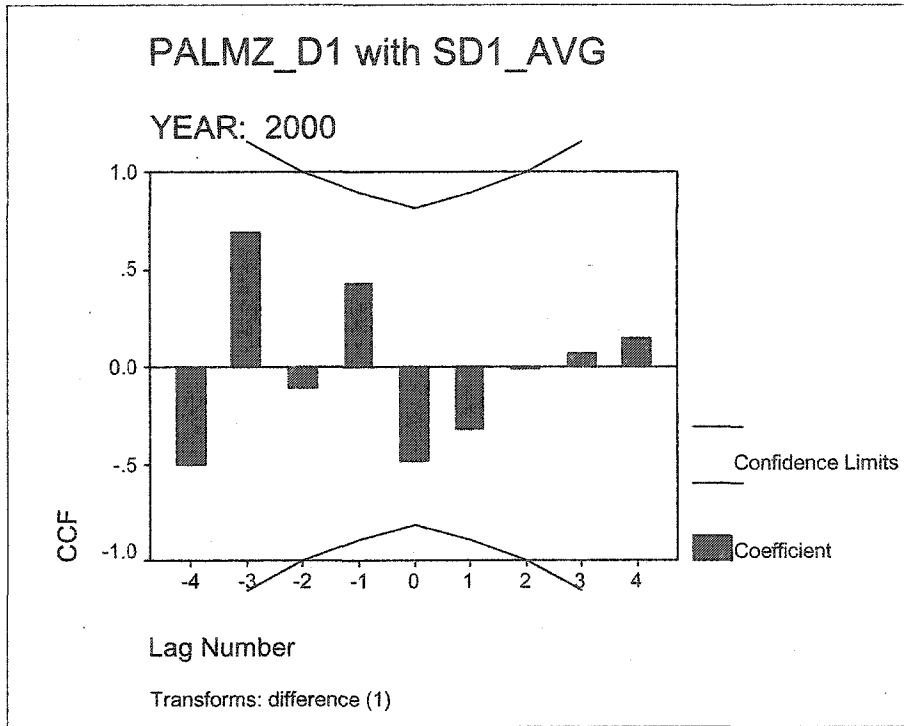


Figure A.3.b: Climate Division 2 cross-correlogram of Palmer Z and SMI, by year.

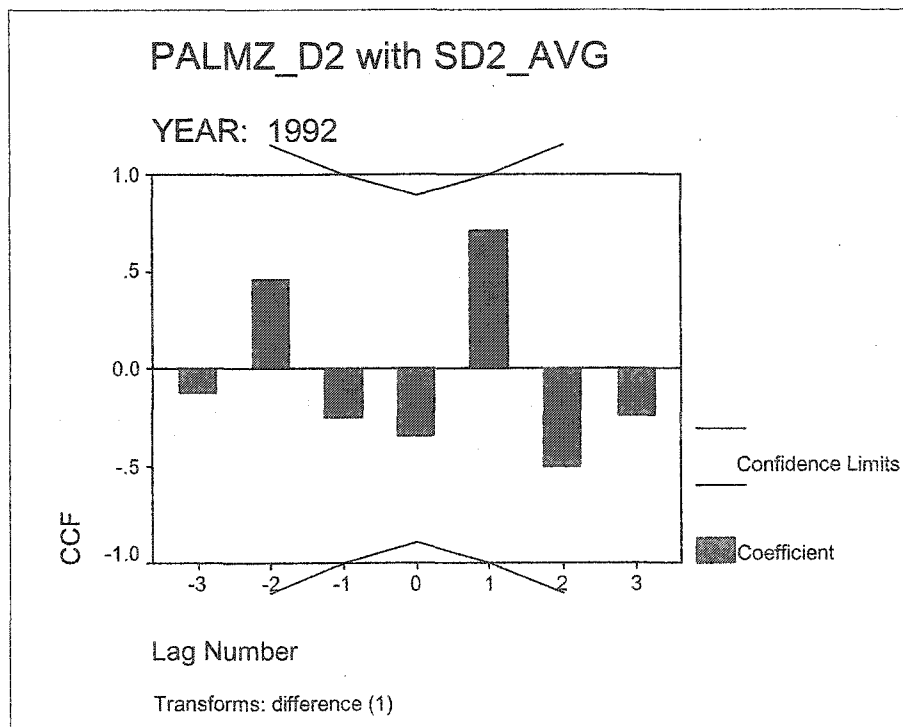
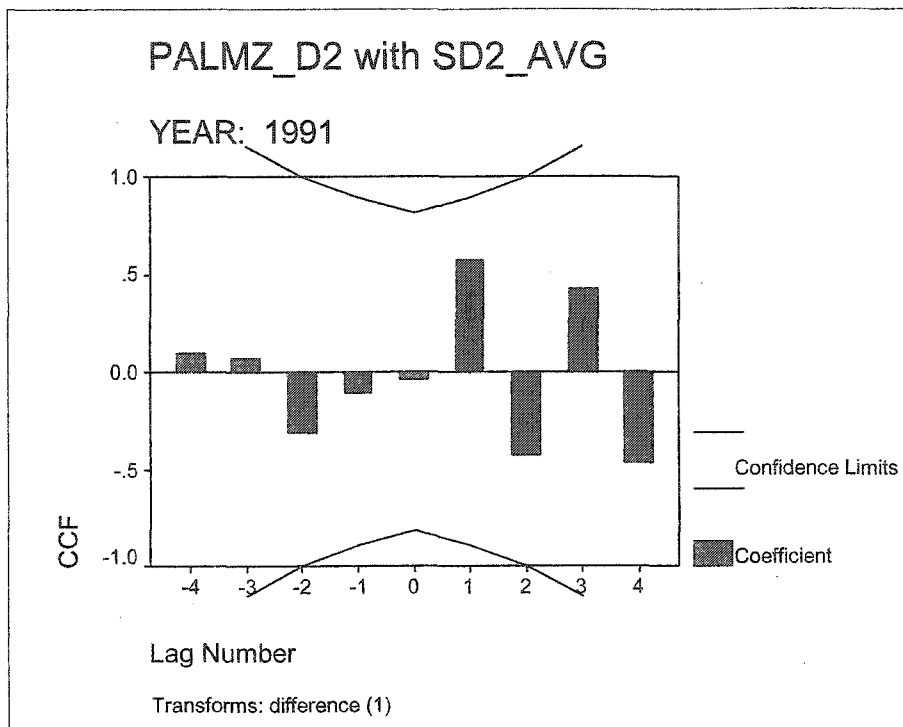


Figure A.3.b: Climate Division 2 cross-correlogram of Palmer Z and SMI, by year.
(CONTINUED).

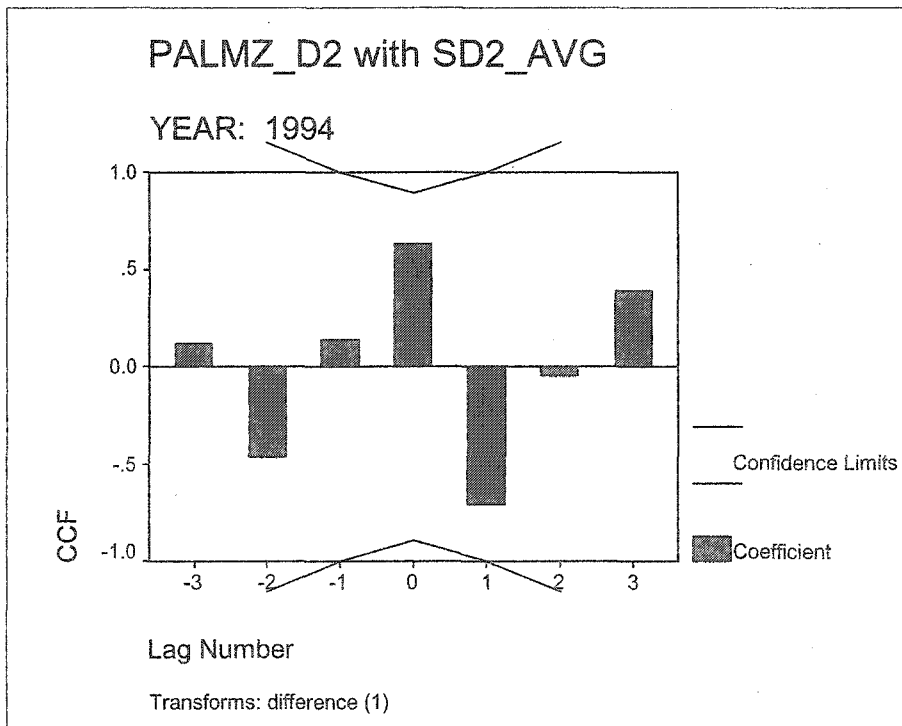
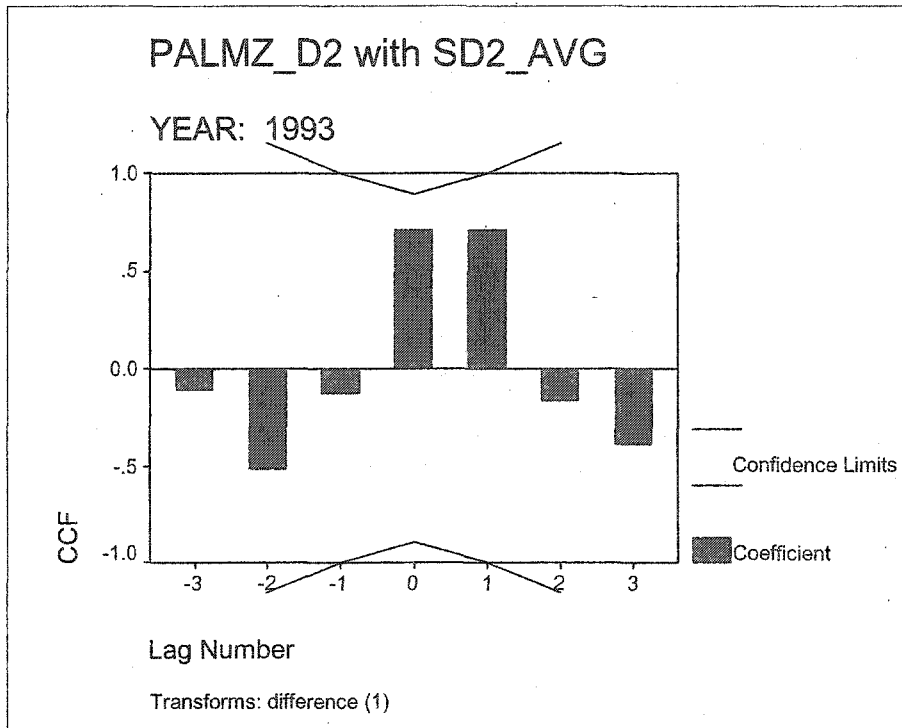


Figure A.3.b: Climate Division 2 cross-correlogram of Palmer Z and SMI, by year.
(CONTINUED).

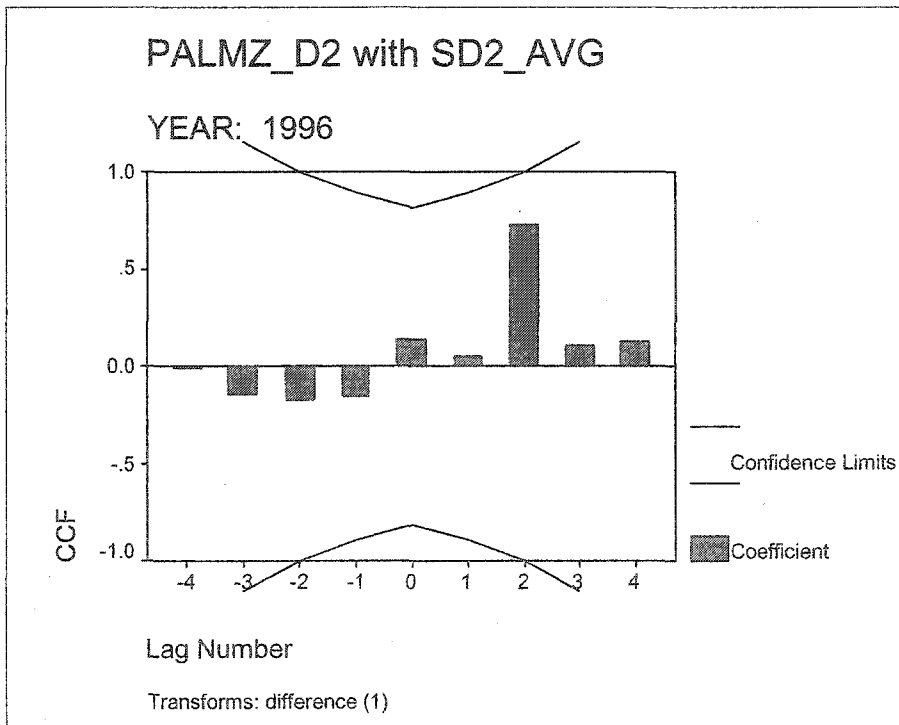
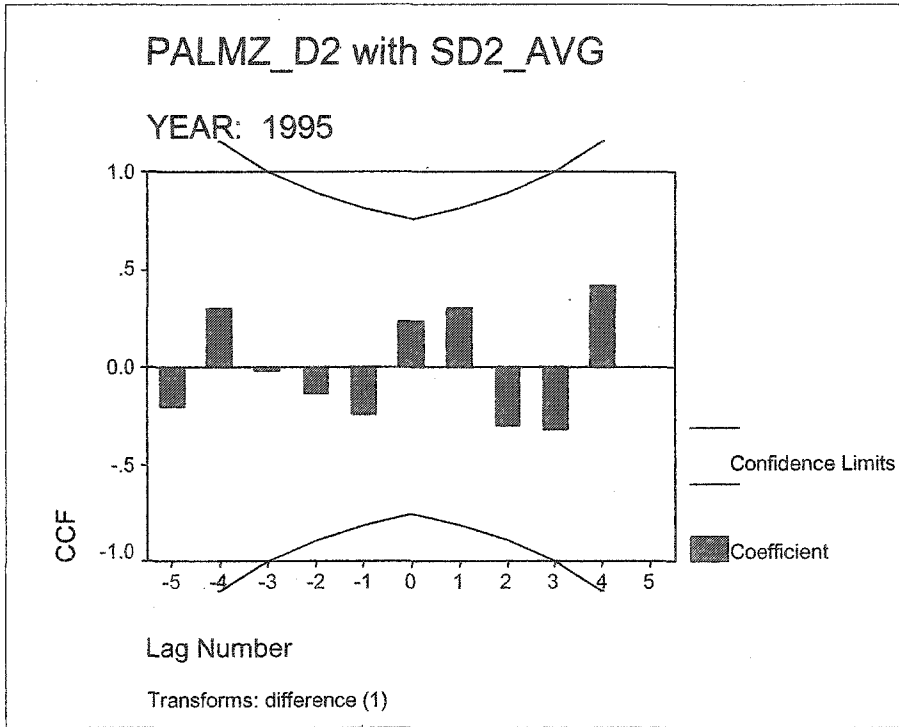


Figure A.3.b: Climate Division 2 cross-correlogram of Palmer Z and SMI, by year.
(CONTINUED).

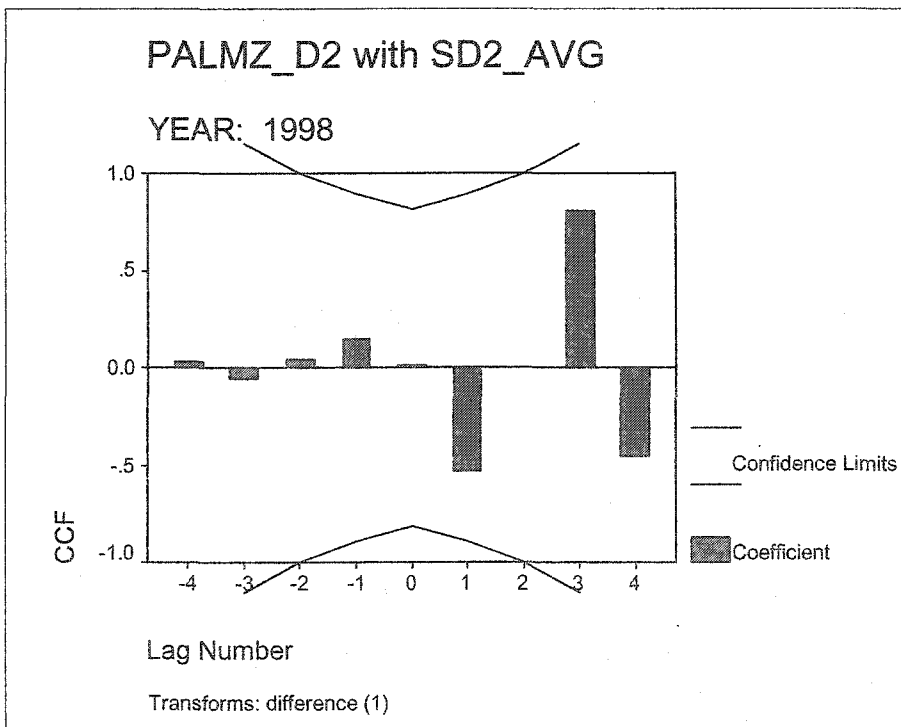
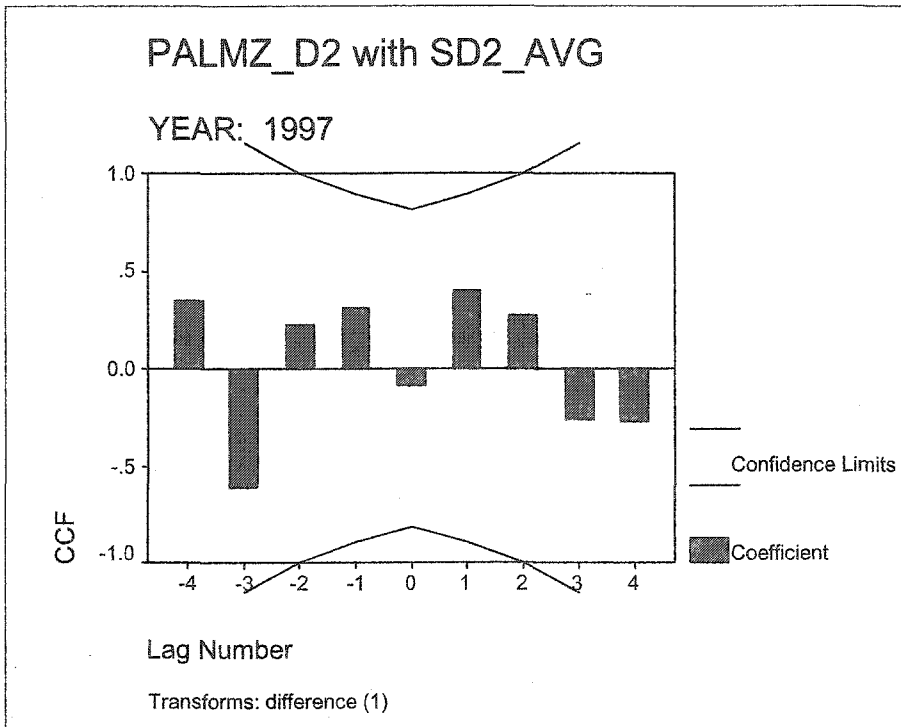


Figure A.3.b: Climate Division 2 cross-correlogram of Palmer Z and SMI, by year.
(CONTINUED).

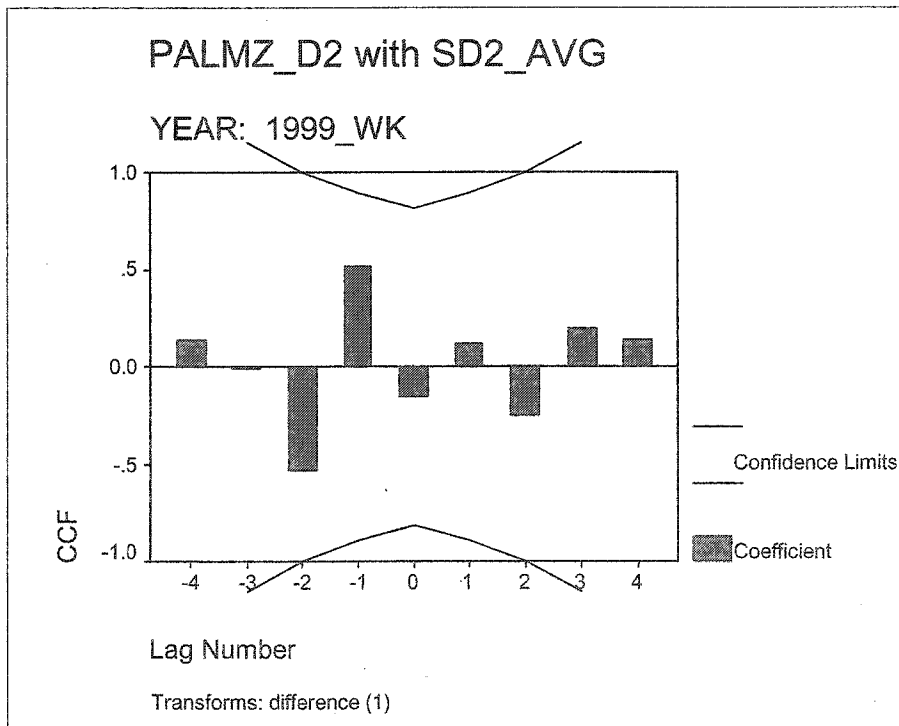
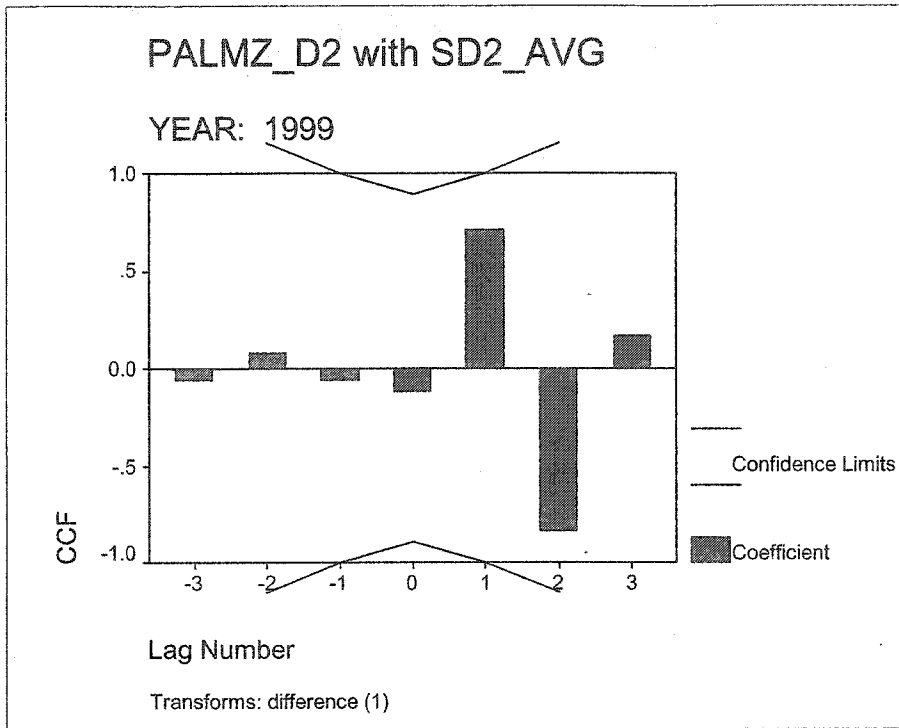


Figure A.3.b: Climate Division 2 cross-correlogram of Palmer Z and SMI, by year.
(CONTINUED).

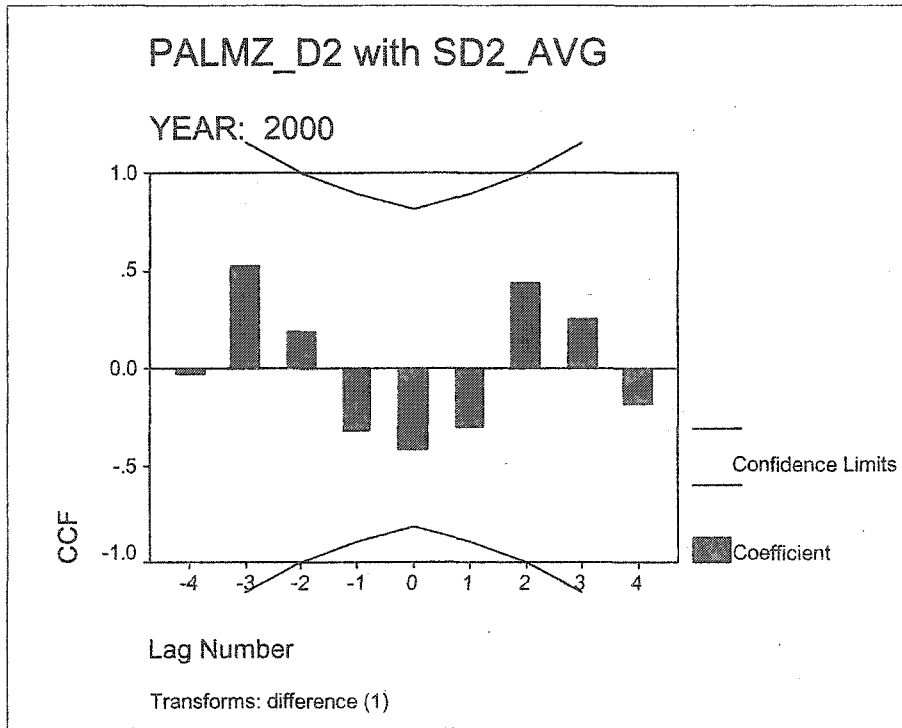


Figure A.3.c: Climate Division 3 cross-correlogram of Palmer Z and SMI, by year.

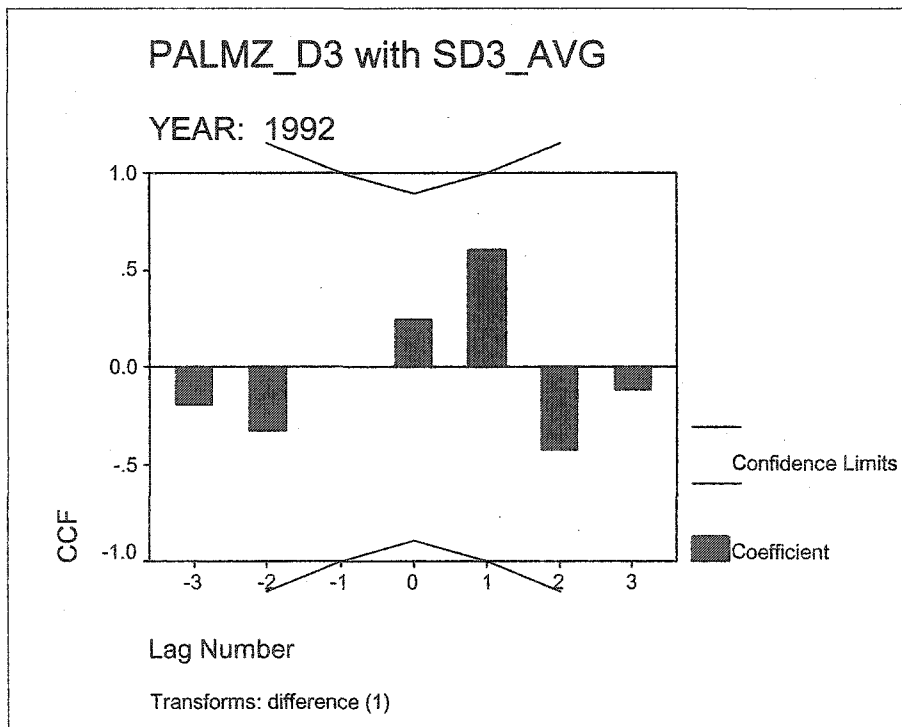
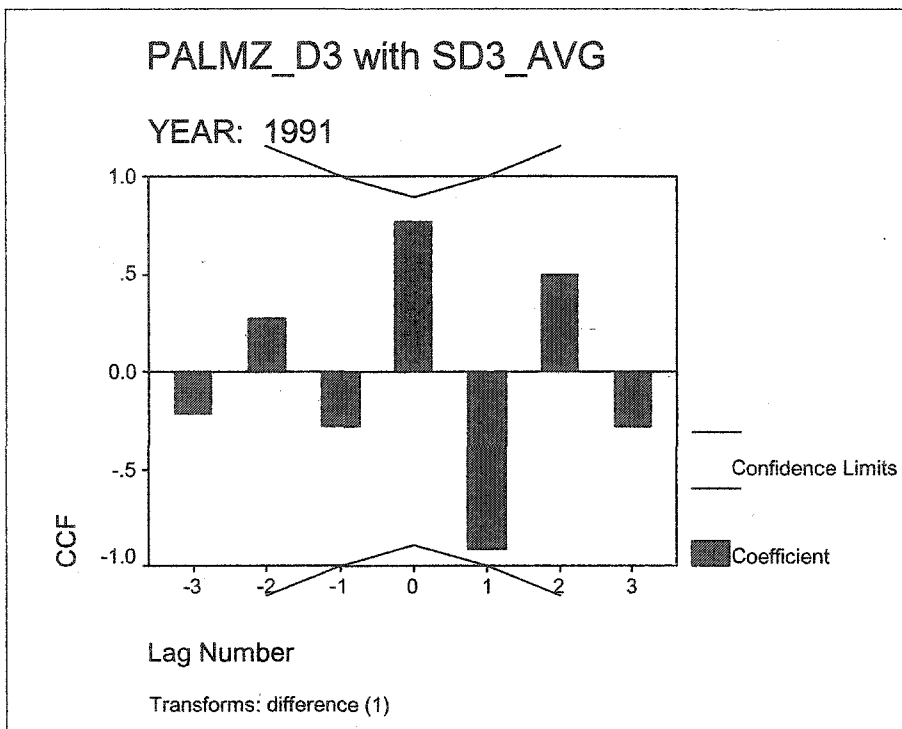


Figure A.3.c: Climate Division 3 cross-correlogram of Palmer Z and SMI, by year.
(CONTINUED)

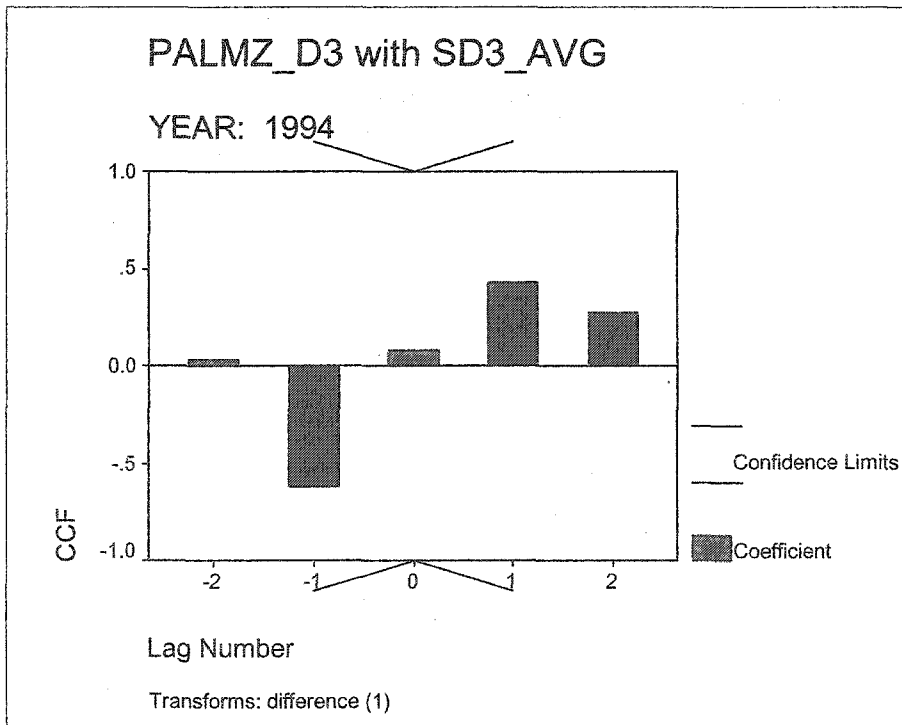
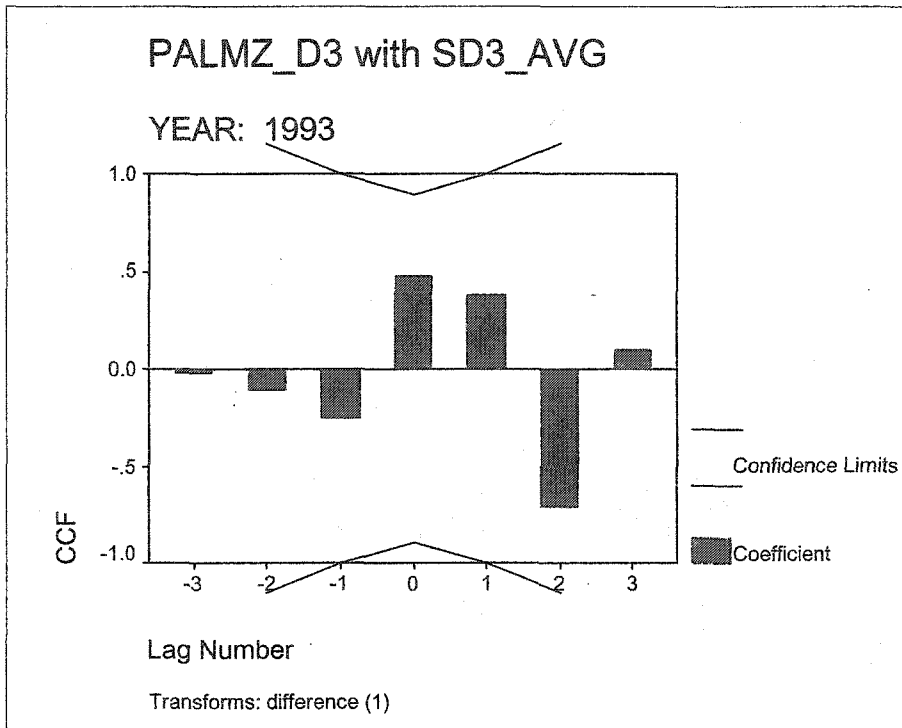


Figure A.3.c: Climate Division 3 cross-correlogram of Palmer Z and SMI, by year.
(CONTINUED)

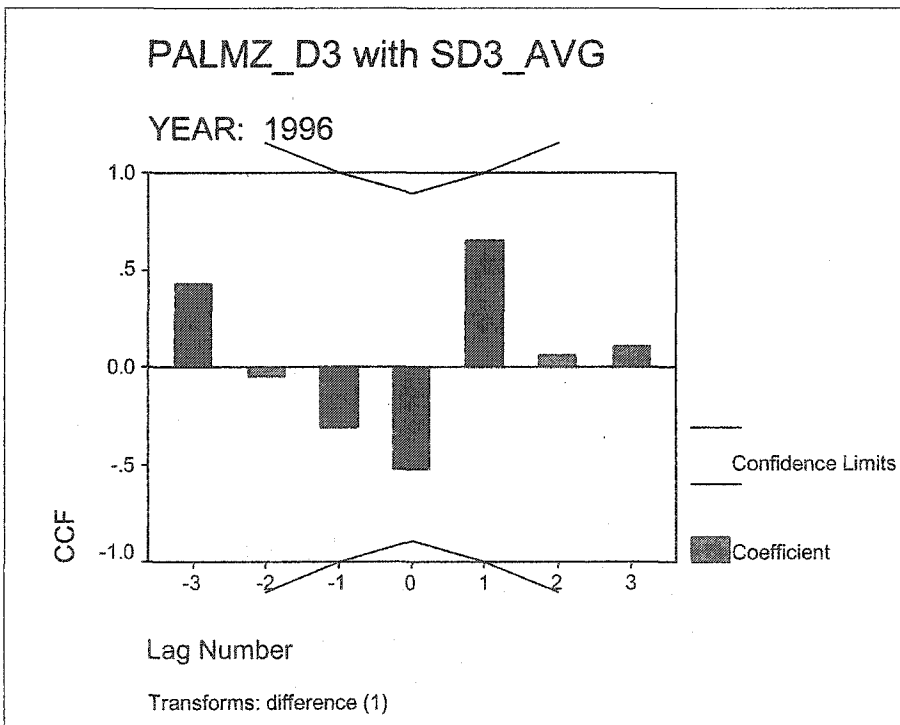
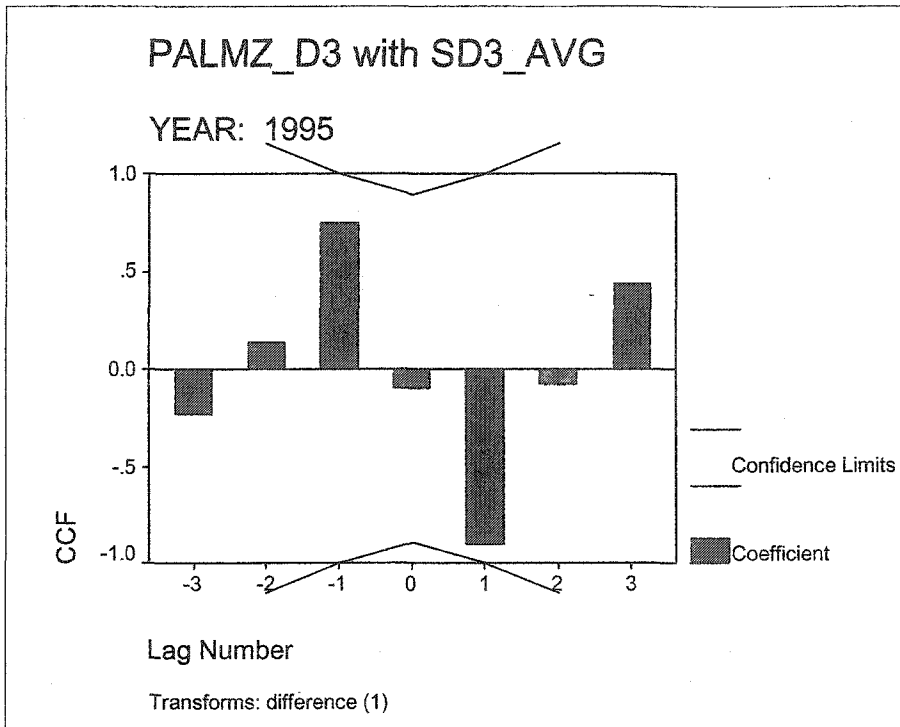


Figure A.3.c: Climate Division 3 cross-correlogram of Palmer Z and SMI, by year.
(CONTINUED)

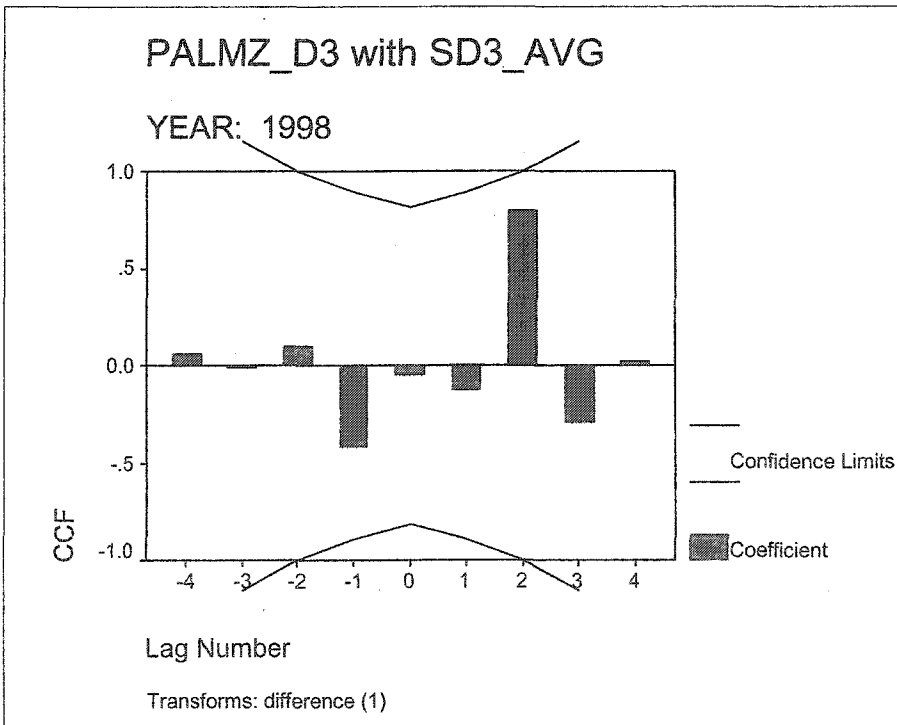
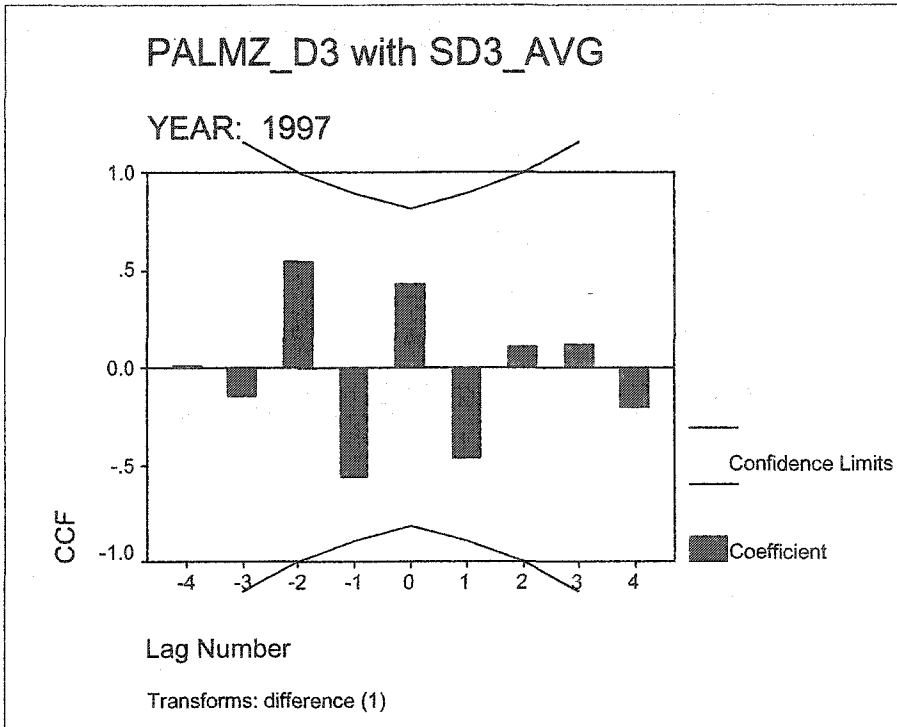


Figure A.3.c: Climate Division 3 cross-correlogram of Palmer Z and SMI, by year.
(CONTINUED)

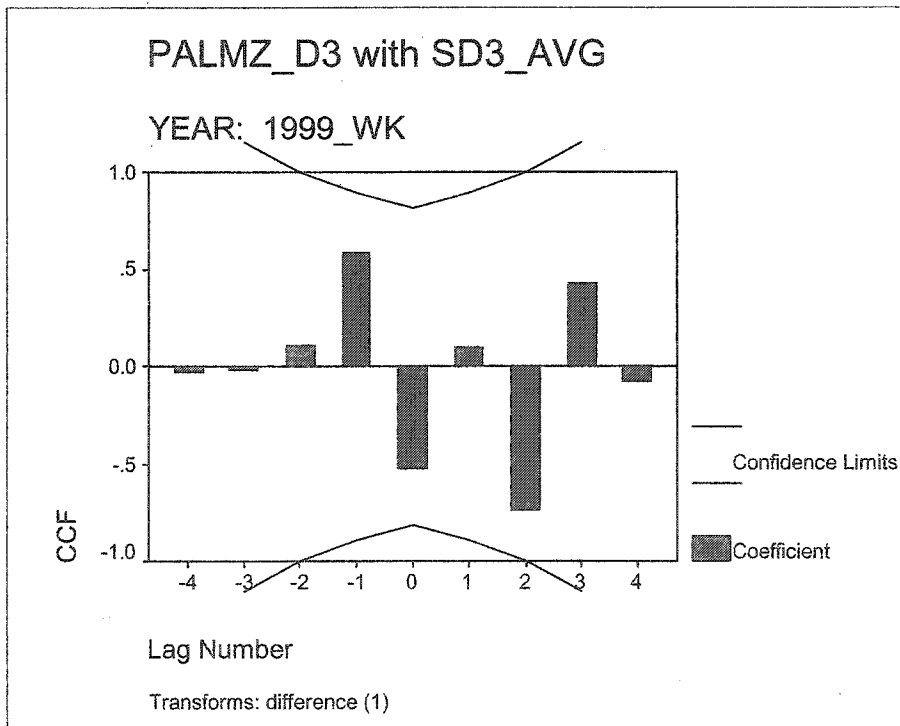
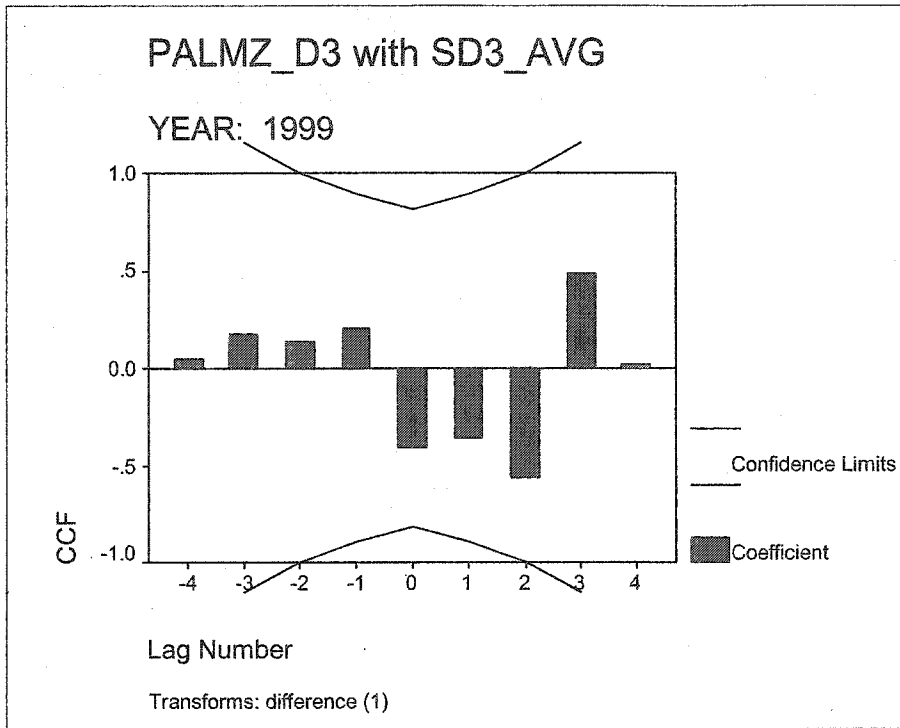


Figure A.3.c: Climate Division 3 cross-correlogram of Palmer Z and SMI, by year.
(CONTINUED)

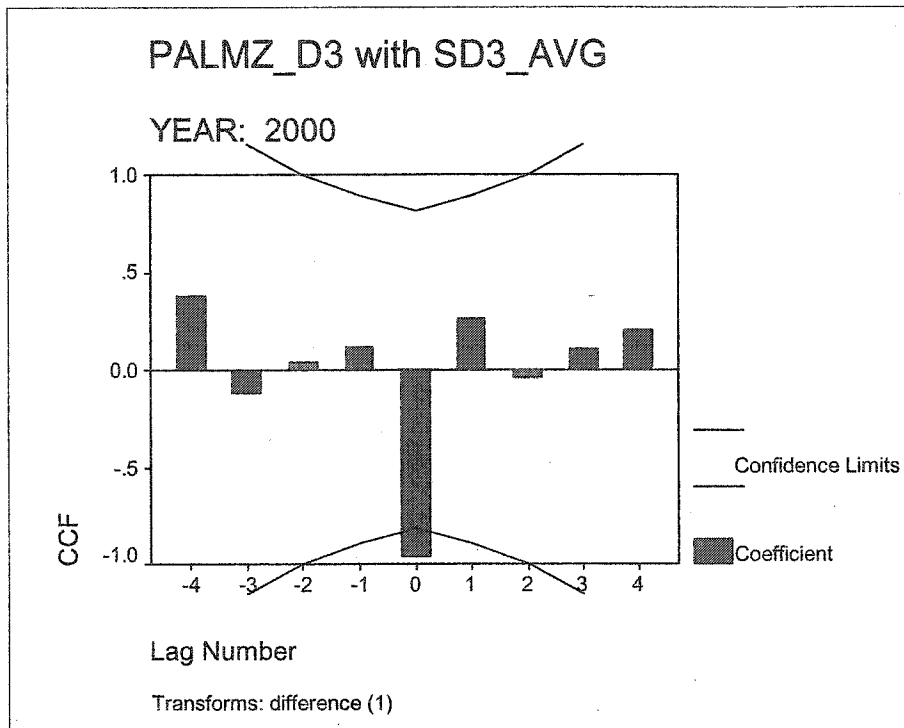


Figure A.3.d: Climate Division 4 cross-correlogram of Palmer Z and SMI, by year.

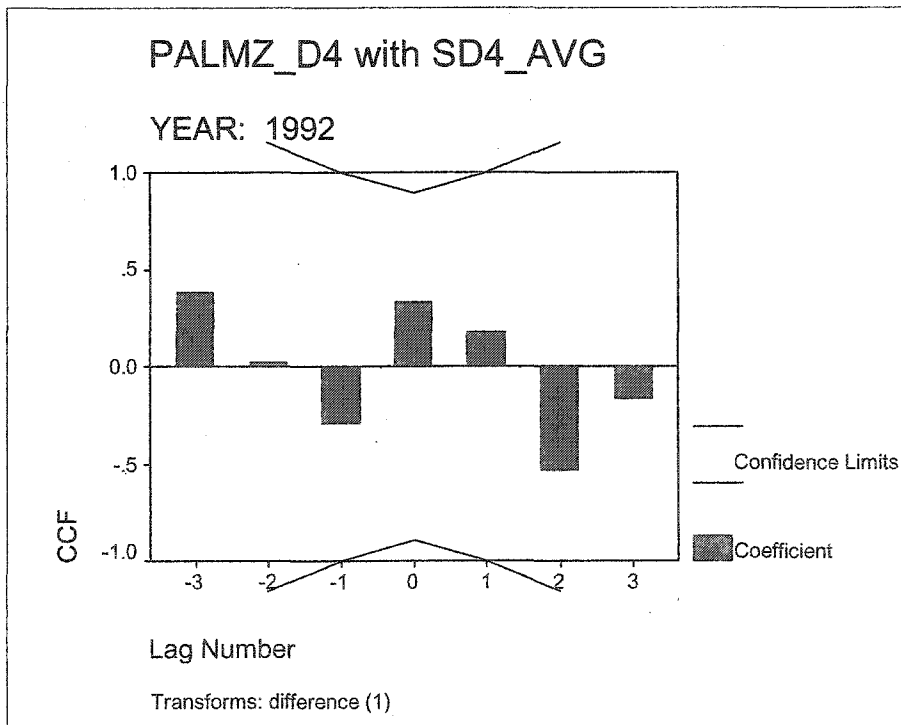
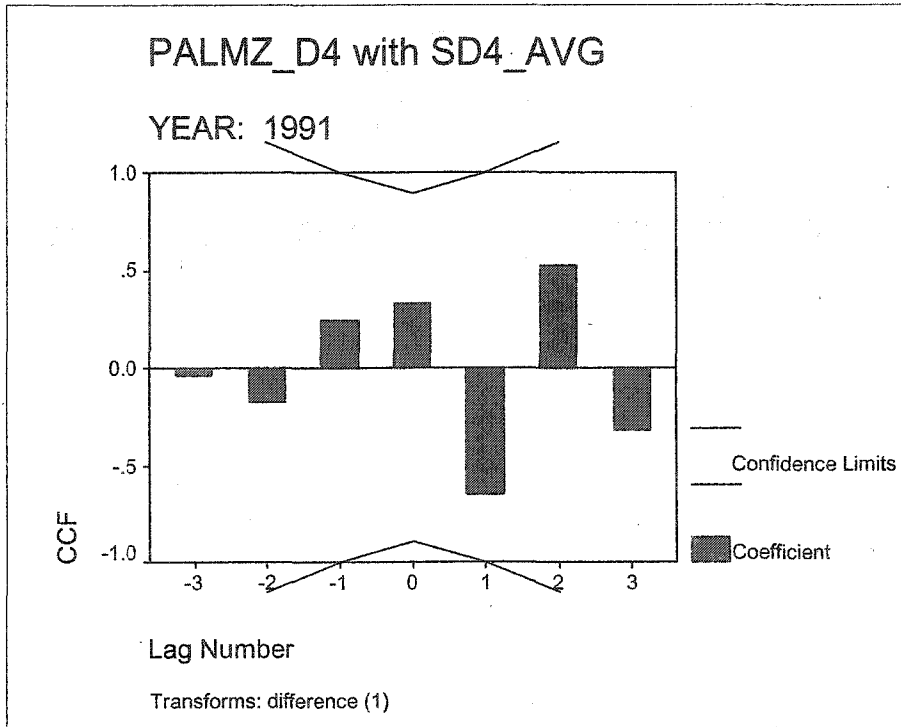


Figure A.3.d: Climate Division 4 cross-correlogram of Palmer Z and SMI, by year.
(CONTINUED).

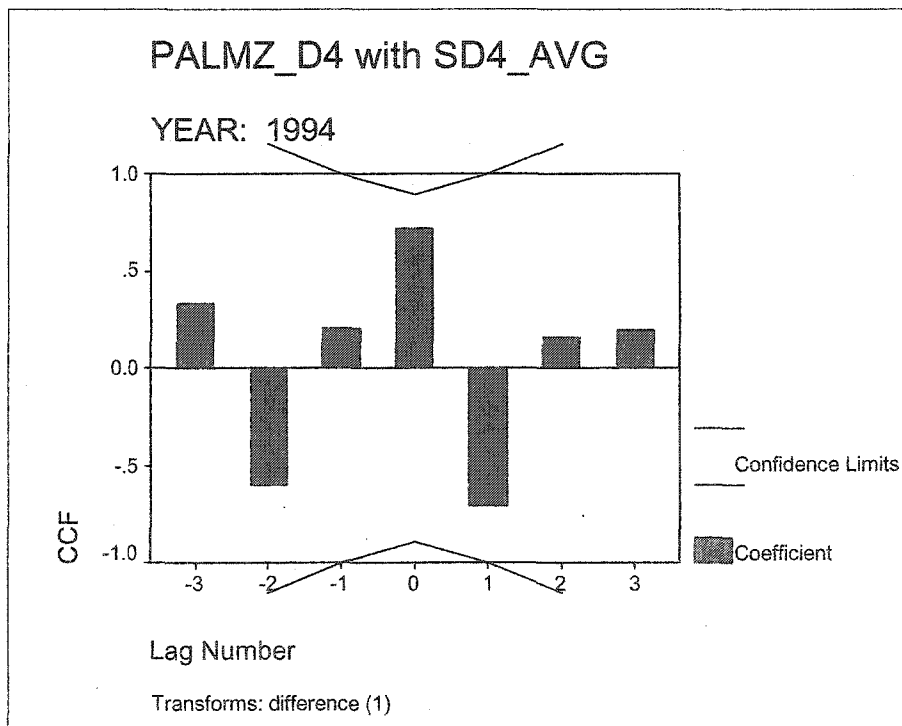
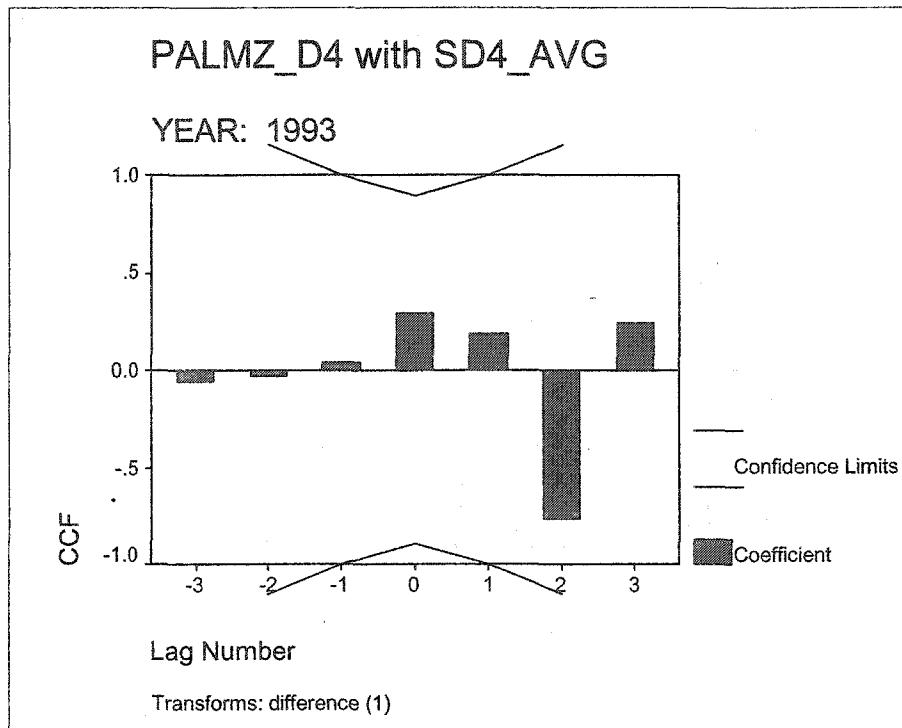


Figure A.3.d: Climate Division 4 cross-correlogram of Palmer Z and SMI, by year.
(CONTINUED).

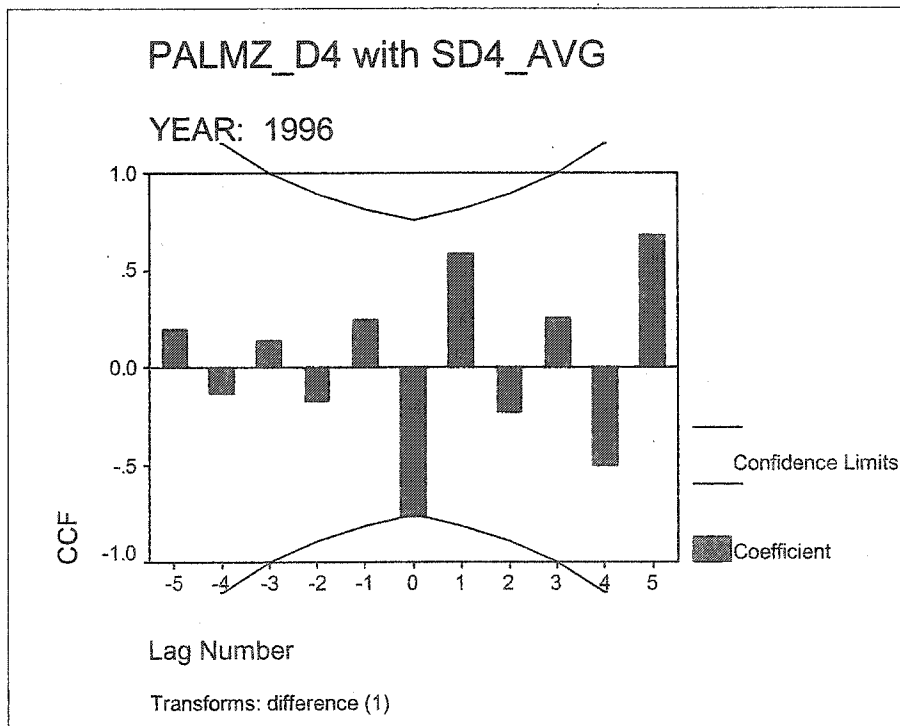
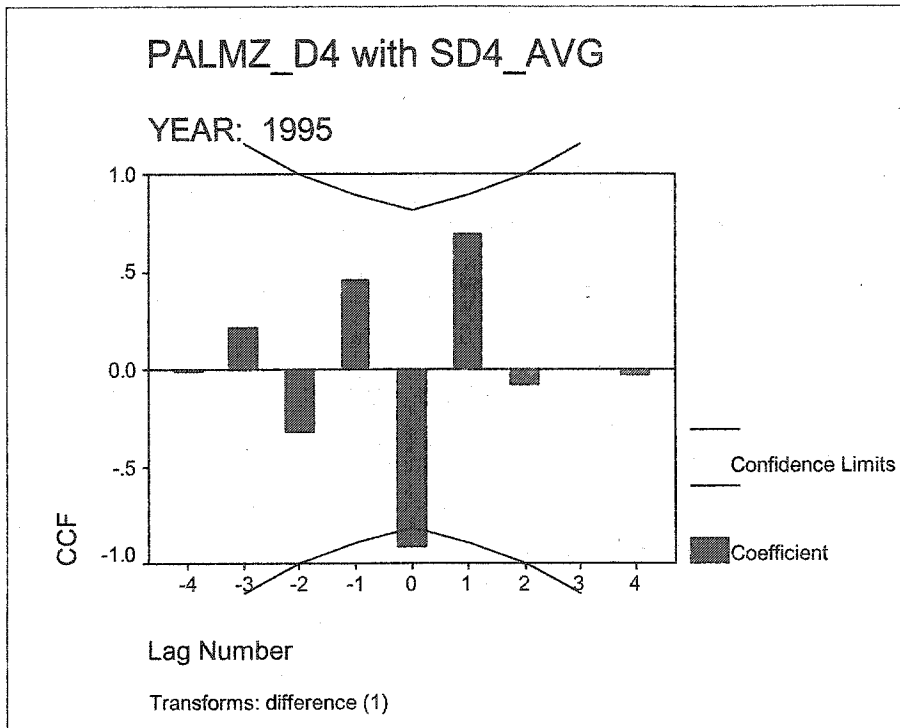


Figure A.3.d: Climate Division 4 cross-correlogram of Palmer Z and SMI, by year.
(CONTINUED).

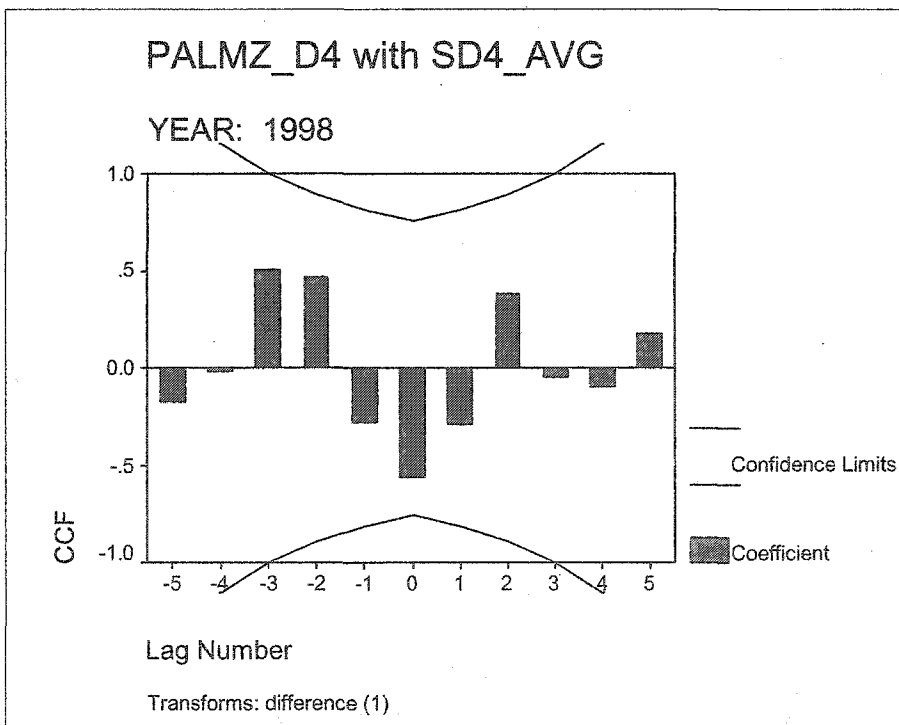
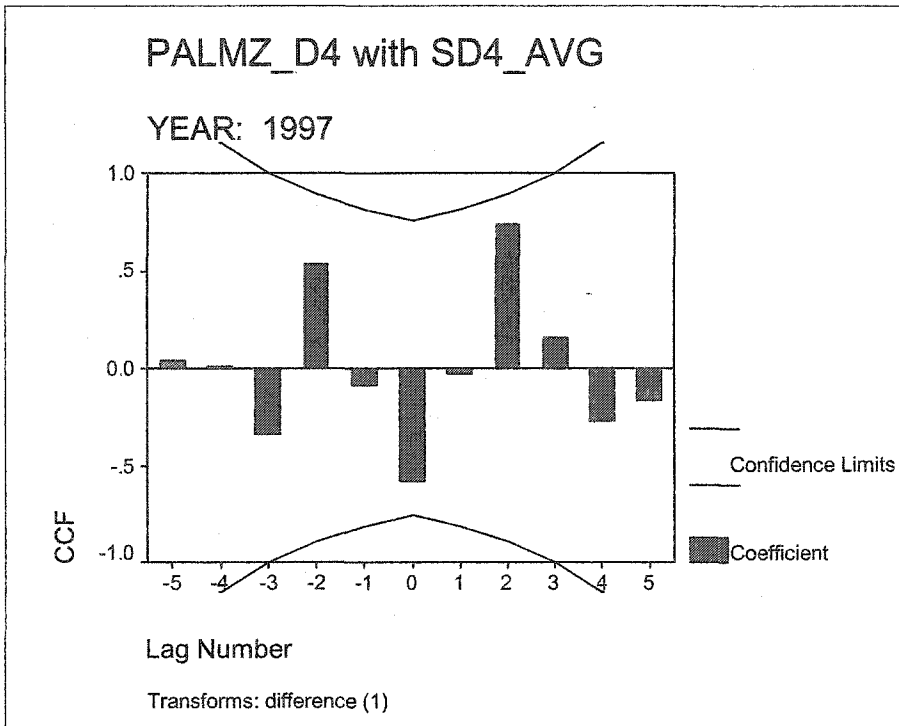


Figure A.3.d: Climate Division 4 cross-correlogram of Palmer Z and SMI, by year.
(CONTINUED).

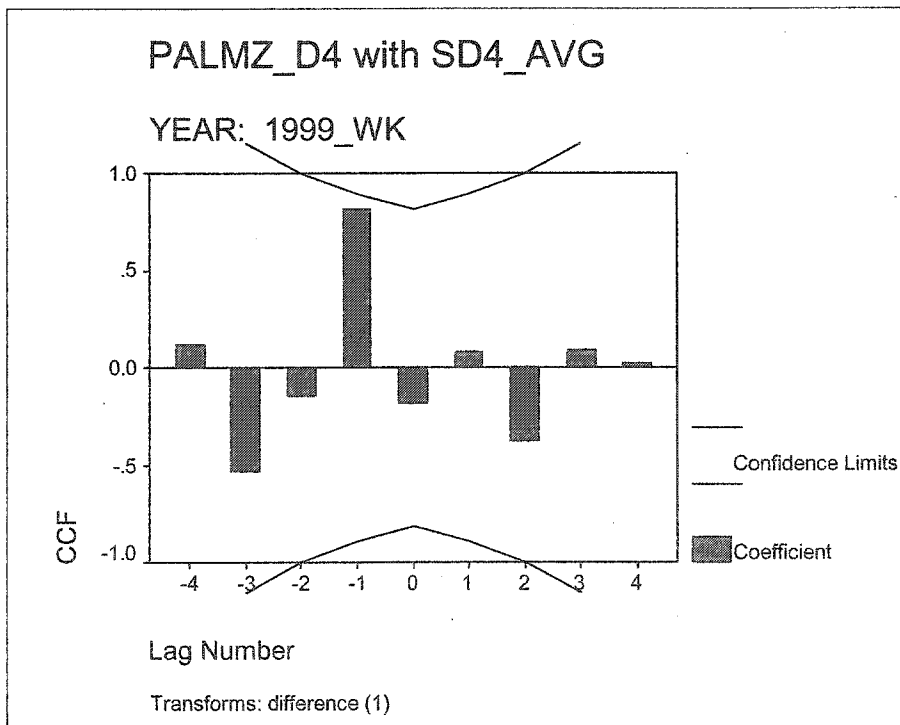
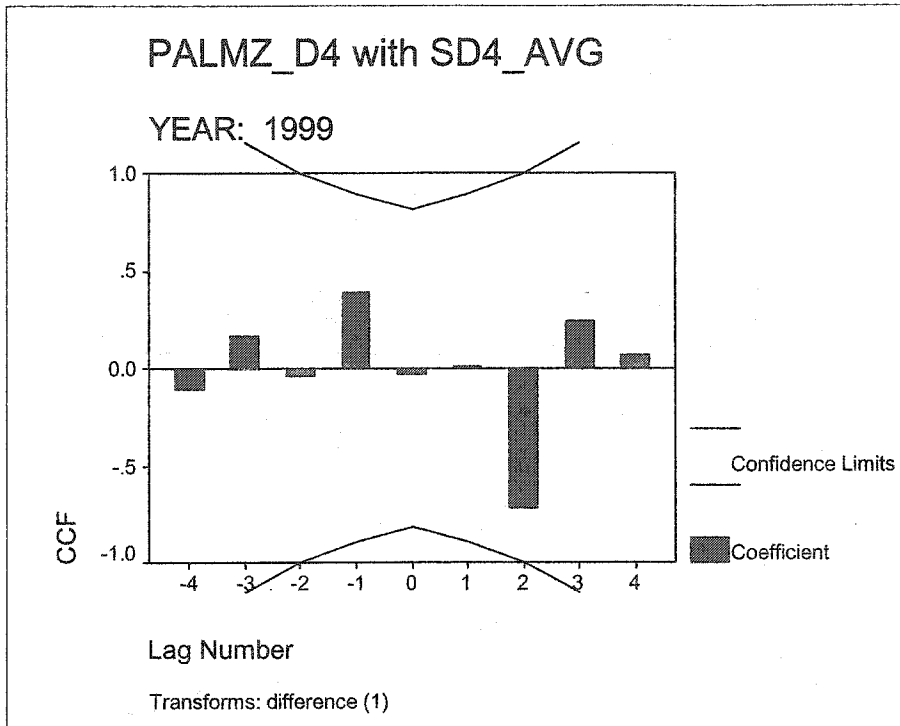


Figure A.3.d: Climate Division 4 cross-correlogram of Palmer Z and SMI, by year.
(CONTINUED).

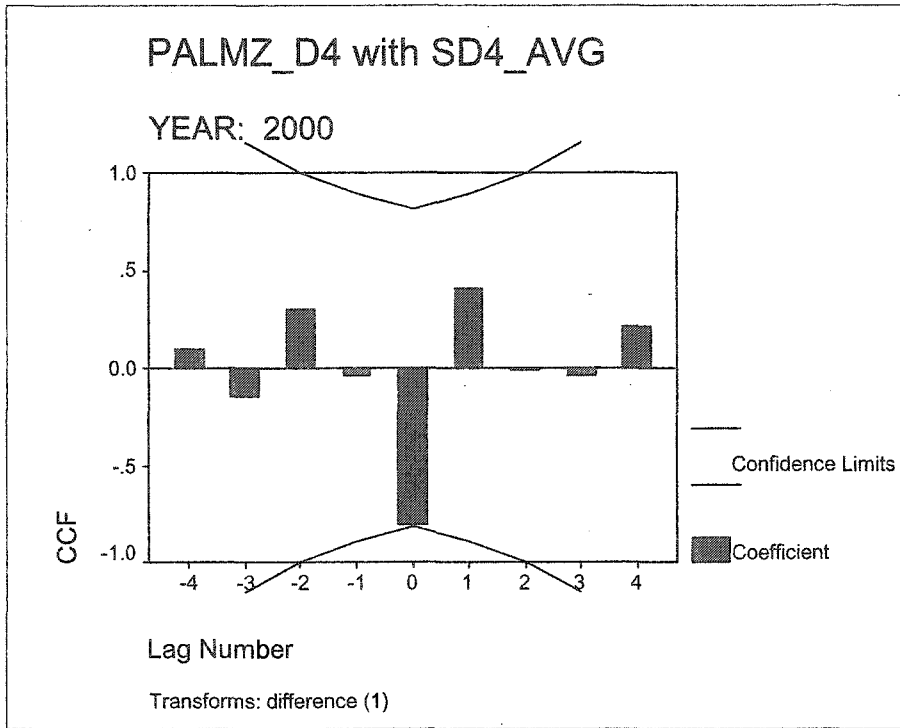


Figure A.3.e: Climate Division 5 cross-correlogram of Palmer Z and SMI, by year.

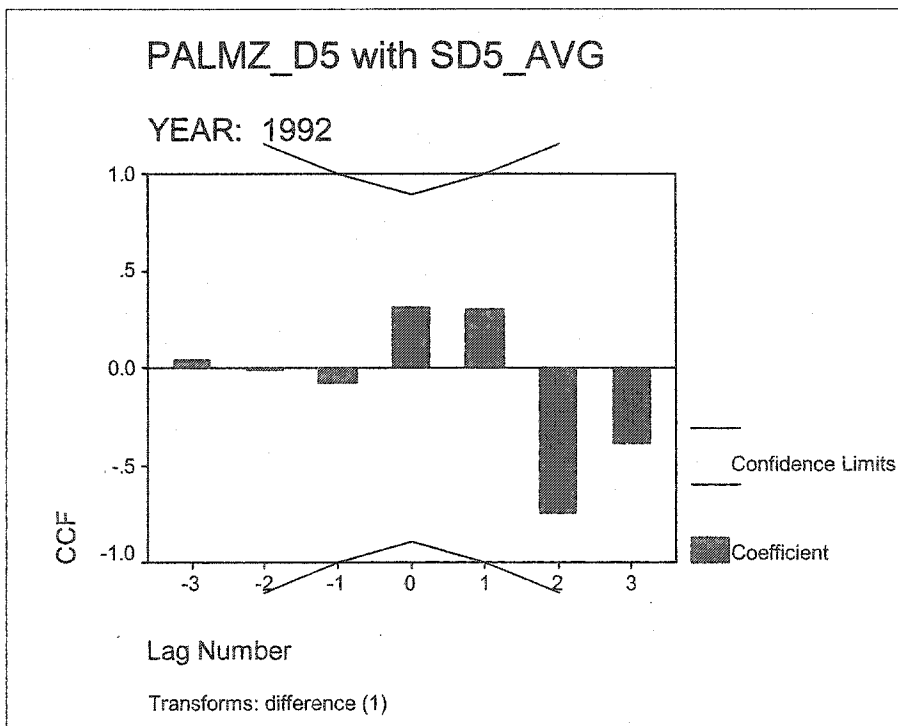
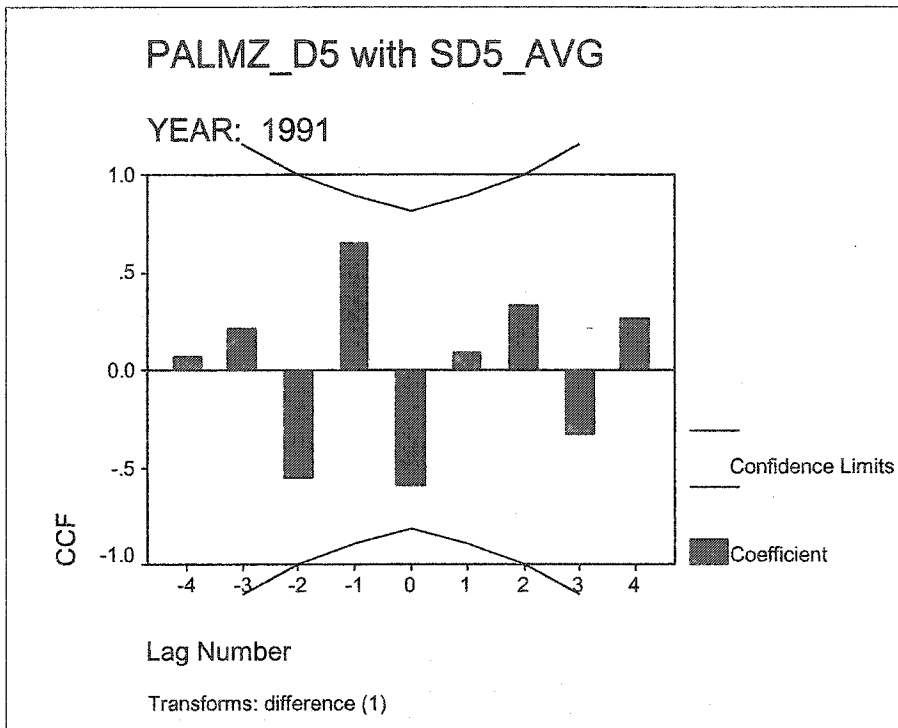


Figure A.3.e: Climate Division 5 cross-correlogram of Palmer Z and SMI, by year.
(CONTINUED)

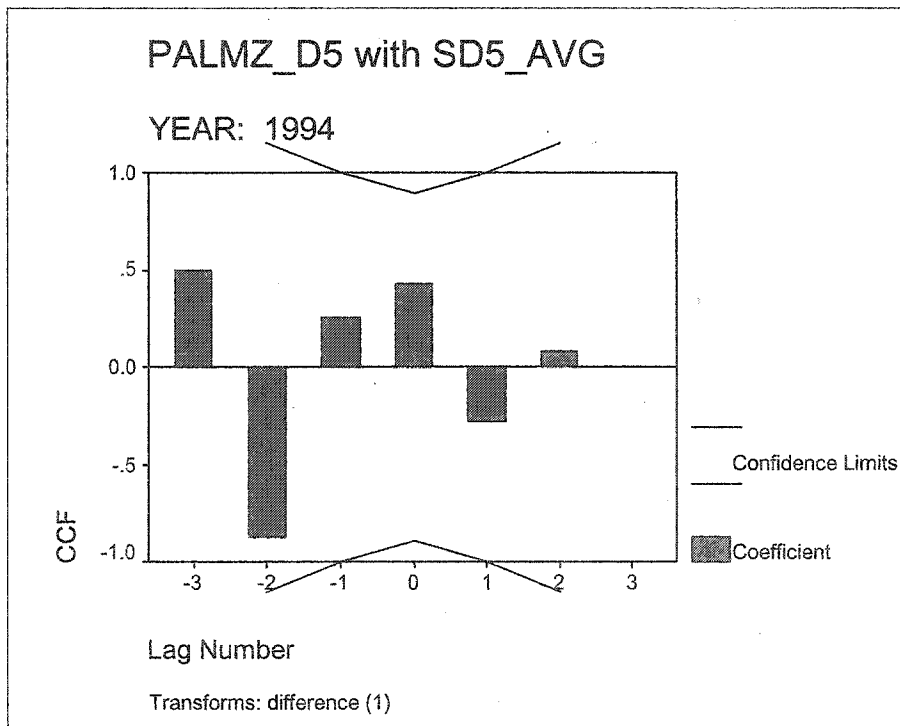
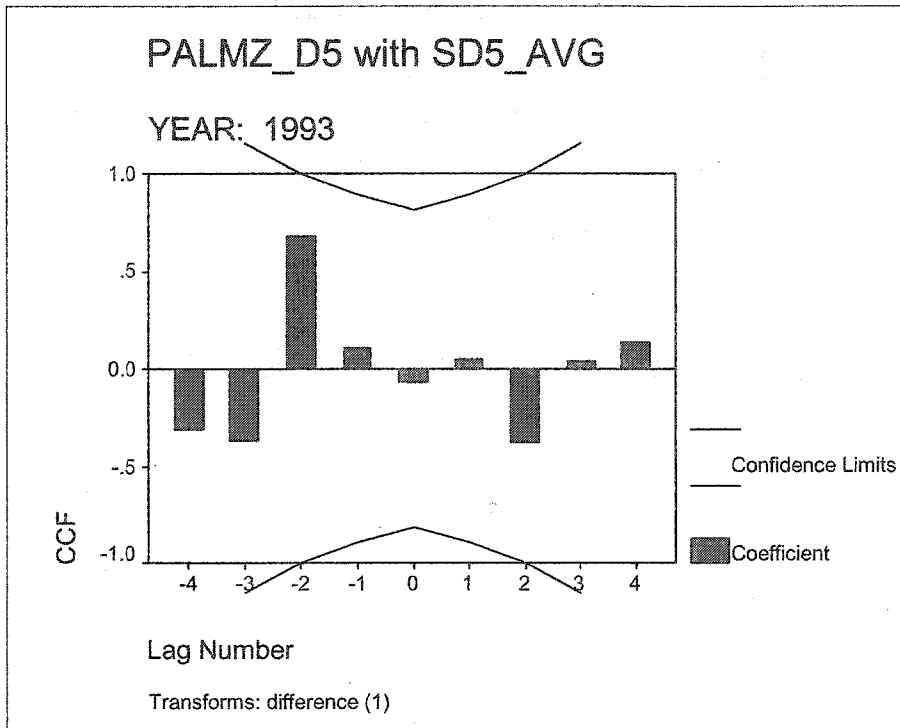


Figure A.3.e: Climate Division 5 cross-correlogram of Palmer Z and SMI, by year.
(CONTINUED)

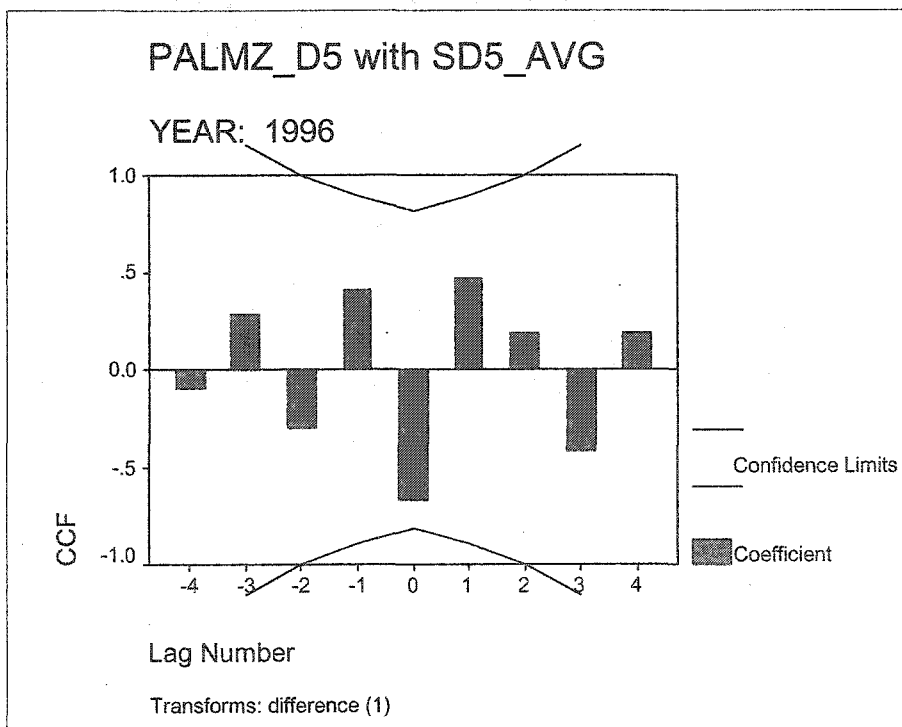
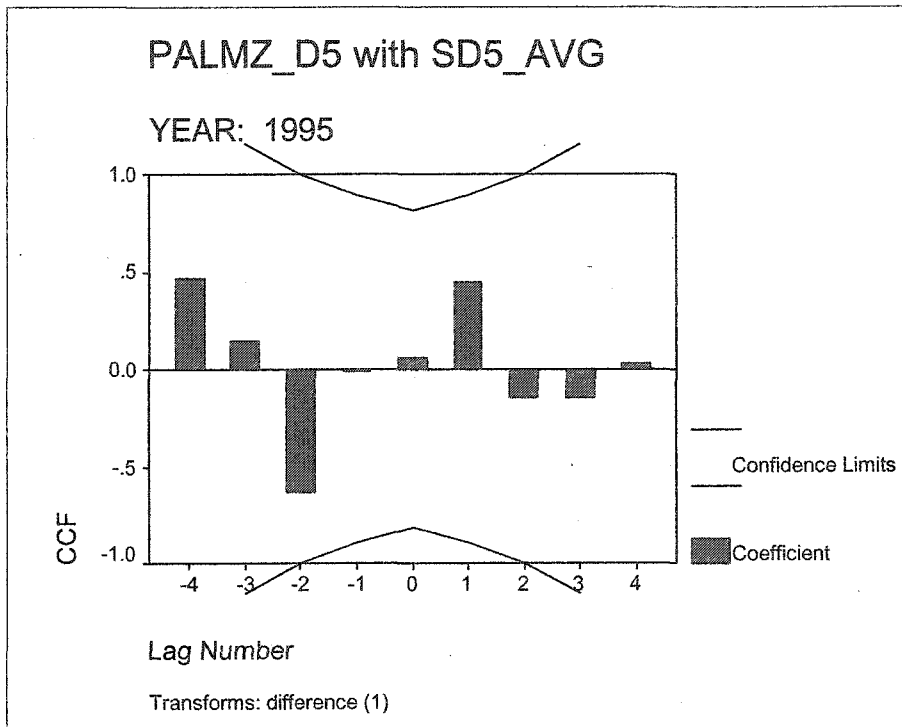


Figure A.3.e: Climate Division 5 cross-correlogram of Palmer Z and SMI, by year.
(CONTINUED)

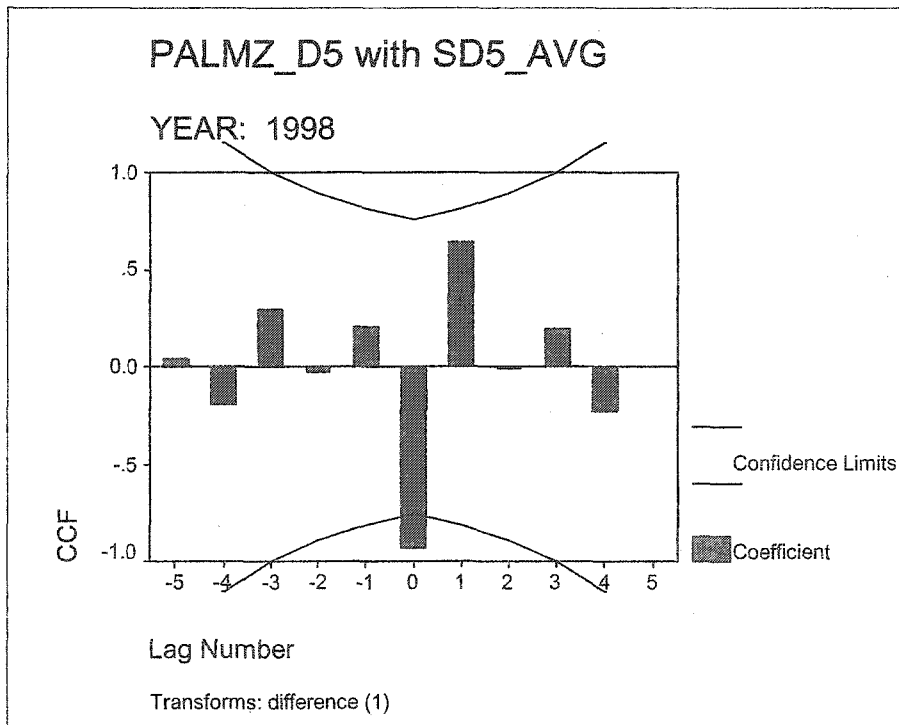
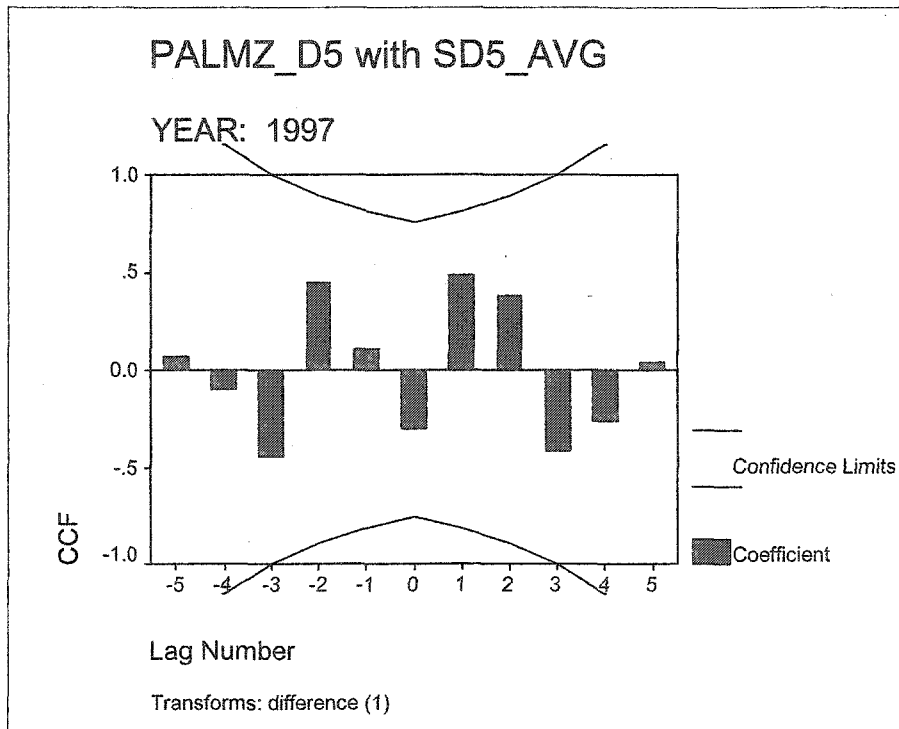


Figure A.3.e: Climate Division 5 cross-correlogram of Palmer Z and SMI, by year.
(CONTINUED)

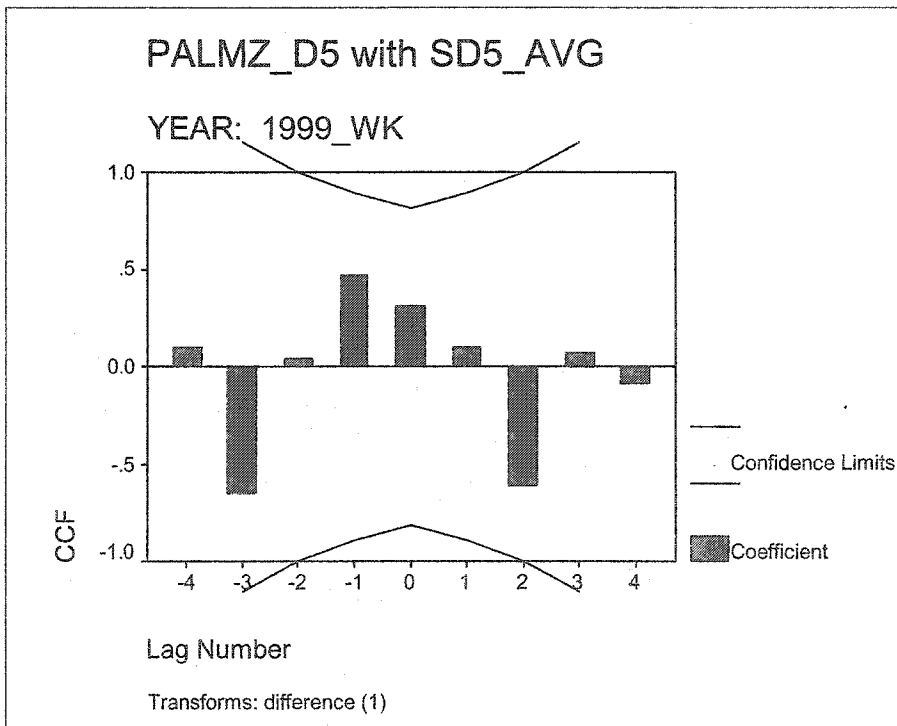
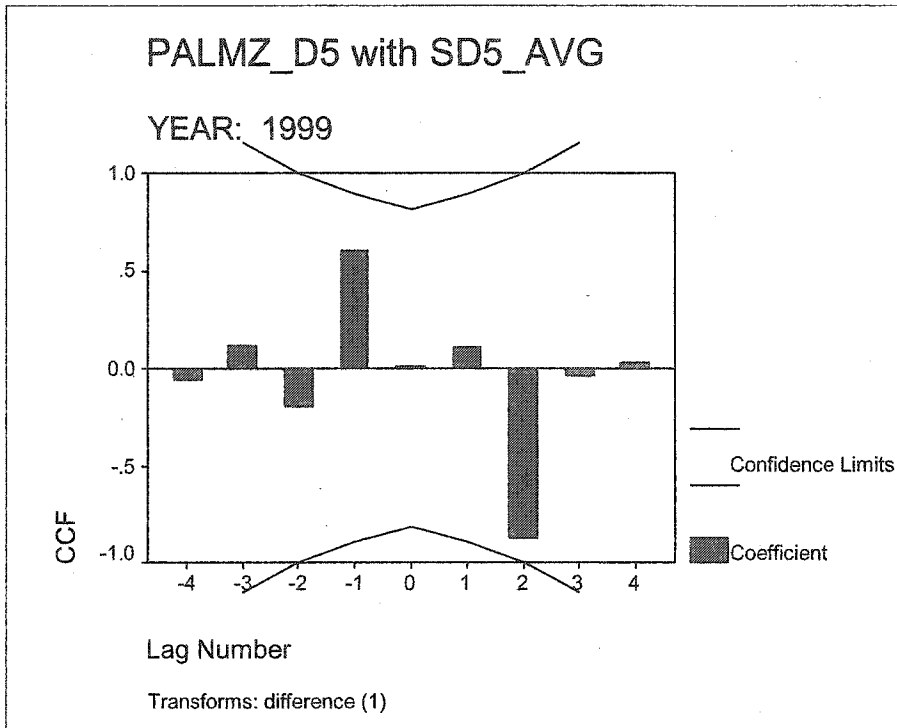


Figure A.3.e: Climate Division 5 cross-correlogram of Palmer Z and SMI, by year.
(CONTINUED)

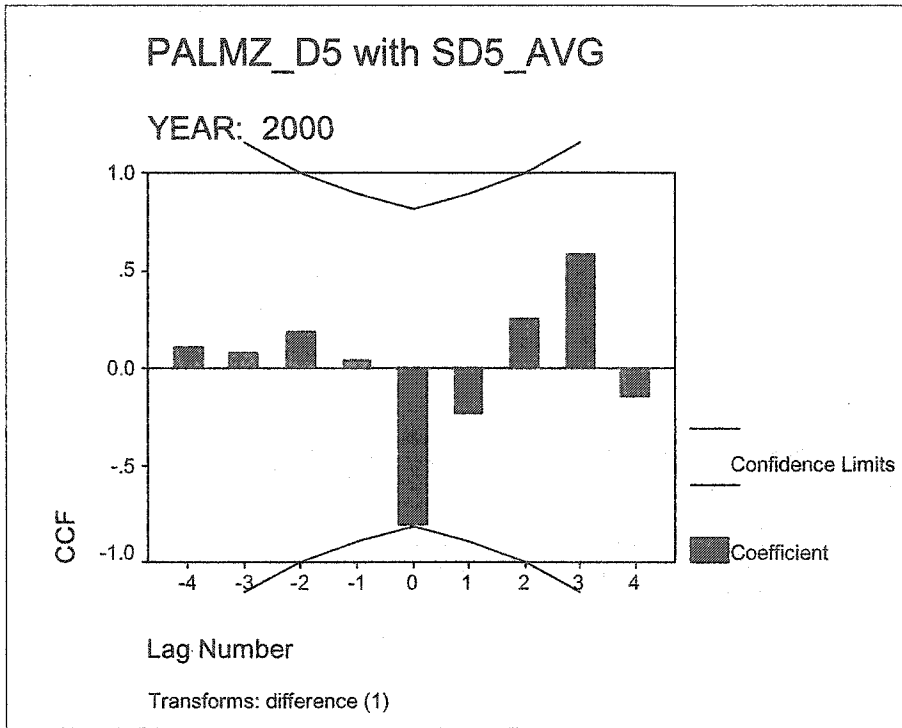


Figure A.3.f: Climate Division 6 cross-correlogram of Palmer Z and SMI, by year.

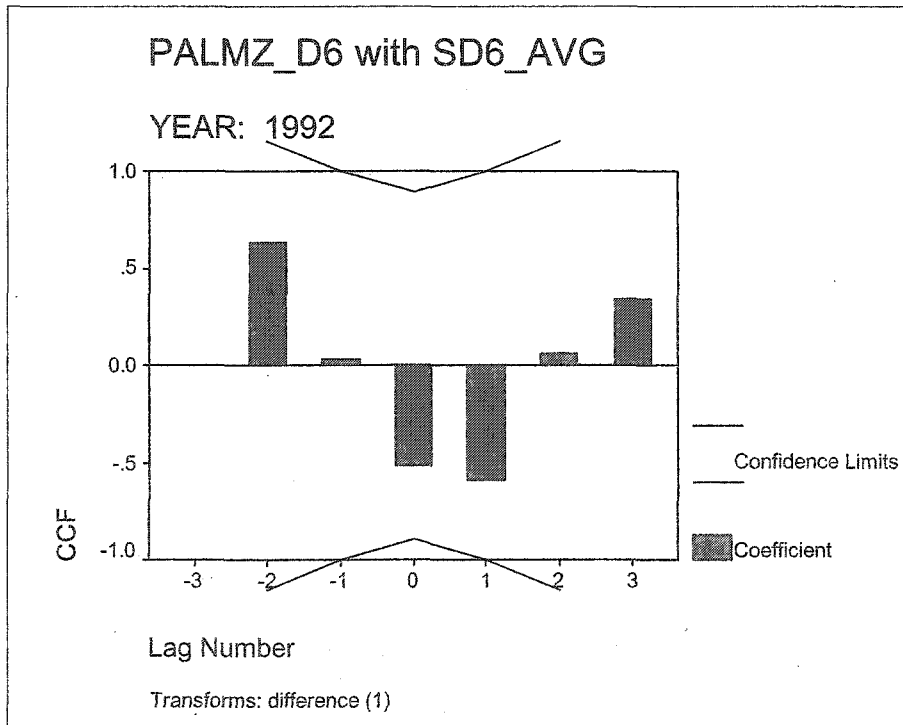
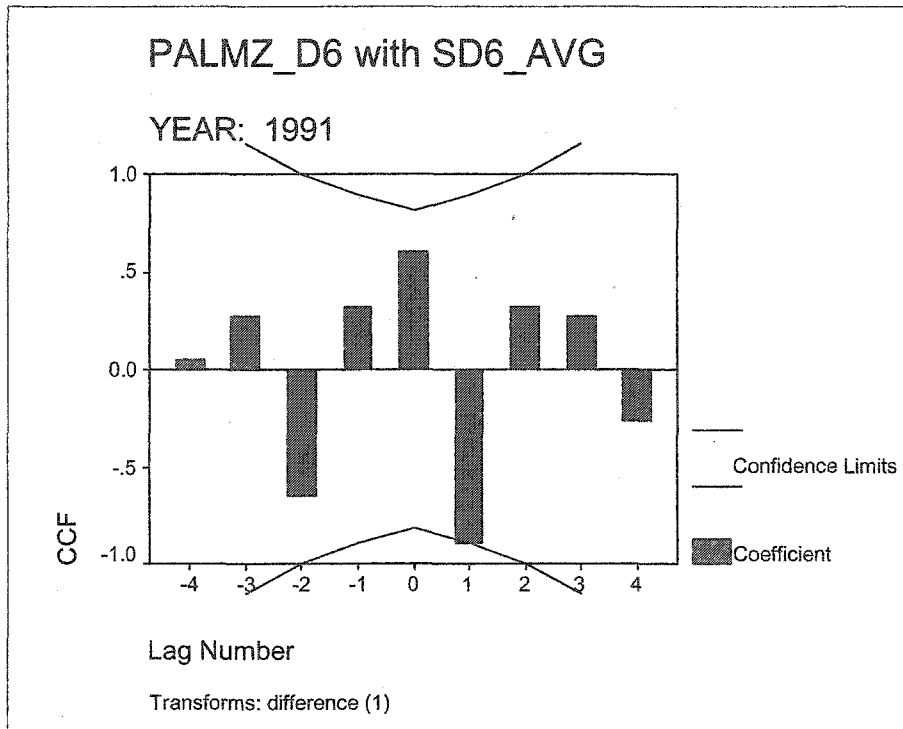


Figure A.3.f: Climate Division 6 cross-correlogram of Palmer Z and SMI, by year.
(CONTINUED)

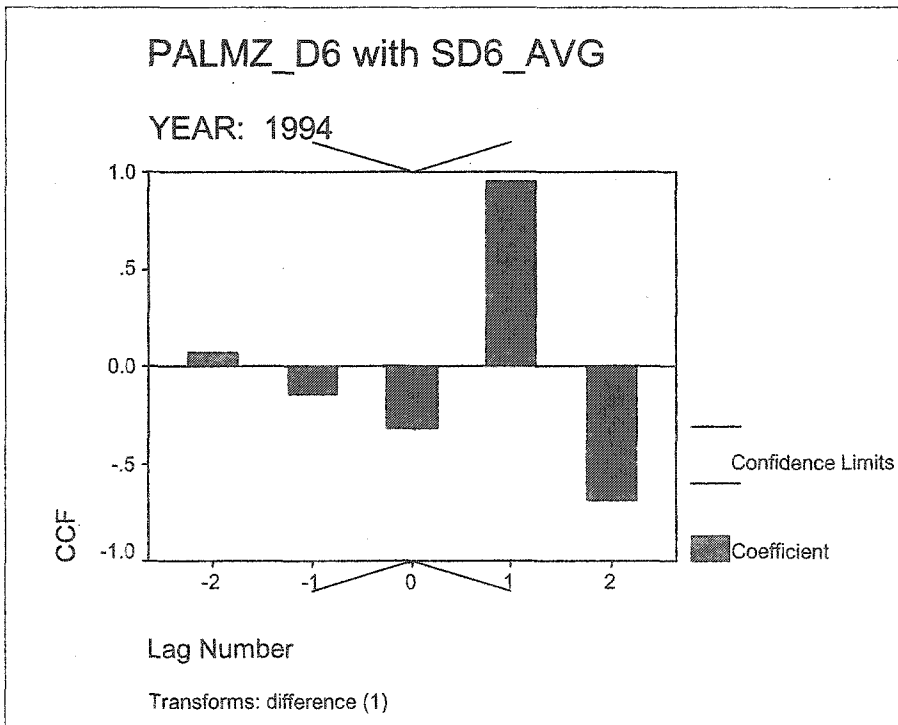
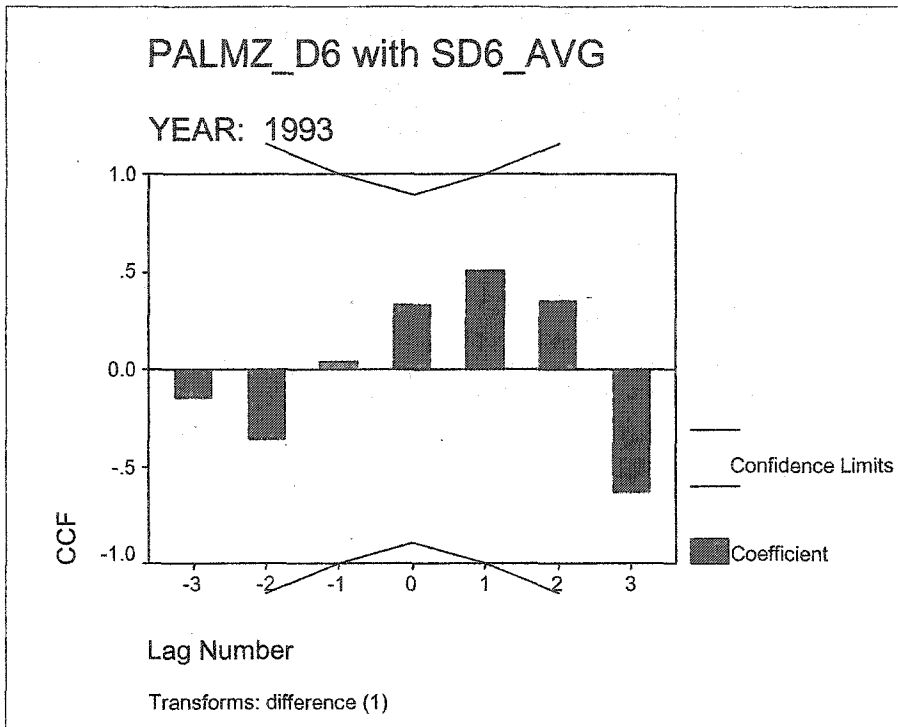


Figure A.3.f: Climate Division 6 cross-correlogram of Palmer Z and SMI, by year.
(CONTINUED)

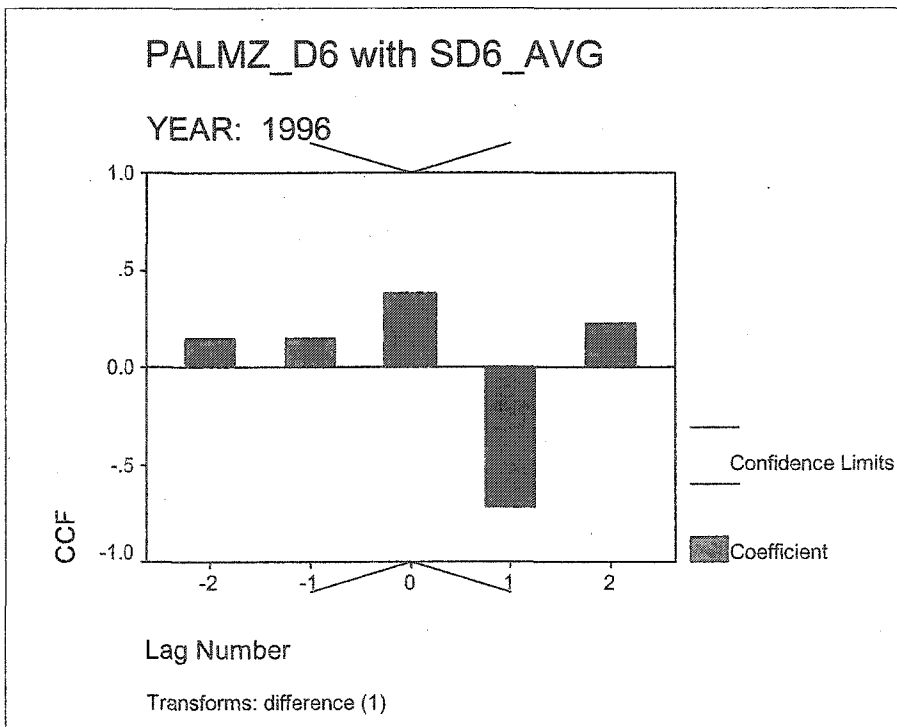
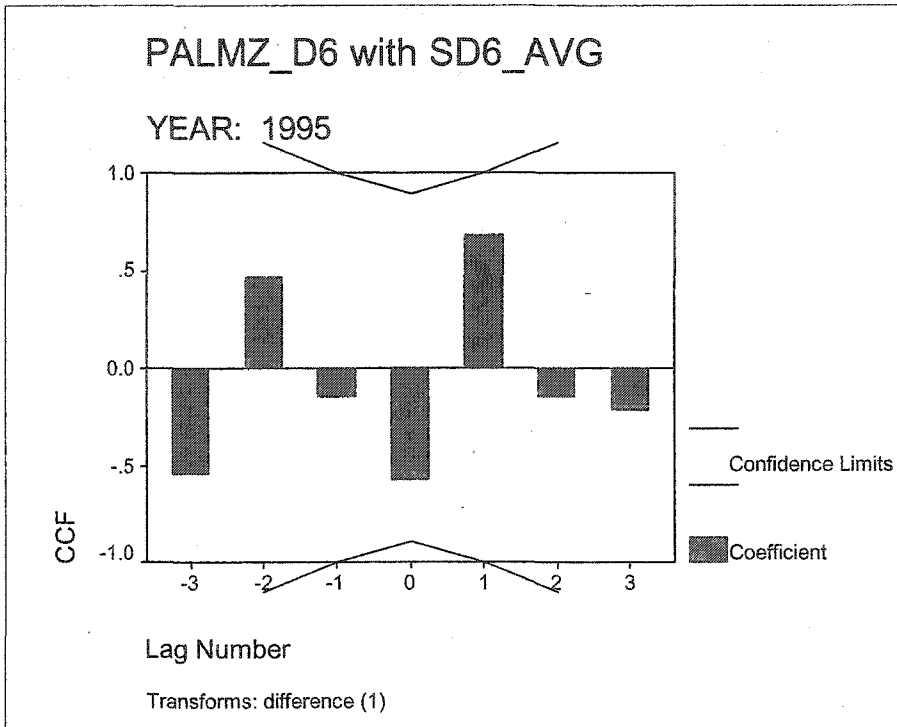


Figure A.3.f: Climate Division 6 cross-correlogram of Palmer Z and SMI, by year.
(CONTINUED)

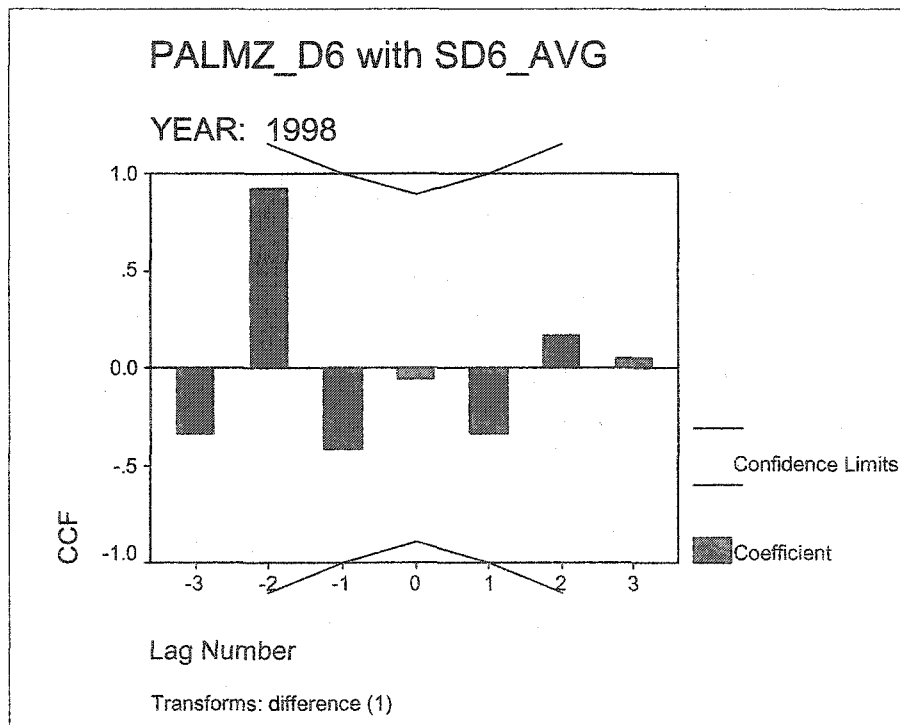
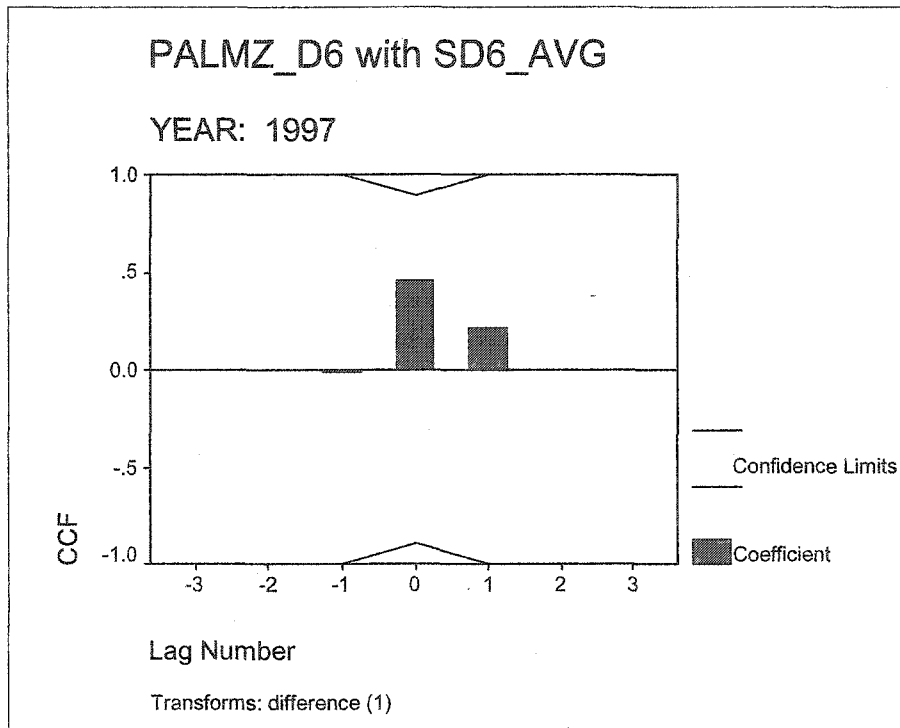


Figure A.3.f: Climate Division 6 cross-correlogram of Palmer Z and SMI, by year.
(CONTINUED)

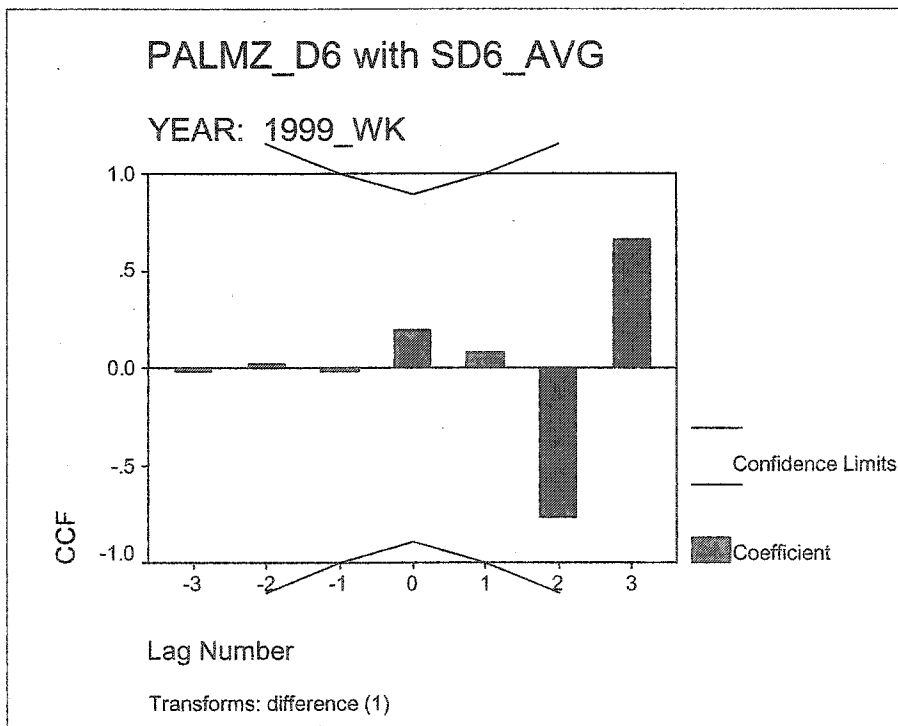
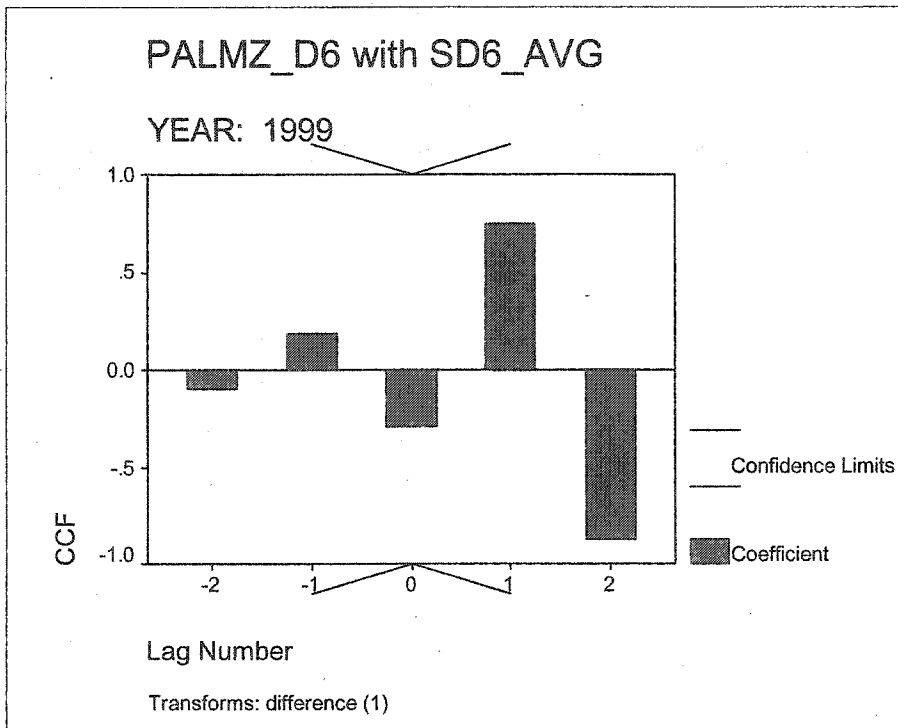


Figure A.3.f: Climate Division 6 cross-correlogram of Palmer Z and SMI, by year.
(CONTINUED)

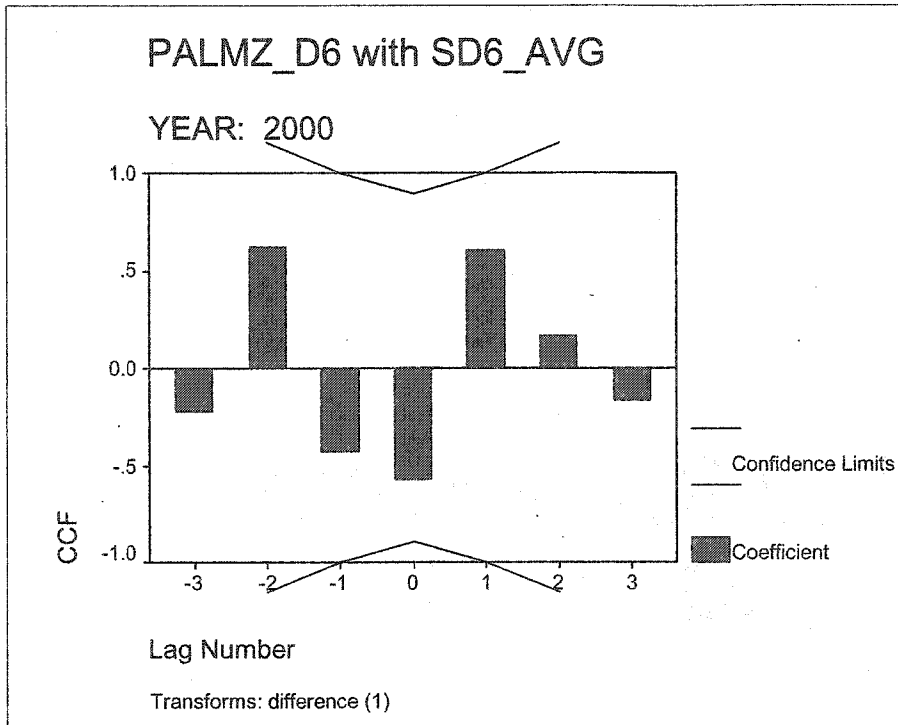


Figure A.3.g: Climate Division 7 cross-correlogram of Palmer Z and SMI, by year.

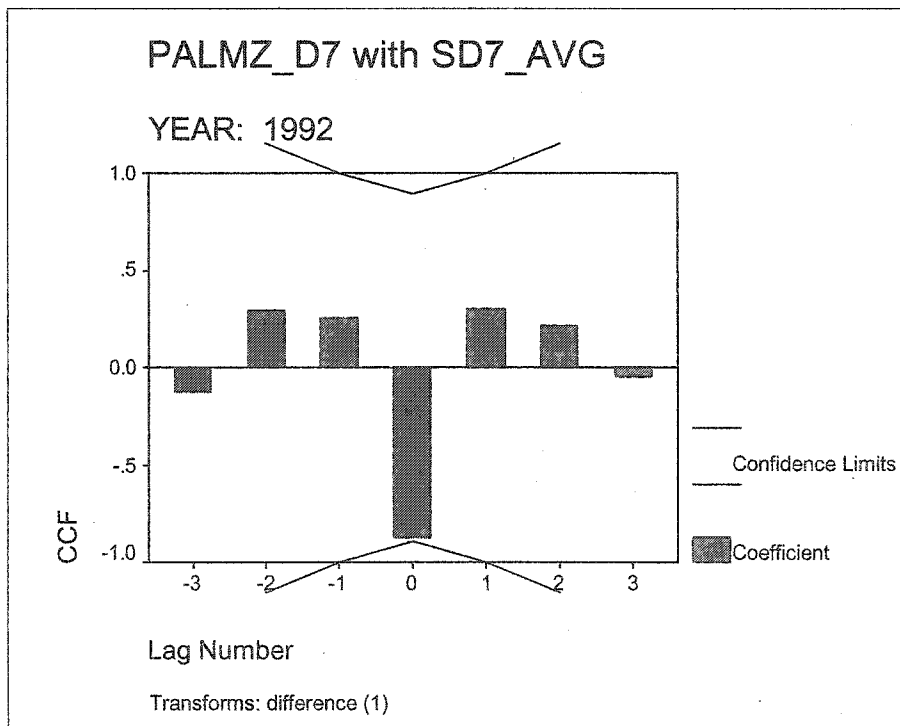
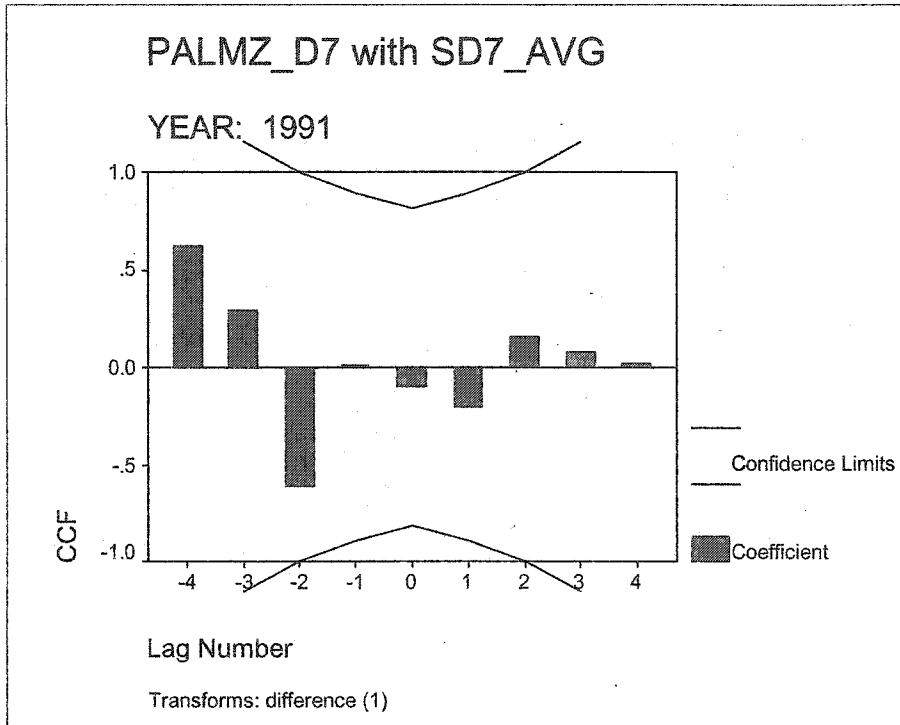


Figure A.3.g: Climate Division 7 cross-correlogram of Palmer Z and SMI, by year.
(CONTINUED)

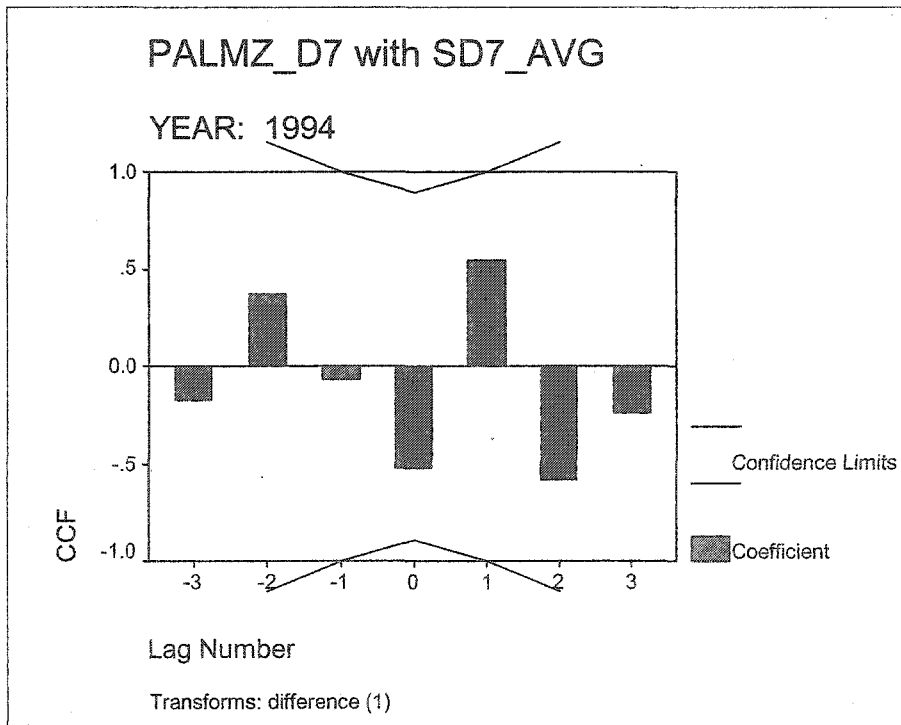
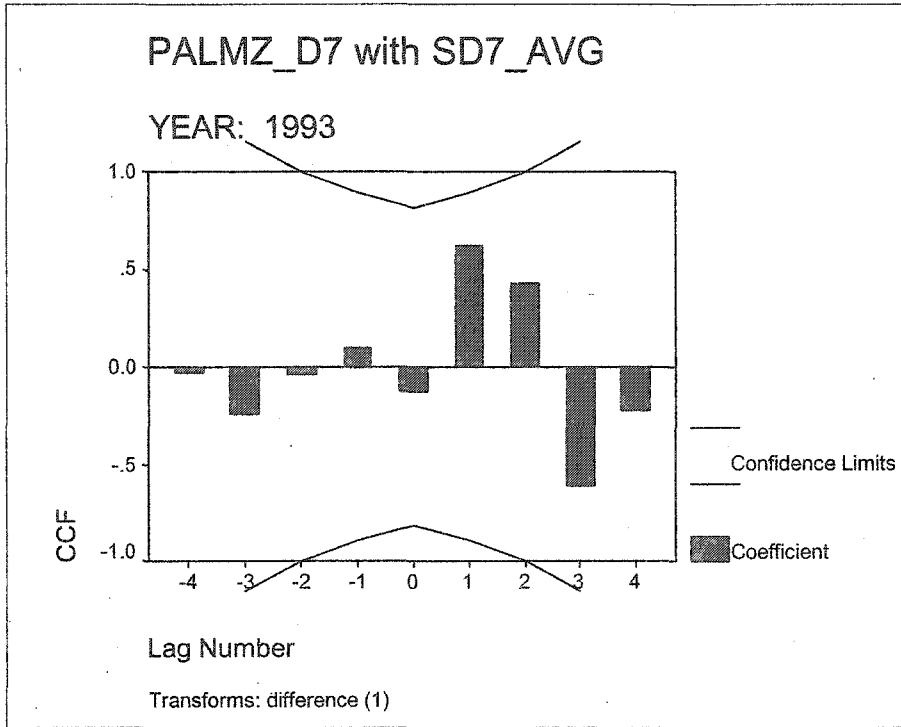


Figure A.3.g: Climate Division 7 cross-correlogram of Palmer Z and SML, by year.
(CONTINUED)

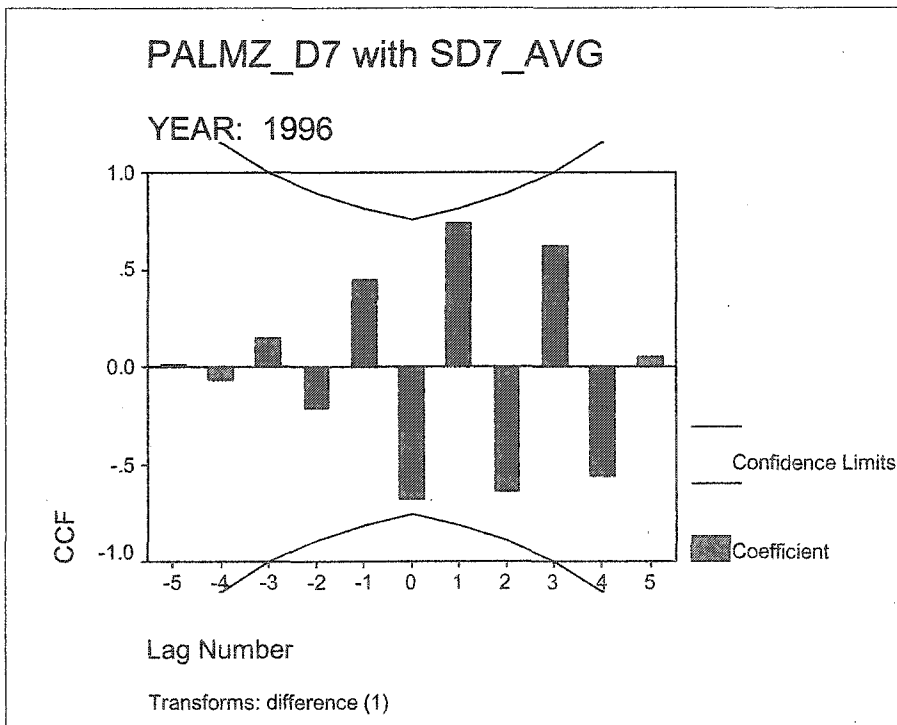
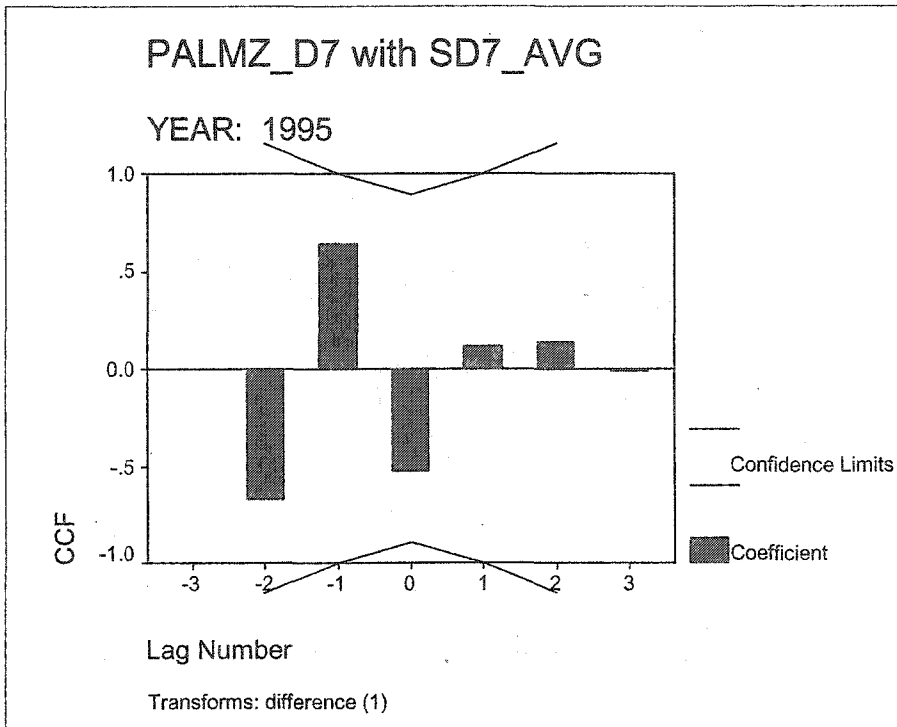


Figure A.3.g: Climate Division 7 cross-correlogram of Palmer Z and SMI, by year.
(CONTINUED)

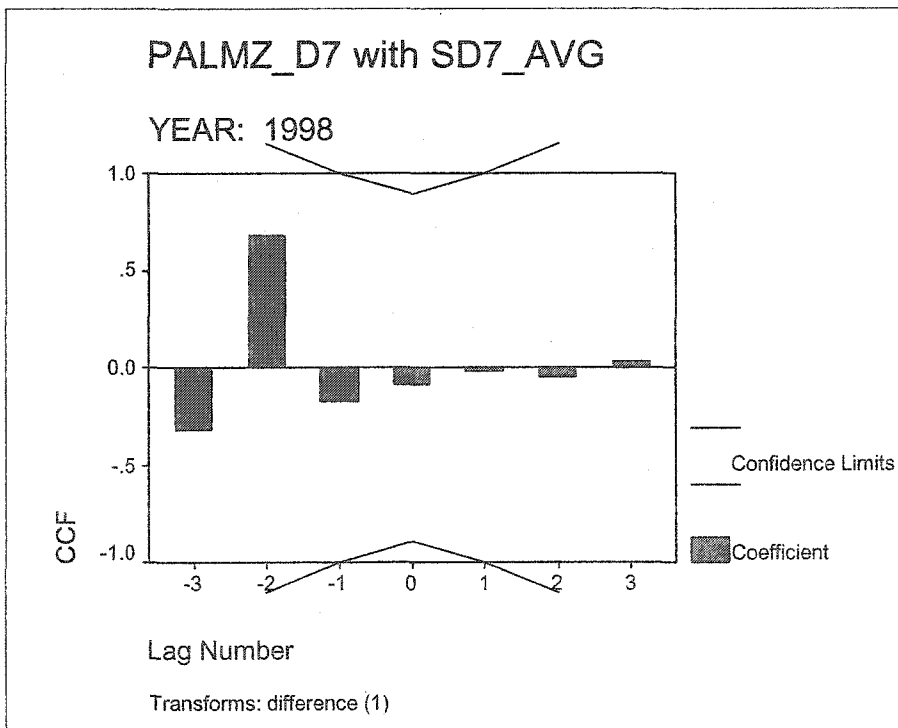
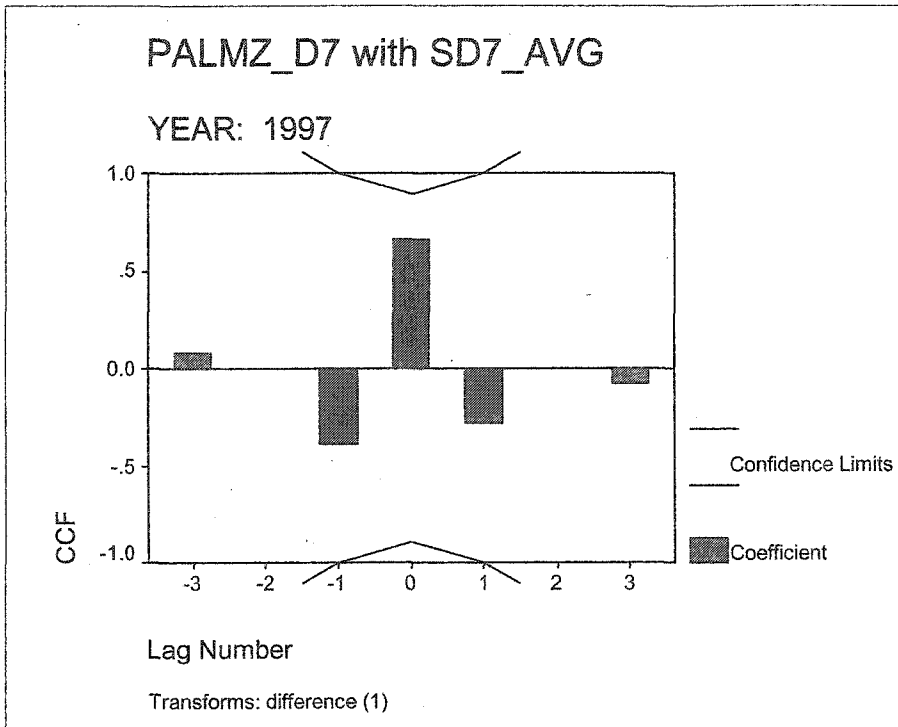


Figure A.3.g: Climate Division 7 cross-correlogram of Palmer Z and SMI, by year.
(CONTINUED)

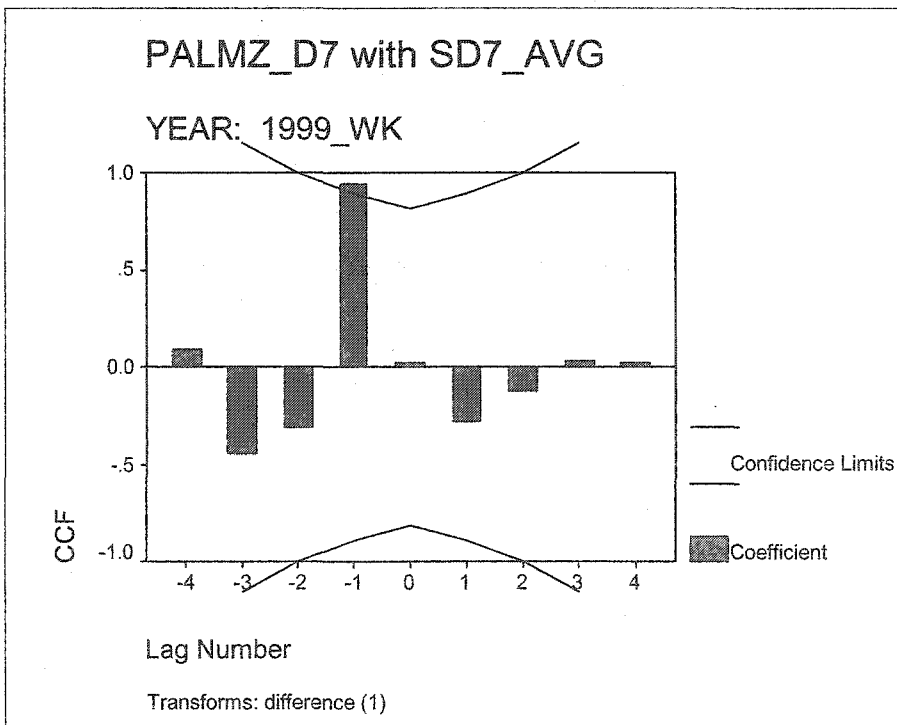
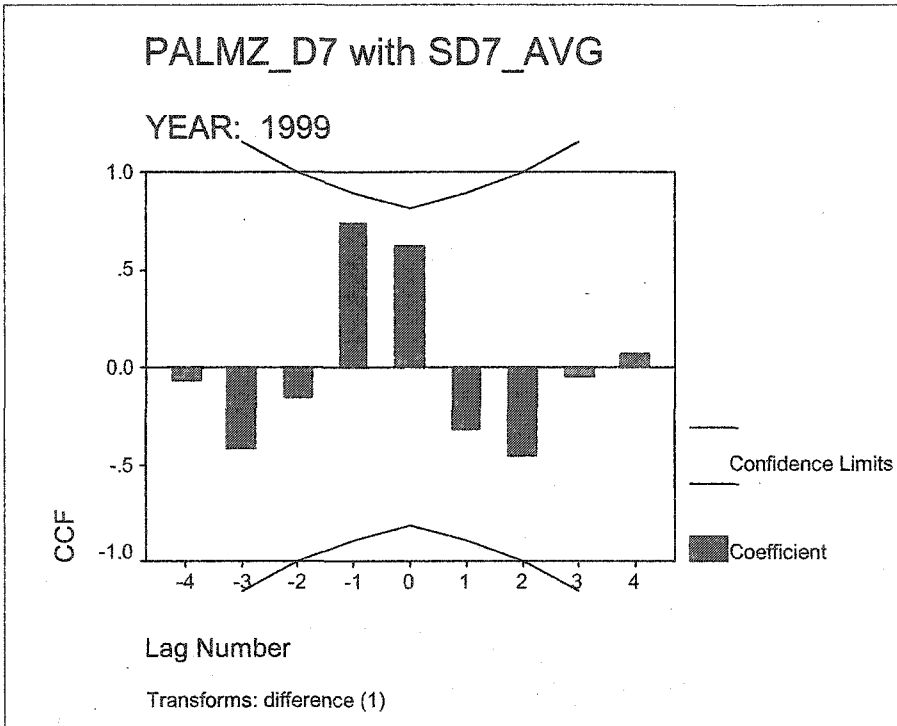


Figure A.3.g: Climate Division 7 cross-correlogram of Palmer Z and SMI, by year.
(CONTINUED)

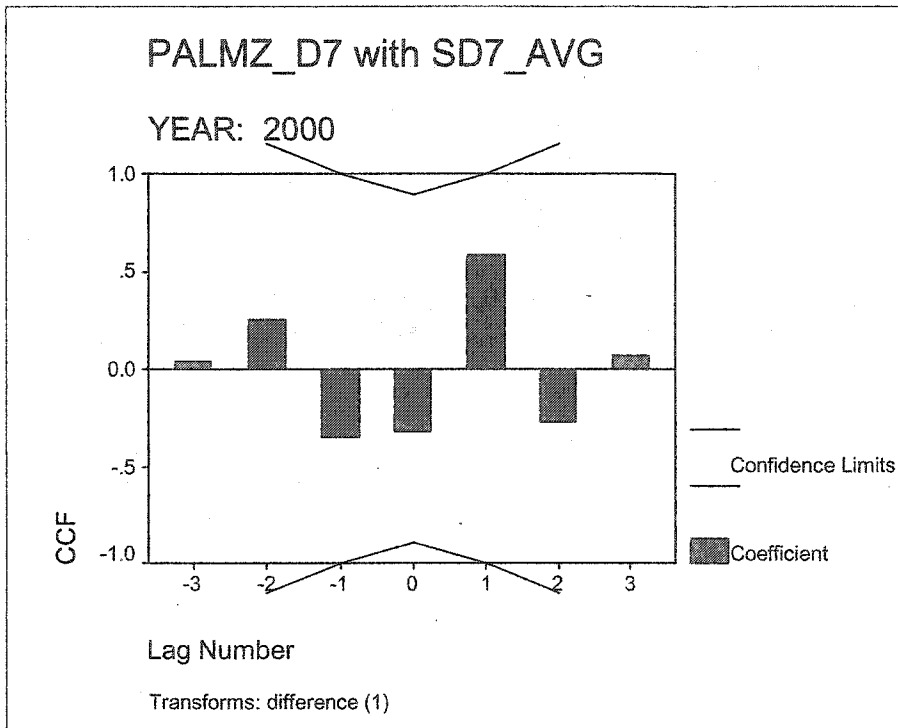


Figure A.4: Palmer Z and predicted Palmer Z (from SMI) for all divisions. Gaps in predicted sequences denote removed years. Line breaks denote year steps.

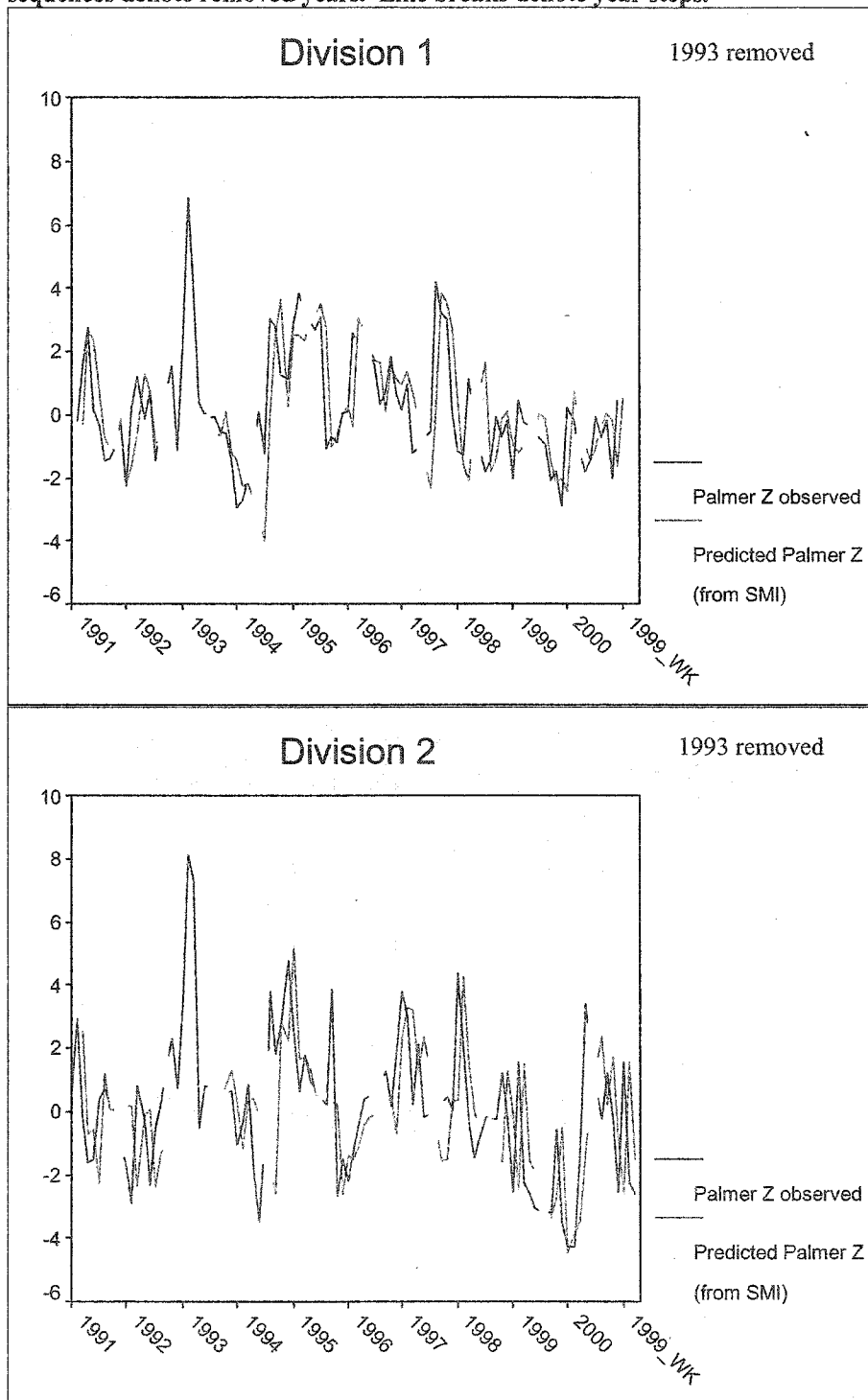


Figure A.4: (CONTINUED)

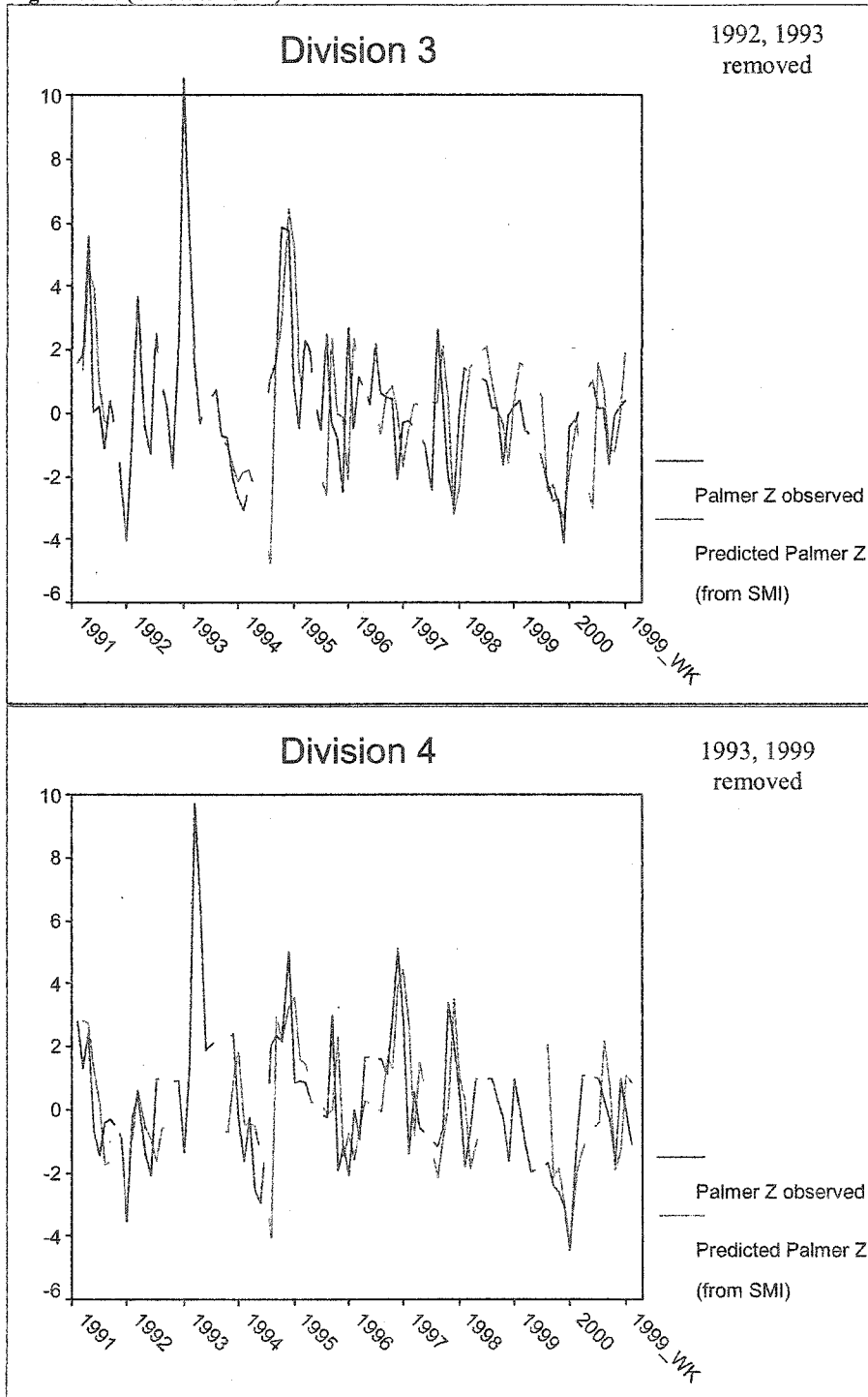


Figure A.4: (CONTINUED)

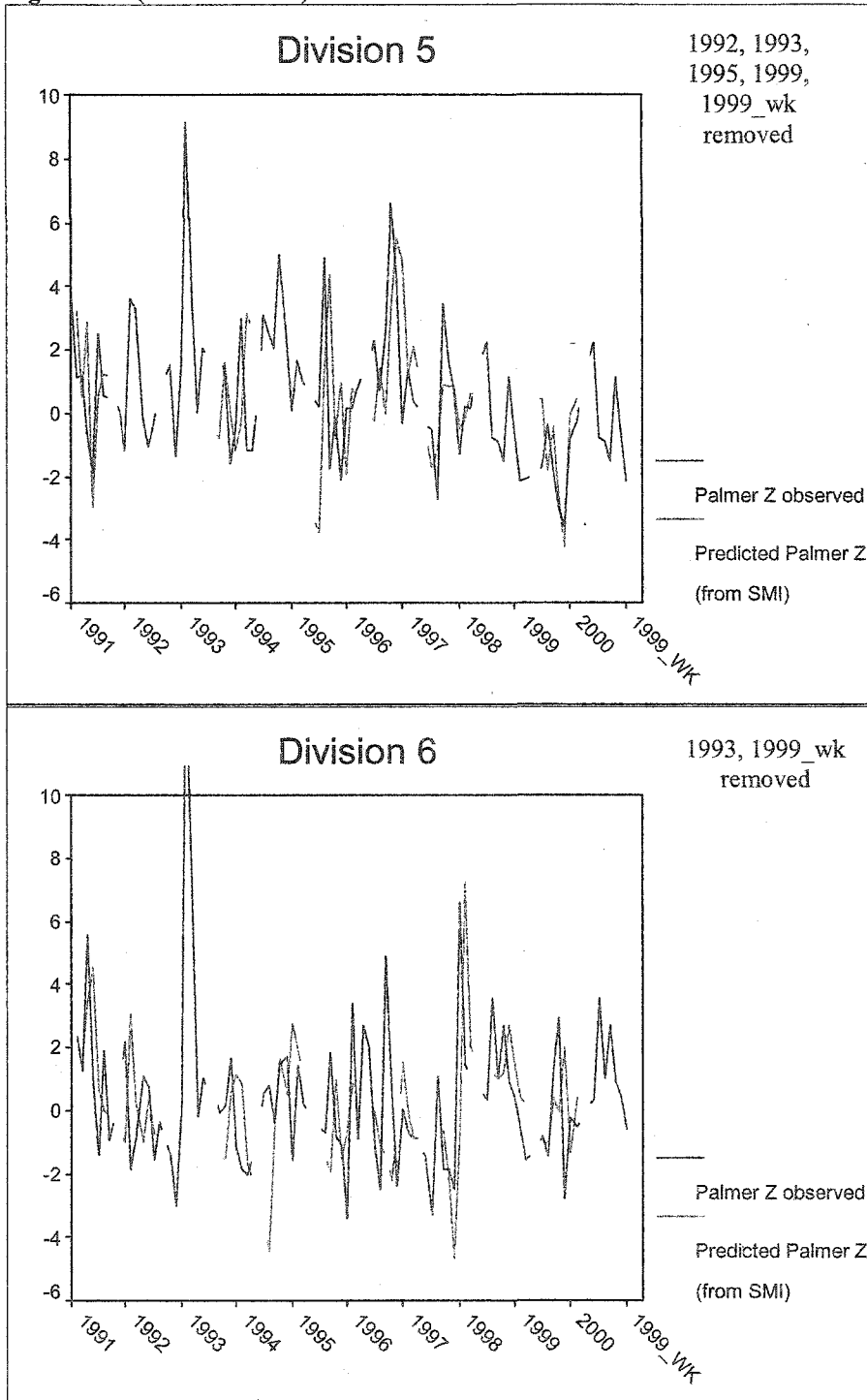


Figure A.4: (CONTINUED)

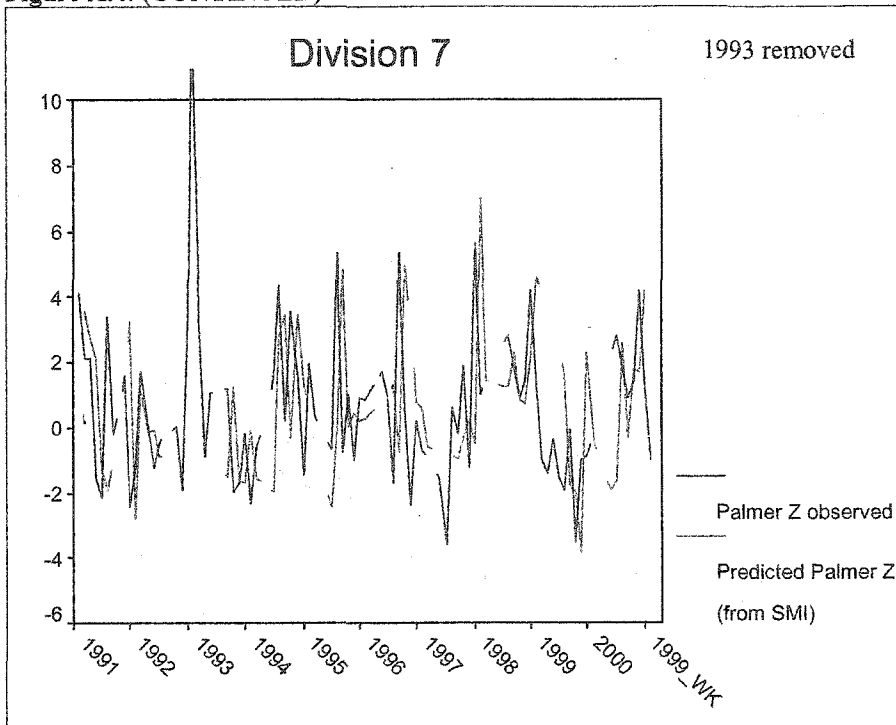


Figure A.5: P-P plots of ARIMA residuals by state climate division.

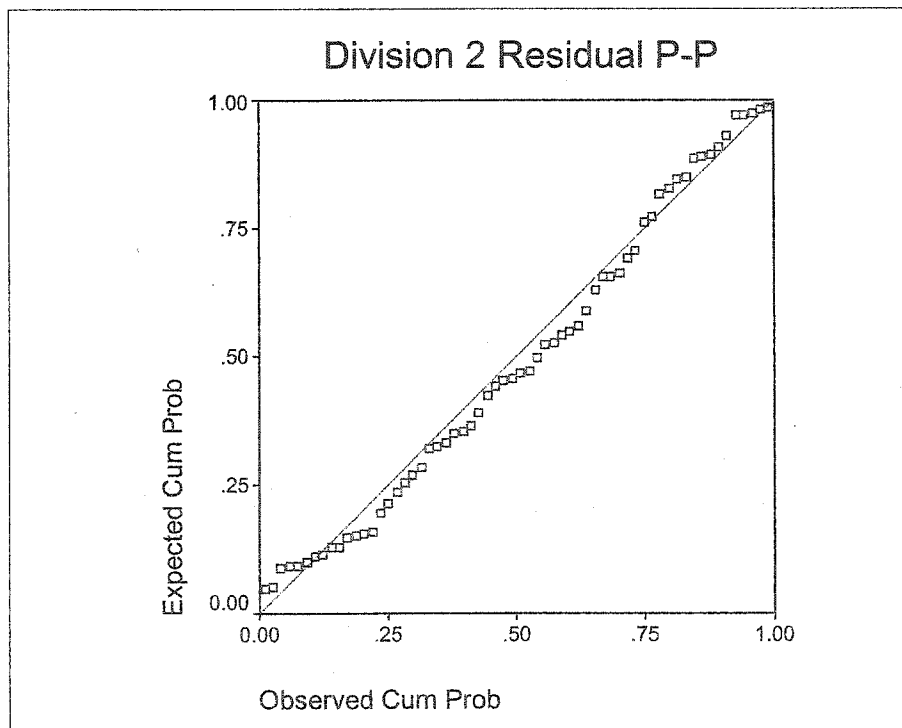
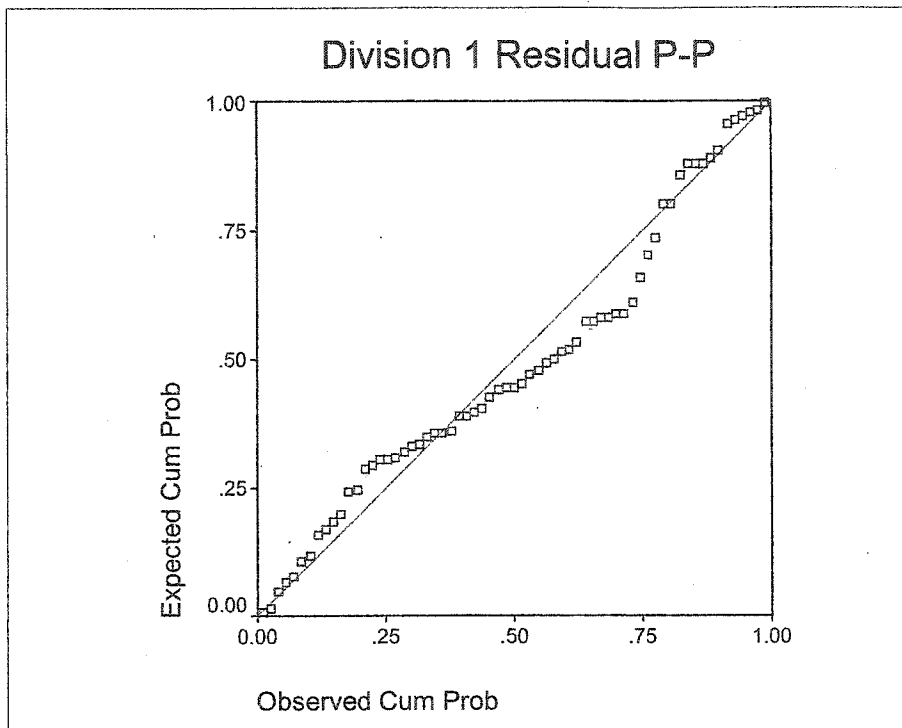


Figure A.5: P-P plots of ARIMA residuals by state climate division (CONTINUED).

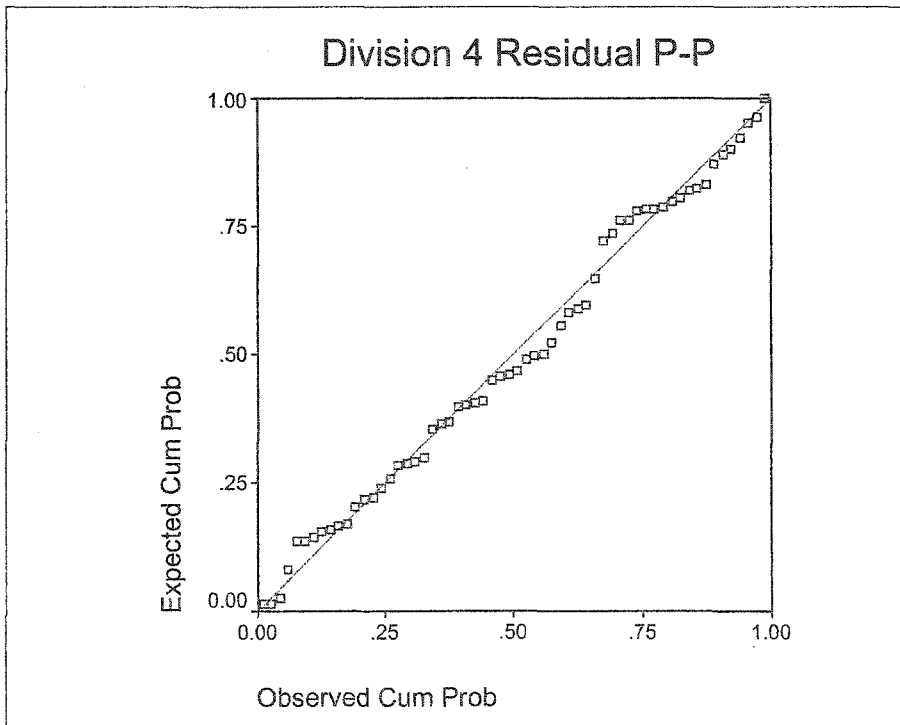
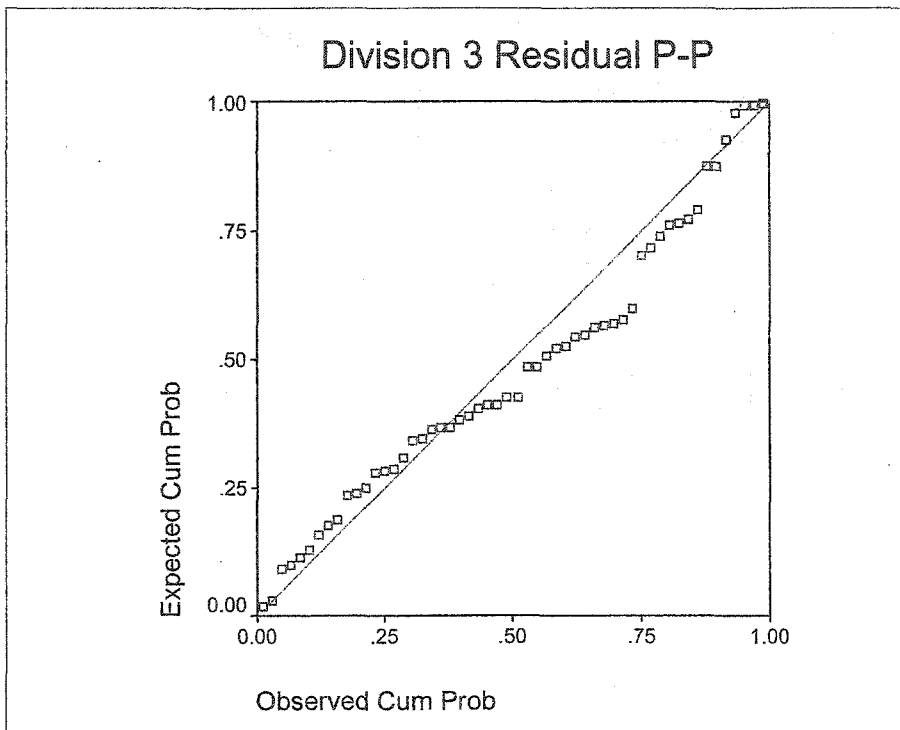


Figure A.5: P-P plots of ARIMA residuals by state climate division (CONTINUED).

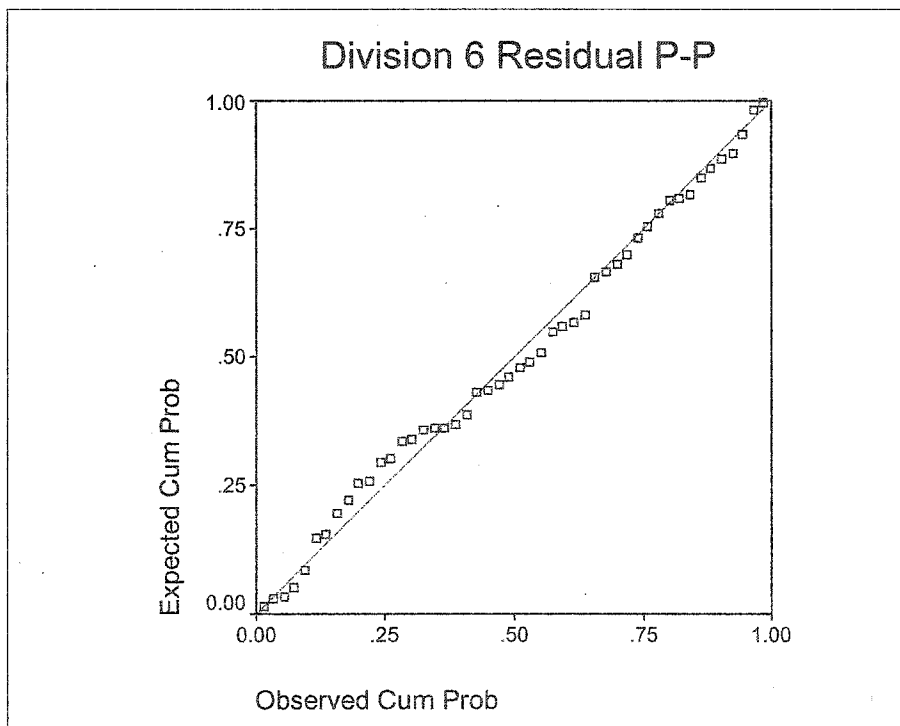
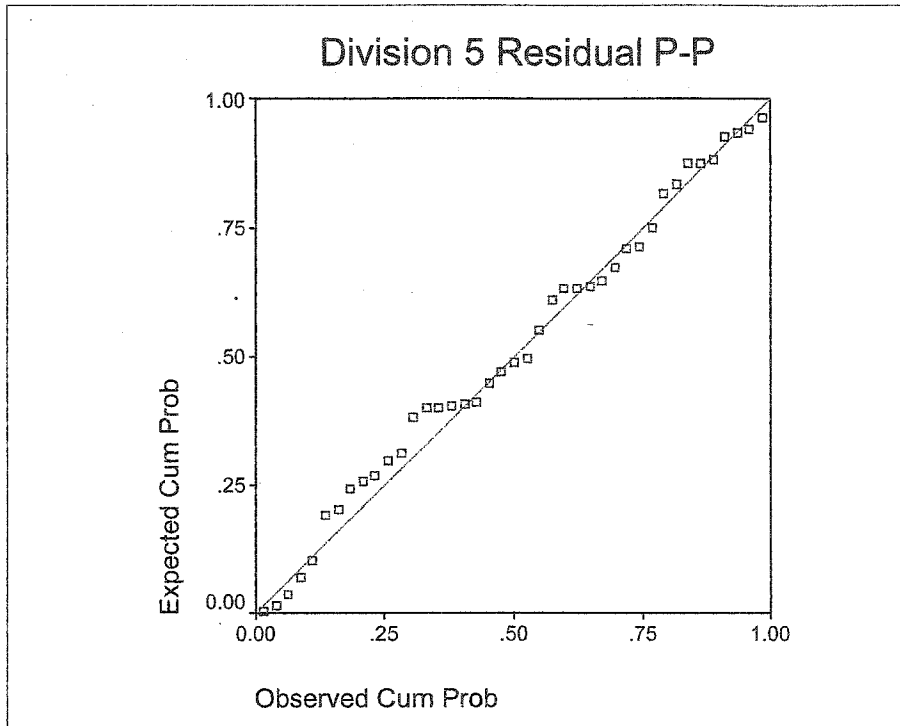


Figure A.5: P-P plots of ARIMA residuals by state climate division (CONTINUED).

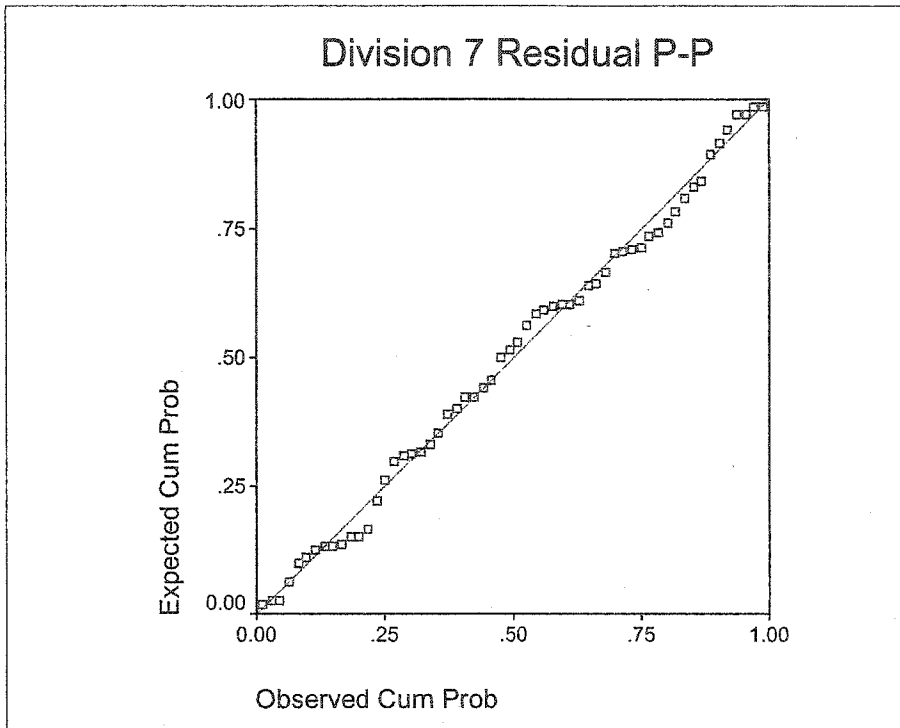


Figure A.6: Palmer Z residuals versus SMI residuals, by climate division.

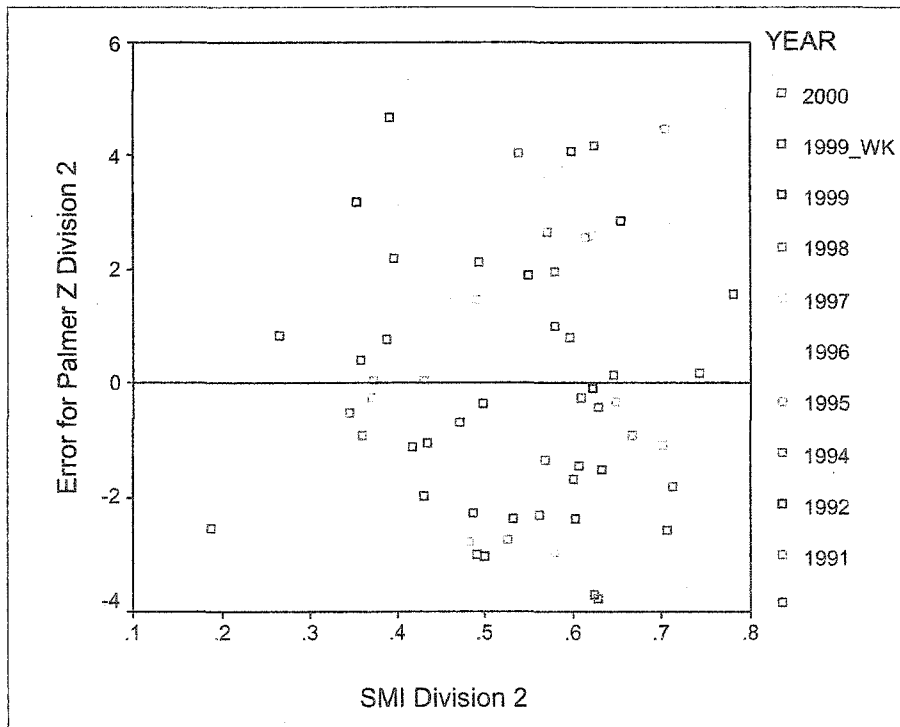
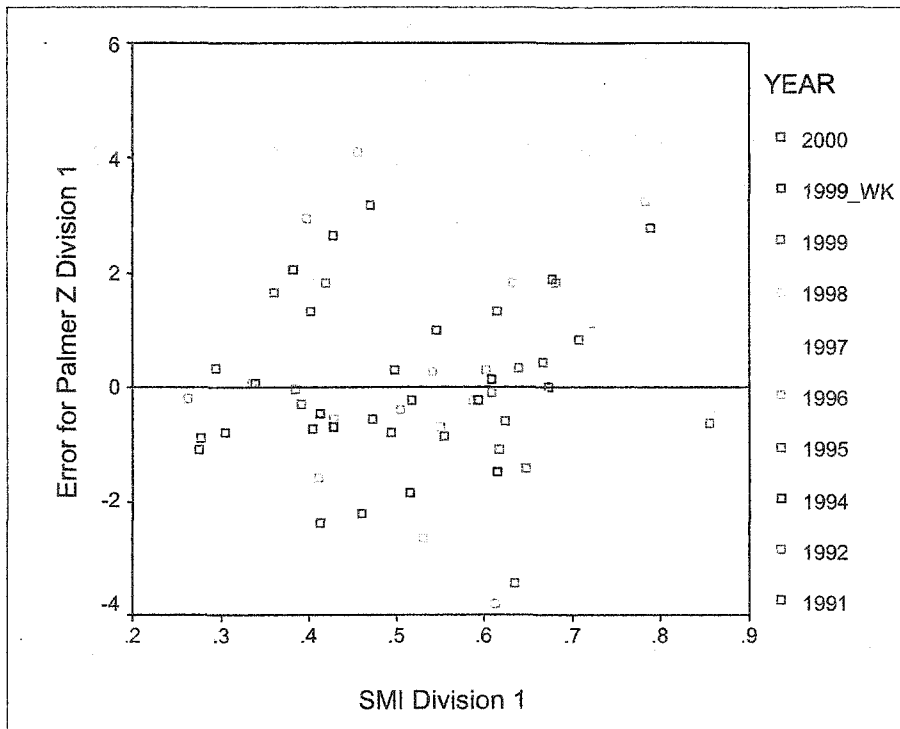


Figure A.6: Palmer Z residuals versus SMI residuals, by climate division (CONTINUED).

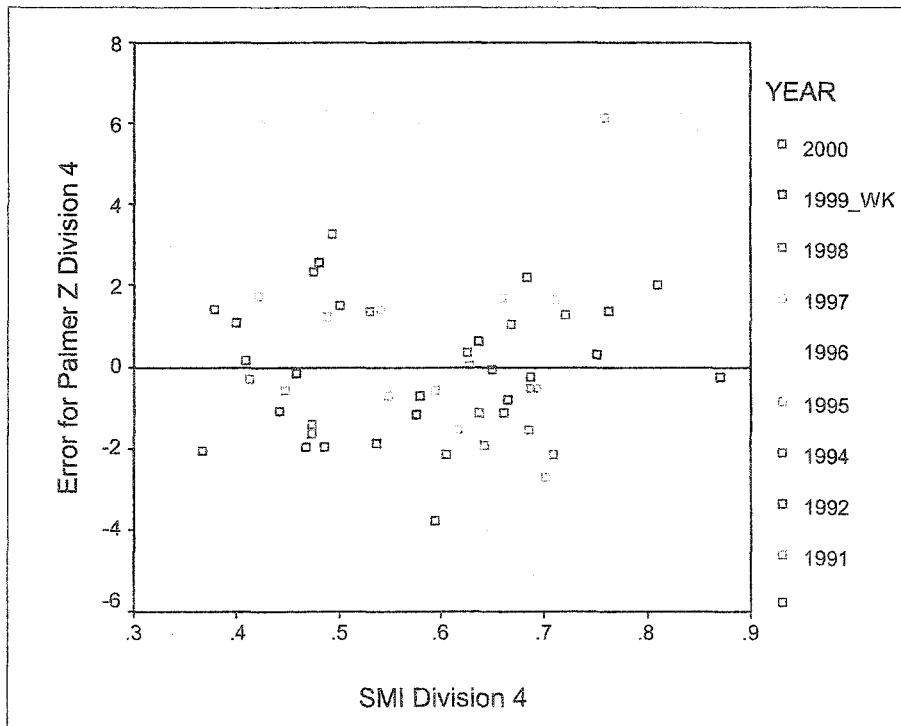
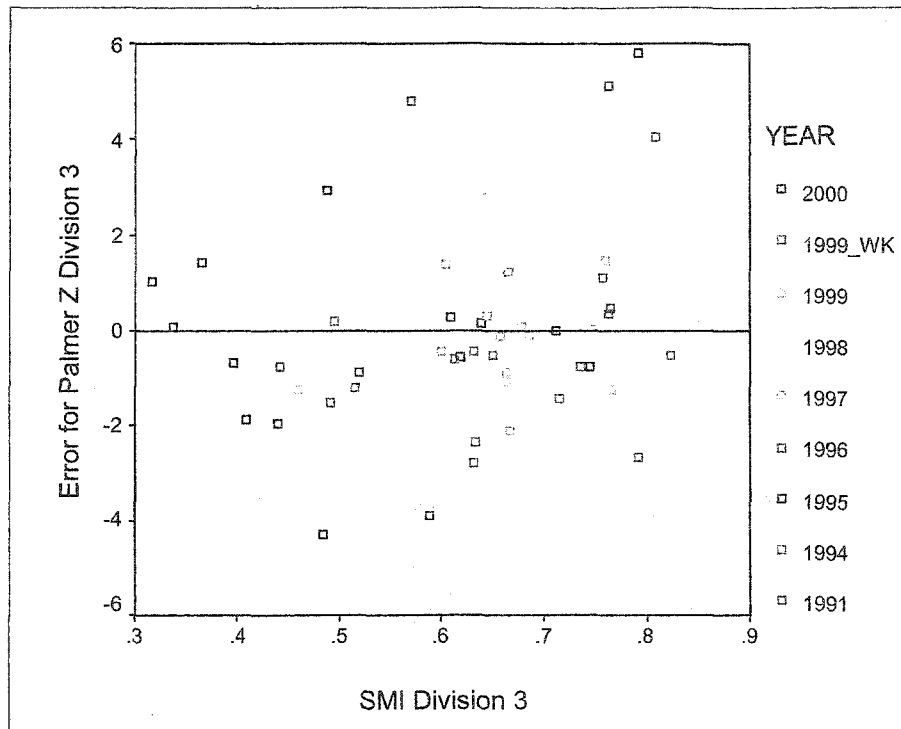


Figure A.6: Palmer Z residuals versus SMI residuals, by climate division (CONTINUED).

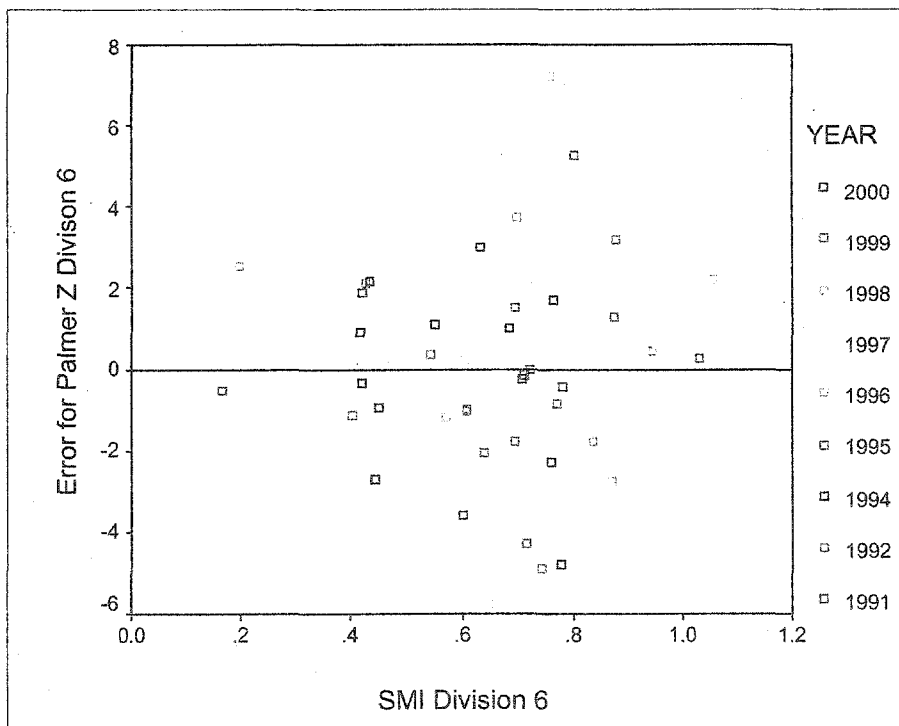
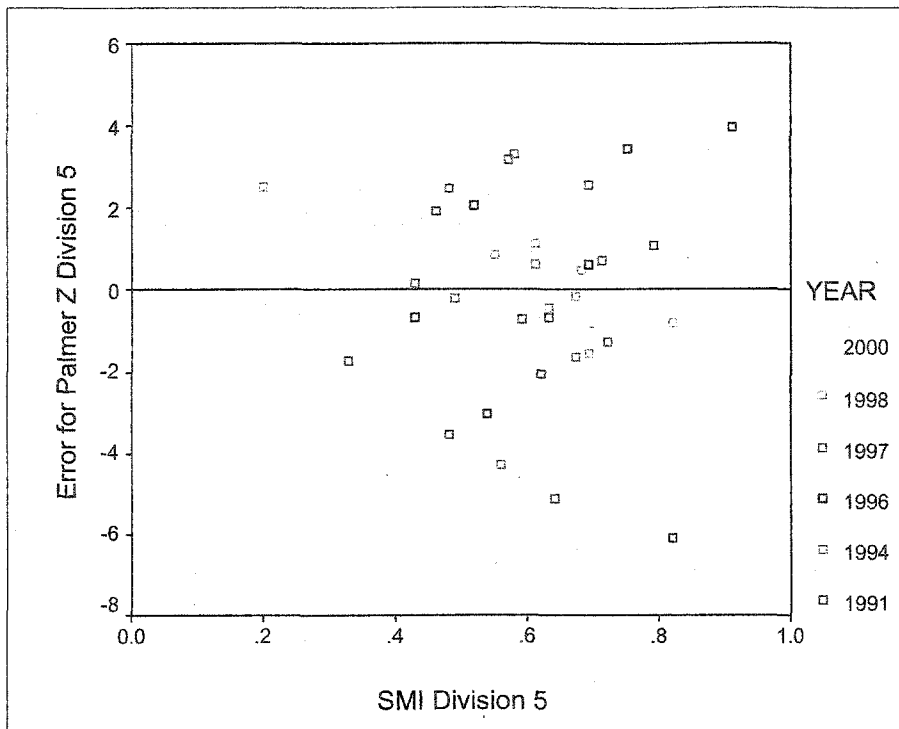
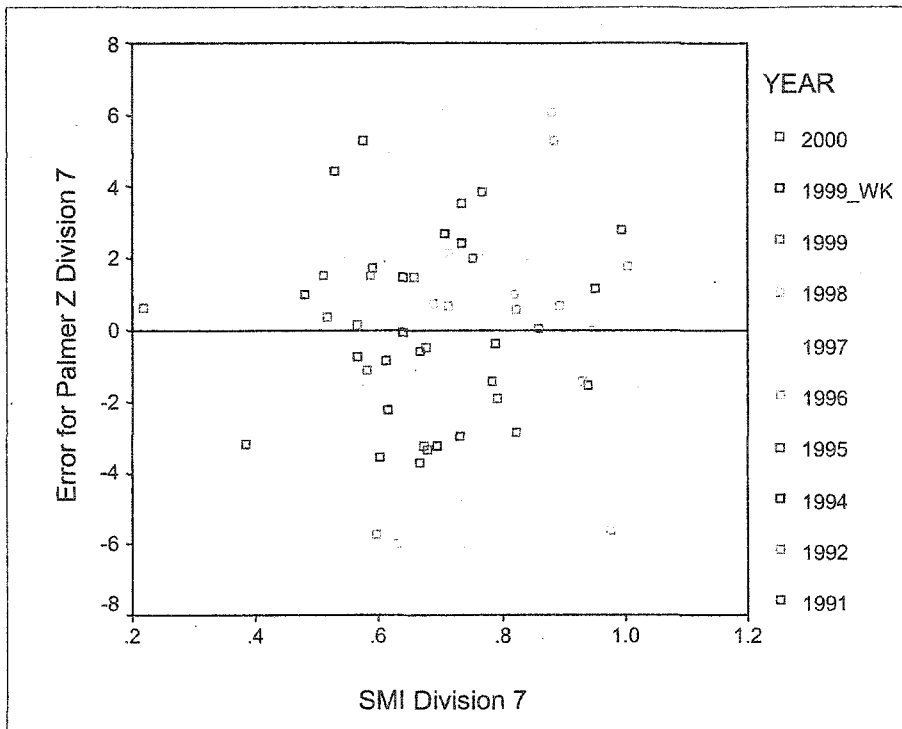


Figure A.6: Palmer Z residuals versus SMI residuals, by climate division (CONTINUED).



LITERATURE CITED

- Alley, W.M., 1984. The Palmer Drought Severity Index: Limitations and Assumptions. *Journal of Climate and Applied Meteorology*, 23: 1100-1109.
- Box, G.E.P. and Jenkins, G.M., 1970. *Time Series Analysis: Forecasting and Control*. Holder Day, San Francisco, 553 pp.
- Doesken, N.J., McKee, T.B. and Kleist, J., 1991. Development of a Surface Water Supply Index for the Western United States. *Climatology Reprints 91-3*. Colorado Climate Center, Department of Atmospheric Science, Colorado State University, Fort Collins, CO., 76 pp.
- Heim, R.R., 2002. A Review of Twentieth-Century Drought Indices Used in the United States. *Bulletin of the American Meteorological Society*(August 2002): 1149-1165.
- Hu, Q. and Willson, G.D., 2000. Effects of Temperature Anomalies on the Palmer Drought Severity Index in the Central United States. *International Journal of Climatology*, 20: 1899-1911.
- Karl, T.R., 1986. The Sensitivity of the Palmer Drought Severity Index and Palmer's Z-Index to Their Calibration Coefficients Including Potential Evapotranspiration. *Journal of Climate and Applied Meteorology*, 25: 77-86.
- Keetch, J.J. and Byram, G.M., 1968. *A Drought Index for Forest Fire Control*. Southeastern Forest Experiment Station, Asheville, N.C., 33 pp.
- Kennedy, P., 2003. *A Guide to Econometrics*. The MIT Press, Cambridge, MA, 623 pp.
- McCuen, R.H., 2003. *Modelling Hydrologic Change: Statistical Methods*. Lewis Publishers, Boca Raton, FL, 433 pp.
- McKee, T.B., Doesken, N.J. and Kleist, J., 1993. The Relationship of Drought Frequency and Duration to Time Scales, Eighth Conference on Applied Climatology. American Meteorological Society, Anaheim, CA., pp. 179-184.
- Palmer, W.C., 1965. *Meteorological Drought*. U.S. Weather Bureau Research Paper 45, 58 pp.
- Quiring, S.M. and Papakryiakou, T.N., 2003. An Evaluation of Agricultural Drought Indices for the Canadian Prairies. *Agricultural and Forest Meteorology*, 118: 49-62.
- Shear, J.A. and Steila, D., 1974. The Assessment of Drought Intensity by a New Index. *Southeastern Geographer*, 13: 195-201.
- Stoms, D.M., Bueno, M.J. and Davis, F.W., 1997. Viewing Geometry of AVHRR image Composites Derived Using Multiple Criteria. *Photogrammetric Engineering and Remote Sensing*, 6: 681-689.
- Thornthwaite, C.W., 1931. The Climate of North America According to a New Classification. *Geographic Reviews*, 21: 633-655.
- Vidal, A. and Devaux-Ros, C., 1995. Evaluating Forest Fire Hazard with a LANDSAT TM Derived Water Stress Index. *Agricultural and Forest Meteorology*, 77: 207-224.

White, M.A., Thornton, P.E. and Running, S.W., 1997. A Continental Phenology Model for Monitoring Vegetation Response to Interannual Climatic Variability. *Global Biogeochemical Cycles*, 11(2): 217-234.